

# **Retrieval and analysis of tropospheric bromine monoxide enhancements in polar regions using satellite measurements**

Sora Seo



 **Universität Bremen**

*Dissertation zur Erlangung des Grades Doktor der Naturwissenschaften  
(Dr.rer.nat.)*

Institut für Umweltphysik  
Fachbereich Physik und Elektrotechnik  
Universität Bremen  
Oktober 2020



1. Gutachter:	Prof. Dr. John P. Burrows
2. Gutachter:	Prof. Dr. Thomas Wagner
Betreuer:	PD Dr. Andreas Richter
Dissertation eingereicht am:	15. Oktober 2020
Datum des Kolloquiums:	9. Dezember 2020



# Abstract

Bromine compounds have received growing attention due to their impact on the atmospheric chemistry in particular ozone chemistry and the resulting oxidation capacity. Reactive bromine is involved in chain reactions that deplete ozone in the stratosphere as well as catalytically destroy ozone in the troposphere leading to nearly complete removal near the surface called as an ozone depletion event (ODE). Bromine monoxide (BrO) is the most commonly observed bromine species and large amounts of BrO are observed in the polar regions during spring time through bromine explosion events. In addition to polar sea ice regions, high BrO concentrations are also detected over salt lakes/marshes, in the marine boundary layer and volcanic plumes. Over the last decades, BrO vertical column density has been retrieved with satellite-based UV-visible instruments such as GOME, SCIANACHY, OMI and GOME-2 for the monitoring of bromine amounts in various source regions. In particular, TROPOMI which was launched in October 2017 provides daily global coverage as the predecessor instruments, but with its unprecedented high spatial resolution ( $3.5 \times 5.5 \text{ km}^2$ ), this instrument enables to detect spatial variations and small-scale emission sources in more detail.

The aim of my doctoral project is to develop an advanced algorithm to derive accurate total and tropospheric BrO columns by using the improved spatial resolution of TROPOMI data. In the first part of this thesis, a description of total/tropospheric BrO retrieval algorithm is presented. Optimized DOAS settings for the BrO retrieval are determined based on sensitivity tests under various measurement conditions. Approaches for the stratospheric correction to separate the tropospheric partial columns from total BrO columns are tested using several different methods. Also, air mass factor calculations for TROPOMI are performed by considering various observation conditions. As a consistency test, TROPOMI BrO columns are compared with OMI and GOME-2 retrieval results on both global and regional scales.

Satellite BrO retrievals for a large spatial coverage over a long-term period can be used to explain the causes of BrO enhancements in the polar regions during spring and the role and characteristics of meteorological factors contributing to them. In the next chapter, the relationship between satellite total BrO vertical columns and meteorological fields including sea level pressure, surface level wind

speed and direction, surface air temperature, and tropopause height are investigated. Statistical analysis using decadal GOME-2A/B observations reveals spatial and temporal behaviors of total BrO column enhancements in the Arctic and Antarctic. Also, differences in meteorological conditions and their regional characteristics between enhanced BrO situations and the mean field are identified, which shows effects of meteorological parameters on BrO enhancement processes.

Finally, the satellite BrO retrieval algorithm developed in this thesis is verified by comparing satellite BrO columns with ground-based MAX-DOAS BrO measurements in Ny-Ålesund, Svalbard, operated by IUP-Bremen DOAS group. The possibilities and needs for improving the BrO retrieval algorithm are discussed based on the satellite retrieval algorithm validation results. Also, using both satellite and ground-based MAX-DOAS tropospheric BrO retrievals, bromine explosion event cases in Ny-Ålesund are investigated in detail, and moreover, capabilities of TROPOMI to investigate small-scale halogen chemistry are discussed.

# Publications

Large parts of this thesis, including text passages, figures, and tables, are based on and/or cited from peer reviewed journals, oral and poster presentations produced during the thesis. Individual sections that contain such text passages, figures, and tables from published articles, are indicated by an asterisk and appropriate footnotes throughout this thesis.

## Articles in peer-reviewed journals

- **Seo, S.**, Richter, A., Blechschmidt, A.-M., Bougoudis, I., and Burrows, J. P.: First high-resolution BrO column retrievals from TROPOMI, *Atmos. Meas. Tech.*, 12, 2913–2932, <https://doi.org/10.5194/amt-12-2913-2019>, 2019.
- **Seo, S.**, Richter, A., Blechschmidt, A.-M., Bougoudis, I., and Burrows, J. P.: Spatial distribution of enhanced BrO and its relation to meteorological parameters in Arctic and Antarctic sea ice regions, *Atmos. Chem. Phys.*, 20, 12285–12312, <https://doi.org/10.5194/acp-20-12285-2020>, 2020.
- Bougoudis, I., Blechschmidt, A.-M., Richter, A., **Seo, S.**, Burrows, J. P., Theys, N., and Rinke, A.: Long-term time series of Arctic tropospheric BrO derived from UV-VIS satellite remote sensing and its relation to first-year sea ice, *Atmos. Chem. Phys.*, 20, 11869–11892, <https://doi.org/10.5194/acp-20-11869-2020>, 2020.

## Conference contributions

### Selected presentations

- **Seo, S.**, Richter, A., Blechschmidt, A.-M., Bougoudis, I., and Burrows, J. P., Retrieval of BrO and its enhancement analysis in polar sea ice regions from satellite measurements, IUP seminar, Bremen, Germany, Jan 2020.
- **Seo, S.**, Richter, A., Blechschmidt, A.-M., Bougoudis, I., and Burrows, J. P., Arctic BrO from Sentinel-5p, IUP-AWI Block seminar, Bremen, Germany, Feb 2019.

- **Seo, S.**, Richter, A., Blechschmidt, A.-M., Bougoudis, I., and Burrows, J. P., Satellite observations of bromine explosion events over the Antarctica, Short Course: "20 Years Bromine Explosion: Atmospheric Chemistry in the Polar Troposphere", Heidelberg University, Heidelberg, Germany, Nov 2017.
- **Seo, S.**, Richter, A., Blechschmidt, A.-M., Bougoudis, I., and Burrows, J. P., Detection of BrO plumes over various sources using OMI and GOME-2 measurements, EGU General Assembly, Vienna, Austria, Apr 2017.

### **Selected posters**

- **Seo, S.**, Richter, A., Blechschmidt, A.-M., Wittrock, F., Huijnen, V., and Burrows, J.P., BrO retrievals using TROPOMI on Sentinel-5 Precursor and comparison with independent satellites and ground-based measurements, AGU Fall meeting, San Francisco, USA, Dec 2019.
- **Seo, S.**, Richter, A., Blechschmidt, A.-M., Bougoudis, I., and Burrows, J. P., First high resolution BrO retrievals and small-scale enhancement analysis from TROPOMI onboard Sentinel-5 Precursor, Living Planet Symposium 2019, May 2019.
- **Seo, S.**, Richter, A., Blechschmidt, A.-M., Bougoudis, I., Burrows, J.P., First BrO retrievals and small-scale enhancement analysis in the Arctic using TROPOMI/S5P, 2nd (AC)<sup>3</sup> Science Conference on Arctic Amplification, Bremerhaven, Germany, November 2018.
- **Seo, S.**, Richter, A., Blechschmidt, A.-M., Burrows, J.P., Developing a BrO product for S-5P, EGU General Assembly, Vienna, Austria, April 2018.
- **Seo, S.**, Richter, A., Blechschmidt, A.-M., Burrows, J.P., Satellite observations of enhanced tropospheric BrO plumes around polar coastal polynyas, EGU General Assembly, Vienna, Austria, April 2018.
- **Seo, S.**, Richter, A., Blechschmidt, A., Burrows, J. P., Combination of different satellite observations of BrO over Antarctica, 8th International DOAS Workshop, Yokohama, Japan, September 2017.

# Acknowledgements

I am very grateful for the opportunity to do my PhD at the Institut für Umweltphysik (IUP) in Bremen and to be part of the wonderful DOAS group. There are so many people, I would like to thank for their support.

First, I would like to express my sincere gratitude to Prof. John P. Burrows for the continuous support of my PhD study and related research. His guidance helped me in all the time of research and writing of this thesis. Thank you for making me part of this excellent research institute and for your advice and support during all these years.

I am deeply thankful to Dr. Andreas Richter for being my supervisor. I appreciate all your support, contributions of time, ideas, and advices to make my PhD experience productive and stimulating. I have been taught by you not only in research, but also in my career and attitude of life. I am lucky to have met you as a good advisor and mentor during my PhD study.

Besides my advisors, my sincere thanks also goes to my thesis committee members for their insightful comments and valuable questions that broaden my scientific perspectives. A special thanks to Dr. Lars Kaleschke for giving valuable guidance and ideas during PhD committee meetings.

Further I would like to express my appreciation to our IUP-DOAS group members. They have contributed immensely to my private and research time in my PhD journey. Thank you for all your advice and discussions which helped to improve my work. In addition to the research, I appreciate all your help in adapting to German life and having a fun and comfortable time.

Special thanks to Dr. Anne-Marlene Blechschmidt and Ilias Bougoudis, who worked on the (AC)<sup>3</sup> research project and papers together. Many discussions and valuable suggestions I got through every BrO meeting helped me a lot in conducting my PhD research.

Last but not the least, I would like to express a deep sense of gratitude to my family: my parents and brother for always believing me and supporting me unconditionally.



# Contents

<b>Contents</b> .....	<b>xi</b>
<b>List of figures</b> .....	<b>xv</b>
<b>List of tables</b> .....	<b>xix</b>
<b>1. Introduction</b> .....	<b>1</b>
<b>2. Scientific background</b> .....	<b>5</b>
2.1 The Earth's atmosphere .....	5
2.2 Halogens in the atmosphere.....	8
2.2.1 Halogens in the stratosphere.....	8
2.2.1.1 Sources of reactive halogen species in the stratosphere.....	8
2.2.1.2 Stratospheric halogen chemistry .....	10
2.2.2 Halogens in the troposphere .....	12
2.2.2.1 Sources of reactive halogen species in the troposphere.....	12
2.2.2.2 Tropospheric halogen chemistry .....	14
2.3 Absorption spectroscopy.....	17
2.3.1 Electromagnetic radiation .....	17
2.3.2 Energy states and molecular transitions.....	18
2.3.3 Solar spectrum.....	19
2.3.4 Atmospheric radiative transfer .....	21
2.3.5 Scattering in the atmosphere .....	21
2.3.6 Absorption in the atmosphere .....	25
2.3.7 Differential Optical Absorption Spectroscopy .....	26
2.3.8 Atmospheric air mass factor .....	29
2.4 Description of instruments.....	31
2.4.1 Satellite instruments .....	31
2.4.1.1 OMI.....	31

2.4.1.2 GOME-2 .....	32
2.4.1.3 TROPOMI .....	32
2.4.2 Ground-based MAX-DOAS instrument.....	34
<b>3. Tropospheric BrO retrievals from high spatial resolution satellite data ..</b>	<b>35</b>
3.1 Introduction.....	35
3.2 Satellite BrO retrieval algorithm description.....	37
3.3 DOAS BrO slant column retrievals .....	38
3.3.1 Sensitivity test of retrieval fitting interval.....	38
3.3.1.1 BrO retrievals over the polar sea ice region.....	41
3.3.1.2 BrO retrievals over a salt marsh.....	44
3.3.1.3 BrO retrievals in a volcanic plume.....	45
3.3.1.4 BrO retrievals over clear scenes in the Pacific background region	46
3.3.1.5 BrO retrievals over cloudy scenes in the Pacific background region	47
3.3.1.6 Selection of optimal fitting window .....	48
3.3.2 Destriping and offset correction.....	51
3.4 Observations of total BrO column from space .....	52
3.4.1 Global observations of BrO and satellite intercomparison.....	52
3.4.2 BrO plumes over polar sea ice regions .....	56
3.4.3 BrO plumes over salt lakes/salt marsh .....	59
3.4.4 BrO enhancements in volcanic plumes.....	60
3.5 Stratospheric correction.....	62
3.5.1 3-D atmospheric chemistry transport model .....	64
3.5.2 Climatological approach.....	67
3.5.3 Empirical multiple linear regression model.....	68
3.5.4 Comparison of different stratospheric correction methods.....	69
3.6 Tropospheric air mass factor calculation .....	71
3.7 Tropospheric BrO vertical column retrievals .....	77

3.8 Summary and conclusions .....	79
<b>4. BrO enhancements in polar sea ice regions .....</b>	<b>81</b>
4.1 Introduction .....	81
4.2 Dataset and method .....	84
4.2.1 Dataset.....	84
4.2.1.1 GOME-2 total BrO column.....	84
4.2.1.2 Sea ice data .....	86
4.2.1.3 Meteorological data .....	87
4.2.2 Method .....	88
4.2.2.1 Data matching .....	88
4.2.2.2 Detection of enhanced total geometric BrO columns over sea ice regions.....	88
4.3 Result.....	91
4.3.1 Frequencies of enhanced BrO columns and spatial distributions.....	91
4.3.2 Relationship between enhanced BrO columns and meteorological parameters .....	94
4.3.2.1 Sea level pressure .....	94
4.3.2.2 Surface level temperature.....	97
4.3.2.3 Surface level wind speed and direction .....	101
4.3.2.4 Tropopause height .....	110
4.3.3 Correlation analysis between total BrO vertical column and meteorological parameters .....	113
4.4 Summary and conclusions .....	120
<b>5. Tropospheric BrO retrievals from MAX-DOAS measurements .....</b>	<b>123</b>
5.1 Introduction .....	123
5.2 Measurement site and instrument .....	124
5.2.1 Measurement site .....	124
5.2.2 Instrument.....	125
5.3 MAX-DOAS tropospheric BrO retrieval.....	127

5.4 Comparison of MAX-DOAS and satellite BrO vertical columns.....	130
5.5 Case studies for tropospheric BrO explosion events.....	133
5.6 Summary and conclusions.....	139
<b>6. Conclusions and outlook.....</b>	<b>141</b>
<b>Appendix .....</b>	<b>147</b>
<b>Bibliography .....</b>	<b>150</b>

# List of figures

Figure 2.1	The layers of the Earth's atmosphere with the temperature profile	6
Figure 2.2	A simplified scheme of multiphase chemistry of bromine, especially for bromine explosion reactions in the troposphere	16
Figure 2.3	Sketch of the electromagnetic spectrum with frequency and wavelength	18
Figure 2.4	Diagram of rotational-vibrational energy levels in two electronic states of a molecule	19
Figure 2.5	The solar radiation spectrum for direct light both at the top of the Earth's atmosphere and at sea level	20
Figure 2.6	Polar diagram of the Rayleigh scattering phase function $P(\theta)$ for non-polarised light	23
Figure 2.7	Phase functions of Mie scattering for a small droplet size ( $\alpha=1$ ; left) and for a large droplet size ( $\alpha=5$ ; right).	24
Figure 2.8	The absorptivity of individual atmospheric gases as a function of wavelength	26
Figure 2.9	The differential cross section, $\sigma'$ , is the difference between the total cross section, $\sigma$ and the slowly varying part, $\sigma^s$	27
Figure 2.10	Schematic illustration of the Solar Zenith Angle (SZA) and Viewing Zenith Angle (VZA) for observations from satellite-based instrument	30
Figure 2.11	Schematic of the measurement principle of the TROPOMI instrument	33
Figure 2.12	Spectral ranges for TROPOMI and previous instruments GOME, SCIAMACHY, and OMI	33
Figure 2.13	Schematic representations of the zenith-sky DOAS and MAX-DOAS measurement geometry	34
Figure 3.1	Flow diagram of the tropospheric BrO retrieval algorithm from the satellite Level 1b spectra	37
Figure 3.2	Reference absorption cross sections used in the sensitivity test of DOAS BrO retrieval	41
Figure 3.3	Color-coded means of BrO SCDs and fitting rms values retrieved over the selected Arctic sea ice region for a BrO explosion event using TROPOMI measurements at different wavelength intervals	43
Figure 3.4	Color-coded means of HCHO SCDs and relative difference between BrO SCDs retrieved including the HCHO absorption cross section and those without HCHO for the Arctic BrO measurement scenario	43
Figure 3.5	As Fig. 3.3 but for the Rann of Kutch salt marsh	44
Figure 3.6	As Fig. 3.3, but for the selected volcanic plume case	45
Figure 3.7	TROPOMI UV aerosol index and OMI SO <sub>2</sub> vertical columns from the OMSO2 product for a volcanic BrO measurement scenario	46

Figure 3.8	Mean values of BrO SCDs, fitting rms values, and root-mean square deviation of BrO SCDs retrieved over the clear part of the scene in the Pacific background region using TROPOMI measurements at different wavelength intervals	47
Figure 3.9	As Fig. 3.8 but for the cloudy part of the Pacific background region	48
Figure 3.10	Example of a BrO fit result applying DOAS settings of Table 3.2 in the Arctic BrO measurement case	50
Figure 3.11	Illustration showing destriping and offset correction steps using TROPOMI orbit 2207 on 17 March 2018	52
Figure 3.12	Global distributions of monthly mean BrO vertical columns retrieved from TROPOMI, OMI, and GOME-2B measurements as well as distribution of BrO SCDs and fitting rms values over a clean equatorial Pacific region	55
Figure 3.13	Intercomparison between three different satellite BrO retrievals in the selected Arctic region of enhanced BrO plumes	56
Figure 3.14	BrO geometric vertical columns observed over the Arctic sea ice region on 10 April 2018 by TROPOMI, OMI, and GOME-2B	57
Figure 3.15	BrO geometric vertical columns observed over the Arctic sea ice region on 19 April 2018 from TROPOMI, OMI, and GOME-2B. MODIS Aqua true color image and image using combinations of 7-2-1 bands for the same scene.	58
Figure 3.16	Daily BrO geometric vertical columns over the Rann of Kutch salt marsh from TROPOMI and OMI measurements as well as MODIS Aqua true color images	60
Figure 3.17	Volcanic BrO vertical columns on 29 November 2017 after volcanic eruptions at Mount Agung observed by TROPOMI and OMI	61
Figure 3.18	Maps of stratospheric O <sub>3</sub> and NO <sub>2</sub> vertical column densities from GOME-2A measurements, CB05-BASCOE, MOCAGE, and MOZART model data for March 23, 2011 over the northern hemisphere	66
Figure 3.19	Tropospheric BrO slant column densities calculated from GOME-2B measurements applying three different stratospheric correction methods	70
Figure 3.20	Comparison of tropospheric BrO SCD calculated by three different stratospheric correction methods for the data shown in Fig. 3.19	70
Figure 3.21	Maps of surface albedo, tropospheric AMF, and the retrieved tropospheric BrO VCD from TROPOMI data using GOME-2 LER climatology and TROPOMI G3_LER	75
Figure 3.22	Maps of surface albedo and the retrieved tropospheric BrO VCD from TROPOMI data using GOME-2 LER climatology and TROPOMI G3_LER with zoomed in the study area labeled (i) in Fig. 3.21	76
Figure 3.23	As Fig. 3.22, but zoomed in the study area labeled in (ii) in Fig. 3.21	76
Figure 3.24	Maps of tropospheric BrO VCD from TROPOMI and GOME-2C over Svalbard from 3 May to 7 May 2019	78
Figure 4.1	Monthly histograms of the total BrO VCD from GOME-2 measurements during the study period of 2008-2018 for the Arctic	90

	and Antarctic	
Figure 4.2	Monthly spatial distribution of the occurrence frequency of enhanced total BrO columns over the Arctic and Antarctic sea ice region during the study period	93
Figure 4.3	Frequency distribution of sea level pressure for all data and enhanced BrO cases in the Arctic and Antarctic in spring	95
Figure 4.4	Monthly sea level pressure for the mean field, the enhanced BrO case, and sea level pressure anomalies over the Arctic in March and April	96
Figure 4.5	As Fig. 4.4, but for the Antarctic in September and October	97
Figure 4.6	Frequency distribution of surface air temperature for all data and the enhanced BrO cases in the Arctic and Antarctic in spring	98
Figure 4.7	Monthly surface air temperature for the mean field, the enhanced BrO case, and surface air temperature anomalies over the Arctic in March and April	99
Figure 4.8	As Fig. 4.7, but for the Antarctic in September and October	100
Figure 4.9	Frequency distribution of wind speed at 10 m for all data and the enhanced BrO cases in the Arctic and Antarctic in spring	102
Figure 4.10	Monthly wind speed at 10 m for the mean field, the enhanced BrO case, and wind speed anomalies over the Arctic in March and April	103
Figure 4.11	As Fig. 4.10, but for the Antarctic in September and October	104
Figure 4.12	Spatial distributions of the relative frequency of high wind speeds during the enhanced BrO occurrences in the Arctic and Antarctic sea ice region in spring	104
Figure 4.13	Relative frequency maps of surface level wind direction for data with BrO enhancements over the Arctic during spring	107
Figure 4.14	Spatial distributions of the differences in relative frequencies of wind direction between enhanced BrO cases and the mean field for the Arctic in spring	108
Figure 4.15	As Fig. 4.13, but for the Antarctic during spring	108
Figure 4.16	As Fig. 4.14, but for the Antarctic during spring	109
Figure 4.17	Frequency distribution of tropopause height for all data and the enhanced BrO cases in the Arctic and Antarctic in spring	111
Figure 4.18	Monthly tropopause height for the mean field, the enhanced BrO case, and tropopause anomalies over the Arctic in March and April	112
Figure 4.19	As Fig. 4.18, but for the Antarctic in September and October	113
Figure 4.20	Spatial distributions of the Spearman correlation coefficients between total BrO VCD and four meteorological parameters for the Arctic and Antarctic in spring	116
Figure 4.21	Box and whisker plots of the time-lagged correlation between the total BrO VCD and each meteorological parameter in the Arctic	119
Figure 4.22	As Fig. 4.21, but for the Antarctic sea ice region	120

Figure 5.1	Map showing the location of Ny-Ålesund, Svalbard in the Arctic and a landscape photo around Ny-Ålesund during summer	125
Figure 5.2	Illustration of the MAX-DOAS instrument installed at the NDACC station in Ny-Ålesund	126
Figure 5.3	Photos of the MAX-DOAS instrument installed at the NDACC station in Ny-Ålesund	126
Figure 5.4	Example of BrO and O <sub>3</sub> fit result applying the DOAS setting for MAX-DOAS measurements at elevation angle of 6° on 17 April 2014	127
Figure 5.5	MAX-DOAS BrO dSCDs at different elevation viewing angles and BrO VCDs using the geometrical approximation at 15° elevation angle	129
Figure 5.6	Time series of tropospheric BrO VCDs over Ny-Ålesund retrieved from MAX-DOAS measurements and GOME-2B satellite measurements	131
Figure 5.7	Scatter plots of MAX-DOAS tropospheric BrO vertical columns versus GOME-2B tropospheric vertical columns applying three different stratospheric corrections	132
Figure 5.8	Time series of tropospheric BrO VCDs retrieved from MAX-DOAS measurements and different meteorological parameters	135
Figure 5.9	Box and whisker plots for meteorological parameters according to MAX-DOAS tropospheric BrO VCDs	136
Figure 5.10	Wind rose diagram showing the average value of MAX-DOAS tropospheric BrO VCD for each wind direction at 45°	136
Figure 5.11	GOME-2 tropospheric BrO VCDs and various meteorological conditions for selected tropospheric BrO event days over Ny-Ålesund	138
Figure 5.12	CALIOP vertical feature masks during tropospheric BrO explosion events	139
Figure A1	Color-coded means of BrO SCDs and fitting rms values retrieved when including the Taylor series approach for O <sub>3</sub> in the DOAS analysis	148
Figure A2	Color-coded means of differences for BrO SCDs and fitting rms values between analyses including the Taylor series approach and the standard DOAS	149

# List of tables

Table 2.1	Compositions of Earth's atmosphere with respect to dry air in fractional concentrations in volume	7
Table 2.2	Input information used for radiative transfer simulations of tropospheric trace gases	31
Table 3.1	Geographical and time information for the different scenarios of the sensitivity tests in Sect. 3.3.1	40
Table 3.2	DOAS settings used for the BrO slant column retrievals and instrumental intercomparison	50
Table 3.3	Parameters in the pre-calculated box air mass factor look-up table	72
Table 4.1	Summary of DOAS settings used for the GOME-2 BrO slant column retrievals	86
Table 4.2	Relative frequency (expressed in %) of surface level wind directions for all data, the enhanced BrO case and the enhanced BrO with high wind speeds for the Arctic and Antarctic in spring	109
Table 4.3	Spearman rank correlation coefficients between total BrO VCDs and four meteorological parameters. The results are shown separately for different months in spring in the Arctic and Antarctic. Note that all Spearman's rank correlation coefficients are significant ( $p < 0.001$ )	117
Table 4.4	Cross-correlations of meteorological parameters for the enhanced total BrO cases in the Arctic and Antarctic sea ice region	118
Table 5.1	DOAS BrO fit settings used for MAX-DOAS measurements	127



# 1

## Introduction

Bromine compounds play an important role in atmospheric chemistry in particular with respect to removal of ozone. It has been estimated that bromine contributes about 25% to the global destruction of stratospheric ozone, and up to 50% to polar stratospheric O<sub>3</sub> depletion (McElroy et al., 1986; Harder et al., 2000). Stratospheric bromine is mostly present in its inorganic form, originating from both natural and anthropogenic organic source gases. Man-made halogenated hydrocarbons (halons) and methyl bromide (CH<sub>3</sub>Br) released from the ocean by natural processes are stable and long-lived, which allows them to reach the stratosphere mainly in the tropics (Harder et al., 2000; Theys et al., 2009a). In addition to the contribution of these long-lived organic source gases, short-lived bromine compounds which are mainly of natural origin could also affect the stratospheric bromine budget (Sinnhuber et al., 2005; Liang et al., 2010). In the stratosphere, organic bromine source gases are converted into inorganic forms of Br<sub>y</sub>, such as Br, BrO, BrONO<sub>2</sub>, HOBr, HBr, BrCl, Br<sub>2</sub>, either by direct photolysis or by reaction with OH and O (Sinnhuber et al., 2005; Theys et al., 2009). Inorganic bromine is then involved in various stratospheric chemical reactions.

Bromine is present in the troposphere as well as in the stratosphere. One of the major tropospheric bromine sources is the polar sea ice region. Release of reactive bromine in polar regions in spring was first deduced from tropospheric ozone depletion events (Bottenheim et al., 1986; Barrie et al., 1988). Large amounts of active bromine compounds can be released by an autocatalytic heterogeneous mechanism called “bromine explosion” and act as a primary oxidant for many species including ozone, methane and mercury (Fan and Jacob, 1992; McConnell et al., 1992; Simpson et al., 2007). Potential sources of reactive bromine in the polar boundary layer are sea salt aerosols (Fan and Jacob, 1992), surfaces of first year sea ice (Simpson et al., 2007; Wagner et al., 2007), frost flowers (Kaleschke et al., 2004), or blowing snow triggered by strong winds (Yang et al., 2008; Jones et al., 2009; Blechschmidt et al., 2016). Although more localized and small-scale,

## 1. Introduction

tropospheric bromine is also detected over salt lakes or marshes (Hebestreit et al., 1999; Hörmann et al., 2016), in volcanic plumes (Bobrowski et al., 2003; Theys et al., 2009a) and in the marine boundary layer (Sander et al., 2003; Saiz-Lopez et al., 2004). In recent years, in line with the climate warming in the Arctic, studies on the tropospheric bromine trends and chemistry have become more important. As Arctic air temperature has risen at twice the rate of the global mean over the decades, which is called Arctic Amplification, the sea ice extent has been decreased and the production of younger sea ice has been increased. As a result, more of the incoming solar radiation is absorbed by the open water and its biosphere (i.e. phytoplankton), which leads to changes in radiative forcing, atmospheric loading of halogens and chemistry including oxidative capacity.

Bromine monoxide (BrO), an intermediate in the catalytic loss of ozone, is one of the most commonly observed indicators of reactive bromine species and can be measured by both ground-based and satellite measurements. BrO absorbs ultraviolet radiation with specific absorption features, which enables a measurement using remote sensing technique, in particular, Differential Optical Absorption Spectroscopy (DOAS). Ground-based and in-situ observation methods of BrO reported so far are (1) Long Path DOAS (LP-DOAS) measurements (Hausmann and Platt, 1994; Hönninger et al., 2004), (2) sky and direct sun DOAS (Eisinger et al., 1997; Hendrick et al., 2007) (3) Multi-AXis DOAS (MAX-DOAS) measurements (Hönninger, 2004; Frieß et al., 2011), and (4) in-situ Chemical-Ionization Mass Spectrometry (CIMS) (Neuman et al., 2010; Liao et al., 2011). Although it is not a fixed ground-based instrument, balloon-born instruments also can measure profiles of bromine compounds using a variety of spectroscopic methods (Fitzenberger et al., 2000; Dorf et al., 2008).

Ground-based instruments can provide good temporal coverage and some vertical profile resolution, whereas space-based observations of BrO are much superior to the spatial coverage available from ground-based measurements and good for monitoring large-scale bromine explosion events. The first satellite observations of polar BrO events were performed using the GOME (Global Ozone Monitoring Experiment) instrument (Wagner and Platt, 1998; Richter et al., 1998; Chance, 1998; Burrows et al., 1999). A long time-series of total BrO columns and the spatial distribution of regions with enhanced BrO in both hemispheres were investigated using 6 years of GOME data (Hollwedel et al., 2004), finding that general features of the BrO distribution are similar between years but the strength

## 1. Introduction

of BrO explosion events varies from year to year with an increasing trend in both polar regions. SCIAMACHY (SCanning Imaging Absorption spectrometer for Atmospheric CHartography), which was launched after GOME, could measure scattered and reflected solar radiation in limb and nadir geometry (Burrows et al., 1995; Bovensmann et al., 1999). Thus, both BrO vertical profiles and BrO column densities could be retrieved from two different observation modes of SCIAMACHY and an averaged global background of tropospheric BrO was estimated by comparing the integrated stratospheric BrO profile with the simultaneously measured total BrO column (Sinnhuber et al., 2005; Rozanov et al., 2011). OMI (Ozone Monitoring Instrument) and GOME-2 (Global Ozone Monitoring Experiment-2), which were launched in 2004 and 2006, respectively, provide data with improved spatial resolution and signal to noise ratio enabling to answer additional scientific questions related to polar springtime BrO explosion events. Salawitch et al. (2010) showed that the locations of some total BrO column hotspots during Arctic spring observed by OMI are coincident with high total O<sub>3</sub> column and low tropopause height, suggesting a stratospheric contribution for the BrO enhancements. Theys et al. (2011) developed and applied an algorithm to retrieve tropospheric BrO columns from GOME-2 measurements and investigated polar tropospheric BrO hotspot areas. They found that elevated BrO columns are occasionally related to stratospheric processes due to tropopause descent in line with the result of Salawitch et al. (2010). However, they argued that the stratospheric origin cannot account for all cases and the release of bromine in the troposphere also contributes to satellite observed BrO plumes. Choi et al. (2012) conducted a comparison of satellite-derived tropospheric BrO and aircraft in-situ BrO profiles obtained from the ARCTAS and ARCPAC field campaigns for several events of rapid enhancement of BrO columns. From the two Arctic field campaigns, they showed that retrievals of tropospheric BrO columns from OMI and GOME-2, combined with modelled stratospheric BrO estimates, show reasonably good agreement with in-situ tropospheric BrO observations. Recently, the improved spatial resolution (3.5x5.5 km<sup>2</sup>) of TROPOMI (TROPOspheric Monitoring Instrument) onboard Sentinel-5 Precursor which was launched in October 2017 has enabled the detection of spatial variations and small-scale emission sources in more detail (Veefkind et al., 2012). Seo et al. (2019) showed the advantage of the high spatial resolution and signal to noise ratio of TROPOMI BrO retrievals in various source regions.

This thesis aims to develop an improved BrO retrieval algorithm for various

## 1. Introduction

platforms including the latest TROPOMI which provides much improved spatial resolution. The resulting satellite retrievals will then be used to investigate meteorological conditions and mechanisms involved in bromine explosion events especially focusing on polar regions where are sensitive to climate warming. With these research goals, the thesis is structured as follows: scientific background about halogens and their chemical mechanisms in the stratosphere and troposphere, absorption spectroscopy, differential optical absorption spectroscopy, and descriptions of instruments including both space-borne and ground-based remote sensing instruments are given in Chapter 2. In Chapter 3, a complete description of the algorithm developed for total and tropospheric BrO columns from satellite measurements is presented. Sensitivity tests for the optimization of the DOAS BrO fitting window, multiple stratospheric correction methods, tropospheric air mass factor calculations from a radiative transfer model, intercomparisons of BrO retrievals from different satellite instruments are included in detail. In Chapter 4, spatial distributions of the occurrence of total BrO column enhancements and the associated changes in various meteorological parameters are investigated in both the Arctic and Antarctic sea ice regions using long-term satellite measurements and meteorological model data. Validation of satellite tropospheric BrO retrieval algorithm is performed through comparisons with MAX-DOAS tropospheric BrO columns measured at the NDACC station in Ny-Ålesund in Chapter 5. Additional tropospheric bromine explosion events which occurred over Ny-Ålesund will also be discussed using both satellite and ground-based MAX-DOAS BrO measurements. Finally, a summary of the main findings and conclusions obtained in this study is presented, as well as an outlook and suggestions for future studies.

# 2

## Scientific Background

### 2.1 The Earth's atmosphere\*

The Earth's atmosphere is divided into five layers: the troposphere, stratosphere, mesosphere, thermosphere, and exosphere, which are generally defined by vertical changes in temperature (Seinfeld and Pandis, 2006). Figure 2.1 shows the vertical structure of the atmosphere with the temperature profile. The troposphere is the lowest layer of Earth's atmosphere, which extends from the surface to an average height of ~12 km, although this altitude varies depending on the latitude and season. Temperature in this layer generally decreases with height. Above the tropopause lies the stratosphere up to ~50 km. In the stratosphere, atmospheric temperature increases with altitude due to absorption of ultraviolet (UV) radiation by ozone (O<sub>3</sub>) molecules. Due to this temperature inversion, the stratosphere is dynamically stable. The mesosphere is the third highest layer of Earth's atmosphere, and extends from the stratopause at ~ 50 km to the mesopause at 80-85 km. Temperature decreases as altitude increases in the mesosphere, similar to the pattern in the troposphere. This layer also contains ratios of nitrogen and oxygen similar to the troposphere, except that the concentrations are 1000 times less. Above the mesopause, the thermosphere starts. In this layer, the temperature increases with altitude because it is directly heated by the solar radiation. Although few particles including N<sub>2</sub> and O<sub>2</sub> have very high kinetic energies which corresponds to high temperature, an observer or object will experience cold temperatures in this layer due to the extremely low density which is insufficient to conduct heat. The exosphere is the outermost layer of the atmosphere which extends up to space. Here, molecules such as hydrogen and helium are able to escape the gravitational field and therefore this layer is almost at vacuum. Basically, the atmosphere becomes thinner and thinner with increasing altitude until the

---

\* This section is based on Ahrens (2009, Chapter 1, 5, 6, and 10), Roedel and Wagner (2011, Chapter 2 and 4), Seinfeld and Pandis (2006, Chapter 5), and Wallace and Hobbs (2006, Chapter 1).

## 2. Scientific background

gases dissipate in space since molecules are pulled close to the Earth's surface by gravity.

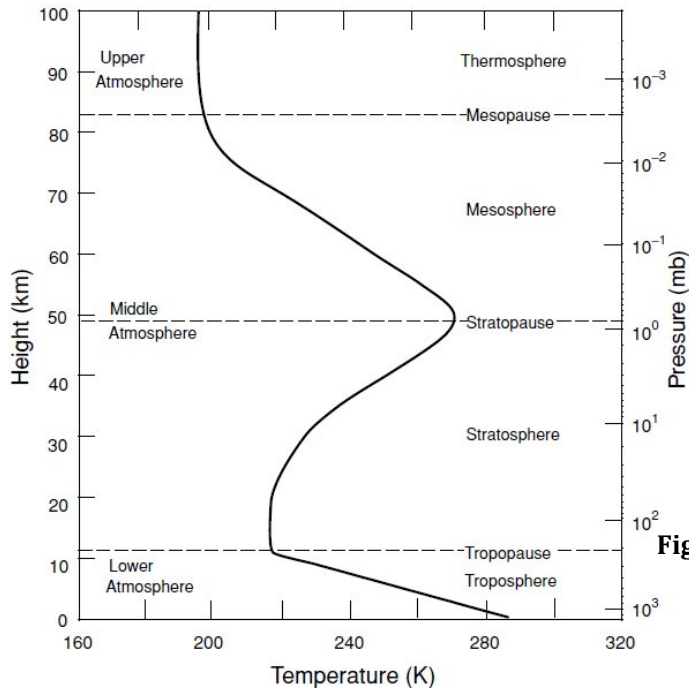


**Figure 2.1.** The layers of the Earth's atmosphere with the temperature profile (adapted from *Liou, 2002*).

The composition of today's atmosphere is a mixture of gases as listed in Table 2.1. The three major components of Earth's atmosphere are nitrogen ( $N_2$ ), oxygen ( $O_2$ ), and argon (Ar) with mixing ratios of 78 %, 21 % and 0.9 %, respectively. Water vapor accounts for 0.25% of the atmosphere approximately, but its volume mixing ratio varies significantly depending on latitude and season because it is affected by changes in temperature. The remaining gases are present in small concentrations and are referred to as trace gases. In particular, some gas species absorb the outgoing infrared radiation and re-emit radiant energy. They are known as greenhouse gases, the most important ones being carbon dioxide ( $CO_2$ ), ozone ( $O_3$ ), methane ( $CH_4$ ), nitrous oxide ( $N_2O$ ), water vapor and chlorofluorocarbons (CFCs). Greenhouse gases cause the greenhouse effect which is a natural process that warms a planet's surface by trapping the heat that reflects back from the surface to the atmosphere. Without greenhouse gases, the average temperature of Earth's surface would be about  $-18^\circ C$ , rather than the present average of  $15^\circ C$ . Not only gases but also solid and liquid particles called aerosols are present in the atmosphere. Aerosols can be generated from both natural (e.g.

## 2. Scientific background

sea salt, dust) and anthropogenic (e.g. industrial activity, biomass burning) sources. They influence climate directly and indirectly by changing the radiation energy through scattering and absorption and affecting cloud microphysical processes.

**Table 2.1.** Compositions of Earth's atmosphere with respect to dry air in fractional concentrations in volume (adapted from Wallace and Hobbs, 2006).

Constituent	Volume mixing ratio
Nitrogen (N <sub>2</sub> )	78.08 %
Oxygen (O <sub>2</sub> )	20.95 %
Argon (Ar)	0.93 %
Water vapor (H <sub>2</sub> O)	0 – 5 %
Carbon dioxide (CO <sub>2</sub> )	403.3 ppm
Neon (Ne)	18 ppm
Helium (He)	5 ppm
Methane (CH <sub>4</sub> )	1.85 ppm
Krypton (Kr)	1 ppm
Hydrogen (H <sub>2</sub> )	0.5 ppm
Nitrous oxide (N <sub>2</sub> O)	0.33 ppm
Ozone (O <sub>3</sub> )	0 – 0.1 ppm

## 2. Scientific background

### 2.2 Halogens in the atmosphere

Halogen compounds are reactive atmospheric chemicals known to play an important role in atmospheric chemistry by depleting ozone and changing the oxidation pathways of several atmospheric species. Halogen compounds are present in both the stratosphere and troposphere. In this section, important sources and chemical reactions of halogen compounds will be described.

#### 2.2.1 Halogens in the stratosphere

##### 2.2.1.1 Sources of reactive halogen species in the stratosphere

The main source of halogens in the stratosphere is transport of chlorofluorocarbon compounds (CFCs) or halogenated hydrocarbons (halons), which are stable and long-lived, from the ground level to the stratosphere principally in the tropical regions. The emission of these long-lived organic halogen components have been controlled by the Montreal Protocol which is a global agreement to protect the stratospheric ozone layer by restricting production and consumption of ozone-depleting substances. In addition, several studies have demonstrated a possible contribution to the stratospheric halogen budget by short-lived organic substances (VSLs) or direct intrusion of tropospheric  $\text{Cl}_y$  and  $\text{Br}_y$  into the lower stratosphere (Pundt et al., 2002; Salawitch et al., 2005; Sinnhuber et al., 2005). Here, we focus on chlorine, bromine, and iodine.

Most compounds containing long-lived chlorine in the stratosphere are released at the surface as a result of human activities such as CFCs, chlorocarbon and hydrochlorofluorocarbons (HCFCs) (Lovelock, 1977; Brasseur and Solomon, 2005). Chlorocarbon are used primarily as industrial solvents, degreasing compounds, and CFC precursors. The CFCs and HCFCs are used as refrigerants and air conditioning agents, and aerosol propellants. Methyl chloride ( $\text{CH}_3\text{Cl}$ ) is the only relevant natural source of stratospheric chlorine produced biologically in the oceans. Naturally produced HCl is also assumed to affect the stratospheric chlorine budget (Stolarski and Cicerone, 1974), but tropospheric HCl is easily washed out before it enters the stratosphere even the fast injection into the stratosphere by volcanic eruptions (von Clarmann, 2013). These long-lived chlorine compounds are broken apart by solar ultraviolet radiation, releasing chlorine atoms to initiate

## 2. Scientific background

ozone destruction. Each chlorine atom can initiate a cycle that can destroy up to 100,000 ozone molecules.

Inorganic bromine is the second most important chemical component following chlorine with respect to removal of stratospheric ozone (McElroy et al., 1986; Harder et al., 2000). The ozone catalytic removal cycles involving bromine atoms, Br, and bromine monoxide (BrO), together known as BrOx, have higher chain lengths than those involving chlorine atoms, and chlorine monoxide (ClO), together known as ClOx. Although a single bromine atom is an even more efficient destroyer of O<sub>3</sub> than a chlorine atom, there has been much less bromine released by man than chlorine. Stratospheric bromine is predominantly present in its inorganic form, originating from both natural and anthropogenic organic sources. Man-made halogenated hydrocarbons (halons) and methyl bromide (CH<sub>3</sub>Br) released from the ocean by natural processes are stable and long-lived, which allows them to reach the stratosphere mainly in the tropics (Harder et al., 2000; Theys et al., 2009b). In addition to the contribution of these long-lived organic source gases, short-lived bromine compounds which are mainly of natural origin could also affect the stratospheric bromine budget (Sinnhuber et al., 2005; Liang et al., 2010). In the stratosphere, organic bromine source gases are converted into inorganic forms of Br<sub>y</sub>, such as Br, BrO, BrONO<sub>2</sub>, HOBr, HBr, BrCl, 2Br<sub>2</sub>, either by direct photolysis or by reaction with OH and O (Sinnhuber et al., 2005; Theys et al., 2009b). Inorganic bromine is then involved in various stratospheric chemical reactions.

Although all the natural sources of iodine are short-lived, their transport through rapid convection in the tropics can supply iodine to the lower stratosphere (Solomon et al., 1994; Davis et al., 1996). Saiz-Lopez et al (2012) showed that significant levels of reactive iodine (0.25-0.7 ppt) can be injected into the stratosphere via tropical convective outflow from the combination of aircraft IO profile measurements together with two modeling simulations. Even at low stratospheric iodine levels compared to other halogen components, iodine atoms could affect ozone chemistry in the lower stratosphere.

## 2. Scientific background

### 2.2.1.2 Stratospheric halogen chemistry

The heterogeneous halogen reaction is important in polar winter as polar stratospheric cloud (PSC) is formed in the cold and dark polar stratosphere. These PSCs are composed of solid and liquid sulphate aerosols and on the PSCs, inactive chlorine from reservoirs such as ClONO<sub>2</sub> and HCl are transferred to active chlorine species like ClONO, Cl<sub>2</sub> and BrCl. These PSCs are composed of solid and liquid sulphate aerosols and on the PSCs, inactive chlorine from reservoirs such as ClONO<sub>2</sub> and HCl are transferred to active chlorine species like ClONO, Cl<sub>2</sub> and BrCl. At the end of the polar winter when short wave ultraviolet radiation from the sun is reaching the polar stratosphere, the halogen source gases are chemically converted to more reactive halogen gases (ClO, BrO, Cl, Br, HBr, BrONO<sub>2</sub>, ClONO<sub>2</sub>, HCl etc). The most reactive forms are chlorine monoxide (ClO) and bromine monoxide (BrO), and chlorine and bromine atoms (Cl and Br). This process is responsible for the rapid ozone loss in spring over the Antarctic and Arctic region. A large fraction of available stratospheric bromine is generally in the form of ClO and BrO which are produced by the fast reactions between atomic halogen (Cl and Br) and O<sub>3</sub> by following chemical reaction:



Here, X is the halogen radicals Cl, Br, and I. These species are reproduced in the process and are able to destroy ozone until they are converted into stable reservoirs.

During high chlorine activation inside the polar vortex, the dominant chemical reactions which convert BrO into Br are:



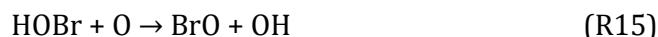
These reactions link other catalytic cycles enhancing the efficiency of cycles. The influence of reactive halogen on the depletion of ozone is moderated by the formation of the reservoirs in reactions with NO<sub>2</sub>, HO<sub>2</sub>, and HCHO.



## 2. Scientific background

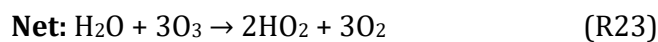
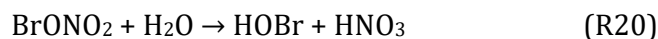


Bromine nitrate ( $\text{BrONO}_2$ ) is the most important bromine reservoir in the stratosphere. The next important bromine reservoir is HOBr. HOBr has a lower photolysis stability, but is considered as major night-time reservoir as a result of heterogeneous reactions. These bromine reservoirs are converted into reactive bromine through the following reactions:



Heterogeneous reactions can also affect significantly the  $\text{O}_3$  and halogen chemistry. One of the most important heterogeneous reactions in the bromine chemistry is the hydrolysis of the stratospheric reservoir bromine nitrate ( $\text{BrONO}_2$ ) by the following two catalytic cycles (Lary, 1996a):

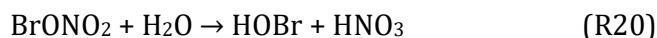
### *Cycle A (I)*



## 2. Scientific background

Cycle A (I) is very efficient since only one hydrolysed bromine molecule destroys three ozone molecules and produces two HO<sub>2</sub> radicals with the potential to destroy more ozone molecules (Lary, 1996a).

### *Cycle A (II)*



Cycle A (II) is similarly efficient because one hydrolysed bromine can deplete three ozone molecules as well. But the reaction strongly depends on temperature as the chemical reaction (R23) occurs only at temperatures below 200 K. These heterogeneous reactions take place on the surface of aerosols and PSC particles. This process is responsible for the rapid ozone loss in early spring over the Arctic and Antarctic region when the first sunlight is reaching the polar stratosphere (Solomon, 1999).

## 2.2.2 Halogens in the troposphere

### 2.2.2.1 Sources of reactive halogen species in the troposphere

Halogens are released into the troposphere from the photochemical breakdown of organo-halogens from both natural and anthropogenic sources and the oxidation of Cl<sup>-</sup> and Br<sup>-</sup> in sea water. One of the main sources for natural halogen compounds are the oceans. Sea water contains large amount of chloride and bromide and they are released from sea salt aerosols in the marine boundary layer (MBL) photochemically as reactive radicals or their precursors (Simpson et al., 2015). Unlike chloride and bromine, which are abundant in the oceans and not

## 2. Scientific background

significantly removed by marine biological processes, iodine is at low levels by its consumption as a nutrient by oceanic biological systems. Thus, the sources of reactive iodine in the MBL are different from chlorine and bromine. In the MBL, emissions of biogenic alkyl iodides produced in the ocean by various types of microalgae and phytoplankton are a main source of reactive iodine. These biogenic alkyl iodides are rapidly destroyed by photolysis or degradation with OH radical, which potentially has a significant influence on ozone chemistry in the boundary layer. The open ocean is also a source of very short-lived (VSL) halogenated organic compounds such as  $\text{CH}_3\text{Cl}$ ,  $\text{CH}_3\text{Br}$ ,  $\text{CH}_3\text{I}$ ,  $\text{CHBr}_3$ ,  $\text{CH}_2\text{Br}_2$ , and  $\text{CH}_2\text{I}_2$  which have lifetimes from a few weeks to few months (Barrie et al., 1988). For the anthropogenic sources, Tolbert et al. (1988) and Finlayson-Pitts et al. (1990) found that the nocturnal  $\text{NO}_x$  reservoir species,  $\text{N}_2\text{O}_5$ , reacted with HCl or NaCl to produce photolabile species, such as nitryl chloride,  $\text{ClNO}_2$ , providing a connection between nitrogen oxide and halogen activation. High concentrations of  $\text{ClNO}_2$  and chlorine were detected in the polluted coastal in Los Angeles. Anthropogenic production of strong acids can cause acid-mediated displacement of  $\text{Cl}^-$  from sea salt aerosols and high levels of gas phase HCl which can be activated to atomic chlorine.

Sudden increases in BrO concentrations observed in both polar sea ice regions in every springtime are called “bromine explosion” events (Wennberg, 1999; Wagner et al., 1998; Richter et al., 1998). This chemical mechanism is responsible for tropospheric ozone depletion from hours to days via autocatalytic release from sea salt. In addition to the  $\text{O}_3$  depletion, reactive halogen species lead to the depletion of gaseous mercury in polar regions. The Arctic, in particular, is influenced by pollution affecting the biosphere and people, for example by deposition of mercury (Hg). Schroeder et al. (1998) found the first rapid depletions of measured gaseous elemental mercury (GEM) in the marine boundary layer concurrently with tropospheric ozone depletion during the bromine explosion event. These photochemical and heterogeneous reactions will be discussed in detail in section 2.2.2.2. Biogenic oceanic sources have been discussed from early days, but the exact mechanism for the release of reactive bromine as the gas phase in polar regions are not fully understood and still under debate. First year sea ice surfaces, sea salt aerosols, blowing snow particles, and frost flowers have raised a lot of interest as bromine sources in recent studies.

Additionally, volcanic eruptions are one of the sources of halogenated species. Several studies showed high levels of bromine monoxide and iodine monoxide in

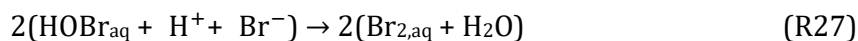
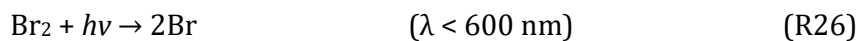
## 2. Scientific background

volcanic plumes using both ground-based and satellite measurements (Bobrowski et al., 2003; von Glasow et al., 2009; Theys et al., 2009, Schönhardt et al., 2017). Volcanic plumes contain halogen species initially in acidic form such as HF, HCl, HBr, and HI (Aiuppa, 2009). Observations of reactive halogen have also been reported over salt lakes and marshes (Hebestreit et al., 1999; Tas et al., 2005; Hörmann et al., 2016). Hörmann et al (2016) describes a seasonal cycle of tropospheric BrO formation over the Rann of Kutch salt marsh using long-term ground-based MAX-DOAS and satellite measurements.

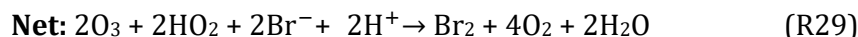
### 2.2.2.2 Tropospheric halogen chemistry

According to recent studies, the mechanisms for the release of reactive halogen species in the troposphere are mainly liberation of halogens from sea salt aerosols and degradation of halogenated organic compounds. In the marine boundary layer outside the polar regions, bromide ( $\text{Br}^-$ ) is generally injected into the atmosphere in association with sea salt aerosols by the breaking of waves and biological processes on the ocean surfaces (Vogt et al., 1996; Sander et al., 2003). In polar regions, snow and fresh sea ice contaminated with sea salt ions are considered as a major source of reactive bromine sources. In addition, frost flowers which are fragile ice crystals growing on open leads and polynyas when their surfaces begin to freeze. Since they wick brine from the sea ice surface, they exhibit enhanced salinities of about  $\approx 100\%$  and can act as sources of bromine activation. Several chemical processes for releasing and recycling the reactive bromine from the sea salt have been proposed and confirmed from previous studies (Fan and Jacob, 1992; Vogt et al., 1996). Reaction chemical cycles converting  $\text{Br}^-$  to  $\text{Br}_2$  are as follows:

#### ***Cycle B (I)***

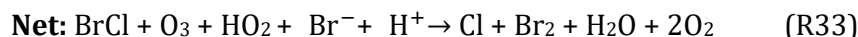
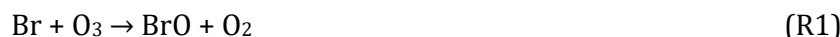
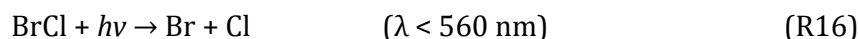


## 2. Scientific background



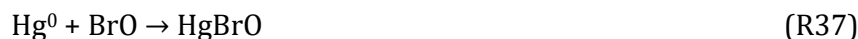
However, the direct reaction (cycle B (I)) is not fast enough, Vogt et al (1996) proposed the following reaction sequence:

### *Cycle B (II)*



In cycle B (I) and (II), the bromine released as  $\text{Br}_2$  or  $\text{BrCl}$  is photolysed to produce Br atoms, which catalytically deplete  $\text{O}_3$ . Also,  $\text{Br}^-$  ion is released to the gas phase ( $\text{Br}_2$ ) upon uptake of  $\text{HOBr}$ , which makes these cycles autocatalytic. In particular, the reaction (R30) is acid-catalysed, and therefore this chemical reaction can be activated at lower pH by triggering precipitation of calcium carbonate ( $\text{CaCO}_3$ ) from freezing sea water at low temperature (Martin et al., 1996; Kaleschke et al., 2004; Sander et al., 2006). Sander et al. (2006) demonstrated the temperature dependence of the equilibrium  $\text{Br}_2\text{Cl}^- \rightleftharpoons \text{Br}_2 + \text{Cl}^-$  to be important.

Halogen species are also responsible for mercury depletion events in the polar regions as gaseous elemental Hg ( $\text{Hg}^0$ ) is rapidly oxidized to gaseous divalent Hg ( $\text{Hg}^{\text{II}}$ ) and then subsequently deposits to the ground (Seigneur and Lohman, 2008). The following chemical mechanism is considered for the oxidation of  $\text{Hg}^0$  by Br and  $\text{BrO}$ :



## 2. Scientific background

These oxidized inorganic Hg species (i.e. HgBr, HgBrO, HgBrOH and HgBr<sub>2</sub> etc) are more reactive than gaseous elemental Hg and may directly deposit to snow/ice or associate with particles in the air that can deposit onto the snow/ice surfaces (Simpson et al., 2007).

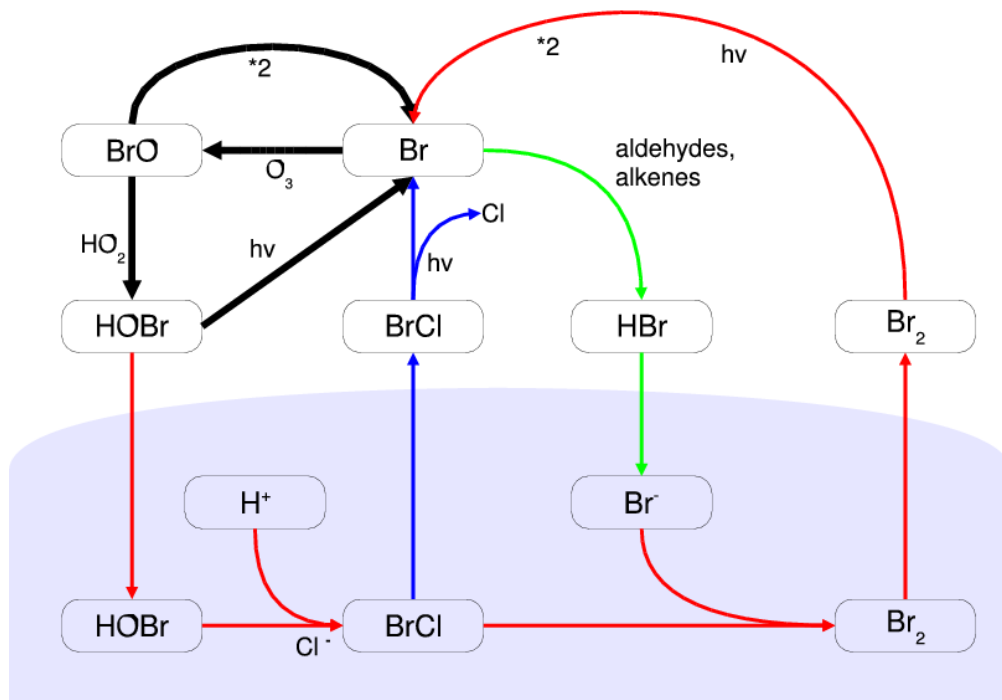


**Figure 2.2.** A simplified scheme of multiphase chemistry of bromine, especially for bromine explosion reactions in the troposphere. The blue area represents the condensed phase (e.g. sea salt aerosol surfaces or liquid brine). (Simpson et al., 2007)

### 2.3 Absorption spectroscopy

#### 2.3.1 Electromagnetic radiation

Electromagnetic radiation refers to the waves of the electromagnetic field, propagating through space at the speed of light ( $c \approx 2.998 \times 10^8$  m/s) and carrying electromagnetic radiant energy. Electromagnetic radiation is distinguished by its frequency ( $\nu$ ) and wavelength ( $\lambda$ ) by

$$c = \nu \times \lambda \quad (\text{E 2.1})$$

Based on the wavelength or frequency range, the electromagnetic spectrum can be divided into several groups such as radio waves, microwaves, infrared (IR), visible light (Vis), ultraviolet (UV), X-rays, and gamma rays (see Fig. 2.3) depending on the energy and frequency. Radio waves have the smallest energy with  $\lambda > 30$  cm, followed by microwaves with  $\lambda = 1$  mm-30 cm. In the microwave spectral range mostly rotational spectra are important. Microwaves are followed by the infrared spectral range with  $\lambda = 800$  nm - 1mm which is separated into far and near infrared. In this IR range, rotational and vibrational spectra of molecules can be measured. In the visible ( $\lambda \approx 400$  nm-800 nm) and ultraviolet ( $\lambda \approx 60$  nm-400 nm) wavelength range, electronic transitions and overlaid changes in rotational and vibrational states occur. Shorter wavelengths correspond to X- and  $\gamma$ -rays which are high energetic electromagnetic radiation.

In quantum mechanical systems, electromagnetic radiation is also described as a stream of photons. Each photon has an energy related to the frequency of the wave given by Planck's relation

$$E = h\nu = hc/\lambda \quad (h = 6.626 \times 10^{-34} \text{ Js; Planck's constant}) \quad (\text{E 2.2})$$

Depending on the energy level, different types of interactions of radiation with the matter occur, which will be discussed briefly in section 2.3.2.

## 2. Scientific background

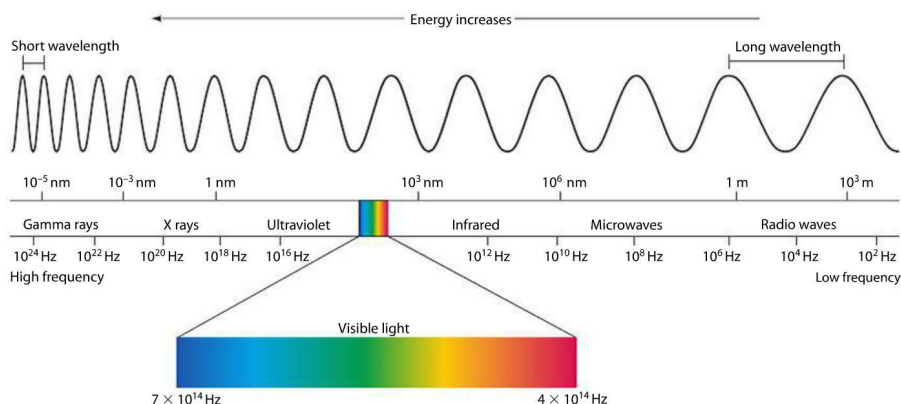


**Figure 2.3.** Sketch of the electromagnetic spectrum with frequency and wavelength. (image credit: [https://www.miniphysics.com/electromagnetic-spectrum\\_25.html](https://www.miniphysics.com/electromagnetic-spectrum_25.html))

### 2.3.2 Energy states and molecular transitions

A molecule is an electrically neutral group of two or more atoms held together by chemical bonds. Quantum mechanically, this molecule is considered as a multi-particle system and therefore it has discrete energy states. The most commonly observed molecular spectra include electronic (change in the configuration of the electrons), vibrational (vibration of the atoms in the molecule), and rotational (rotation of the complete molecule) transitions. For a diatomic molecule, the electronic states can be described by a plot of potential energy as a function of inter-nuclear distance as shown in Fig. 2.4.

Incident electromagnetic waves can excite the rotational levels of molecules provided they have an electronic dipole moment by exerting a torque on the molecule. The rotational transitions of molecules are typically in the microwave region of the electromagnetic spectrum and associated with the ground vibrational state. The vibrational transitions of diatomic molecules can be approximated by the quantum harmonic oscillator and can be used to imply the bond force constants for small oscillations. The energy levels are given by

$$E_v = (n+1/2) \cdot h\omega_0 \quad (\text{E 2.3})$$

where  $n$  is the vibrational quantum number (vibration level) and  $1/2 h\omega_0$  is the zero-point energy of the molecular oscillator. Therefore, the energy levels are proportional to the vibrational quantum number  $n$ . During the vibrational

## 2. Scientific background

excitation, the molecules are also likely to be rotationally excited at ambient temperature, which results in that the vibrational state splits into a series of rotational-vibrational states (see Fig. 2.4). The vibrational transitions mainly occur in the infrared spectra region.

Electronic transitions are caused by changes in the configuration of the electrons. The molecular bond length and strength change with the electronic configuration, which indicates that each electronic state has its own set of vibrational and rotational states. The energies associated with molecular electronic spectra are mainly in the visible or ultraviolet spectral region, which are much larger than those associated with vibrational and rotational transitions ( $E_{el} > E_{vib} > E_{rot}$ ). Figure 2.4 is an example of an electronic transition, which represents the potential energy diagram with the rotational-vibrational energy levels of two electronic states in a molecule. The electronic transition occurs vertically, as governed by the Franck-Condon principle, which can be explained as the unchanged nuclei position during the fast electron reconfiguration.

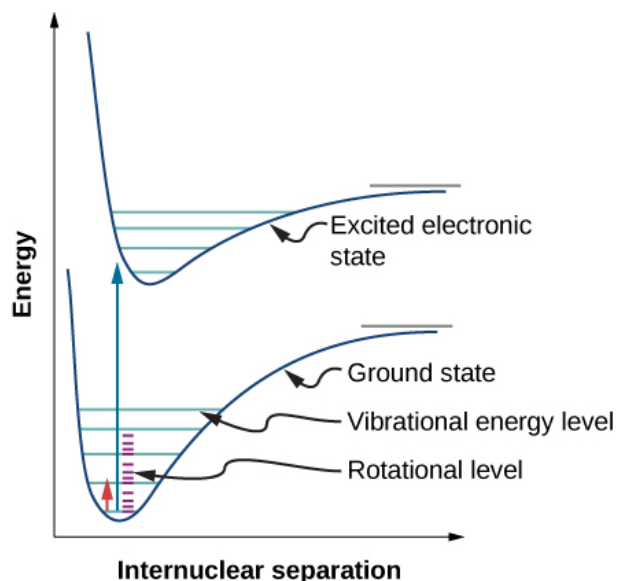


**Figure 2.4.** Diagram of rotational-vibrational energy levels in two electronic states of a molecule. Three types of energy levels (electronic, vibrational, and rotational) are shown here. (<https://chem.libretexts.org/>)

### 2.3.3 Solar spectrum

The main source of the electromagnetic radiation reaching the Earth from space is solar radiation. Solar radiation provides light and heat for the Earth and energy for photosynthesis, and thus this radiant energy is essential for the metabolism of the

## 2. Scientific background

environment and its inhabitants. The sun is composed primarily of the chemical gases hydrogen (around three parts) and helium (one part). The energy in the outer layers of the sun is coming from the core and is transferred by electromagnetic radiation. The solar radiation received on the Earth is emitted in the photosphere (around 500 km above the Sun's surface) can be approximated by black-body radiation corresponding to its temperature of  $\approx 5800$  K. The spectral distribution can be described by Planck's law, which describes the radiation emitted by a black-body in thermal equilibrium at a given temperature as given in the following equation:

$$B(\lambda, T) = \frac{2\pi hc^2}{\lambda^5} \frac{1}{\exp\left(\frac{hc}{\lambda k_B T}\right) - 1} \quad (\text{E 2.4})$$

where  $\lambda$  is the wavelength,  $T$  the temperature,  $c$  the speed of light,  $h \approx 6,626 \times 10^{-34}$  J s the Planck constant and  $k \approx 1.381 \times 10^{-23}$  J K<sup>-1</sup> the Boltzmann constant. However, the sun is not a perfect blackbody as there are several substances in the sun's atmosphere that emit and absorb light at characteristic wavelengths, which leads to dark lines in the sun spectrum called Fraunhofer lines.

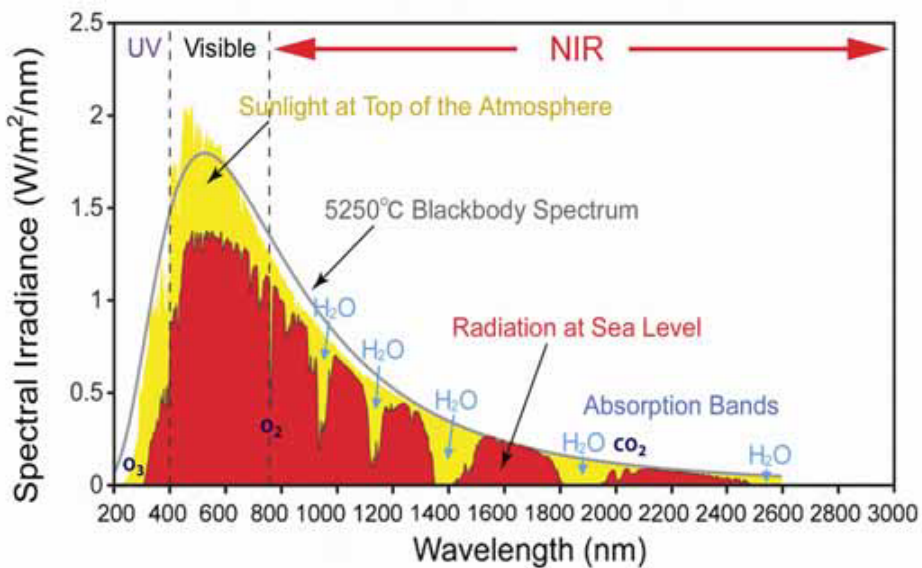


**Figure 2.5.** The solar radiation spectrum for direct light both at the top of the Earth's atmosphere (yellow) and at sea level (red). The gray line indicates the radiation distribution of an assumed 5250 °C blackbody. As light passes through the atmosphere, some is absorbed by gases with specific absorption bands (blue). (image credit: [https://en.wikipedia.org/wiki/Solar\\_irradiance](https://en.wikipedia.org/wiki/Solar_irradiance)).

## 2. Scientific background

### 2.3.4 Atmospheric radiative transfer

Radiative transfer in the atmosphere is the physical phenomenon of energy transfer by the propagation of radiation through a medium including absorption, emission and scattering processes. The radiative transfer equation (RTE) describes these processes mathematically as:

$$\frac{dI(\lambda)}{ds} = -I(\lambda)\varepsilon(\lambda) + \varepsilon(\lambda)B(\lambda) \quad (\text{E 2.5})$$

here, the left side of the equation is the change of radiation along the light path  $ds$ , whereas the first term of the right side presents the attenuation of radiation due to extinction including absorption and scattering,  $\varepsilon$  being the extinction coefficient, the sum of the absorption and scattering coefficients. The second term of the right side describes the gained radiation by emission process through absorption and scattering (Rozanov et al., 2013). These processes will be discussed in detail in sections 2.3.5, 6 and 7.

For simulations of the radiation transfer, various radiative transfer models (RTMs) have been developed, and the SCIATRAN (Rozanov et al., 2013) developed at the Institute of Environmental Physics at the University of Bremen (IUP-Bremen) was used in this study.

### 2.3.5 Scattering in the atmosphere

In the atmosphere, radiance can be scattered by atmospheric gas molecules and suspended particles (aerosols or cloud particles). The scattering processes can be divided into two types: elastic scattering (no change of photon energy during the change of propagation direction of a photon) and inelastic scattering (change in the photon energy during the process). The elastic scattering including Rayleigh and Mie scattering occurs on time scales of  $10^{-14}$  seconds, and this scattering does not change the high frequency spectral features, which are used by the DOAS approach. The elastic scattering depends on the ratio of the particle size to the incident radiation wavelength. On the other hand, the most important inelastic scattering, which is a process where the emitted radiation has a wavelength different from that of the incident radiation, is Raman scattering.

## 2. Scientific background

### Rayleigh scattering

Rayleigh scattering describes the dominant elastic scattering of light by small particles and occurs when the size of the particle responsible for the scattering event is much smaller than the wavelength of the scattered light. The scattered light intensity is inversely proportional to the fourth power of the wavelength. Thus, for visible and shorter wavelengths, this scattering effect by air molecules (e.g. N<sub>2</sub> and O<sub>2</sub>) becomes significant and the Rayleigh scattering is responsible for the blue color of the sky during a clear day due to more efficient scattering by air molecules at shorter wavelengths.

The Rayleigh scattering cross section  $\sigma_{Ra}$  (m<sup>2</sup> mol<sup>-1</sup>) can be calculated theoretically,

$$\sigma_{Ray}(\lambda) = \frac{8\pi^3}{3\lambda^4 N_{air}^2} \cdot (n_0(\lambda)^2 - 1)^2 \cdot F_K(\lambda) \quad (\text{E 2.6})$$

where  $n_0(\lambda)$  is the refractive index of air depending on the wavelength,  $N_{air}$  is the number density of air, and  $F_K(\lambda) \approx 1.061$  the correction for the polarisability factor of air molecules. Equation 2.4 can be simplified for the wavelength range of  $0.2 \mu\text{m} < \lambda < 0.55 \mu\text{m}$  (Nicolet, 1984):

$$\sigma_{Ray}(\lambda) \approx \frac{4.02 \cdot 10^{-28}}{\lambda^{4.04}} \quad (\text{E 2.7})$$

The angular distribution of scattered light can be expressed by the phase function, which describes the distribution probability of scattered intensity as a function of scattering angle  $\theta$ , the angle between the direction of the incoming light and the scattered light. The Rayleigh phase function is given by:

$$P(\theta) = \frac{3}{4} (1 + \cos^2(\theta)) \quad (\text{E 2.8})$$

For Rayleigh scattering, the distribution of intensity of scattered radiation is equally distributed between forward and backward directions as shown in Fig. 2.6.

## 2. Scientific background

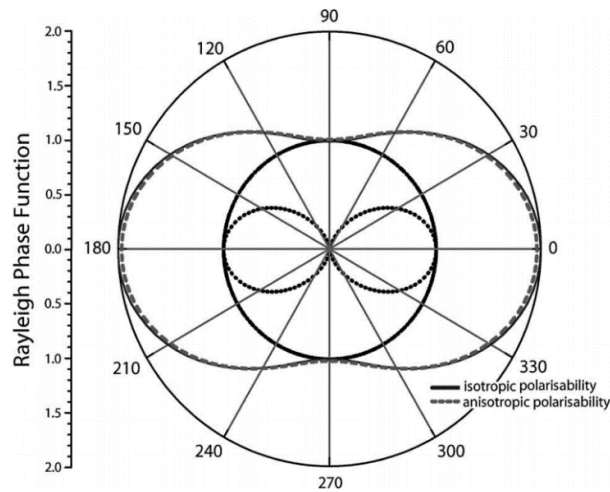


**Figure 2.6.** Polar diagram of the Rayleigh scattering phase function  $P(\theta)$  for non-polarised light (image credit: Platt and Stutz, 2008).

### Mie scattering

When UV and visible radiation is scattered by a particle comparable in size to the wavelength of the incident radiation, this is known as Mie scattering. Mie scattering occurs mainly on particles such as aerosols, cloud droplets, and suspended matter in liquids. Similar to Rayleigh scattering, Mie scattering can be defined as (Platt and Stutz, 2008):

$$\sigma_{Mie}(\lambda) \propto \frac{1}{\lambda^\alpha} \quad (\text{E 2.9})$$

where  $\alpha$  is the Ångström exponent. Small particles have larger values for  $\alpha$ , while large particles  $\alpha$  decreases. A normal distribution of particles in the atmosphere have a characteristic value of  $\alpha \approx 1.3$ . With increasing particle size ( $r$ ), the asymmetry between the probability for backward and forward scattering increases (see Fig. 2.7). In general, the scattered radiation in Mie scattering is mainly confined within a small angle about the forward direction. The greater the particle size, the more of the light is scatted in the forward direction. Also, Mie scattering is not polarizing in contrast to the Rayleigh scattering.

## 2. Scientific background

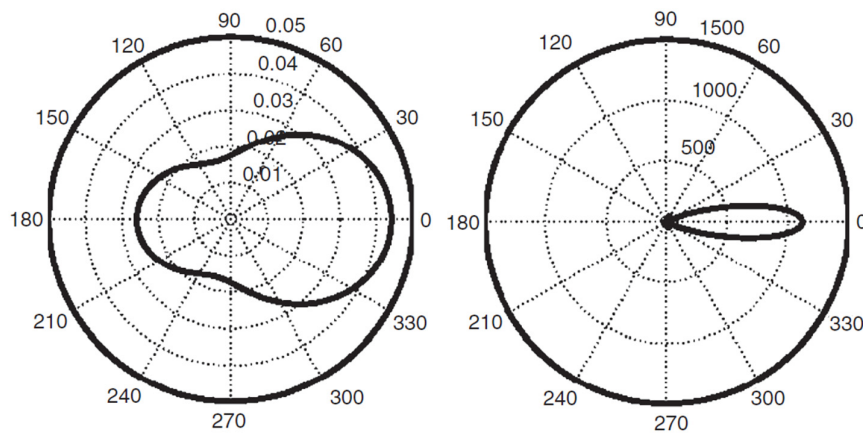


**Figure 2.7.** Phase functions of Mie scattering for a small droplet size ( $\alpha=1$ ; left) and for a large droplet size ( $\alpha=5$ ; right) (image adapted from Burrows et al., 2011).

### Raman scattering and Ring effect

In contrast to Rayleigh and Mie scattering, Raman scattering is an inelastic scattering where energy states are changed during the scattering process. The photon can transfer part of its energy to the molecule which results in Stokes lines or can lose part of its energy which results in Anti-Stokes lines. Only discrete amounts of energy can be transferred between the photon and the molecule, defined by the differences between the discrete excitation levels. If only the rotational excitation is affected, this type of scattering is referred to as rotational Raman scattering, while if also the vibrational state changes, it is called rotational-vibrational Raman scattering. The rotational-vibrational Raman scattering probability is an order of magnitude smaller than the rotational Raman scattering in the atmosphere. The rotational Raman scattering has an important effect on the spectrum of scattered solar radiation in the atmosphere compared to direct sunlight (unscattered solar radiation). Presences of absorption features such as Fraunhofer lines created by Raman scattering at air molecules change the spectrum of scattered radiation. Through the change in wavelength which happens during the Raman scattering, the depth of absorption lines is smaller in scattered light than in direct light. This filling-in of absorption lines is not exclusive to the Fraunhofer structures but also occurs for as absorption for example by ozone. The combination of the highly structured solar spectrum and inelastic scattering

## 2. Scientific background

processes can therefore lead to an effect which is called the Ring effect (Grainger and Ring, 1962). The amount of filling-in depends on the relative amounts of inelastic and elastic scattering and can be simulated with radiative transfer models. In the DOAS retrieval, the Ring effect is accounted for by including a pseudo-absorber, referred to as Ring spectrum, computed by RTM.

### 2.3.6 Absorption in the atmosphere

A part of the incoming solar radiation is absorbed by gases in the Earth's atmosphere. Atmospheric gases absorb the solar radiation in distinct spectral regions usually at more or less broad bands. Best known is the broad absorption of ozone in the UV range (e.g. Hartley, Huggins and Chappuis bands), which is essential for the existence of biological organisms on Earth's surface. Gases known as greenhouse gases, e.g. CO<sub>2</sub>, CH<sub>4</sub>, N<sub>2</sub>O and water vapor absorb a wide range of infrared radiation outgoing from the surface, and thus are responsible for the greenhouse effect. Since the atmospheric lifetime of these gases (except water vapor) is considerable, their distribution around the globe is fairly homogeneous. Consequently, atmospheric absorptions help the Earth's environment by preventing high-energy radiation at shorter wavelengths from reaching the surface and by absorbing outgoing infrared radiation to increase the global atmospheric temperature (Horvath, 1993).

With the absorption of a photon by a molecule, electronic, vibrational and rotational transitions can occur by uptaking energy, an electron jump from a lower energy state to another higher energy state. Quantitatively the absorption of radiation is described by Beer-Lambert's law (Platt and Stutz, 2008):

$$I(\lambda) = I_0(\lambda) \exp[-\sigma(\lambda)\rho s] \quad (\text{E 2.10})$$

where  $I_0(\lambda)$  represents the initial radiation intensity,  $I(\lambda)$  the intensity after passing through the path,  $\lambda$  the wavelength,  $\rho$  the concentration of the absorber,  $s$  the optical path and  $\sigma(\lambda)$  represents the absorption cross-section of the measured species.

## 2. Scientific background

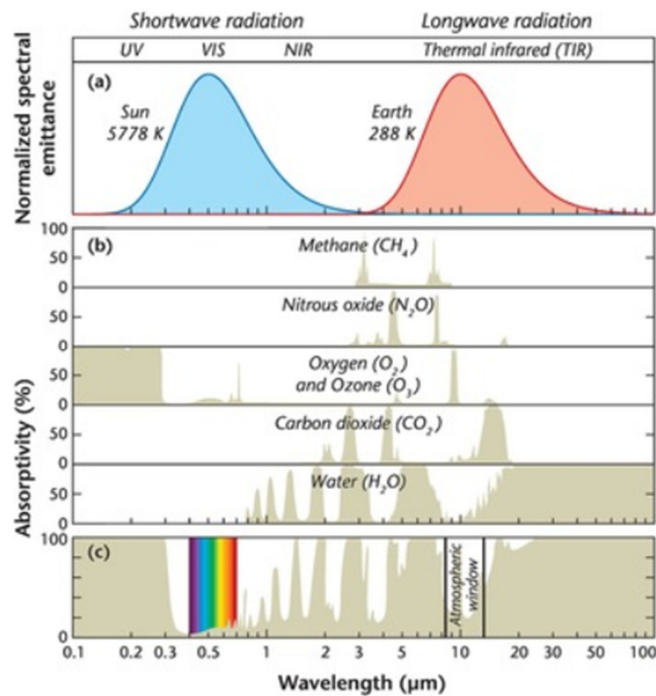


**Figure 2.8.** The absorptivity of individual atmospheric gases as a function of wavelength (image credit: <https://www.cambridge.org/>).

### 2.3.7 Differential Optical Absorption Spectroscopy

The Differential Optical Absorption Spectroscopy (DOAS) technique is a widely used method to calculate concentrations and columns of atmospheric trace gases by analyzing broadband spectra in the UV and visible range which have been transmitted through the atmosphere along a certain light path. The DOAS method is based on Beer-Lambert's law:

$$I(\lambda) = I_0(\lambda) \exp[-\sigma(\lambda)\rho s] \quad (\text{E 2.10})$$

where  $I(\lambda)$  is the measured intensities,  $I_0(\lambda)$  the unattenuated reference intensities,  $s$  the path length [cm],  $\sigma(\lambda)$  the wavelength dependent absorption cross sections [ $\text{cm}^2 \text{ molecule}^{-1}$ ] and  $\rho$  the number density of the species [ $\text{molecules cm}^{-3}$ ]. The dimensionless quantity  $\sigma \cdot \rho \cdot s$  is often referred to as the optical depth, denoted  $\tau$ . In the atmosphere, Rayleigh and Mie scattering also

## 2. Scientific background

contribute to the radiation extinction. Light from the sun is either scattered by molecules, particles and cloud droplets, or is reflected at the surface towards the atmosphere again. Along its path through the atmosphere, part of the light is absorbed by trace gases and the resulting reduction in the light intensity can be used to calculate the amount of the trace gas species present in the atmosphere. Adding Rayleigh and Mie scattering to the equation,

$$\begin{aligned} \tau(\lambda) &= \ln \frac{I_0(\lambda)}{I(\lambda)} = s(\sigma(\lambda)\rho + \varepsilon^R(\lambda) + \varepsilon^M(\lambda)) \\ &= s \left( \sum_i \sigma_i(\lambda)\rho_i + \varepsilon^R(\lambda) + \varepsilon^M(\lambda) \right) A(\lambda) \end{aligned} \quad (\text{E 2.11})$$

where  $\varepsilon^R(\lambda)$  is the Rayleigh extinction coefficient and  $\varepsilon^M(\lambda)$  is the Mie extinction coefficient. Several atmospheric species which have significant absorption cross sections (e.g. O<sub>3</sub>, NO<sub>2</sub>, HCHO, and SO<sub>2</sub>) in the given wavelength interval should be included and Beer-Lambert's law must be further extended. In addition, the attenuation function  $A(\lambda)$  describes the scattering efficiency if scattered light is being measured which depends on the surface reflectance and the presence of clouds etc.

Cross sections for a specific species can be separated into two components, one slowly varying with wavelength,  $\sigma_i^s(\lambda)$ , and the other, rapidly varying part,  $\sigma_i'(\lambda)$  (see Fig. 2.9). The total absorption cross section  $\sigma_i(\lambda)$  is simply the sum of the two components:  $\sigma_i(\lambda) = \sigma_i^s(\lambda) + \sigma_i'(\lambda)$ .

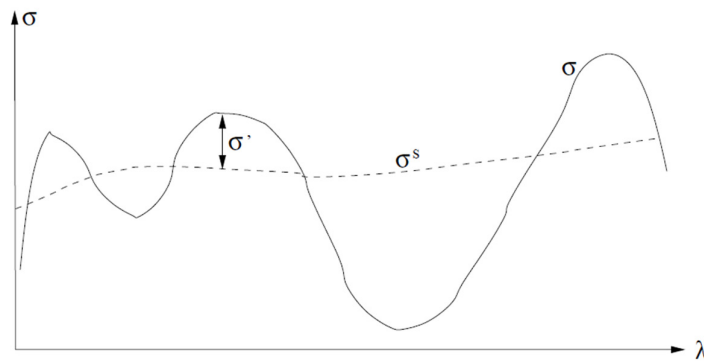


**Figure 2.9.** The differential cross section,  $\sigma'$ , is the difference between the total cross section,  $\sigma$  and the slowly varying part,  $\sigma^s$ .

## 2. Scientific background

This high frequency part of the spectrum is also called differential cross section and used for the retrieval of atmospheric absorptions. On the other hand, the slowly varying low frequency part is treated as a closure term and is approximated by a low order polynomial function. Note that both Rayleigh and Mie scattering as well as the attenuation term are slowly varying with wavelength, and therefore they can be approximated by one closure polynomial.

$$\begin{aligned}\tau(\lambda) = \ln \frac{I_0(\lambda)}{I(\lambda)} &= s \sum_i \sigma'_i(\lambda) \rho_i + s \left( \sum_i \sigma_i^s(\lambda) \rho_i + \varepsilon^R(\lambda) + \varepsilon^M(\lambda) \right) A(\lambda) \\ &= \sum_i \sigma'_i(\lambda) SCD_i + \sum_p a_p \lambda^p\end{aligned}\quad (\text{E 2.12})$$

As shown in this equation, the measured optical depth is finally expressed in a linear equation with the quantities of interest (the slant column density, SCD) and a closure polynomial. If  $I(\lambda)$ ,  $I_0(\lambda)$ , and absorption cross-sections  $\sigma'_i(\lambda)$  are known, the  $SCD_i$  can be determined by a least-square fit. The absorption cross-section of the atmospheric species can be obtained from the literature or laboratory measurements. To correctly determine the slant column density, cross sections of the atmospheric species have to be convoluted with the instrument slit function, since the measured intensity is not fully resolved spectrally but is taken at instrument wavelength resolution.

Here, Eq 2.12 represents the ideal case and the measurements are generally affected by noise. Therefore, the measured optical depth  $\tau(\lambda)$  needs to be replaced by the fitted  $\tau_{fit}(\lambda)$ , which differs from the measured optical depth as

$$\tau(\lambda_i) = \tau_{fit}(\lambda_i) + r(\lambda_i) \quad (\text{E 2.13})$$

where  $r(\lambda_i)$  is the residual spectrum at the respective wavelength point. A small residual without remnants of absorption structures are request for a most successful retrieval. Thus, to judge the fit performance, the fitting root mean square (rms) is used as a quality criterion,

$$\text{rms} = \sqrt{\frac{1}{N} \sum_{i=1}^N r_i^2} \quad (\text{E 2.14})$$

## 2. Scientific background

### 2.3.8 Atmospheric air mass factor

The slant column density which is the trace gas concentration integrated along the light path depends on the observation geometry. Thus, to express quantities in a universal unit, the SCD is converted into the VCD which is the concentration of one absorber integrated along the vertical path ( $z$ ) through the atmosphere:

$$\text{VCD} = \int \rho(z) dz \quad (\text{E 2.15})$$

For the conversion between the SCD and VCD, a factor is needed which is referred to as air mass factor (AMF), the ratio between the SCD and VCD:

$$\text{AMF} = \frac{\text{SCD}}{\text{VCD}} \quad (\text{E 2.16})$$

If we consider only the viewing geometry and single scattering, the AMF for a satellite instrument can be simply determined as:

$$\text{AMF} = \frac{1}{\cos(\text{SZA})} + \frac{1}{\cos(\text{VZA})} \quad (\text{E 2.17})$$

where VZA denotes the angle between the local zenith and the line of sight to the satellite, and SZA the solar zenith angle defined with respect to the zenith direction (see Figure 2.10). This geometric approximation can be applied for nadir observations of stratospheric trace gases since the air density in the stratosphere is low and most scattering events occur below the stratosphere. However, for nadir satellite observations of tropospheric trace gas columns at visible and UV wavelength range, the light path through the atmosphere is more complex due to Rayleigh scattering on atmospheric molecules. Therefore, in such cases, radiative transfer simulations should be performed for determining the AMF. Besides the dependence of the AMF on viewing geometry (SZA and VZA), it also depends on various parameters such as the wavelength, surface spectral reflectance (albedo), air pressure, trace gas profile, properties of aerosols and clouds and so on. The ratio between SCD and VCD can be calculated for each atmospheric layer  $i$  individually to represent the vertical dependence of the measurement sensitivity. This height-resolved partial AMF is referred to as Box-AMF:

$$\text{BAMF}_i = \frac{\delta \text{SCD}}{\delta \text{VCD}_i} \quad (\text{E 2.18})$$

The total AMF can be directly determined by integrating the height profiles of

## 2. Scientific background

Box-AMFs and the relative gas concentration profile:

$$\text{AMF} = \frac{\sum_i \text{BAMF}_i \cdot \text{VCD}_i}{\text{VCD}} \quad (\text{E 2.19})$$

Here,  $\frac{\text{VCD}_i}{\text{VCD}}$  describes the relative trace gas concentration profile (also called shape factor) and the BAMF does not depend on the absorber profile. Thus, different a priori profiles can be applied to calculate the total AMF depending on the assumed absorber profile. This approach is convenient for large number of air mass factor calculations as in the case of satellite retrievals. Depending on the trace gas of interest, in addition to the viewing geometry and solar position, various physical input data are required to investigate the altitude-dependent sensitivity of radiance measurements from radiative transfer simulations. In particular, the radiative transfer simulations for tropospheric trace gases are sensitive to the effect of the surface albedo, surface elevation, clouds, aerosols, and the vertical distribution of the trace gas as described in Table 2.2. The impact of these a priori data on the retrieval results is large, and therefore collection of accurate input information is important.

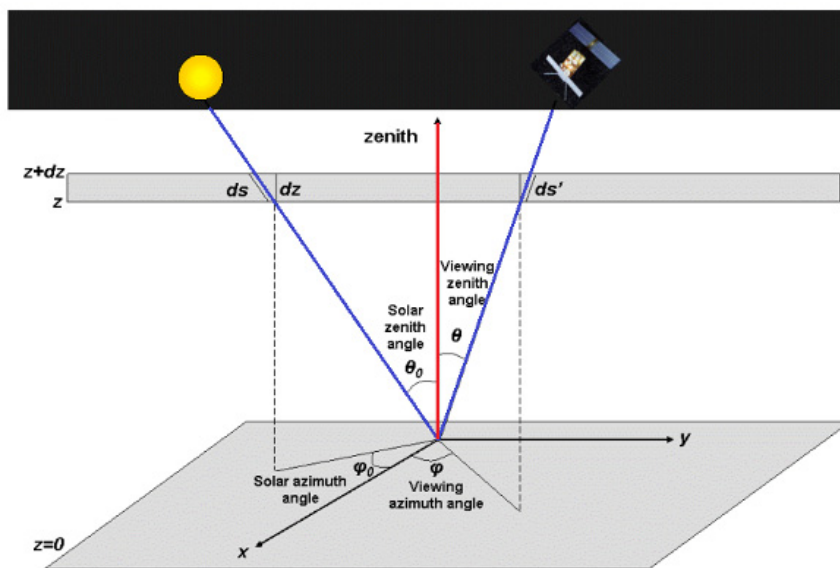


**Figure 2.10.** Schematic illustration of the Solar Zenith Angle (SZA) and Viewing Zenith Angle (VZA) for observations from satellite-based instrument. (image credit: ESA homepage)

## 2. Scientific background

**Table 2.2.** Input information used for radiative transfer simulations of tropospheric trace gases (Burrows et al., 2011).

<b>Input data</b>	<b>Importance</b>	<b>Typically used</b>	<b>Source of information</b>
Trace gas profile	High	Yes	Independent information, e.g., from atmospheric models or general assumptions
Surface albedo	High	Yes	Climatology, e.g., created from the same satellite instrument, sometimes also retrieved from the measurements
Cloud properties	High	Yes	Simultaneous measurements, e.g., cloud fraction and cloud top height
Aerosol properties	High	No	General assumptions, atmospheric models, potentially also simultaneous measurements
Surface elevation	Medium	No	Databases
Solar zenith angle	Medium	Yes	Observation description
Viewing zenith angle	Medium	No	Observation description
Relative azimuth angle	Medium	No	Observation description
Pressure and temperature profile	Low	Yes	Standard profiles

## 2.4 Description of instruments

### 2.4.1 Satellite instruments

#### 2.4.1.1 OMI

The Ozone Monitoring Instrument (OMI) is a nadir-viewing space-borne imaging spectrometer launched on the NASA Earth Observing System (EOS) Aura platform in July 2004 (Levelt et al., 2006). It is a push-broom imaging spectrometer that observes solar backscattered radiation in the visible and ultraviolet from 270 to 500 nm in three channels (UV1: 270–310 nm, UV2: 310–365 nm, visible: 350–500 nm) at a spectral resolution of 0.42–0.63 nm and a spatial resolution of 13 x 24 km<sup>2</sup> at direct nadir. OMI has a large swath of 2600 km providing daily global coverage, but in case of high latitudes, it can provide observations more than once

## 2. Scientific background

per day due to its wide swath. The equator-crossing time of OMI is 13:45 local time in the ascending node. Since 2007, as a consequence of physical obstructions of OMI instrument, radiance errors known as row anomalies occur (Torres et al., 2018). Initially, the row anomaly only affected a few viewing positions, but since 2009, this anomaly effect has become more serious and reduced spatial coverage by removing affected viewing position data. A flagging has been introduced in the OMI level 1b data to classify whether pixels are affected by the instrument anomaly and almost one third of the pixels are not recommended for scientific use. OMI measures various trace gases such as O<sub>3</sub>, HCHO, SO<sub>2</sub> and BrO in the UV channel, while NO<sub>2</sub> and CHOCHO can be retrieved in the visible channel. Not only trace gases, but aerosols, clouds and surface properties are also retrieved from the OMI data. In this study, we use OMI UV2 channel for BrO retrievals.

### 2.4.1.2 GOME-2

The Global Ozone Monitoring Experiment-2 (GOME-2) is an optical spectrometer that measures backscattered solar radiation by using a scan mirror which enables across-track scanning in nadir as well as side-ways viewing for polar coverage (Callies et al., 2000; Munro et al., 2016). This instrument was launched on the European Meteorological Operational satellite series (MetOp-A, B and C) in October 2006, September 2012, and November 2018, respectively (hereafter referenced as GOME-2A, GOME-2B and GOME-2C, respectively). GOME-2 measures radiance between 240 and 790 nm at a spectral resolution of 0.26-0.51 nm and comprises four main optical channels (Channel 1: 240-324 nm, Ch2: 310-403 nm, Ch3: 397-604 nm, Ch4: 593-790 nm). The instrument's spatial resolution is 40 x 80 km<sup>2</sup> with a scan width of 1920 km. In case of GOME-2A, the ground pixel size was reduced to 40x40 km<sup>2</sup> as the swath of GOME-2A was reduced to 960 km in July 2013. GOME-2 overpasses the equator at 9:30 local time in the descending node. For BrO retrievals, GOME-2 channel 2 was used in this study.

### 2.4.1.3 TROPOMI

The tropospheric Monitoring Instrument (TROPOMI) on board ESA's Sentinel-5 Precursor (S5P) satellite was launched in October 2017. TROPOMI is a push-broom imaging spectrometer similar in concept to OMI (see Fig. 2.11). The local

## 2. Scientific background

overpass time is also almost the same with OMI on EOS Aura (~13:30 local time in the ascending node), which is beneficial for investigating a long-term trend using the combined OMI and TROPOMI data record. TROPOMI has eight spectral bands covering the UV and visible from 270 to 500 nm, the NIR from 675 to 775 nm and the SWIR band from 2305 to 2385 nm, which allows to observe various atmospheric components including O<sub>3</sub>, NO<sub>2</sub>, SO<sub>2</sub>, HCHO, BrO, CO, CH<sub>4</sub>, aerosols and clouds. The instrument has a large swath of 2600 km providing daily global coverage with high spatial resolution of 3.5x 7km<sup>2</sup>, and since August 2019 up to 3.5 x 5.5 km<sup>2</sup> at nadir.

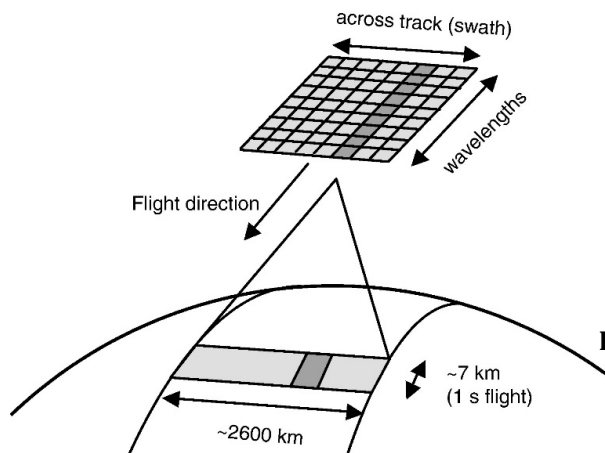


**Figure 2.11.** Schematic of the measurement principle of the TROPOMI instrument. (image credit: Veeffkind et al., 2012)

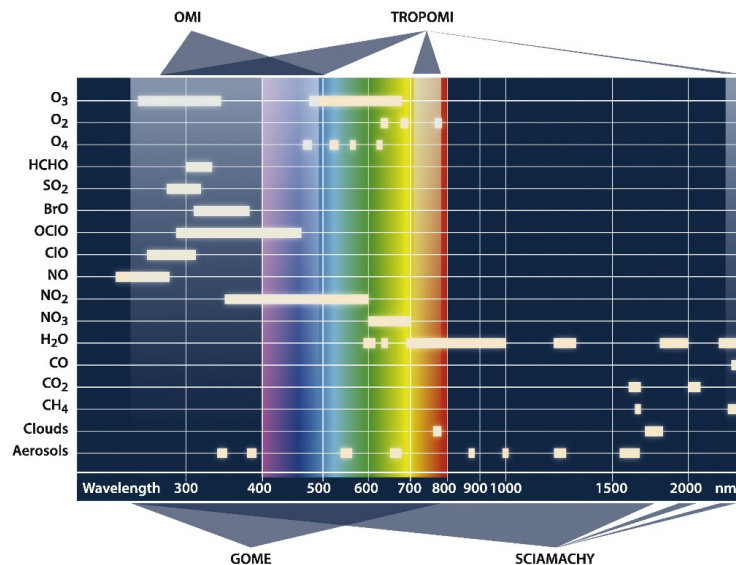


**Figure 2.12.** Spectral ranges for TROPOMI and previous instruments GOME, SCIAMACHY, and OMI. (image credit: Veeffkind et al., 2012)

## 2. Scientific background

### 2.4.2 Ground-based MAX-DOAS instrument

The DOAS technique can not only be applied to satellites but also to ground-based platforms. Passive DOAS instruments based on the observation of light scattered in the zenith (elevation angle =  $90^\circ$ ) were used to study several stratospheric species such as stratospheric  $O_3$ ,  $NO_2$ ,  $OCIO$ , and  $BrO$  (see Fig. 2.13, left panel) (Noxon, 1975; Aliwell et al, 1997; Hönninger et al., 2004). To get sensitivity and information for tropospheric species, a new type of ground-based DOAS instrument was developed allowing for off-axis (elevation angle =  $0-90^\circ$ ) observations as well as the zenith geometry. Multi-Axis Differential Optical Absorption Spectroscopy (MAX-DOAS) instruments observe scattered sunlight under different elevation angles between zenith and horizon (see Fig. 2.13, right panel) (Leser et al., 2003; Van Roozendael et al., 2003; Hönninger et al., 2004, Wittrock et al., 2004). Measurements of scattered sunlight at different elevation angles provide us a vertical distribution of trace gases and aerosols. Details of the instrument used in this study will be described in section 5.2.2.

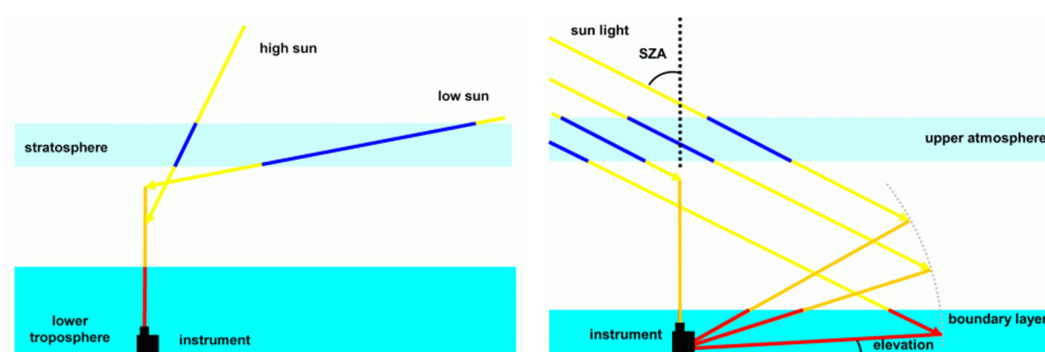


**Figure 2.13.** Schematic representations of the zenith-sky DOAS (left) and MAX-DOAS (right) measurement geometry.  
(image credit: [http://www.iup.uni-bremen.de/doas/maxdoas\\_instrument.htm](http://www.iup.uni-bremen.de/doas/maxdoas_instrument.htm))

# 3

## Tropospheric BrO retrievals from high spatial resolution satellite data

### 3.1 Introduction\*

Bromine monoxide (BrO) plays an important role in atmospheric chemistry. In the lower stratosphere, it is involved in chain reactions that deplete ozone (Wennberg et al., 1994), and bromine in the troposphere changes the oxidizing capacity through the destruction of ozone, which is a primary precursor of atmospheric oxidation in the troposphere (von Glasow et al., 2004). In particular, large amounts of BrO are often observed in the polar boundary layer during springtime, known as “bromine explosion”, and lead to severe tropospheric ozone depletion by autocatalytic reactions (McConnell et al., 1992; Simpson et al., 2007). In addition to polar sea ice regions, enhanced BrO concentrations were also detected over salt lakes/marshes (Hebestreit et al., 1999; Tas, 2005; Hörmann et al., 2016), in the marine boundary layer (Leser et al., 2003; Sander et al., 2003; Saiz-Lopez et al., 2004), and in volcanic plumes (Bobrowski et al., 2003; Theys et al., 2009; Schönhardt et al., 2017).

To understand the formation of BrO and the various chemical reactions involving halogen oxides in the troposphere, BrO observations have been carried out by in situ chemical ionization mass spectrometry (CIMS) (Liao et al., 2011; Choi et al., 2012), ground-based differential optical absorption spectroscopy (DOAS) measurements such as long-path DOAS (LP-DOAS) (Hönninger et al., 2004; Liao et al., 2011; Stutz et al., 2011), and multi-axis DOAS (MAX-DOAS) (Hönninger et al., 2004; Frieß et al., 2011; Zhao et al., 2016). Space-born measurements as well as ground-based measurements have been used for the monitoring of BrO distributions on global and regional scales for more than two decades. Since the

---

\* This section was partly published in *Seo et al. (2019)*.

### 3. Tropospheric BrO retrievals from high spatial resolution satellite data

launch in 1995 of the Global Ozone Monitoring Experiment (GOME) on ERS-2, a series of UV-visible spectrometers on board satellites including SCIAMACHY, GOME-2, and OMI have been observed the global distribution of BrO columns and large-scale BrO events. The first global observations of BrO were retrieved from the measurements of GOME and large-scale tropospheric BrO plumes in the polar sea ice region were detected (Wagner and Platt, 1998; Richter et al., 1998; Chance, 1998). SCIAMACHY, which followed GOME, not only measured BrO columns but also vertical profiles of BrO in the stratosphere from limb measurements (Rozanov et al., 2005; Kuhl et al., 2008). The higher spatial resolution data of GOME-2 and OMI have been successfully used to monitor daily global distribution as well as BrO emissions from various source regions such as volcanoes (Theys et al., 2009; Hörmann et al., 2013; Schönhardt et al., 2017), salt lakes (Hörmann et al., 2016), and polar sea ice regions (Begoïn et al., 2010; Salawitch et al., 2010; Theys et al., 2011; Sihler et al., 2012; Blechschmidt et al., 2016). However, OMI's coverage has been reduced since 2008 due to the so called "row anomaly", which is the result of a physical obstruction of the instrument, and currently the anomaly effect extends over about 50% of the sensor's viewing positions (Torres et al., 2018). This reduced viewing ability affects the observation of emission events as well as the accuracy of the long-term time series. Existing satellite BrO time series can potentially be extended with data from the TROPospheric Monitoring Instrument (TROPOMI) on board the Copernicus Sentinel-5 Precursor platform, which was launched in October 2017 for a mission of 7 years (Veefkind et al., 2012).

In this chapter, an advanced algorithm to retrieve total and tropospheric BrO columns from TROPOMI measurements will be presented. This retrieval algorithm is based on the heritage from earlier satellite missions. The aim of this study is a first demonstration of the feasibility of BrO retrievals on TROPOMI data, investigation of their precision, and the comparison to data from other satellites. In order to determine the best retrieval window, sensitivity tests are performed for various measurement scenarios by a systematic investigation of retrieval results in different retrieval wavelength intervals. TROPOMI BrO columns are assessed by comparison with those from the two existing satellite instruments, GOME-2 and OMI, with the consistency of the set of measurements being investigated. Various methods for the separation of stratospheric and tropospheric structures in the total BrO columns are tested and evaluated. Also, air mass factor calculations for TROPOMI are performed by taking into account various observation conditions such as viewing geometry, varying surface albedo, and BrO vertical profile shape.

### 3. Tropospheric BrO retrievals from high spatial resolution satellite data

Finally, some examples of interesting cases in the TROPOMI BrO data are investigated and described for different source regions, such as the Arctic sea ice, salt lakes, and volcanoes.

## 3.2 Satellite BrO retrieval algorithm description

The general method used for the tropospheric BrO VCD from the UV-vis nadir spectral measurements is the DOAS method, which involves three main steps. As a first step, the BrO slant column densities (SCDs) are derived through a least-squares fit of the measured Earth reflectance spectrum by absorption cross-sections. To obtain the amount of BrO in the troposphere, total BrO columns should be divided into their stratospheric and tropospheric contributions through a process referred to as stratospheric correction. Finally, the tropospheric BrO slant columns are converted into vertical columns by applying air mass factors obtained from radiative transfer calculations accounting for viewing geometry, surface properties, BrO vertical profile and so on. Each separate step of the tropospheric BrO retrieval algorithm will be described in detail in the next sections of this chapter: the DOAS BrO fitting in Sect. 3.3, stratospheric correction in Sect. 3.4, tropospheric air mass factor calculation in Sect. 3.5, and tropospheric BrO VCD retrievals in Sect. 3.6. The overall structure of the tropospheric BrO retrieval algorithm is outlined in Fig. 3.1.

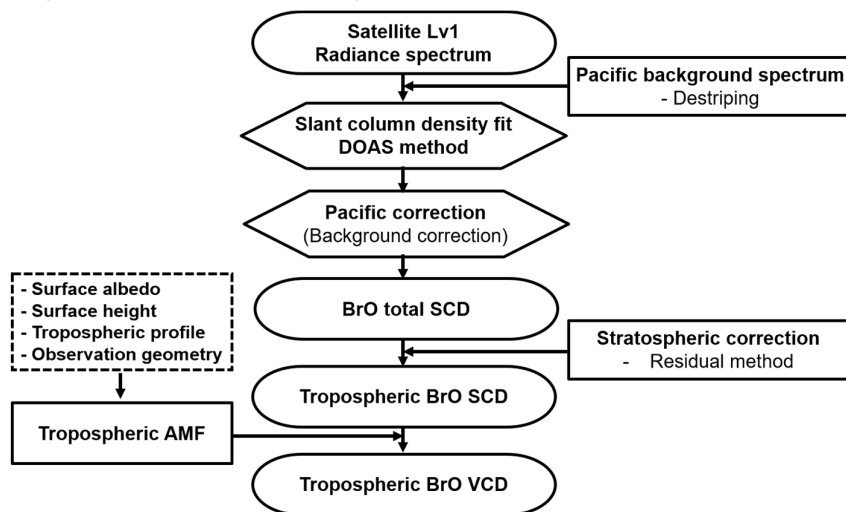


**Figure 3.1.** Flow diagram of the tropospheric BrO retrieval algorithm from the satellite Level 1b spectra.

### 3. Tropospheric BrO retrievals from high spatial resolution satellite data

## 3.3 DOAS BrO slant column retrievals<sup>§</sup>

The retrieval algorithm for BrO uses the differential optical absorption spectroscopy (DOAS) technique (Platt and Stutz, 2008) as applied for space observations (Burrows et al., 2011). The concept of DOAS is to separate the wavelength dependent extinction signal into two components, the low frequency and the high-frequency part. The absorption by atmospheric gases is identified from their higher-frequency structures of absorption cross sections in spectral space and the low-frequency parts are treated as a closure term fitted by a low-order polynomial. The absorber concentration integrated along the light path, the slant column density (SCD), is determined assuming the Beer–Lambert law is applicable.

BrO SCD retrievals are typically performed within the wavelength range from 320 to 364 nm, which covers nine absorption peaks of BrO. In this spectral region, interferences with O<sub>3</sub> (Serdyuchenko et al., 2014), NO<sub>2</sub> (Vandaele et al., 1998), HCHO (Meller and Moortgat, 2000), SO<sub>2</sub> (Bogumil et al., 2003), OCIO (Kromminga et al., 2003), and O<sub>4</sub> (Thalman and Volkamer, 2013) can be found. Thus, not only the absorption cross section of BrO (Wilmouth et al., 1999; Fleischmann et al., 2004) but also those of these related molecules are included in the BrO retrieval. In addition to the absorption cross sections of interfering species, a synthetic Ring spectrum calculated using the SCIATRAN model (Vountas et al., 1998) is included to account for the effect of rotational Raman scattering and a linear intensity offset used as an additional closure term. All absorption cross sections are convoluted with satellite’s row and wavelength dependent slit function. In this section, we focus on the BrO SCD retrieval for the TROPOMI with optimized retrieval settings.

### 3.3.1 Sensitivity test of retrieval fitting interval

For the retrieval of a weak absorber such as BrO, the selection of the optimal fitting wavelength window is one of the most important things in the DOAS retrieval process (Vogel et al., 2013; Alvarado et al., 2014). The optimal fitting window is a retrieval wavelength range that maximizes the differential absorption structures for the trace gas of interest while minimizing interferences of other gases. In

---

<sup>§</sup> Parts of this section were published in *Seo et al.* (2019).

### 3. Tropospheric BrO retrievals from high spatial resolution satellite data

general, larger fitting windows can improve the quality of DOAS retrievals by using more spectral points, but at the same time, they can increase the noise and bias resulting from interfering signals from other absorbers and wavelength-dependent light path lengths. Smaller fitting windows allow the fit to better compensate for errors caused by interferences of other absorption gases, but can also lead to increased cross correlation between reference absorption cross sections and higher noise. Thus, finding a compromise for a fitting window that avoids the disadvantages as well as making the best use of the advantages from the retrieval wavelength interval is important to yield the best quality DOAS retrieval result.

In this study, a sensitivity test of the wavelength interval on DOAS BrO retrievals was performed by evaluating the BrO SCDs and fitting rms values in many different wavelength ranges. In addition, the scatter of the slant columns was also investigated over a clean background region. Vogel et al. (2013) conducted a detailed study of the influence of the wavelength interval on the quality of DOAS retrievals based on a novel method and visualization of the results as contour plots. They applied this technique to a theoretical study of BrO retrievals for stratospheric BrO and BrO in volcanic plumes by using synthetic spectra, modeling zenith-sky DOAS measurements of stratospheric BrO and tropospheric measurements of volcanic plumes. In this way, effects of different wavelength intervals on DOAS retrievals and appropriate spectral ranges for different study cases could be easily identified from visualized maps. A similar systematic approach was taken in this study. However, one important objective of this study is the investigation of the TROPOMI BrO retrieval results for various measurement cases and the identification of the overall best fitting window for TROPOMI BrO measurements. Therefore, sensitivity tests were performed for different BrO emission scenarios using real satellite data to identify a spectral region with the best BrO results and the fewest interference problems. The different measurement scenarios selected are enhanced BrO plumes in the Arctic sea ice region, BrO plumes over a salt marsh, BrO enhancements in volcanic plumes, and clear and cloudy scenes over the Pacific background region. The selected scenarios have very different BrO amounts, slant columns of interfering species, solar zenith angle, temperatures, and geographical conditions. The influence of variations in the parameters for these different cases is included, thereby enabling an optimal fitting window to be identified for application in a global BrO retrieval. The selected regions and dates for the different scenarios are summarized in Table 3.1.

### 3. Tropospheric BrO retrievals from high spatial resolution satellite data

The sensitivity tests were performed over a wide range of retrieval wavelength intervals, which have start limits of 320–338 nm and end limits of 342–364 nm with an interval step of 0.2 nm (Fig. 3.2). This retrieval wavelength interval can contain up to nine absorption peaks, always including at least the strongest absorption peak of BrO at 338–342 nm.

Apart from the retrieval wavelength range, other DOAS fit parameters were kept constant to isolate the effect of the retrieval wavelength range on the resulting BrO SCDs. The reference absorption cross sections used in this sensitivity test include not only BrO but also the interfering species as discussed in Sect. 3.3. Also, a row-dependent daily earthshine radiance spectrum taken as the average of measurements over the Pacific region was used as a reference background spectrum to minimize across-track variability. In this sensitivity test, a polynomial of the order of 4 was used and kept constant, which is problematic for small fitting windows for which a lower-order polynomial might have been more appropriate, but changing the polynomial degree within the sensitivity test would have introduced another level of ambiguity.

**Table 3.1.** Geographical and time information for the different scenarios of the sensitivity tests in Sect. 3.3.1.

	<b>Latitude [°N]</b>	<b>Longitude [°E]</b>	<b>Date</b>	<b>No. of pixels</b>
Polar sea ice	72.5±2.5	200.0±20.0	17 Mar 2018 (orbit no. 2206)	31261
Salt marsh	24.0±0.3	70.0±0.5	31 Mar 2018 (orbit no. 2397)	137
Volcanic plume	-16.0±1.0	169.0±1.0	17 Nov 2017 (orbit no. 492)	1748
Clear ocean	-7.0±1.0	-140.0±14.0	9 Apr 2018 (orbit no. 2533)	14254
Cloudy ocean	-3.0±1.0	-142.0±14.0	9 Apr 2018 (orbit no. 2533)	14255

### 3. Tropospheric BrO retrievals from high spatial resolution satellite data

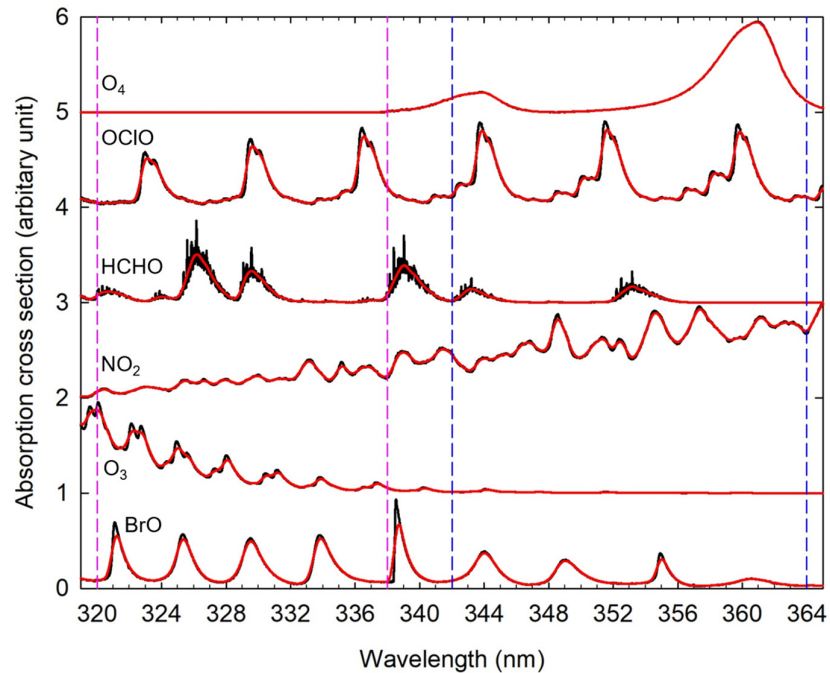


**Figure 3.2.** Reference absorption cross sections used in the sensitivity test of DOAS BrO retrieval. The spectra have been scaled to the order of 1 for presentation purposes. Black lines are the original cross sections and red lines are absorption cross sections convolved with the TROPOMI slit function (TROPOMI ISRF calibration key data v1.0.0, row xxx). Pink vertical dashed lines indicate start wavelength ranges and blue lines end wavelength ranges of fitting windows for this sensitivity test.

#### 3.3.1.1 BrO retrievals over the polar sea ice region

Satellite observations have shown large-scale BrO plumes (1000s of km) occurring over polar sea ice regions in spring, which indicates that this area is one of the most important BrO source regions (Simpson et al., 2007; Begoin et al., 2010). Thus, one of the retrieval wavelength interval sensitivity tests was performed for a BrO explosion event in the Arctic. The results are shown in Fig. 3.3, where each pixel corresponds to the mean of the retrieval results from a particular fitting wavelength interval taken over the first region in Table 3.1 and is displayed on a color-coded scale. As can be seen in Fig. 3.3, negative BrO SCDs with relatively high fitting rms values are found in general for BrO fitting windows with start wavelengths below 327 nm and end wavelengths below roughly 352 nm. These

### 3. Tropospheric BrO retrievals from high spatial resolution satellite data

unphysical negative SCDs and high fitting rms values may be attributed to interferences of other absorbers, which have strong absorption structures at shorter wavelengths, in particular O<sub>3</sub>, which has a maximum at high latitudes in the spring season (Monks, 2000; Aliwell et al., 2002). This can potentially be improved by introducing additional ozone cross sections, which attempt to account for effects arising from changes in the light path with wavelength (Puķīte al., 2010) (see Appendix A).

Also, the map of mean BrO SCDs shows a strong gradient near start wavelengths of 333.4 nm. As shown in Fig. 3.2, strong absorption features of O<sub>3</sub> are located at the wavelength range shorter than 333.4 nm, which indicates that the sudden increase in BrO SCDs at the corresponding wavelength is likely due to the interference of gases other than O<sub>3</sub>. In order to find the gas that interferes the most with the BrO retrieval, we investigated the retrieved SCDs maps of other reference gases used in this DOAS retrieval test and found that HCHO has a sharp change in SCDs in the vicinity of 333.4 nm similar to BrO with anti-correlations of both gases (Fig. 3.4). This implies that HCHO has a significant interference in the DOAS BrO retrieval at the wavelength range with a start limit of 333.4 nm. Thus, to further examine the potential HCHO interference on the BrO retrieval, we performed additional sensitivity tests in the same way as before but excluding the HCHO absorption cross section for the Arctic BrO measurement scenario where very low HCHO columns are expected. The mean relative difference between BrO SCDs retrieved including the HCHO cross section (S1) and those retrieved without including HCHO (S2) is defined as

$$\Delta_{rel} = 100 \% \times \frac{1}{N} \sum_{i=1}^N \frac{(S1_i - S2_i)}{(S1_i + S2_i)/2} \quad (\text{E 3.1})$$

(see Fig. 3.4). Exclusion of the HCHO absorption cross section leads to reduction of the retrieved BrO SCDs at start limits above ~333 nm and in the range of start limits < 325 nm and end limits < 351 nm, while an increase in BrO SCDs is observed mostly at the wavelength range with a start limit below ~333 nm. The pattern of variations in the retrieved BrO SCDs changes at the wavelength range between start limits of 333 and 333.4 nm where a strong absorption peak is present in BrO, while it is absent in HCHO. Possible artifacts in the DOAS BrO retrieval caused by a spectral cross correlation between BrO and HCHO were also identified in Theys et al. (2011) and Vogel et al. (2013). From this sensitivity test for the polar BrO measurement scenario, we can confirm that the main issues

### 3. Tropospheric BrO retrievals from high spatial resolution satellite data

impacting the accuracy of the DOAS BrO retrievals are the influence of the strong O<sub>3</sub> absorptions at the wavelength range < 327 nm and potential interferences between BrO and HCHO absorptions. In consequence, we should choose a wavelength range that avoids strong O<sub>3</sub> absorption features as well as minimizing the interference between BrO and HCHO to obtain the most accurate BrO retrieval results.

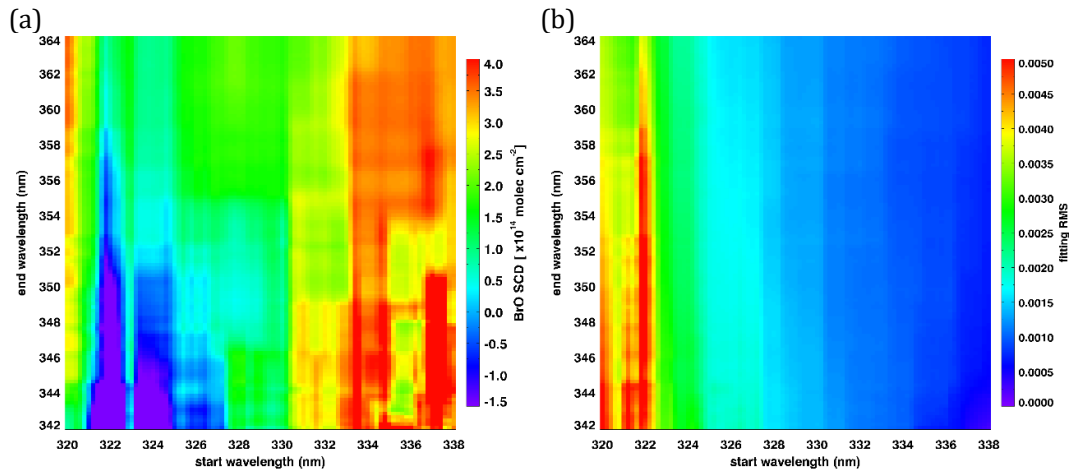


**Figure 3.3.** Color-coded means of (a) BrO SCDs and (b) fitting rms values retrieved over the selected Arctic sea ice region for a BrO explosion event using TROPOMI measurements at different wavelength intervals.

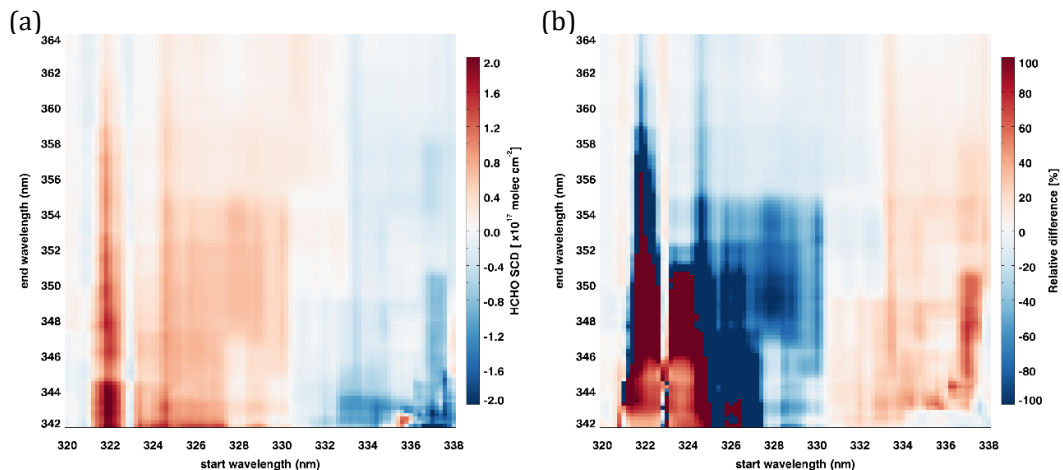


**Figure 3.4.** Color-coded means of (a) HCHO SCDs and (b) relative difference between BrO SCDs retrieved including the HCHO absorption cross section and those without HCHO for the Arctic BrO measurement scenario.

### 3. Tropospheric BrO retrievals from high spatial resolution satellite data

#### 3.3.1.2 BrO retrievals over a salt marsh

In addition to polar sea ice regions, salt lakes and marshes are important BrO source regions. The selected study region (see Table 3.1), Rann of Kutch, is known as one of the strongest natural sources of reactive bromine compounds and has been monitored by satellite measurements for long-term variations in BrO columns (Hörmann et al., 2016). In order to determine the appropriate DOAS fitting wavelength range for BrO retrievals over salt marshes, the sensitivity test was performed in the same way as for the polar event. As shown in Fig. 3.5, BrO retrieval results in the salt marsh show relatively high fitting rms values at shorter wavelengths below 322 nm, but unlike for BrO retrievals in the Arctic sea ice region (Fig. 3.3), no negative values are found for BrO SCDs. This is because the interference of  $O_3$  is smaller in this mid-latitude region scenario than in the polar region where the influence of  $O_3$  absorption is large. In general, high BrO SCDs with low fitting errors are shown in the evaluation wavelength range at start limits of 333–338 nm and end limits of 354–364 nm. This behavior is similar to the appropriate retrieval wavelength range in the previous polar BrO sensitivity test results.

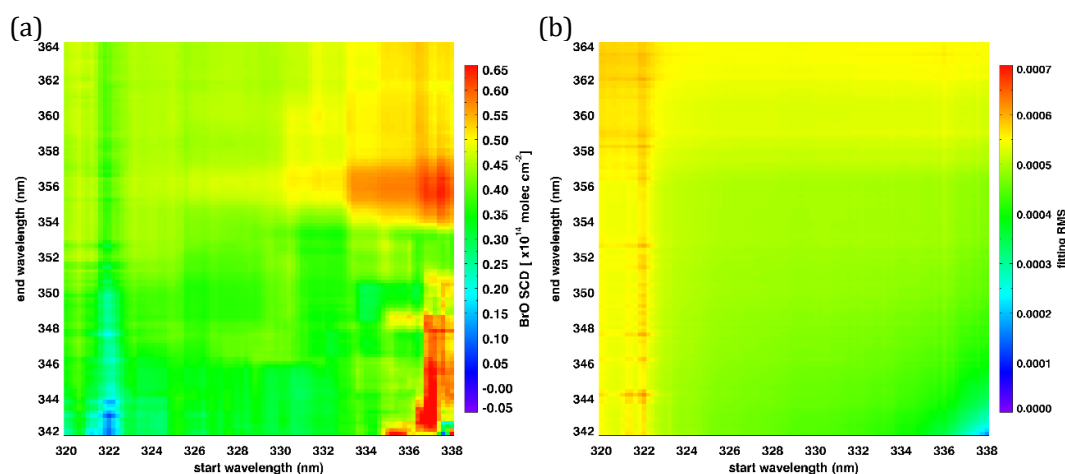


**Figure 3.5.** As Fig. 3.3 but for the Rann of Kutch salt marsh.

### 3. Tropospheric BrO retrievals from high spatial resolution satellite data

#### 3.3.1.3 BrO retrievals in a volcanic plume

Volcanic eruptions emit various gases into the atmosphere and BrO is often also detected in volcanic plumes (Bobrowski et al., 2003). The selected volcanic BrO retrieval scenario is a small-scale BrO plume emitted by volcanic activity at Ambae. In the sensitivity test for volcanic BrO, an SO<sub>2</sub> absorption cross section was added to the general DOAS BrO retrieval settings due to high SO<sub>2</sub> concentrations expected in the volcanic plume. If we use a retrieval wavelength interval with start wavelengths below 323 nm included or narrow fitting windows less than 8 nm wide, negative BrO SCDs and high fitting rms values are found, as can be seen in Fig. 3.6. These features may be attributed to the SO<sub>2</sub> interference at shorter wavelengths and the increase in cross correlation between BrO and other absorption gases, in particular SO<sub>2</sub> (Fig. 3.7). Relatively higher fitting rms values are also found in the retrieval wavelength intervals extending to longer wavelengths (> 358 nm). This is attributed to the impact of the Ring effect, i.e., the in-filling of Fraunhofer lines resulting from high aerosol loads and or the formation of clouds after the volcanic eruption (Theys et al., 2009) (see Fig. 3.7).

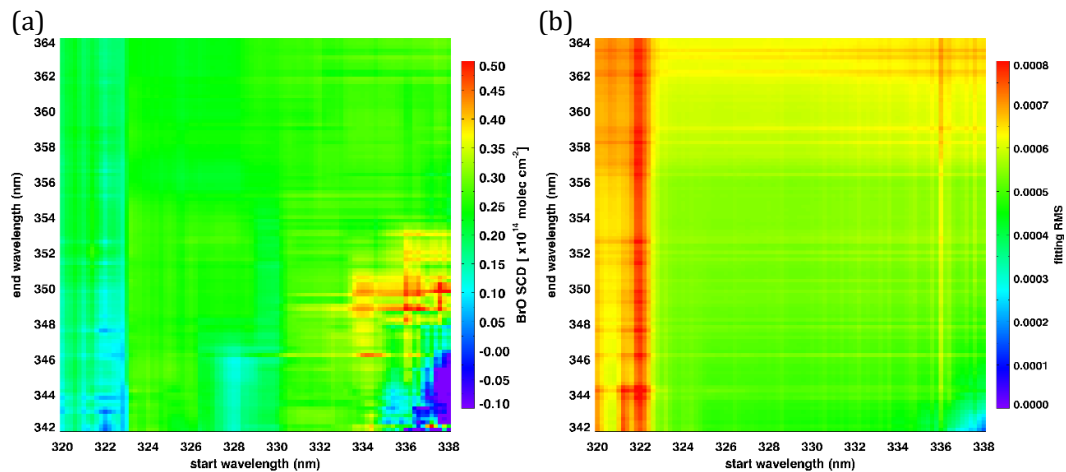


**Figure 3.6.** As Fig. 3.3, but for the selected volcanic plume case.

### 3. Tropospheric BrO retrievals from high spatial resolution satellite data

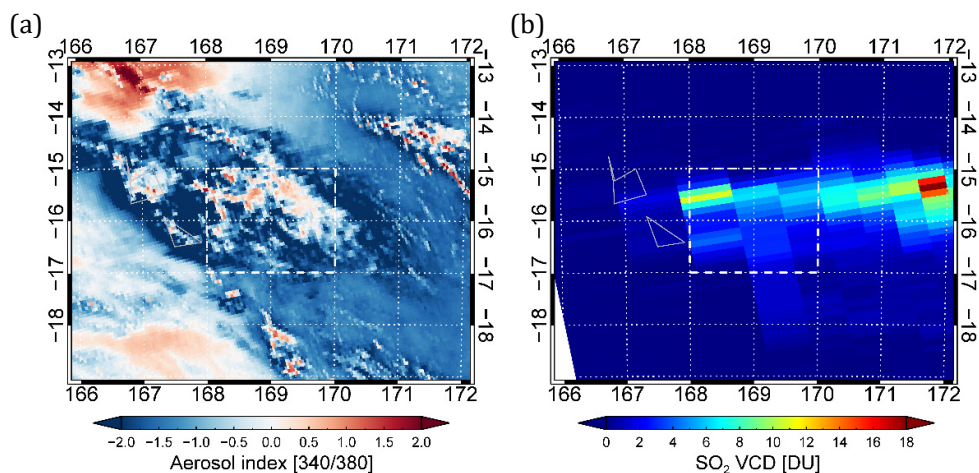


**Figure 3.7.** (a) TROPOMI UV aerosol index (340/380 nm) from the operational Level 2 product and (b) OMI SO<sub>2</sub> vertical columns (DU) from the column amount SO<sub>2</sub> TRM (mid-troposphere) of the operational OMSO2 product for a volcanic BrO measurement scenario. The domain used for the sensitivity test is indicated by a gray dashed box.

#### 3.3.1.4 BrO retrievals over clear scenes in the Pacific background region

The effect of different wavelength intervals on the BrO retrieval was also tested for the case of a clear scene in the Pacific background region without strong BrO sources and clouds. As this area is located within the background region used for the mean background spectrum, the BrO SCD should be minimal. As shown in Fig. 3.8a, in most of the retrieval wavelength intervals, retrieved BrO SCDs are in fact close to the detection limit. Retrieval wavelength intervals having a start wavelength smaller than 330 nm yield overestimations of SCDs, while retrieval wavelength intervals which start at wavelengths longer than 333.4 nm show mainly underestimations. In addition to the mean of the retrieved BrO SCDs, the root-mean-square error (RMSE) of the BrO SCDs in the clear background measurement scenario was also computed for each retrieval wavelength interval (Fig. 3.8c). The RMSE value represents the scatter of the BrO SCDs around the true BrO SCD, and thus a lower RMSE value indicates a better retrieval result with reduced uncertainty on the slant column. As can be seen in Fig. 3.8c, wider fitting windows show lower RMSEs, while more narrow fitting windows show higher RMSEs in general. This is reasonable because if the fitting window is extended, we

### 3. Tropospheric BrO retrievals from high spatial resolution satellite data

can exploit more spectral points in the retrieval and improve the quality of the columns from more available information (Richter et al., 2011). However, this advantage is reduced by the increasing importance of interfering species, which is the reason for the increased RMSEs for fitting windows starting between 321 and 323 nm. In the BrO fitting rms map, the values change abruptly at the wavelength of 322.6 nm, and high fit errors occur at wavelengths < 322.6 nm. This reduced fitting quality in the short wavelength range is attributed to the influence of absorption by stratospheric O<sub>3</sub>.

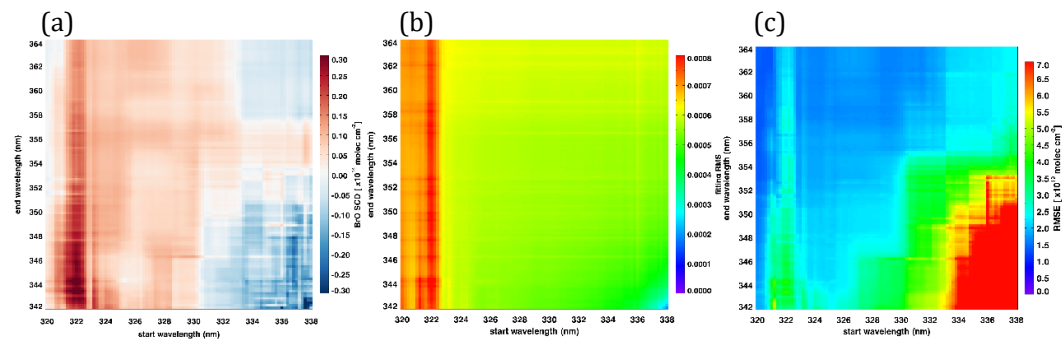


**Figure 3.8.** Mean values of (a) BrO SCDs, (b) fitting rms values, and (c) root-mean square deviation of BrO SCDs retrieved over the clear part of the scene in the Pacific background region using TROPOMI measurements at different wavelength intervals.

#### 3.3.1.5 BrO retrievals over cloudy scenes in the Pacific background region

In order to investigate the effects of clouds on the retrieval of BrO at different evaluation wavelength ranges, a cloudy area was selected in the Pacific background region and the sensitivity test was performed in the same way as in Sect. 3.3.1.4. Figure 3.9 shows the means of retrieved BrO SCDs, root mean square errors of BrO SCDs, and fitting rms values for the measurement scenario of cloudy scenes over the background region. The retrieved BrO SCDs in the cloudy scene are closer to the true value (0) than in the clear scene measurement scenario. In addition, the RMSEs for the cloudy sky measurement scenario are lower than for the clear sky case, but the variation pattern of RMSEs as a function of the retrieval wavelength interval is similar. Both fewer over- and underestimations of the BrO SCDs and smaller deviations from the true BrO indicate lower uncertainties on the

### 3. Tropospheric BrO retrievals from high spatial resolution satellite data

cloudy sky BrO SCDs. This is expected because clouds are bright compared to the dark ocean surface and thus the instrument receives a much larger signal. However, cloud effects are complex in DOAS retrievals using UV-vis measurements and the sensitivity depends on cloud properties such as cloud fraction, thickness, and top height (Burrows et al., 2011; Theys et al., 2011). The dependence of the retrieved BrO SCDs on the Ring effect due to the presence of clouds is also shown in the map of fitting rms values (Fig. 3.9b). Unlike the fitting rms variations in the cloud-free condition (Fig. 3.8b), the cloudy sky measurement scenarios show relatively higher fitting rms values at wavelengths longer than 358 nm, in agreement with the findings for the volcanic plume.

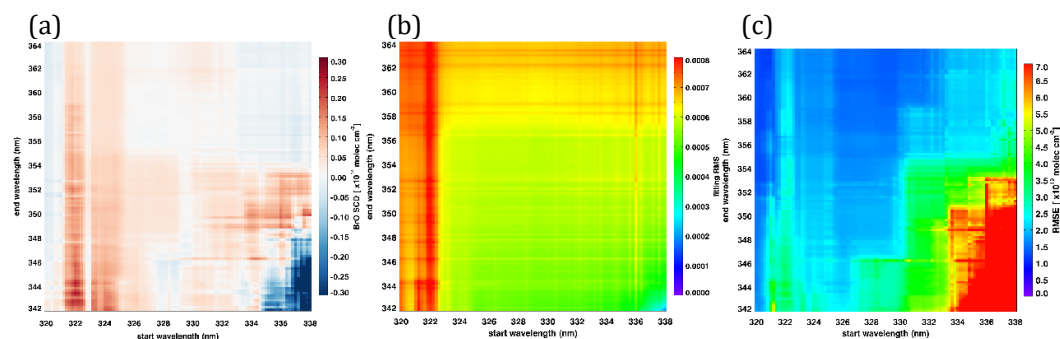


**Figure 3.9.** As Fig. 3.8 but for the cloudy part of the Pacific background region.

#### 3.3.1.6 Selection of optimal fitting window

In the previous sections, the influence of the retrieval wavelength interval on the DOAS BrO retrieval was tested for different measurement scenarios. Based on these test results, we can determine the best fitting window for TROPOMI BrO retrievals for global analysis as well as for the primary BrO source regions. The optimal retrieval fitting windows can be defined as those wavelength intervals which show higher BrO signals with lower fitting residuals in the BrO source regions, while the BrO SCDs should be minimal with narrow distributions of SCDs over the clean Pacific background region. The test for polar BrO retrievals showed unphysical values in wavelength intervals including lower wavelengths smaller than 327 nm due to strong O<sub>3</sub> interferences. The effect of SO<sub>2</sub> interference with strong absorptions at lower wavelengths was also confirmed in the volcanic BrO measurement scenario. Their interfering influences are reduced at longer

### 3. Tropospheric BrO retrievals from high spatial resolution satellite data

wavelengths as overall absorption cross section structures decrease; thus retrieval wavelength intervals with a start limit above 327 nm are preferred to avoid the strong dependency on the lower wavelength limit. In addition to O<sub>3</sub> and SO<sub>2</sub> absorptions at shorter wavelengths, HCHO can also interfere in DOAS BrO retrievals through anti-correlation between the two gases, especially at ~333 nm. This potential artifact may be attributed to the cross correlation caused by the absorption band shape of BrO and HCHO, and it is necessary to find a retrieval wavelength interval that minimizes possible errors caused by the BrO–HCHO cross correlation. In the case of DOAS retrievals over the cloudy background region and the volcanic plume, higher fitting errors were found in the wavelength intervals extending beyond 362 nm because of imperfect correction of the Ring effect and possibly also poorer fitting of O<sub>4</sub> related to the temperature dependency of the cross section. While minimizing these sources of uncertainty on the retrieval, the range of reasonable BrO SCDs and low retrieval errors for all measurement scenarios are observed in the wavelength range of start limits of 334–338 nm and end limits of 358–362 nm. Finally, the fitting window 334.6–358 nm was selected for TROPOMI BrO retrievals with other retrieval parameters set as shown in Table 3.2, by comparing fit residuals and SCD distributions for the remaining fitting windows. Figure 3.10 shows a spectral fitting example of a pixel from orbit 2207 on 17 March 2018 passing over the Arctic sea ice region (72.55 °N, 200.40 °E in Fig. 3.13c). The large BrO SCD of  $4.72 \times 10^{14}$  molecules cm<sup>-2</sup> was retrieved with relative small fitting error of 6.2 %. Although the choice of the optimal fitting window may seem arbitrary to some degree, the analysis of several different relevant scenarios for many possible combinations of fitting windows described above demonstrates that this is an overall robust selection. However, further studies are needed to address the remaining challenges identified through the sensitivity tests, in particular the possible spectral cross correlation of BrO with HCHO around the selected fitting window.

### 3. Tropospheric BrO retrievals from high spatial resolution satellite data

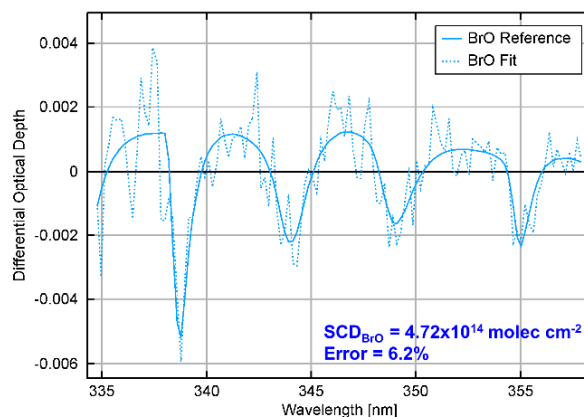


**Figure 3.10.** Example of a BrO fit result applying DOAS settings of Table 3.2 in the Arctic BrO measurement case. The dashed line shows fit results including the fitting residual and the solid line is the reference spectrum scaled according to the fit result.

**Table 3.2.** DOAS settings used for the BrO slant column retrievals and instrumental intercomparison.

Parameter	Description
Fitting window	334.6-358 nm
Absorption cross sections	BrO (Wilmouth et al., 1999), 228K O <sub>3</sub> (Serdyuchenko et al., 2014), 223 and 243K NO <sub>2</sub> (Vandaele et al., 1998), 220K OCIO (Kromminga et al., 2003), 213K HCHO (Meller and Moortgat, 2000), 298K O <sub>4</sub> (Thalman and Volkamer, 2013), 293K
Ring effect	Ring cross section calculated by SCIATRAN model
Polynomial	5 coeff
Solar reference spectrum	Kurucz solar spectrum (Chance and Kurucz, 2010)
Background spectrum	For TROPOMI and OMI one spectrum per row, daily averaged earthshine spectrum in selected Pacific region
Intensity offset correction	Linear offset

### 3. Tropospheric BrO retrievals from high spatial resolution satellite data

#### 3.3.2 Destriping and offset correction

TROPOMI is an imaging spectrometer operating in push broom configuration where one direction of the two dimensional charge-coupled device (CCD) detector is used for the wavelength axis and the other for the across-track image of the instrument's 2600 km wide field of view. This is similar in concept to OMI but with 450 instead of 60 spatial rows resulting in much higher spatial resolution (Veefkind et al., 2012). In this instrument configuration, across-track variability can appear as stripes in trace gas columns due to small variations between the rows, which are not completely compensated for by Lv1B spectra calibration. Indeed, OMI has shown this across-track striping problem (Boersma et al., 2007) and explicit destriping is applied in many OMI products. In TROPOMI data, stripes are also apparent in some trace gas maps when using solar irradiance measurements as background. Two different approaches can be carried out to correct for this: either (1) the across-track variability is determined on a daily basis over a region with minimal variability in trace gas columns and subtracted from all retrieved slant columns, or (2) irradiance background spectra are replaced by averages of nadir observations taken over a reference region.

In this study, the second approach is used and daily row dependent mean radiances measured over a selected Pacific region (30°S–30°N, 150–240°E) are used as background spectrum. This approach can effectively remove across-track stripes, but the retrieved differential BrO SCDs have to be corrected for the viewing angle dependency of the column over the reference region. Here, BrO SCDs were normalized to an assumed background level of a BrO vertical column density (VCD) of  $3.5 \times 10^{13}$  molecules  $\text{cm}^{-2}$  over the Pacific background as suggested by previous studies (Richter et al., 2002; Sihler et al., 2012) using a two-step approach (see Fig. 3.11). First, an offset value for normalization of the differential BrO SCDs is determined as the mode of the Gaussian distribution of differences between the differential SCDs in the reference sector and the normalized SCDs estimated by multiplying the background VCD and a geometric air mass factor defined as  $\text{AMF}_{\text{geo}} = \frac{1}{\cos(\text{SZA})} + \frac{1}{\cos(\text{VZA})}$ . In a second step, this offset value is modified for each row depending on the viewing zenith angle (VZA) to account for variations in the BrO air mass factor. The normalized SCDs are finally calculated by subtracting the VZA-dependent offset values from the measured SCDs.

### 3. Tropospheric BrO retrievals from high spatial resolution satellite data

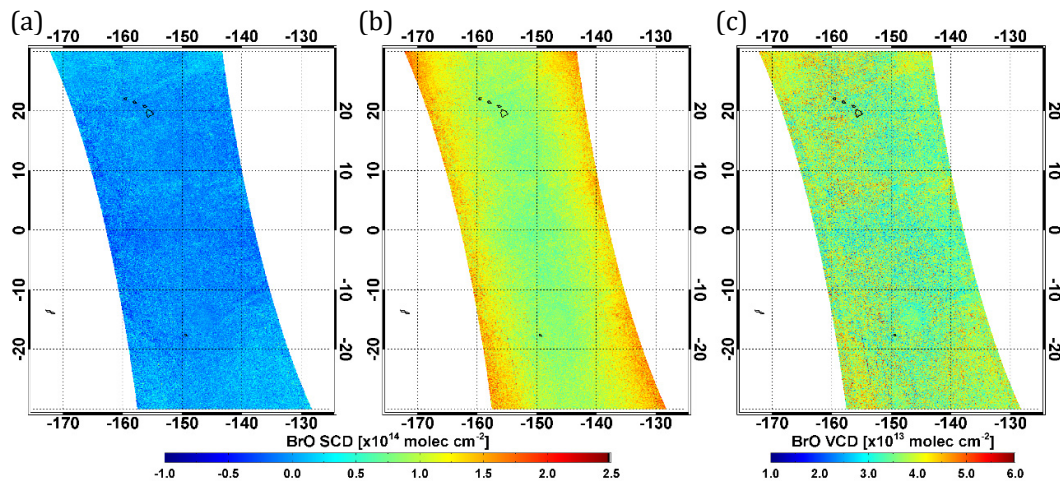


**Figure 3.11.** Illustration showing destriping and offset correction steps described in Sect. 3.2 using TROPOMI orbit 2207 on 17 March 2018. (a) BrO SCDs retrieved by daily row-dependent mean radiances in the Pacific reference sector as background spectrum for the across-track correction, (b) offset-corrected BrO SCDs treated by applying the normalization approach including the VZA dependency on the BrO SCDs, and (c) BrO VCDs computed by dividing the offset-corrected BrO SCDs by geometric AMFs.

## 3.4 Observations of total BrO column from space<sup>††</sup>

### 3.4.1 Global observations of BrO and satellite intercomparison

Applying the retrieval settings described in Table 3.2, BrO vertical columns have been computed from TROPOMI, OMI, and GOME-2B Level 1 spectra. It should be noted that BrO VCDs were calculated using geometrical stratospheric air mass factors and data for solar zenith angles larger than  $85^\circ$  and chi-square values greater than 0.01 were excluded in this section. For OMI, ground/atmospheric scenes affected by the row anomaly were also excluded by using the OMI XTrackQualityFlags. The data in rows 42 to 45 were additionally ignored because it was apparent from the BrO SCDs that they were affected by the row anomaly although they were not marked as bad pixels. No cloud screening was applied here. Figure 3.12 shows the global distributions of the monthly averaged BrO total vertical columns from the three satellite instruments for April 2018.

<sup>††</sup> Parts of this section were published in *Seo et al. (2019)*

### 3. Tropospheric BrO retrievals from high spatial resolution satellite data

The spatial distributions of BrO columns show a good consistency in spite of the differences in instrument resolution and overpass times. High BrO values are found in the northern high latitude region because of tropospheric bromine explosions over the Arctic sea ice during springtime as discussed in previous studies (Richter et al., 2002; Simpson et al., 2007; Begoin et al., 2010), whereas BrO values are low in the tropics and mid-latitudes where BrO columns are primarily of stratospheric origin. Relatively higher BrO values are found in the subpolar and Antarctic region compared to tropics and mid-latitudes. This might reflect real BrO column increases but could at least partially be related to the use of geometric air mass factors (AMFs), which do not consider the effects of surface albedo and clouds. The number of photons detected at the satellite is larger over bright surface areas than over dark surface areas. Therefore, the use of a simple AMF which does not consider the sensitivity to surface albedo can underestimate BrO vertical columns over dark surfaces such as the ocean in comparison to high-surface-albedo regions such as the Antarctic region, north of Russia and Canada. In addition to the surface albedo, clouds also affect signals detected at the satellite. The light path length and intensity are significantly changed depending on cloud top height, cloud thickness, and cloud fraction. Using an AMF that does not take into account the cloud effects can therefore result in errors in the computed vertical columns, as can be seen from the slightly higher BrO VCDs in the subpolar regions where cyclones are frequently observed due to the subpolar low-pressure system (Fig. 3.12). Consequently, an improved AMF reflecting the sensitivity of surface albedo, cloud properties, and BrO vertical profile should be calculated to obtain more accurate vertical column densities (Theys et al., 2011; Sihler et al., 2012), and this will be investigated in detail in the next sections.

To assess the random noise of the BrO retrievals for the different instruments, distributions of SCDs and retrieval fitting rms values over a clean Pacific region (10 °S–10 °N, 150–260 °E) were analyzed for April 2018. Here, differential BrO SCDs without the background offset correction were used for ease of interpretation. As shown in Fig. 3.12b, all three satellite BrO SCD distributions show nearly Gaussian shape and are centered around zero with full width at half maximums (FWHMs) of 0.50, 0.80, and  $0.79 \times 10^{14}$  molecules  $\text{cm}^{-2}$  for TROPOMI, GOME-2B, and OMI, respectively. However, while TROPOMI and GOME-2B columns are symmetrically distributed close to the detection limit, OMI data are slightly shifted towards positive values. The latter is attributed to be a consequence of systematic biases caused by the relatively lower quality of Level 1b radiance due to

### 3. Tropospheric BrO retrievals from high spatial resolution satellite data

the instrument degradation. TROPOMI shows the smallest scatter of BrO SCDs, with OMI and GOME-2B having about 60 % larger FWHMs. TROPOMI retrievals also show by far the smallest mode of the fitting rms distributions, demonstrating the excellent signal-to-noise ratio per pixel even at the unprecedented small footprint.

An intercomparison of BrO satellite retrievals was performed using GOME-2B and OMI retrievals obtained by applying the same retrieval setting (Table 3.2) to Level 1b data to evaluate the consistency of TROPOMI BrO retrievals with those from other satellites. However, for the comparison of different satellite retrievals, several things have to be considered. First of all, the three satellites have different spatial resolution, 40x80 km<sup>2</sup> for GOME-2B, up to 13x24 km<sup>2</sup> for OMI, and 3.5x7 km<sup>2</sup> for TROPOMI. To establish a relationship between different satellite values with different pixel sizes, a spatial coupling of the different data sets is required. Here, the higher-spatial-resolution TROPOMI data were averaged based on a grid of lower spatial resolution. Each GOME-2 and OMI BrO measurement was compared to the averaged TROPOMI BrO that lay within the distance of 0.3° and 0.1° from their center of pixels, respectively. In addition to different pixel sizes, the effect of different overpass times between satellites should be considered. TROPOMI, which has an ascending orbit with a local Equator crossing time of 13:30 LT, shows a different overpassing time than GOME-2B, which has a descending node equatorial crossing time at 09:30 LT, whereas it has a similar afternoon overpassing time to OMI. Although having a similar overpassing time on the ascending node to TROPOMI, recent OMI data provide only limited data due to the loss of spatial coverage with the expansion of the row anomaly, especially in the middle and east across-track segments of the orbit (Torres et al., 2018). This led to a difficulty in utilizing orbits having similar measurement times for the two satellite instruments.

### 3. Tropospheric BrO retrievals from high spatial resolution satellite data

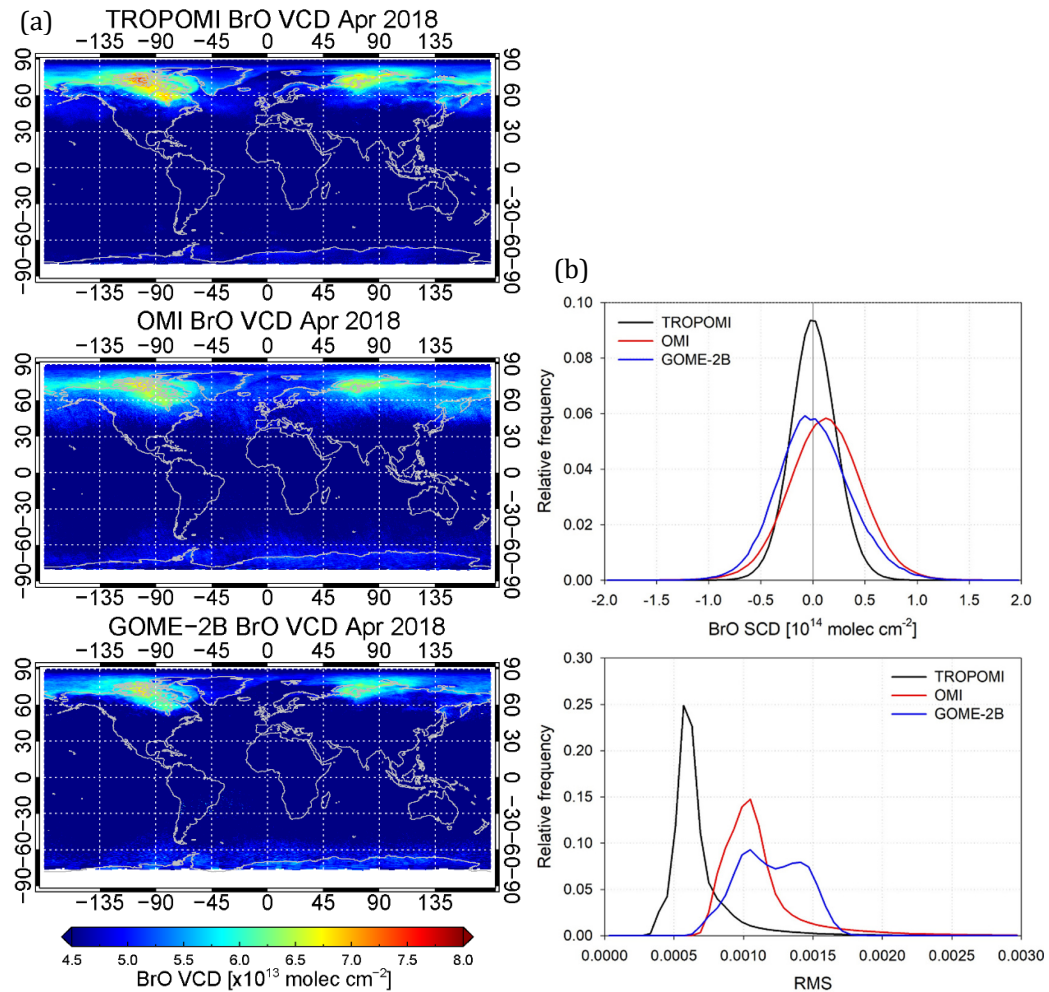


**Figure 3.12.** (a) Global distributions of monthly mean BrO vertical columns retrieved from TROPOMI, OMI, and GOME-2B measurements for April 2018. Data with solar zenith angle lower than  $85^\circ$  were used, and in the case of OMI data, only data not affected by the row anomaly were included. (b) Distribution of BrO SCDs and fitting rms values over a clean equatorial Pacific region ( $10^\circ\text{S}$ – $10^\circ\text{N}$ ,  $150$ – $260^\circ\text{E}$ ) for the same study period.

Figure 3.13a shows a scatter plot comparison between TROPOMI and OMI BrO VCDs, and Fig. 3.13b compares TROPOMI and GOME-2B BrO VCDs. As mentioned before, BrO VCDs were converted from SCDs by dividing through geometric AMFs. The comparison was performed for enhanced BrO plumes in the Arctic sea ice region on 17 March 2018 (Fig. 3.13c). Despite the different spatial resolutions and

### 3. Tropospheric BrO retrievals from high spatial resolution satellite data

measurement times of the instruments, TROPOMI BrO shows good agreement with both OMI and GOME-2B BrO with correlations of 0.84 and 0.84 and slopes of 0.89 and 0.72, respectively. This good agreement and consistency of TROPOMI data with previous satellite sensors suggest that these data could be used to extend the existing long-term data set of space-based BrO observations, in particular for tropospheric BrO explosion events.

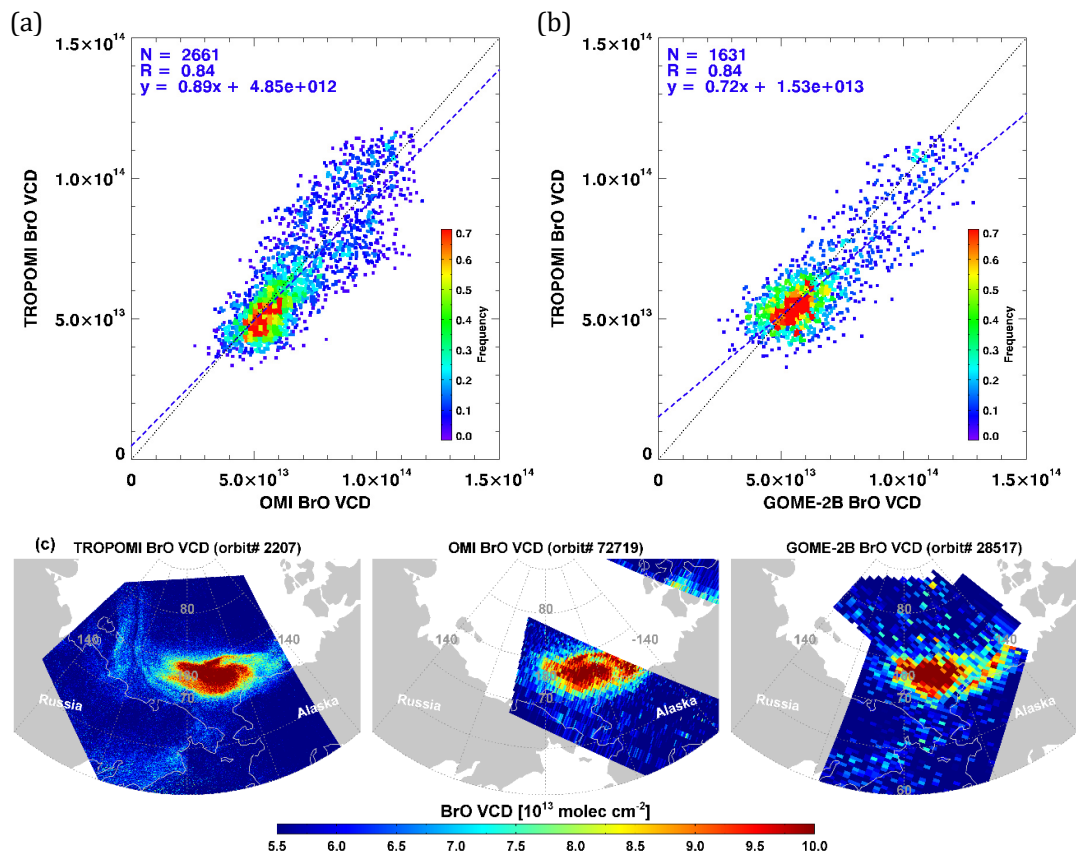


**Figure 3.13.** Scatter plots of (a) TROPOMI and OMI BrO vertical columns and (b) TROPOMI and GOME-2B BrO vertical columns in (c) the selected region of enhanced BrO plumes on 17 March 2018.

#### 3.4.2 BrO plumes over polar sea ice regions

Explosive enhancements of BrO in the troposphere taking place in the polar boundary layer during spring have been reported from ground-based

### 3. Tropospheric BrO retrievals from high spatial resolution satellite data

measurements and satellite observations (Hönninger et al., 2004; Begoin et al., 2010; Choi et al., 2012). As an illustration of the signature of such events in TROPOMI data, Fig. 3.14 presents maps of the TROPOMI, OMI, and GOME-2 measurements of total column BrO on 10 April 2018. A small compact BrO enhancement as well as a long BrO plume extending along the coastline can be identified in the figures. The long and thin enhanced BrO plume near the coastline is prominent in the map of TROPOMI, while it can hardly be discerned in the OMI and GOME-2B maps. For the OMI retrievals, a significant part of the scene is missing because of filtering for pixels affected by the row anomaly. The GOME-2B orbit shown was taken about 1 h before the TROPOMI and OMI measurement times but the BrO plumes are detected in similar locations and have a size comparable to that in the TROPOMI data. However, the details of the spatial distribution and plume shape cannot be confirmed due to the lower spatial resolution of GOME-2.

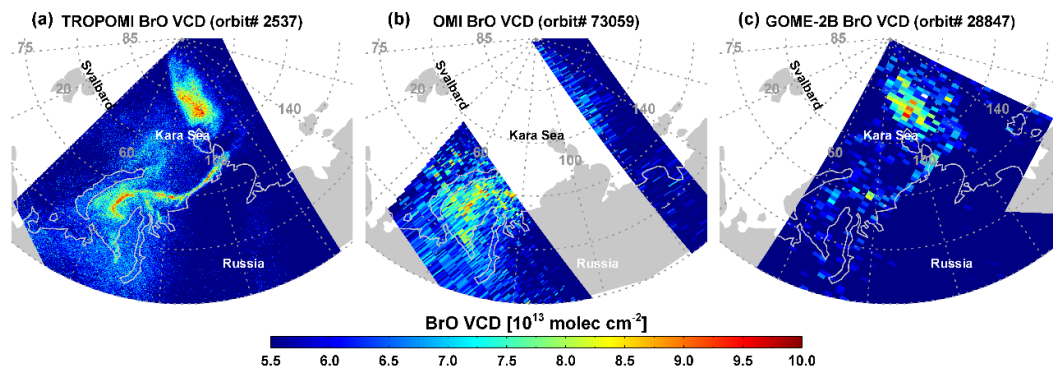


**Figure 3.14.** BrO geometric vertical columns observed over the Arctic sea ice region on 10 April 2018 by (a) TROPOMI, (b) OMI, and (c) GOME-2B.

Another example of a BrO explosion event case is shown in Fig. 3.15. A relatively narrow and long shape of enhanced BrO over the Beaufort Sea can be found in all three satellite maps. As discussed for the previous example, TROPOMI data with the high spatial resolution of 3.5x7 km<sup>2</sup> yield a more detailed view of the BrO explosion event compared to OMI and GOME-2B. The enhanced BrO plumes appear around open leads and sea ice cracks shown as slightly darker areas in the matching MODIS image (arrows pointing at examples). In particular, the elevated BrO around the Banks Island and the eastern Beaufort Sea (70–77 °N, -140 to -120 °E) could be significantly linked to open leads because frost flowers and sea salt aerosols, which act as the source of reactive bromine, can be formed in such

### 3. Tropospheric BrO retrievals from high spatial resolution satellite data

areas (Simpson et al., 2007). Also, opening of sea ice leads can locally create enhanced vertical mixing and uplifting of bromine sources. However, the analysis of the long enhanced BrO plume from the coast of Alaska towards the north should be cautious. The MODIS image composed of the 7-2-1 bands can distinguish clouds (as white) from the sea ice (as sky blue), and this image shows that the shape of the enhanced BrO plume is similar to that of clouds. Convective clouds can be formed around open leads due to the supply of water vapor and enhanced vertical mixing, but computed BrO enhancement over clouds may have an error because of the use of AMFs, which do not consider the effects of clouds. In spite of this uncertainty, the enhancement of vertical columns by up to  $4 \times 10^{13}$  molecules  $\text{cm}^{-2}$  compared to the surrounding values indicates that open leads could be associated with the BrO enhancement.

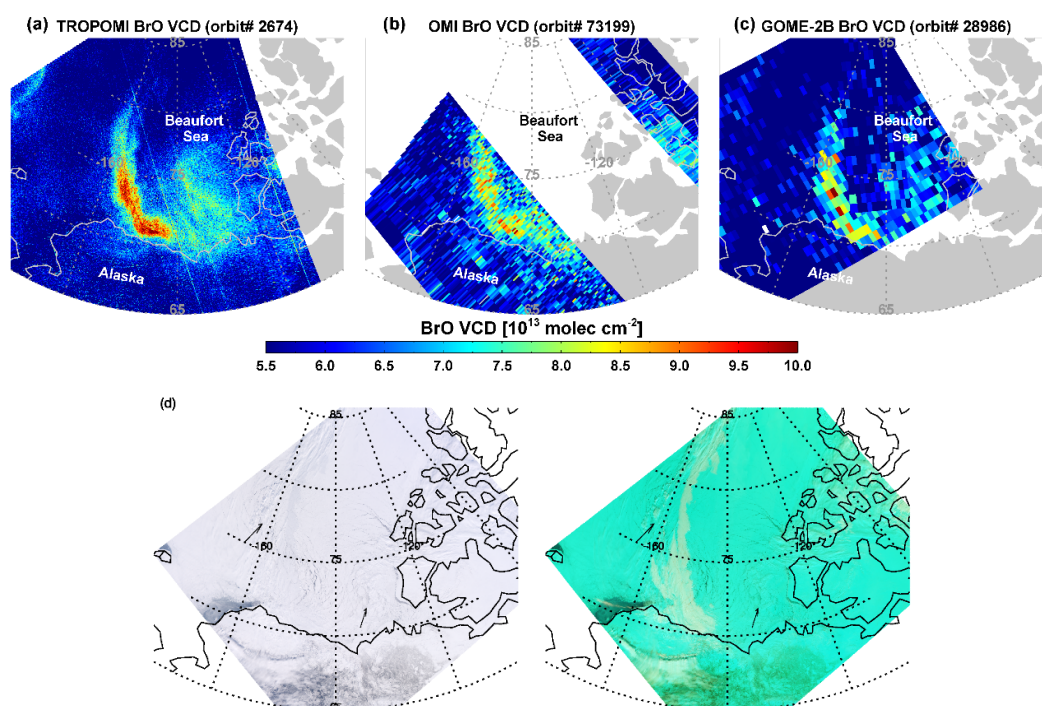


**Figure 3.15.** BrO geometric vertical columns observed over the Arctic sea ice region on 19 April 2018 from (a) TROPOMI, (b) OMI, and (c) GOME-2B. (d) MODIS true color image (left) and image using combinations of 7-2-1 bands (right) from the Aqua satellite for the same scene on the same day. Leads are slightly darker in the MODIS image as indicated by the arrows.

### 3. Tropospheric BrO retrievals from high spatial resolution satellite data

#### 3.4.3 BrO plumes over salt lakes/salt marsh

Salt lakes are one of the strongest and most localized natural sources of reactive bromine. A model study by Tas et al. (2006) focusing on the Dead Sea revealed that aerosols could play an important role in the release of reactive bromine, whereas another study by Smoydzin and von Glasow (2009) suggested an additional direct release of bromine from sea water. Consequently, BrO amounts over multiple salt lakes and marshes have been determined by ground-based DOAS instruments and satellites to establish environmental conditions and chemical mechanisms associated with the reactive bromine production at salt lakes and marshes. High BrO concentrations with peak mixing ratios of 86 ppt at the Dead Sea were observed by long-path DOAS measurements in 1997 (Hebestreit et al., 1999), followed by studies of the diurnal cycle of BrO and the relationships between BrO and O<sub>3</sub> and meteorological factors in the Dead Sea region (Matveev et al., 2001; Tas, 2005). BrO over salt lakes was also studied using satellite measurements. Chance (2006) showed BrO enhancement over the Great Salt Lake using OMI measurements and Hörmann et al. (2016) found a typical annual BrO formation cycle over the Rann of Kutch seasonal salt marsh using long-term GOME-2 and OMI data.

The release of reactive bromine and enhanced BrO plumes over the Rann of Kutch salt marsh are also readily detected in TROPOMI data. Daily mean BrO VCDs over the Rann of Kutch area for TROPOMI and OMI, and MODIS true color images for the time period from 11 April to 14 April 2018 are shown in Fig. 3.16. It should be noted that the AMFs used in this work do not consider surface albedo and cloud effects, and therefore BrO VCDs may be overestimated over the bright salt marsh. BrO enhancements of up to  $4.5 \times 10^{13}$  molecules cm<sup>-2</sup> over background values are detected as hot spots by both satellites. However, as can be seen in Fig. 3.16, TROPOMI data show BrO plumes and small-scale variabilities much more clearly with more spatial details than OMI data. In the case of OMI data, BrO plumes are detected by only a few pixels, whereas TROPOMI can detect the same plumes by hundreds of data points (~150 pixels). This illustrates that TROPOMI data will facilitate in-depth studies of localized small-scale BrO events for multiple salt lakes and marshes.

### 3. Tropospheric BrO retrievals from high spatial resolution satellite data

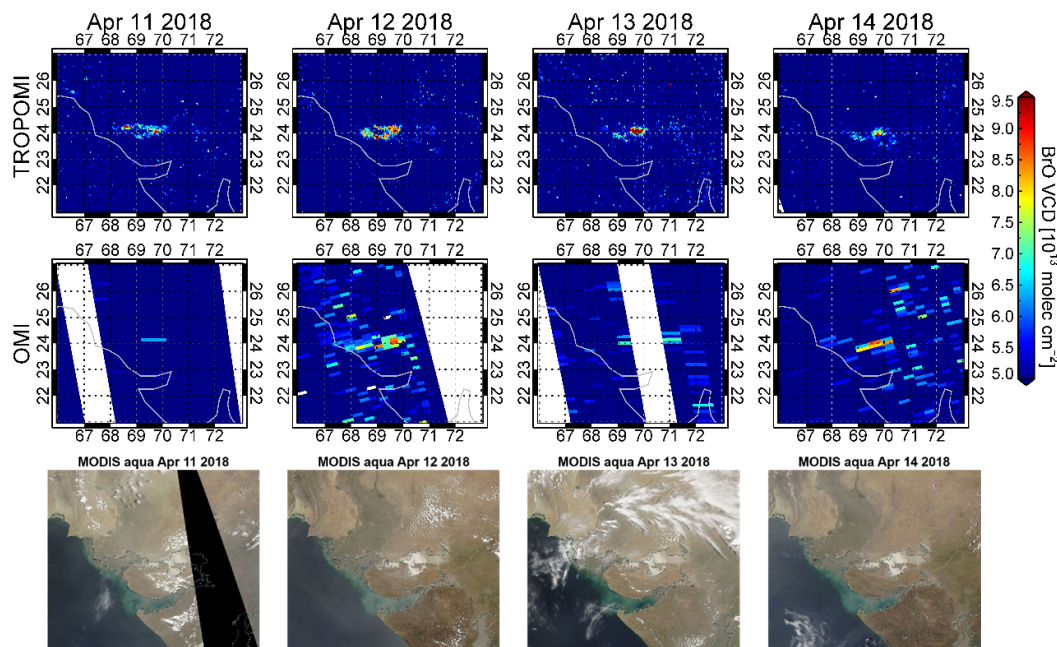


**Figure 3.16.** Daily BrO geometric vertical columns ( $10^{13}$  molecules  $\text{cm}^{-2}$ ) over the Rann of Kutch salt marsh on 11, 12, 13, and 14 April 2018 from TROPOMI (top row) and OMI (middle row) measurements as well as MODIS Aqua true color images over the study region for the same days (bottom row).

#### 3.4.4 BrO enhancements in volcanic plumes

Explosive volcanic eruptions lead to the formation of BrO in the troposphere and lower stratosphere. The detections of BrO in volcanic plumes has been reported by ground-based DOAS measurements for several volcanoes (Bobrowski et al., 2003; Oppenheimer et al., 2006; Boichu et al., 2011). In addition to ground-based measurements, BrO in a volcanic plume was first detected in GOME-2 satellite data after the eruption of the Kasatochi volcano by Theys et al. (2009). Following the first satellite volcanic BrO detection, Hörmann et al. (2013) investigated 64 volcanic plumes and BrO/SO<sub>2</sub> ratios using GOME-2. Schönhardt et al. (2017) found not only volcanic BrO but also IO emissions using SCIAMACHY and GOME-2 measurements.

Not surprisingly, volcanic plumes containing BrO are also detected in TROPOMI data. Figure 3.17 shows the plume over the Indonesian island of Bali after volcanic

### 3. Tropospheric BrO retrievals from high spatial resolution satellite data

activity at Mount Agung on 29 November 2017. Enhanced BrO values of up to  $8.5 \times 10^{13}$  molecules  $\text{cm}^{-2}$  and dispersion of plumes by the wind towards the southwest were detected by both TROPOMI and OMI. These volcanic BrO plumes are associated with enhanced  $\text{SO}_2$  values as identified from the NASA operational OMI product (ColumnAmountSO2\_TRM in OMSO2 version 3 product) with a positive correlation between the species. As shown in Fig. 3.17, monitoring of BrO emissions and their relationship to other gases from volcanic activities is possible with TROPOMI data at higher spatial resolution and improved sensitivity, which suggests that more detailed analysis of volcanic BrO will be possible in the future.

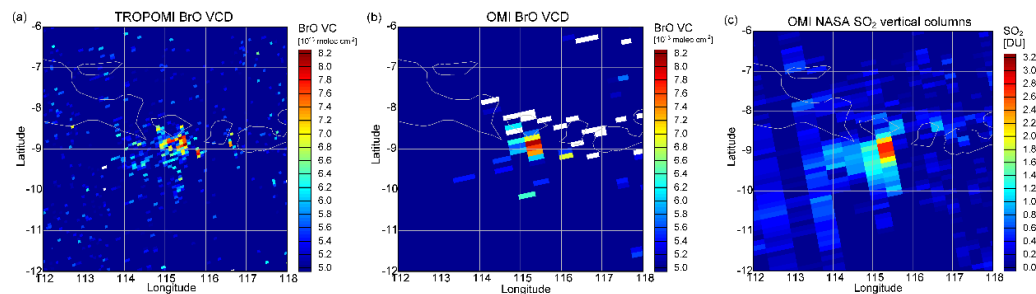


**Figure 3.17.** Volcanic BrO vertical columns ( $10^{13}$  molecules  $\text{cm}^{-2}$ ) on 29 November 2017 after volcanic eruptions at Mount Agung on the Indonesian island of Bali observed by (a) TROPOMI and (b) OMI. (c) Volcanic  $\text{SO}_2$  vertical columns (DU) from the column amount  $\text{SO}_2$  TRM (mid-troposphere) of the NASA operational OMSO2 product ([https://disc.gsfc.nasa.gov/datasets/OMSO2\\_V003/summary](https://disc.gsfc.nasa.gov/datasets/OMSO2_V003/summary), last access: 23 May 2019).

### 3. Tropospheric BrO retrievals from high spatial resolution satellite data

## 3.5 Stratospheric correction

As presented in the previous section, total BrO columns are obtained from satellite measurements based on the DOAS technique. To investigate more precisely quantities and chemical reactions of bromine species at different atmospheric layers, total BrO columns retrieved from satellite data should be separated into their stratospheric and tropospheric contributions. This stratosphere-troposphere separation is called stratospheric correction. In general, tropospheric BrO columns can be derived from satellite measurements based on the residual method, in which an estimated stratospheric BrO column is subtracted from the observed total BrO column as follows:

$$\begin{aligned} \text{VCD}_{\text{trop}} &= \frac{\text{SCD}_{\text{trop}}}{\text{AMF}_{\text{trop}}} = \frac{(\text{SCD}_{\text{total}} - \text{SCD}_{\text{strat}})}{\text{AMF}_{\text{trop}}} \\ &= \frac{(\text{SCD}_{\text{total}} - \text{VCD}_{\text{strat}} \cdot \text{AMF}_{\text{strat}})}{\text{AMF}_{\text{trop}}} \end{aligned} \quad (\text{E 3.2})$$

To estimate stratospheric BrO columns, previous studies have used various methods: (1) atmospheric chemistry model output, (2) SCIAMACHY BrO limb retrievals, (3) stratospheric Br<sub>y</sub> (the total bromine content of all inorganic bromine species) and BrO/Br<sub>y</sub> climatology profile based on long-term model simulations, (4) a parameterization of observed O<sub>3</sub> and NO<sub>2</sub> columns without chemistry model simulations, and (5) local stratospheric background estimation using a spatial polynomial fit.

Salawitch et al. (2010) estimated stratospheric BrO vertical column abundance from atmospheric chemistry model simulations. The vertical distribution of Br<sub>y</sub> was specified in PSS (photochemical steady state) model based on a relationship between Br<sub>y</sub> and CFC-12. Here, CFC-12 profiles were determined from the GEOS-5 (Goddard Earth Observing System Data Assimilation System Version 5) assimilation for the ARCTAS field campaign. Once Br<sub>y</sub> is specified, BrO can be found using the BrO/Br<sub>y</sub> ratio from a run of WACCM (Whole Atmospheric Community Climate Model). Then, stratospheric BrO columns are integrated from the pressure of the tropopause determined by WMO definition of the thermal tropopause based on GEOS-5 temperature to 0.01 hPa.

Sinnhuber et al. (2005) showed the global view of stratospheric BrO columns using the stratospheric BrO profiles retrieved from the limb measurements of SCIAMACHY. SCIAMACHY measures the scattered and reflected spectral radiance in both nadir and limb geometry. Therefore, BrO columns are retrieved from the nadir measurements, while BrO profiles from the limb measurements of

### 3. Tropospheric BrO retrievals from high spatial resolution satellite data

SCIAMACHY. In that study, they compared the observed SCIAMACHY stratospheric BrO with the modeled BrO and results showed good agreements with a stratospheric bromine loading of  $18 \pm 3$  ppt.

Theys et al. (2009) developed a climatology of stratospheric BrO profiles based on a parameterization using three years of output data from the BASCOE 3D chemistry transport model (CTM). The impact of atmospheric dynamics on the stratospheric BrO distribution is captured by means of Br<sub>y</sub>/ozone correlations calculated by the BASCOE model, whereas photochemical effects are considered using stratospheric NO<sub>2</sub> column as an indicator of BrO/Br<sub>y</sub> ratio. Simulated stratospheric BrO profiles showed good agreement with stratospheric BrO retrievals from ground-based, balloon-borne and satellite limb (SCIAMACHY) measurements, which indicates that the climatological approach is optimized for bromine chemistry and budget. The stratospheric BrO vertical columns are derived by integrating simulated stratospheric BrO profiles based on the climatology between the tropopause and the top-of-atmosphere.

Stratospheric BrO columns derived from direct atmospheric chemistry model simulations or the climatology BrO profile obtained from the parameterization using dynamical and chemical indicator based on model simulations may be used for the stratospheric BrO correction as shown in previous studies. However, these two methods using the atmospheric chemistry model have potential bias and systematic errors since the chemical mechanisms built in the model may be incomplete in some parts and model results depend on the choice of initial condition set up. To overcome the limitations based on the model simulations, Sihler et al. (2012) developed a stratospheric correction method using only the measurements themselves. This approach is basically similar to the Theys et al. (2009) method for the estimation of stratospheric BrO column, but it is completely independent from models. In this method, the stratospheric BrO column for each satellite pixel is calculated using the O<sub>3</sub> and NO<sub>2</sub> columns measured from a single satellite instrument to account for dynamic and chemical effects, respectively, and the viewing geometry including the solar zenith angle and the viewing zenith angle.

The last method for stratospheric BrO correction is the estimation of stratospheric background columns using the spatial polynomial fit. This approach is mainly used to retrieve tropospheric BrO vertical columns in small spatial scale of bromine source areas such as active volcanoes or salt lakes/marshes, assuming that stratospheric BrO distribution varies less with latitude and even less with longitude. Hörmann et al. (2013, 2016) calculated the local stratospheric

### 3. Tropospheric BrO retrievals from high spatial resolution satellite data

background column using the polynomial fit as follows:

$$\text{VCD}_{\text{strat},i} \approx \sum_{m,n=0}^p a_{mn} \times x_i^m \times y_i^n \quad (p = 0,1,\dots,4) \quad (\text{E } 3.3)$$

where  $a_{mn}$  are the fitted stratospheric BrO VCD at the centre coordinates  $x$  and  $y$  ( $^{\circ}$ ) of satellite pixel  $i$ . The corresponding local background BrO VCD are approximated by a 2-dimensional polynomial fit of  $p^{\text{th}}$  degree (usually less than 4<sup>th</sup> degree). To minimize the influence of possibly enhanced BrO VCDs in the hot spot, pixels around the source area, for example, whose  $\text{SO}_2$  VCDs lay above  $3\sigma$  of the reference area in the case of volcanic BrO eruption, were excluded from the polynomial fit of the stratospheric correction. Local background stratospheric correction is useful in studies for long-term tropospheric BrO retrievals over small-scale source areas. However, it should be noted that this 2D spatial correction removes a smooth background signal, but cannot completely remove strong spatial gradients of BrO columns, which are generally found in high latitudes.

As mentioned above, many different stratospheric correction methods have been used according to the research purpose and applicable data conditions. In this study, for the stratospheric BrO correction to retrieve tropospheric BrO columns from satellite measurements, three different methods were tested: (1) atmospheric chemistry model, (2) empirical multiple linear regression model, and (3) climatological approach using satellite total  $\text{O}_3$  and stratospheric  $\text{NO}_2$  observations described in Theys et al. (2009, 2011). Detailed descriptions of each method will be provided in the next sections.

#### 3.5.1 3-D atmospheric chemistry transport model

Atmospheric chemistry transfer models (CTMs) help to understand the Earth's atmospheric composition and changes therein (Hollingsworth et al., 2008). For the troposphere, transport and chemical conversion of atmospheric composition influence both air quality and climate change (Marécal et al, 2015). Also, stratospheric atmospheric composition influences the solar irradiance reaching the surface and the chemical composition in the troposphere via stratosphere-troposphere exchange (Vincent et al., 2016). These aspects have been studied in the framework of CTMs. Forecasts of atmospheric composition have been performed by the Copernicus Atmosphere Monitoring Service (CAMS,

### 3. Tropospheric BrO retrievals from high spatial resolution satellite data

<http://atmosphere.copernicus.eu>) with the aim of improving initial conditions for composition fields in terms of reactive gases, aerosols and greenhouse gases from assimilation of satellite and ground-based measurements (Inness et al., 2015; Vincent et al., 2016). In CAMS, tropospheric chemistry schemes have been embedded in ECMWF's Integrated Forecast System, referred to as Composition-IFS (C-IFS, Flemming et al., 2015). Three versions of C-IFS have been developed with different chemical schemes and solvers: one using the C-IFS based on the Carbon Bond chemistry scheme (CB05) in the troposphere and the BASCOE scheme in the stratosphere; another using the MOCAGE scheme and the last using the MOZART scheme. Model O<sub>3</sub> and NO<sub>2</sub> products from three different chemical schemes were evaluated through comparisons with retrieved columns from GOME-2A observations in the northern hemisphere (see Fig. 3.18). Three corresponding simulations show generally similar spatial variations of atmospheric composition including O<sub>3</sub> and NO<sub>2</sub> columns, but they show different value ranges. Among the three model products, the CB05-BASCOE model stratospheric products show the most similar spatial distribution and value range with satellite observed columns as shown in the Fig. 3.18. Thus, the stratospheric product simulated by C-IFS-CB05-BASCOE model was used and evaluated as stratospheric BrO correction in this study.

The horizontal resolution of the CB05-BASCOE model run is 0.75° x 0.75° with 137 vertical levels. Three-hourly CB05-BASCOE model output is interpolated in space and time to match with GOME-2 observations. Evaluations of model simulated stratospheric trace gases including O<sub>3</sub>, NO<sub>2</sub>, and BrO against observations derived from satellite retrievals were performed. Since GOME-2 retrievals are total column amounts including the tropospheric parts, they cannot be quantitatively compared with the model stratospheric output. However, evaluations of the value ranges and spatial distribution of stratospheric compositions are possible. As can be seen in Figure 3.18, the model scheme simulates well the shape of the ozone hole as well as the spatial distribution of the chemical species. However, negative model biases in stratospheric O<sub>3</sub> and positive model biases in stratospheric BrO and NO<sub>2</sub> are found. In particular, O<sub>3</sub> is underestimated in the model result by ~ 30 %, whereas NO<sub>2</sub> is slightly biased high, leading to positive biases in stratospheric halogen components. Therefore, the stratospheric correction has been performed using the bias corrected model stratospheric BrO VCD multiplied by the scale factor of 0.75 to the model stratospheric BrO output in this study.

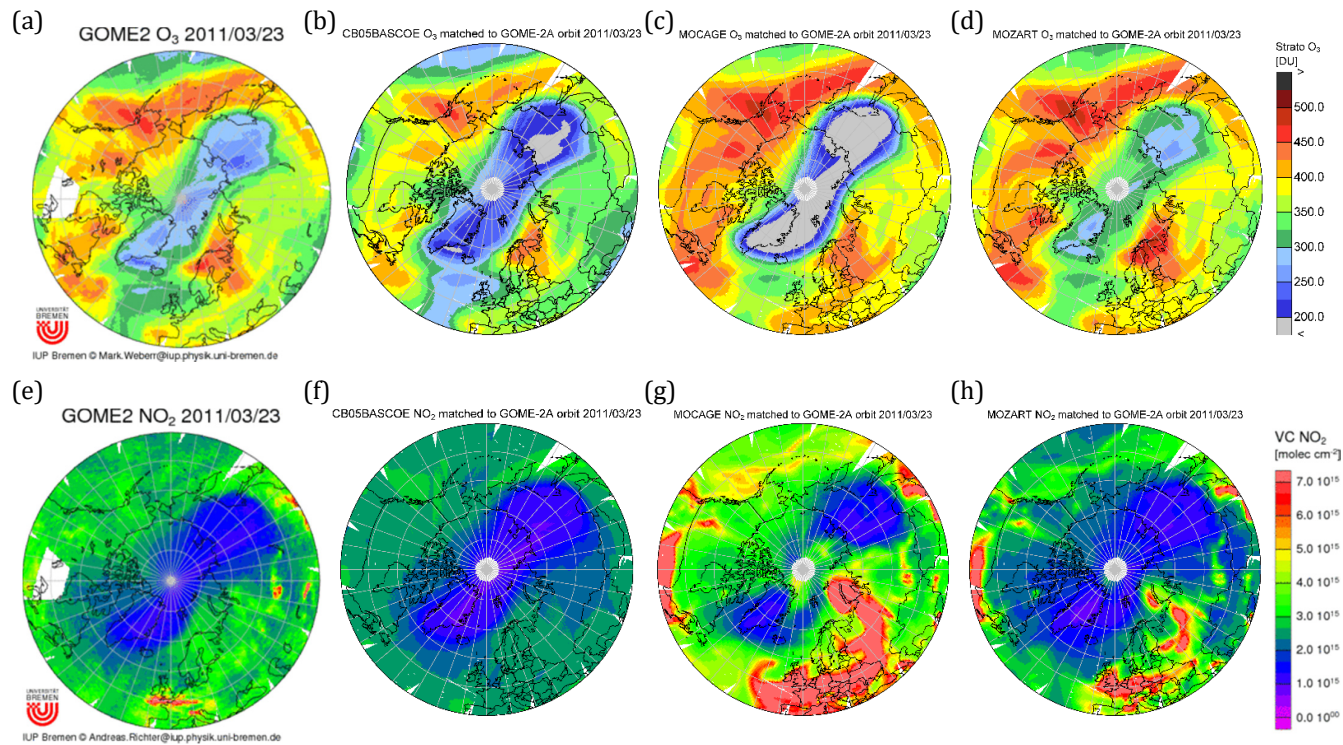


**Figure 3.18.** Maps of stratospheric O<sub>3</sub> (top) and NO<sub>2</sub> (bottom) vertical column densities from GOME-2A measurements (**a**, **e**), CB05-BASCOE (**b**, **f**), MOCAGE (**c**, **g**), and MOZART model data (**d**, **h**) for March 23, 2011 over the northern hemisphere.

### 3. Tropospheric BrO retrievals from high spatial resolution satellite data

#### 3.5.2 Climatological approach

Stratospheric BrO vertical column densities can be derived by the Theys et al. (2009) BASCOE model climatology using satellite retrievals of total O<sub>3</sub> and stratospheric NO<sub>2</sub> as input data. The stratospheric BrO climatology is based on a parameterization which reflects the main dynamical and photochemical processes controlling the distribution of BrO in the stratosphere. Basically, the stratospheric bromine monoxide profile can be written as follows:

$$\text{BrO} = \text{Br}_y \times \frac{\text{BrO}}{\text{Br}_y} \quad (\text{E 3.4})$$

The distribution of inorganic bromine (Br<sub>y</sub>) in the stratosphere results from the effects of dynamical processes, and this influence of stratospheric Br<sub>y</sub> due to short-term transport can be estimated using stratospheric ozone retrieved from the observation as a proxy for the dynamical state of the stratosphere. Also, for the partitioning factor BrO/Br<sub>y</sub> profile can be estimated based on a classification using month, latitude, stratospheric NO<sub>2</sub> column and solar zenith angle. The advantage of using this climatological approach in the stratospheric BrO correction is that, besides the reflection of both dynamical and chemical effects on the stratosphere, the intermediate input data such as total O<sub>3</sub> and stratospheric NO<sub>2</sub> column retrievals from satellite nadir measurements are easily accessible.

In this study, satellite derived total O<sub>3</sub> VCDs from Weber et al. (2013), stratospheric NO<sub>2</sub> VCDs from QA4ECV project (Boersma et al., 2017) and tropopause heights derived from NCEP reanalysis data were used as input. Since the Theys et al. (2009) BASCOE model climatology look-up-table (LUT) was calculated using three years of data from April 2003 to March 2006, the stratospheric BrO climatology should be applied with a correction factor to account for the long-term trend in Br<sub>y</sub> when the climatology is used for recent years. Hendrick et al. (2008) found a positive trend in stratospheric bromine of about +2.5 % per year for the 1995-2001 period, whereas a negative trend of about -1 % per year for the period from 2001 to 2005 was identified. Since bromine emissions into the stratosphere has decreased due to the restriction of the halogen source gases (Montzka et al., 2003), this negative trend should be considered in the estimation of stratospheric BrO vertical columns through the climatological profile. In this study, the correction factor for the long-term trend of bromine emissions in the stratosphere calculated based on ground-based zenith-sky measurements of BrO at Harestua (Hendrick et al., 2008) was applied in the

### 3. Tropospheric BrO retrievals from high spatial resolution satellite data

stratospheric correction.

#### 3.5.3 Empirical multiple linear regression model

In general, the use of 3D-atmospheric chemistry transport models requires a lot of computation time and cost. In addition, due to the high demand in cost and time, spatial and temporal resolution of the 3D-CTM model output is low in many cases. To overcome these limitations, an empirical multiple linear regression model using the viewing geometry from the satellite observation and tropopause height as predictor variables was developed for the stratospheric BrO correction. The variables used in the empirical model potentially have a physical relevance as the stratospheric BrO column. Since the radiance observed by the satellite is basically affected by the viewing geometry and pixel position, geophysical parameters are required to estimate the background BrO column. Also, as the contribution of stratospheric air increases when the tropopause is lower, the tropopause height is highly relevant for predicting the contribution of stratospheric air to the background column. Based on these scientific assumptions, the empirical multiple linear regression model composed of longitude (lon), latitude (lat), viewing geometry including the cosine of solar zenith angle (SZA) and line of sight angle (LOS), and tropopause height (tropoH) was developed as follows:

$$y = a_0 + a_{lon} \cdot lon + a_{lat} \cdot lat + a_{sza} \cdot \cos(SZA) + a_{los} \cdot \cos(LOS) + a_{tropoH} \cdot \frac{1}{tropoH} \quad (E 3.5)$$

Here, the dependent variable  $y$  indicates the estimated background BrO VCD which reflects the influence of stratospheric origins. When estimating the model coefficients ( $a_n$ ), only data points whose geometric total BrO VCDs lay within 2 sigma of a Gaussian fit to the distribution were used to avoid the influence of locally enhanced tropospheric BrO over the study area. Unlike the viewing geometry and pixel position information obtained from the satellite observation data, the tropopause height is computed from ECMWF ERA-Interim reanalysis meteorological data by applying a dynamical criterion and interpolating spatially and temporally with respect to the distance and overpassing time from the satellite pixel. Also, among the independent variables, the longitude parameter used in the model was converted to the normalized value for each satellite orbit, not using the absolute value, for consistency.

### 3. Tropospheric BrO retrievals from high spatial resolution satellite data

Background BrO slant columns with stratospheric contributions can be obtained by multiplying the estimated BrO vertical columns predicted from the empirical multiple linear regression model by stratospheric AMF. Based on the residual method, enhanced tropospheric BrO slant columns are calculated by subtracting the background BrO slant columns from the observed total BrO slant columns. According to the above listed assumptions, this BrO column represents only BrO amounts enhanced by chemical reactions in the tropospheric layer. Thus, the tropospheric BrO SCD can be finally obtained by adding an offset value of  $4.25 \times 10^{13}$  molec  $\text{cm}^{-2}$  in the Arctic region based on the 3D-CTM model as a tropospheric background correction. The empirical multiple linear regression model is able to account for the dynamical effects derived by variations of the tropopause, but it cannot reflect BrO variations due to chemical reactions occurring in the stratosphere. Nevertheless, compared with other methods, this approach is relatively simple to apply to the tropospheric BrO retrieval from satellite measurements in that no intermediate data except for the tropopause height is needed for the stratospheric correction.

#### 3.5.4 Comparison of different stratospheric correction methods

The three different methods for stratospheric correction presented in the previous sections (3.5.1 to 3.5.3) were evaluated by comparing each other. Figure 3.19 shows tropospheric BrO slant column densities calculated by applying the estimated stratospheric BrO columns from the three different methods for the GOME-2B measurements on April 30 2014. Examples presented in Fig. 3.19 show overall good agreements in spatial distributions and magnitudes of tropospheric BrO slant columns between three methods. These tropospheric BrO SCDs calculated by different stratospheric correction methods were also compared with each other using a 1 to 1 scatter plot. As shown in Fig. 3.20, generally good agreement between three methods is found with correlation coefficients (slopes) of the ranges of 0.86-0.92 (0.82-0.88). These good agreements between the three methods show that the atmospheric dynamical and chemical assumptions as well as simulations of each method are valid and applicable to the BrO study. Since exact stratospheric BrO column measurements are not available for comparison, the residual tropospheric BrO columns obtained by applying different stratospheric correction methods will be validated by comparing with ground-based tropospheric BrO observations in chapter 5.

### 3. Tropospheric BrO retrievals from high spatial resolution satellite data

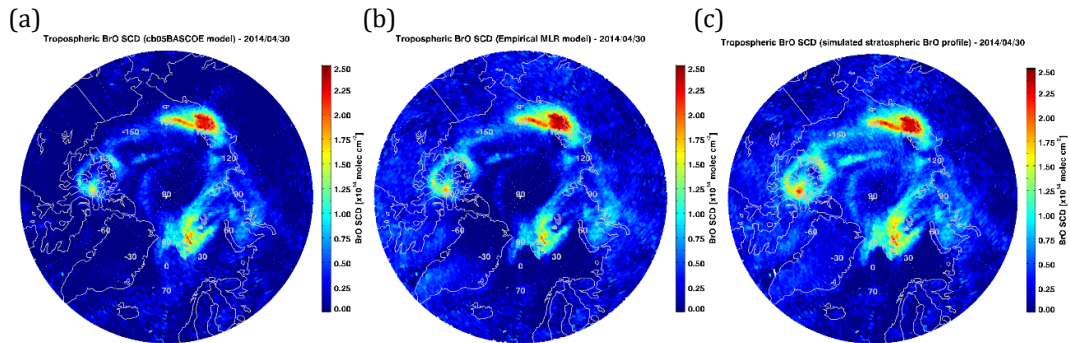


**Figure 3.19.** Tropospheric BrO slant column densities [ $10^{14}$  molec  $\text{cm}^{-2}$ ] calculated from GOME-2B measurements on April 30 2014 applying three different stratospheric correction methods: (a) cb05-BASCOE stratospheric model data, (b) empirical MLR model, and (c) BASCOE climatology stratospheric BrO profile based on Theys et al. (2009, 2011).

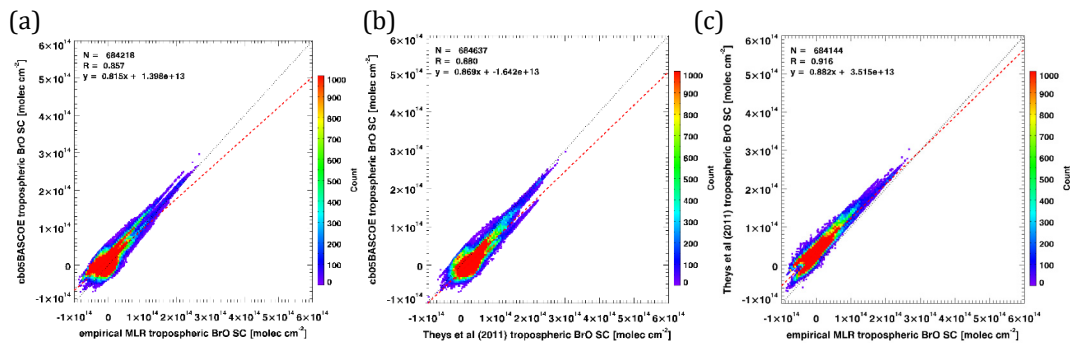


**Figure 3.20.** Comparison of tropospheric BrO SCD calculated by three different stratospheric correction methods for the data shown in Fig. 3.19. (a) x- and y-axis: tropospheric BrO SCD calculated by using the empirical MLR and cb05-BASCOE stratospheric model data, (b) x- and y-axis: tropospheric BrO SCD calculated by using the Theys et al (2009, 2011) climatological approach and cb05-BASCOE stratospheric model data, and (c) x- and y-axis: tropospheric BrO SCD calculated by using the empirical MLR and Theys et al (2009, 2011) climatological approach.

### 3. Tropospheric BrO retrievals from high spatial resolution satellite data

## 3.6 Tropospheric air mass factor calculation

The air mass factor is defined as the ratio of the slant column to the vertical column ( $AMF = SCD/VCD$ , see details in Sect. 2.3.8). To quantify the vertical dependence of the measurement sensitivity, it is useful to define a height-dependent partial AMF for specific atmospheric layers, referred as to Box-AMF (BAMF):

$$BAMF_i = \frac{\delta SCD_i}{\delta VCD_i} \quad (E 3.6)$$

With the BAMF of each layer  $i$  ( $BAMF_i$ ), the total air mass factor can be calculated as average over all altitudes, weighted by the absorber profile  $VCD_i/VCD$  as:

$$AMF = \frac{\sum_i BAMF_i \cdot VCD_i}{VCD} \quad (E 3.7)$$

The sensitivity of UV radiance measurements to the BrO layer amounts are different with the altitude. This variation depends on viewing geometry (mainly solar zenith angle, viewing zenith angle, and relative azimuth angle), surface albedo, surface elevation, cloud properties, and the vertical BrO profile.

In this study, the air mass factor look up table is calculated by the SCIATRAN ver 3.6.5 radiative transfer model (Rozanov et al., 2014) with a large range of physical parameters listed in Table 3.3 at 346 nm (mid-point of fitting window for BrO retrieval). The air mass factor for each pixel is computed by a linear interpolation of the pre-calculated LUT. The linear interpolation is performed along the cosine of solar and viewing zenith angles, relative azimuth angles, surface albedo, and surface elevation. Here, surface albedo and surface elevation information have been taken from GOME-2 surface main science channel Lambertian-equivalent reflectivity (LER) (Tilstra et al., 2017) and Global 30 Arc-Second Elevation (GTOPO30) database, respectively. In particular, surface albedo is one of the most critical variables for trace gas retrievals in polar regions, as the reflectivity varies largely depending on snow/ice conditions. This will be discussed in more detail in the subsection below. The light is reflected not only from the surface but also scattered by cloud particles and aerosols, and the photon path distribution in the troposphere is complicated. For this reason, cloud properties such as cloud fraction and height should be considered in the height-dependent AMF calculation for more accurate BrO VCD results. However, uncertainties of the cloud retrieval algorithm in sea ice regions are large as both clouds and sea ice are white and

### 3. Tropospheric BrO retrievals from high spatial resolution satellite data

bright, making it difficult to distinguish them clearly. Since cloud fraction and cloud height products from S5P/TROPOMI in the polar sea ice region are still not assured of the quality, and also the influence of multiple scattering by clouds is relatively small over sea ice compared to measurements over dark surfaces, parameters for cloud effects are not yet included in the BAMF look-up table. Finally, to calculate the effective AMF, the BAMF computation needs to be combined with an a priori BrO concentration profile because the profile shape has an impact on the AMF value. In this study, a simple box shape was used as priori BrO profile assuming a homogeneous vertical distribution of BrO within the boundary layer (0 to 200 m). It should be noted that the exact value of the BrO mixed layer height may differ in reality. However, radiative transfer simulations showed that its profile shape is not critical for this study case because the sensitivity of nadir measurements only slightly depends on altitude above surfaces with high albedo such as polar sea ice regions.

**Table 3.3.** Parameters in the pre-calculated box air mass factor look-up table.

Parameter	No. of grid points	Grid of values
Solar zenith angle*	19	0.015, 0.03, 0.05, 0.075, 0.11, 0.15, 0.2, 0.25, 0.3, 0.35, 0.4125, 0.475, 0.55, 0.625, 0.7, 0.775, 0.85, 0.925, 1.0
Viewing zenith angle**	8	0.3, 0.4, 0.5, 0.6, 0.7, 0.8, 0.9, 1.0
Relative azimuth angle (°)	7	0, 30, 60, 90, 120, 150, 180
Surface albedo	18	0.0001, 0.02, 0.04, 0.06, 0.085, 0.11, 0.14, 0.18, 0.23, 0.29, 0.36, 0.43, 0.51, 0.6, 0.7, 0.8, 0.9, 1.0
Surface elevation (km)	10	0, 0.1, 0.2, 0.3, 0.5, 1.0, 2.0, 3.0, 4.0, 5.0, 10.0
Altitude (m)	201	0-10 km (100 m interval), 10-60km (1 km interval), 60-100km (2 km interval)

\* Values are expressed in cosine of SZA

\*\* Values are expressed in cosine of VZA

### 3. Tropospheric BrO retrievals from high spatial resolution satellite data

#### **Impact of surface albedo**

The effect of surface albedo on the sensitivity of the satellite measurements to tropospheric species is significant in particular for high spatial resolution satellite observations which changes in trace gas retrievals according to the surface type and reflectivity vary largely on a small scale. In general, information on the surface property is traditionally obtained from Lambertian equivalent reflectivity (LER) climatologies. In this study, the GOME-2 LER climatology was used because of data availability. The main drawbacks of using LER climatologies for the new satellite instrument TROPOMI are: (1) climatologies are typically based on previous satellite missions with lower spatial resolution such as OMI (Kleipool et al., 2008) and GOME-2 (Pflug et al., 2008; Tilstra et al., 2017), (2) the scattering angle dependencies characterized by the bidirectional reflectance distribution function (BRDF) are not fully considered by LER climatologies, and (3) the actual surface conditions of satellite measurement may differ from climatological values especially under snow/ice situations. To overcome these problems, the retrieval of geometry-dependent effective Lambertian equivalent reflectivity (GE\_LER) and the creation of global gapless geometry-dependent LER (G3\_LER) daily data from TROPOMI measurements have been performed (Loyola et al., 2020). The daily gapless geometry-dependent LER, i.e. G3\_LER, contains normalized LER retrieved under clear-sky conditions over several days and its BRDF dependency as function of the wavelength in the fitting window, the viewing zenith angle, and the surface type.

The effects of surface albedo on tropospheric BrO retrievals were evaluated by comparing the retrieved tropospheric BrO VCDs computed using GOME-2 LER climatology and TROPOMI daily G3\_LER data for the same scene. Figure 3.21 shows maps of surface albedo, tropospheric AMF and retrieved tropospheric BrO VCD from the GOME-2 climatology LER and TROPOMI G3\_LER database, respectively. Compared to the GOME-2 LER climatology based on data collected for 7 years (2007 to 2013) with a coarse spatial resolution of  $1.0^\circ \times 1.0^\circ$ , G3\_LER is updated on a daily basis using data of only a few days from a study date with a high spatial resolution of  $0.1^\circ \times 0.1^\circ$  and reflects surface properties better. The TROPOMI G3\_LER daily maps agree well with the surface types visible in the corresponding VIIRS/SNPP images including the snow cover of the inland of Alaska as well as sea ice margins such as the coasts of Chukchi Sea and Beaufort Sea. If we compare the areas with large differences in surface albedo values between the climatology and G3\_LER data, noises and errors in the retrieved tropospheric BrO columns from the climatology LER caused by low spatial resolution and different surface conditions from the actual snow/ice conditions disappear in retrieval results using

### 3. Tropospheric BrO retrievals from high spatial resolution satellite data

the G3\_LER (see Fig. 3.22 and 23).

Due to the availability of data, only a few cases were examined here, but it was confirmed that when daily G3\_LER is used as an input for calculating AMFs, errors derived by surface albedo can be reduced when calculating TROPOMI tropospheric BrO vertical columns. In addition to BrO, according to Loyola et al. 2020, errors in the TROPOMI total ozone between -10 % and +15 % induced by snow/ice misrepresentations in the OMI\_LER climatology are removed with the GE\_LER/G3\_LER TROPOMI products. This GE\_LER/G3\_LER retrieval algorithm will be applied to the Copernicus Sentinel-5 mission that tracks along a sun-synchronous polar orbit in the near future, which will lead to improve the quality of any trace gas, cloud and aerosol product retrieved from satellite measurements.

### 3. Tropospheric BrO retrievals from high spatial resolution satellite data

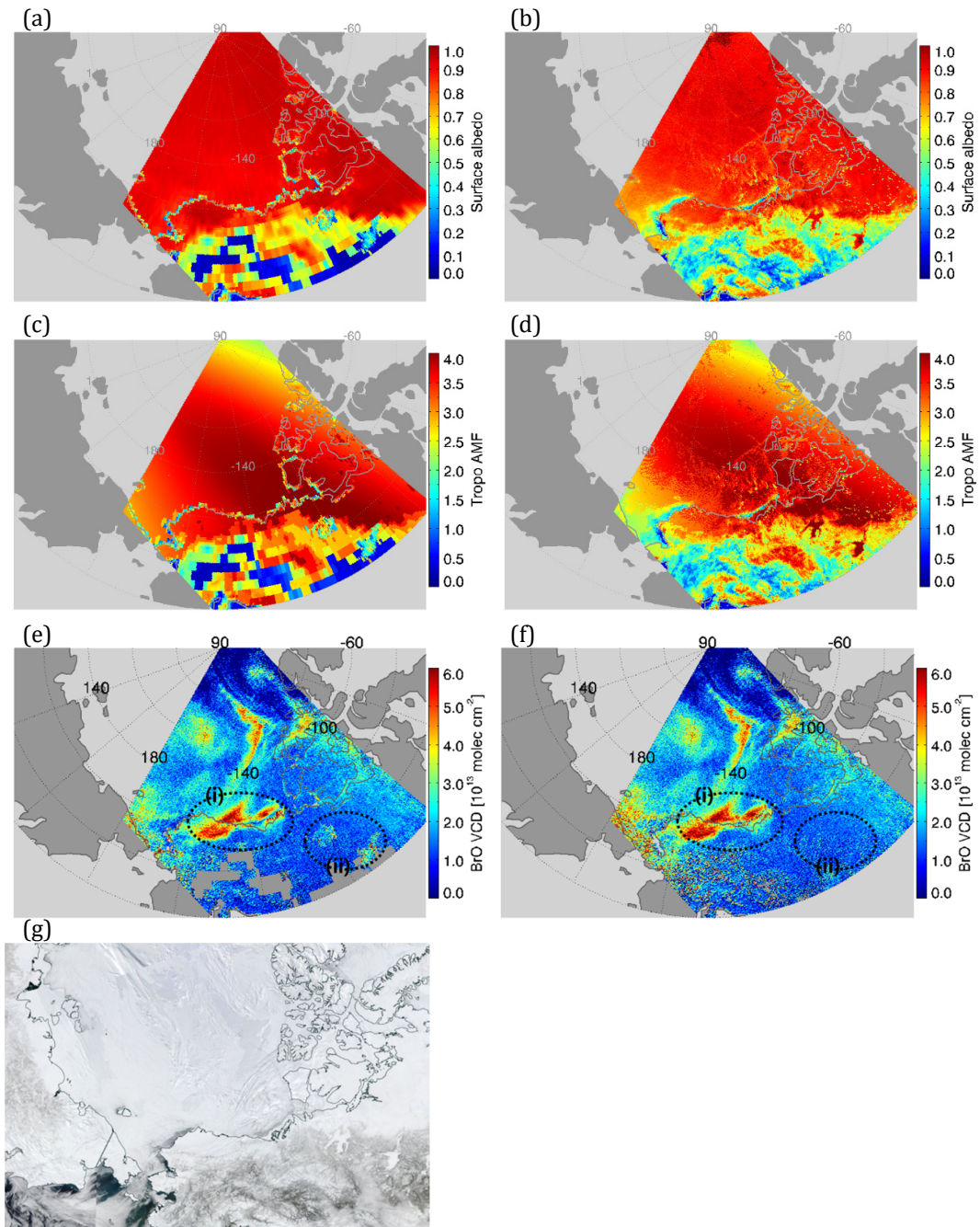


**Figure 3.21.** Maps of surface albedo, tropospheric AMF, and the retrieved tropospheric BrO VCD from TROPOMI data on 12 April 2019 (orbit no. 2574) using the GOME-2 LER climatology (**a**, **c**, **e**) and the TROPOMI G3\_LER (**b**, **d**, **f**), respectively. (**g**) The VIIRS/SNPP image for the corresponding scene.

### 3. Tropospheric BrO retrievals from high spatial resolution satellite data

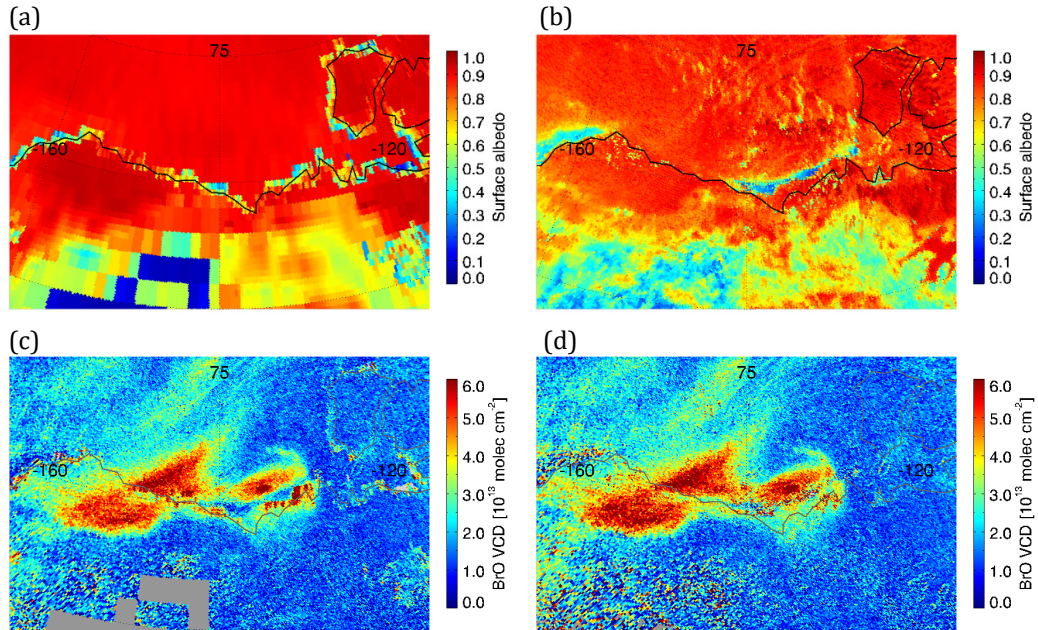


**Figure 3.22.** Maps of surface albedo and the retrieved tropospheric BrO VCD from TROPOMI data on 12 April 2019 (orbit no. 2574) using the GOME-2 LER climatology (**a, c**) and the TROPOMI G3\_LER (**b, d**) with zoomed in the study area labeled (i) in Fig. 3.21.

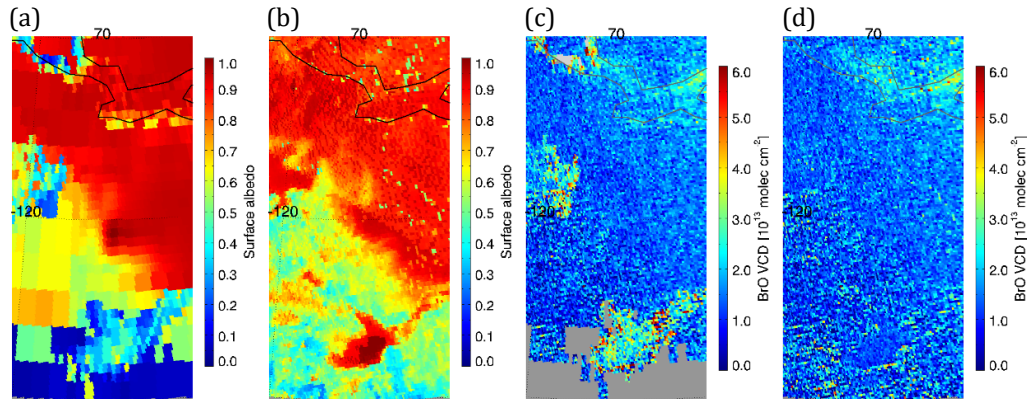


**Figure 3.23.** As Fig. 3.22, but zoomed in the study area labeled in (ii) in Fig. 3.21.

### 3. Tropospheric BrO retrievals from high spatial resolution satellite data

## 3.7 Tropospheric BrO vertical column retrievals

Events of enhancements of tropospheric BrO columns can be detected by satellite observations after adjustment for the stratospheric burden of BrO. Figure 3.24 shows the evolution of tropospheric BrO enhancement events occurring over Svalbard from 3 to 7 May 2019 observed by TROPOMI and GOME-2C. Here, the stratospheric correction was performed using the empirical multiple linear regression model. The retrieved tropospheric BrO vertical columns are only shown when the following conditions are met:  $SZA < 85^\circ$  and surface albedo  $> 0.4$ . Tropospheric sensitivity begins to be weak as SZA increases and tropospheric sensitivity almost disappears when  $SZA > 85^\circ$  even for relatively bright surfaces. Also, for a darker surface such as open water, the retrieval has lower sensitivity to BrO near the surface even when the sun is high. In this case, the retrieval of tropospheric BrO column will be very sensitive to the shape of the BrO profile in the troposphere. Thus, to provide reliable tropospheric BrO information, only the observations that meet the above criteria are presented in Fig. 3.24.

Spatial distributions and magnitudes of tropospheric BrO vertical columns retrieved from GOME-2C and TROPOMI measurements are similar. Good agreements of tropospheric BrO retrievals between TROPOMI and GOME-2C indicate that they may be useful for monitoring long-term time series and trends of tropospheric BrO. Also, these maps show that the developed tropospheric BrO retrieval algorithm can detect the variability induced by the tropospheric release of bromine from satellite measurements. In particular, shapes of the enhanced BrO plume and small-scale variations of BrO can be investigated in more detail from TROPOMI measurements due to higher spatial resolution. Tropospheric BrO explosion events will be investigated in more detail using satellite derived tropospheric BrO retrievals and various meteorological parameters in chapter 4 and 5.

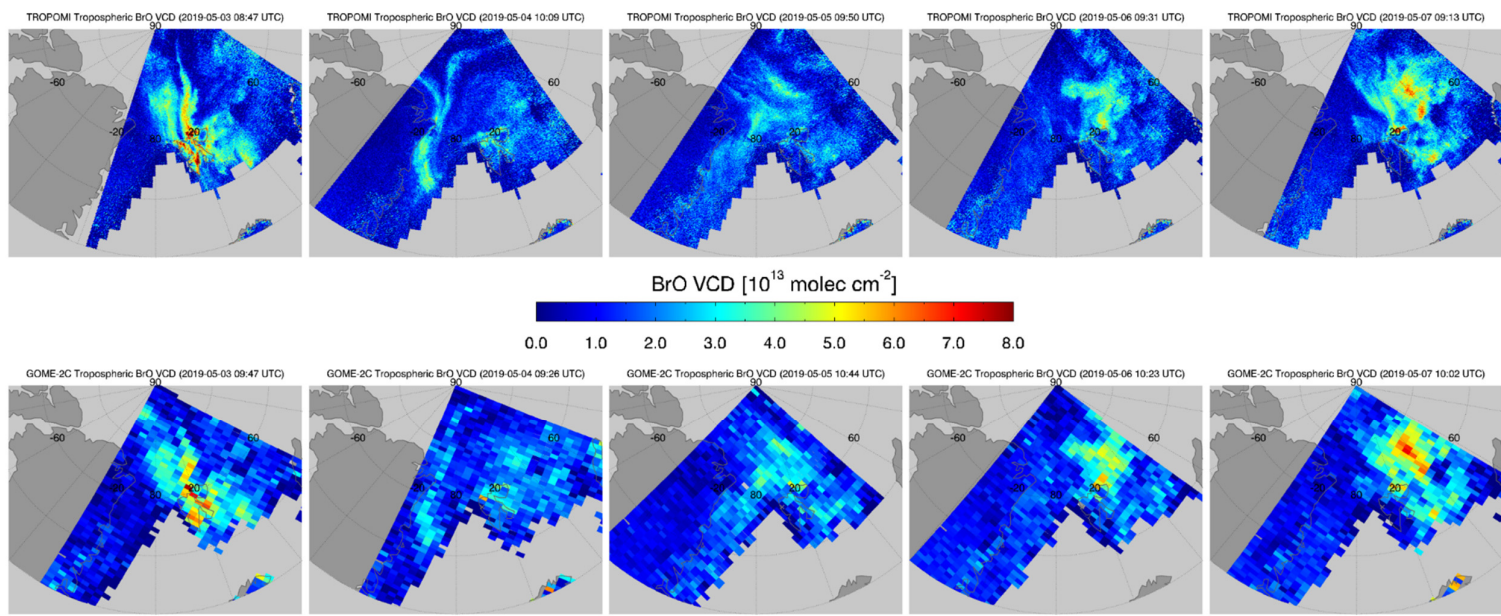


**Figure 3.24.** Maps of tropospheric BrO VCD [ $10^{13}$  molec  $\text{cm}^{-2}$ ] from TROPOMI (top) and GOME-2C (bottom) over Svalbard from 3 May to 7 May 2019.

### 3.8 Summary and conclusions

Adapting and optimizing the DOAS retrieval developed for earlier satellite missions, a first tropospheric BrO column retrieval for measurements of TROPOMI, the new space-borne instrument launched on the European Sentinel 5 Precursor satellite in October 2017, was developed. One of the most important factors in the DOAS retrieval is the wavelength interval selected as the fitting window with the objective being to maximize the differential absorption structures of the specific gas of interest and minimize the influence of other interfering signals. However, finding the optimal retrieval wavelength interval is not straightforward as instrumental factors as well as viewing conditions and study area can impact the results. Similar to the approach by Vogel et al. (2013), color-coded maps of DOAS retrieval results obtained by systematically varying the retrieval wavelength interval were created for various observation scenarios on TROPOMI data to determine the optimal retrieval wavelength interval for BrO. Negative BrO SCDs, large deviations from the expected BrO SCDs, and high fitting errors occur at shorter wavelengths when strong absorption structures of O<sub>3</sub> and SO<sub>2</sub> are included. The sensitivity of BrO retrieval to HCHO was also found by showing anti-correlation between the retrieved amounts of the two gases. At wavelengths longer than 362 nm, poorer results were found in the cloudy scene and volcanic plume measurement scenarios, presumably due to the wavelength dependency of the Ring effect and imperfect fitting of O<sub>4</sub>. Based on the information gathered from the sensitivity tests for different measurement scenarios, 334.6–358 nm was selected as the optimal wavelength range for TROPOMI BrO retrievals for most of the possible measurement situations. This fitting window yields reliable BrO retrieval results with small fitting errors, but future studies on quantitative assessments and cross correlations between BrO and all the interfering absorbers are encouraged to further improve retrieval results.

As imaging instruments such as TROPOMI often show across-track offsets in the retrieved columns, the DOAS BrO retrieval has to include a destriping method. In this study, row-specific daily averaged earthshine radiances from a Pacific background area are used as reference spectrum in the DOAS fitting procedure and a post processing offset correction is applied to convert the resulting differential slant columns to absolute slant columns. The tropospheric columns are derived based on a residual technique that combines measured DOAS total BrO columns and estimated stratospheric BrO columns. To estimate the stratospheric BrO

### 3. Tropospheric BrO retrievals from high spatial resolution satellite data

column, three different methods were tested using 3D atmospheric chemistry model products, empirical multiple linear regression models, and climatology stratospheric BrO profile based on Theys et al. (2009, 2011). These stratospheric correction methods were evaluated by comparing results applying three methods, and their results showed generally good agreements with each other in the polar region. To convert the tropospheric BrO SCDs into VCDs, tropospheric AMFs which take into account viewing geometries, surface albedo, surface altitude, and BrO profile were calculated using the pre-calculated look-up-table simulated by the atmospheric transfer model.

As a first consistency test, TROPOMI BrO columns were compared with OMI and GOME-2 data on both global and regional scales. TROPOMI BrO retrievals show good agreement with OMI and GOME-2 BrO columns with high correlation coefficients (slopes of the regression lines) of 0.84 (0.89) and 0.84 (0.72) for enhanced BrO plumes in the Arctic sea ice region. Global maps of monthly BrO columns also agree well between the three instruments. In addition to the good consistency of TROPOMI BrO retrievals with other satellite products, TROPOMI shows excellent performances with much smaller fitting rms values and lower random scatter of BrO columns than OMI and GOME-2. More small-scale hot spots can be identified in greater detail by TROPOMI with its improved signal-to-noise ratio and the excellent spatial resolution. Thus, studies on small-scale BrO events in specific source regions where comparatively lower spatial resolution satellite sensors such as GOME, SCIAMACHY, GOME-2, and OMI provide only limited information and may even fail to detect the small-scale plume will be enabled by TROPOMI data. Judging from the examples evaluated in this study, BrO columns from TROPOMI will contribute relevant high-resolution information to many future studies exploring the halogen chemistry in the atmosphere. Validation with ground-based measurements and case studies for small-scale tropospheric BrO explosion events will be carried out in chapter 5.

# 4

## BrO enhancements in polar sea ice regions

### 4.1 Introduction\*\*

Bromine has an impact on the atmospheric chemistry, as it is known to cause significant ozone destruction. Although bromine is present in the stratosphere in small quantities relative to chlorine, its high ozone depletion efficiency makes that stratospheric bromine contribute to O<sub>3</sub> loss by about 25 % in mid-latitude and up to 50 % in polar region (Brune et al., 1991). Stratospheric bromine is mostly present in its inorganic form, originating from both natural and anthropogenic organic source gases. Man-made halogenated hydrocarbons gases (halons) and methyl bromide (CH<sub>3</sub>Br) released from the ocean by natural processes are stable and long-lived, which allows them to reach the stratosphere mainly in the tropics (Harder et al., 2000; Theys et al., 2009a). In addition to the contribution of these long-lived organic source gases, short-lived biogenic bromine compounds could also affect the stratospheric bromine budget (Sinnhuber et al., 2005). In the stratosphere, transported organic bromine source gases are converted into inorganic forms of Br<sub>y</sub>, such as Br, BrO, BrONO<sub>2</sub>, HOBr, HBr, BrCl, Br<sub>2</sub>, either by direct photolysis or by reaction with OH and O (Lary, 1996; Theys et al., 2009b). Inorganic bromine is then influence various stratospheric chemical reactions.

Bromine is present in the troposphere as well as in the stratosphere. One of the major tropospheric bromine sources is the polar sea ice region. A large amount of active bromine compounds is released by a heterogeneous mechanism called “bromine explosion” and leads to substantial ozone depletion in the polar boundary layer in spring (Fan and Jacob, 1992; McConnell et al., 1992; Simpson et al., 2007). This bromine explosion reaction is an autocatalytic cycle because the Br<sub>2</sub> released is photolysed to generate Br and the chain reaction accelerates (see Fig.2.2 in section 2.2.2.2). Autocatalytic mechanism for halogen release from sea salt aerosol can start from the reaction of HOBr with Cl<sup>-</sup> in the presence of acid

---

\*\* This section was partly published in *Seo et al.* (2020).

## 4. BrO enhancements in polar sea ice regions

as described in *Cycle B II* in section 2.2.2.2 (Vogt et al., 1996; Sander et al., 2003):



Although relatively lower concentrations compared to polar regions, tropospheric bromine is also detected over salt lakes (Hebestreit et al., 1999; Hörmann et al., 2016), in volcanic plumes (Bobrowski et al., 2003; Theys et al., 2009a) and in the marine boundary layer (Sander et al., 2003; Saiz-Lopez et al., 2004).

BrO can be observed by both ground-based and satellite measurements using the differential optical absorption spectroscopy (DOAS) technique (Platt and Stutz, 2008). Ground-based measurements such as long-path DOAS (Hönninger et al., 2004; Stutz et al., 2011), multi-axis DOAS (Hönninger et al., 2004; Frieß et al., 2011), and chemical ionization mass spectrometry (Liao et al., 2011; Choi et al., 2012) provide good temporal coverage and in some cases the vertical profile of BrO, while UV-visible nadir satellite measurements allow us to study the global distribution of BrO columns with good spatial coverage. In particular, since BrO observation through satellites became possible, studies on the mechanism for large scale release of bromine over both polar sea ice regions, where a management of ground-based instruments is difficult have been carried out. Satellite BrO observations have shown large areas of elevated BrO covering several thousand km<sup>2</sup> over the Arctic and Antarctic sea ice region in polar spring. Therefore, many studies have been performed to identify factors, especially meteorological conditions, affecting the occurrence of bromine explosion events.

Jones et al. (2006) and Jacobi et al. (2006) found that ozone depletion events and elevated BrO concentrations are related to a stable and shallow boundary layer occurring under temperature inversions and low wind speeds. Such conditions allow chemical reactions to proceed efficiently, the boundary layer acting as a closed reaction chamber. However, enhanced BrO events were also detected during episodes of high wind speed. Jones et al. (2010) found that BrO explosion events can occur under environmental conditions consisting of high

#### 4. BrO enhancements in polar sea ice regions

wind speeds and the presence of blowing snow. Choi et al. (2018) also showed a significant association between the temporal and spatial extent of tropospheric BrO explosions observed from OMI and GEOS-5 simulated sea salt aerosol emissions generated by blowing snow. They demonstrated that saline aerosol particles generated during blowing snow events serve as a source of reactive bromine in the bromine explosion mechanism. The role of wind speed and atmospheric stability in determining the lower tropospheric BrO vertical distribution was reported by Peterson et al. (2015) using MAX-DOAS observations. In that study, high wind speeds were linked to some of the high columns of BrO, but based on the low frequency of these cases, they argued that high wind speeds and blowing snow are not the sole driver of halogen activation. Sihler (2012) investigated the relationship between tropospheric BrO vertical columns retrieved from GOME-2 measurements and environmental parameters including meteorological parameters from the ECMWF weather model and cloud properties measured by CALIPSO for selected cases. It was found that the occurrence of enhanced tropospheric BrO vertical columns are related to boundary layer meteorology although the causality is not always clear. A Bromine explosion event linked to cyclone development in the Arctic was investigated by Blechshmidt et al. (2016). The vertical lifting and high wind speeds driven by the front of the polar cyclone can transport cold brine coated snow and salt aerosols into the free troposphere, resulting in bromine explosion events and extending BrO plume lifetime through continuous supply of reactive bromine.

As mentioned above, many studies on the possible sources of BrO enhancements and the driving meteorological conditions in polar regions have been conducted using ground-based and satellite measurements. Study results clearly indicate that meteorological conditions affect the processes of BrO enhancements in several ways. However, these previous studies focus on specific case-studies or relatively short-term data sets, which limits the investigation of favourable meteorological conditions associated with the occurrence of enhanced BrO columns in the polar regions. In this study, to overcome this snapshot treatment of elevated BrO events during polar spring, and to obtain a more general understanding of the enhancements of total BrO columns, the spatial distribution of occurrence frequency of enhanced total BrO column and its relationship to various meteorological parameters in the Arctic and Antarctic sea ice regions is statistically analyzed by using a 10 year long-term dataset. In particular, the relationship between total BrO vertical columns retrieved from GOME-2A/2B and

## 4. BrO enhancements in polar sea ice regions

meteorological fields including sea level pressure, surface level wind speed and direction, surface air temperature, and tropopause height were investigated. The reason for using total BrO columns instead of tropospheric and stratospheric columns separately to examine the relationship with the meteorological fields is that existing separation methods for satellite BrO data are difficult to apply to a long-term data set in both hemispheres. They also have large uncertainties in connection with low pressure systems and large tropopause height changes which affect both stratospheric and tropospheric columns. This study aims to investigate how the meteorological system generally affects the total BrO column, rather than separate the effects on the enhancement of BrO in each atmospheric layer. Differences in meteorological conditions and their regional characteristics between high BrO situations and the mean field were investigated in order to better understand meteorological effects on processes involved in BrO enhancements. Finally, based on Spearman rank correlation analysis, the degree of influence of different meteorological parameters on total BrO columns was evaluated and the most important meteorological parameters, influencing BrO, and their regional patterns were identified.

## 4.2 Dataset and method<sup>††</sup>

### 4.2.1 Dataset

#### 4.2.1.1 GOME-2 total BrO column

The GOME-2 is a series of three identical instruments operating on board the Metop satellites. They were launched sequentially to enable continuous long-term monitoring of atmospheric composition with the same instrument specification (Callies et al., 2000; Munro et al., 2016). The first GOME-2 aboard Metop-A was launched in October 2006, and the second and third onboard Metop-B and Metop-C were launched in September 2012 and November 2018, respectively (hereafter referenced as GOME-2A, GOME-2B and GOME-2C, respectively). GOME-2 is a nadir-viewing scanning UV-vis spectrometer with four channels covering the spectral range between 240 and 790 nm at a spectral resolution of 0.26-0.51 nm (Munro et al., 2016). The spatial resolution of GOME-2 data is typically 80x40 km<sup>2</sup> and the

---

<sup>††</sup> Parts of this section were similarly published in *Seo et al. (2020)*.

## 4. BrO enhancements in polar sea ice regions

Metop platforms all have an equator crossing time of 09:30 local time in the descending node (Munro et al., 2016). More details are described in Sect. 2.4.

In this study, GOME-2A data from 2008 to 2011 and GOME-2B data from 2013 to 2018 are used. The first year of data after the launch of GOME-2A and GOME-2B is not used to avoid sampling bias from incomplete coverage during this time period. Also, as the swath width of GOME-2A was reduced from 1920 km to 960 km in July 2013 resulting in a change in ground pixel size to 40x40 km<sup>2</sup>, the GOME-2B data since 2013 are used. BrO slant column densities (SCDs) were retrieved by applying the DOAS technique to the GOME-2 Level 1 spectra using the settings summarised in Table 4.1. These settings have been selected based on the results from an earlier study on BrO retrievals using data from different satellite instruments (Seo et al., 2019). The absorption cross sections used are BrO (Wilmouth et al., 1999), O<sub>3</sub> at 223 K and 243 K (Serdyuchenko et al., 2014), NO<sub>2</sub> (Vandaele et al., 1998), OCIO (Kromminga et al., 2003), HCHO (Meller and Moortgat, 2000), and O<sub>4</sub> (Thalman and Volkamer, 2013). A Ring spectrum to account for rotational Raman scattering was calculated by the SCIATRAN model (Vountas et al., 1998) and a fourth-order polynomial was included in the BrO retrieval. As background spectrum, daily averaged earthshine spectra from the equatorial Pacific were used ( $\pm 30^\circ\text{N}$ , 150-240°E) and a post-processing of the BrO slant columns was performed to minimize the impact of instrumental degradation and differences between the two instruments.

When using a Pacific background spectrum, the retrieved differential slant columns (DSCD) need to be corrected by adding the BrO slant column over that region. Here, earlier studies (Richter et al., 2002; Sihler et al., 2012; Seo et al., 2019) are followed and a BrO vertical column of  $V_{\text{norm, ref}} = 3.5 \times 10^{13}$  molec cm<sup>-2</sup> over the Pacific is assumed. The corresponding BrO SCD is computed by multiplying the  $V_{\text{norm, ref}}$  with the geometric air mass factor  $A_{\text{geo}}$ .  $A_{\text{geo}}$  is defined as:

$$A_{\text{geo}} = \frac{1}{\cos(\text{SZA})} + \frac{1}{\cos(\text{VZA})} \quad (\text{SZA: solar zenith angle, VZA: viewing zenith angle})$$

As the differential BrO slant columns (DSCD) over the Pacific are not exactly 0, the mode  $\mu$  of a Gaussian fitted to their distribution is taken into account for the normalization correction:

$$\text{SCD} = \text{DSCD} + A_{\text{geo}} \cdot V_{\text{norm, ref}} - \mu$$

To account for differences in the light path through the atmosphere, total

## 4. BrO enhancements in polar sea ice regions

geometric vertical columns were derived from retrieved BrO SCDs by application of a stratospheric air mass factor (AMF), which considers only viewing geometry and wavelength. Only total BrO VCDs having solar zenith angles smaller than 85° were used in this study.

**Table 4.1** Summary of DOAS settings used for the GOME-2 BrO slant column retrievals.

Parameter	Description
Fitting window	334.6-358 nm
Absorption cross-sections	BrO (Wilmouth et al., 1999), 228 K O <sub>3</sub> (Serdyuchenko et al., 2014), 223 and 243K NO <sub>2</sub> (Vandaele et al., 1998), 220 K OCIO (Kromminga et al., 2003), 213 K HCHO (Meller and Moortgat, 2000), 298 K O <sub>4</sub> (Thalman and Volkamer, 2013), 293 K
Ring effect	Ring cross section calculated by SCIATRAN model
Polynomial	5 coeff
Solar reference spectrum	Kurucz solar spectrum (Chance and Kurucz, 2010)
Background spectrum	Daily averaged earthshine spectrum in equatorial Pacific region
Intensity offset correction	Linear offset

### 4.2.1.2 Sea ice data

Sea ice concentrations (Spreen et al., 2008), i.e., the percentage of a given area covered with sea ice relative to the total, retrieved from AMSR-E (Advanced Microwave Scanning Radiometer-EOS) and AMSR2 (Advanced Microwave Scanning Radiometer 2) satellite measurements were used to identify the sea ice domain for the 2008-2011 and 2013-2018 periods, respectively. The reason for the missing of data for 2012 in this study is that there was a gap between AMSR-E and AMSR2. AMSR-E stopped producing data in October 2011 and calibrated brightness temperature data from the AMSR2, the successor of AMSR-E, have been released in January 2013. Sea ice concentrations are retrieved by the ARTIST Sea Ice (ASI) algorithm based on the polarization difference of brightness temperature

## 4. BrO enhancements in polar sea ice regions

at the 89 GHz channel and weather filtering using other channels (Spreen et al., 2008). Sea ice concentration data are provided on a daily basis with high spatial resolution of  $6.25 \times 6.25 \text{ km}^2$  by the Institute of Environmental Physics, University of Bremen (<https://seaice.uni-bremen.de/sea-ice-concentration/>) and these data products were used in this study.

### 4.2.1.3 Meteorological data

To explore meteorological conditions in polar regions, European Centre for Medium-Range Forecasts (ECMWF) ERA Interim reanalysis data (Dee et al., 2011) (<https://apps.ecmwf.int/datasets/data/interim-full-daily/>) were used. More specifically, sea level pressure, air temperature at 2 m, and surface winds at 10 m at a spatial resolution of  $0.75 \times 0.75$  degree and a 6 hour time resolution were extracted from the data. The tropopause height was computed from ECMWF ERA-Interim reanalysis data with 91 levels by applying the dynamical (potential vorticity) criterion of 3 PVU ( $1 \text{ PVU} = 10^{-6} \text{ m}^2 \text{ s}^{-1} \text{ K kg}^{-1}$ ) or higher to define stratospheric air (Ebojie et al., 2014).

## 4. BrO enhancements in polar sea ice regions

### 4.2.2 Method

#### 4.2.2.1 Data matching

To investigate the relationship between BrO and various meteorological factors over the polar sea ice regions, a spatio-temporal matching of the different datasets is required. According to previous studies, enhanced BrO columns are observed over the continent near the coast in the presence of blowing snow, and even over the interior of the continent by long-range transport of air masses from the sea ice regions (Choi et al., 2018). However, development and maintenance of large-scale enhanced BrO plumes requires a continuous supply of reactive bromine over a large area, and the origins of these sources are typically, located on the polar sea ice. Thus, the study domain for long-term analysis to the region is limited where the sea ice remains. Since the spatial resolution of daily sea ice concentration data from AMSR-E and AMSR2 is higher than that of GOME-2 BrO columns, GOME-2 BrO data were selected if an average of sea ice concentration located within the GOME-2 satellite pixel is higher than 5 %. The selected GOME-2 BrO data over the sea ice region are also matched with ECMWF meteorological datasets in both time and space. First, the meteorological datasets were linearly interpolated with respect to the observation time of GOME-2 BrO, and then spatially matched by interpolation with an inverse weighting proportional to the distance of the nearest four pixels from the GOME-2 BrO pixel. The temporally and spatially matched datasets were used to explore the spatial behavior of the relationship between BrO columns and meteorological parameters in the next sections.

#### 4.2.2.2 Detection of enhanced total geometric BrO columns over sea ice regions

To investigate the characteristics of occurrences of enhanced BrO, we first need to establish a reasonable detection criterion for BrO enhancements. In previous studies, satellite observations of enhanced BrO columns during spring, termed as “BrO hotspots”, were defined as the region where the total column BrO is elevated by at least  $2 \times 10^{13}$  molec  $\text{cm}^{-2}$  relative to the zonal mean (Salawith et al., 2010; Theys et al., 2011). Hollwedel et al. (2004) defined the high BrO events as tropospheric BrO columns above the  $5.5 \times 10^{13}$  molec  $\text{cm}^{-2}$ . In addition to these definitions, Theys et al. (2011) analysed the events of possible stratospheric origin

## 4. BrO enhancements in polar sea ice regions

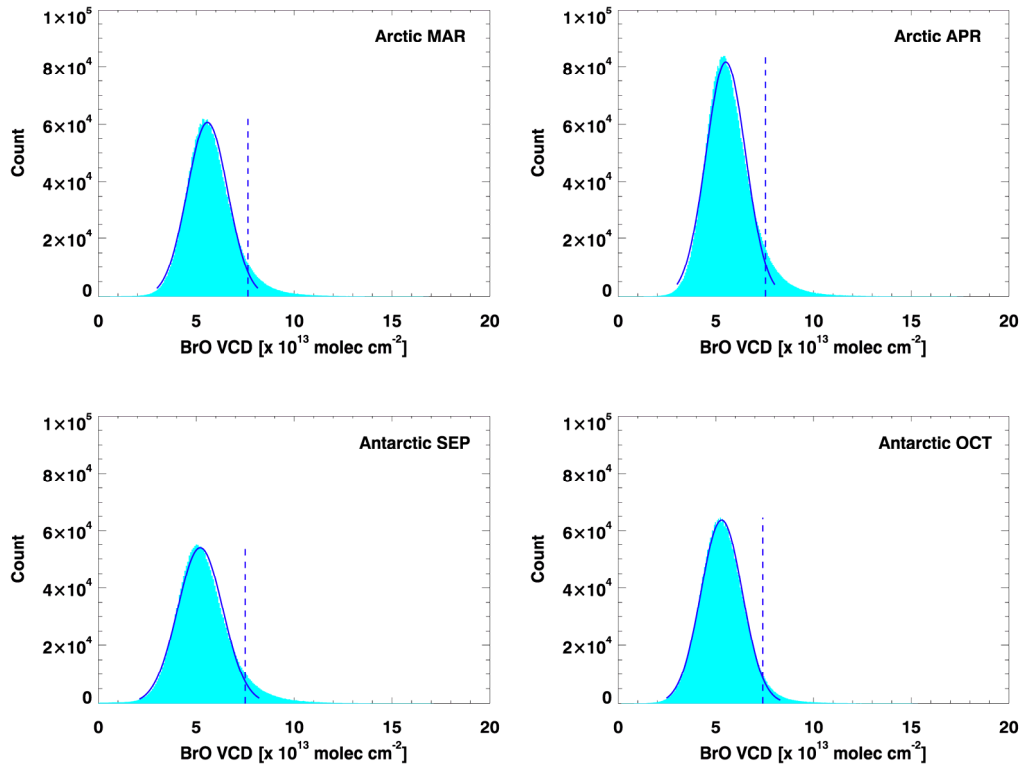
as the case when the retrieved tropospheric BrO column is lower than  $3.5 \times 10^{13}$  molec  $\text{cm}^{-2}$ . Enhanced BrO columns could be detected by applying the same threshold value and method used in previous studies. However, this study is based on 10 years of data in both hemispheres, and not on case studies or analysis of short-term data covering less than 2 years as in previous studies, and therefore a new detection criterion of enhanced BrO valid for long-term data is required.

Figure 4.1 shows the monthly histogram of GOME-2 total BrO VCDs over the Arctic (March and April) and Antarctic sea ice regions (September and October) for the study period from 2008 to 2018. Average total BrO VCDs are in general normally distributed representing the mean background BrO. However, the right side of the BrO column distribution has higher frequencies of occurrence compared to the left side and is long-tailed due to BrO enhancements during polar springtime. A threshold for BrO hotspot detection is defined as the mode of the BrO column distribution  $+2\sigma$  (standard deviation of the distribution) based on the monthly fitted Gaussian distribution using 10 years of GOME-2 data to have a consistent approach for the analysis of the long-term dataset. If a total BrO column is larger than the threshold, it is identified as an occurrence of enhanced BrO. The thresholds for BrO hotspot detection are  $7.64 \times 10^{13}$  and  $7.54 \times 10^{13}$  molec  $\text{cm}^{-2}$  for March and April, respectively, over the Arctic sea ice, and  $7.50 \times 10^{13}$  and  $7.40 \times 10^{13}$  molec  $\text{cm}^{-2}$  for September and October, respectively, over the Antarctic sea ice (see blue dashed lines in Fig. 4.1). Although the thresholds are in a similar range, the limits for the Arctic are slightly higher than those of the Antarctic, and the limits for the early spring of March and September are slightly higher than those for April and October. Our statistical results are consistent with the results of Hollwedel et al. (2004), who also found that high BrO events and areas covered by BrO clouds are usually larger in the Arctic than in the Antarctic from 6 years GOME measurements.

One issue to note is that monthly thresholds for identification of BrO hotspots in each hemisphere determined by this statistical method have a limitation in discerning a clear source of enhanced total BrO column. In principle, there are three conceivable explanations for enhanced total BrO columns observed by satellite: (1) the enhancement results from descending BrO enriched stratospheric air when the tropopause is low, (2) the increased results from bromine explosion events occurring in the troposphere, (3) the enhancements are due to a combination of both stratospheric and tropospheric contributions. Therefore, to assess whether total column BrO enhancements, detected by using the BrO VCD

## 4. BrO enhancements in polar sea ice regions

threshold criteria defined above, is of stratospheric or tropospheric origin, related meteorological factors will be investigated in the next sections.



**Figure 4.1.** Monthly histograms of the total BrO VCD from GOME-2 measurements during the study period of 2008-2018 (March and April for the Arctic, September and October for the Antarctic). The blue solid line is a fitted Gaussian distribution and the blue dashed line indicates a range of mode+2σ (used as the monthly threshold for classifying cases of enhanced BrO columns) for the Gaussian distribution.

## 4. BrO enhancements in polar sea ice regions

### 4.3 Result<sup>\*\*\*</sup>

#### 4.3.1 Frequencies of enhanced BrO columns and spatial distributions

To identify areas where BrO hotspots occur frequently, the spatial distribution of the frequency of enhanced BrO occurrences was investigated over a long time period. To map the spatial distribution of frequency, a reference grid is required because the positions of the satellite pixels are not constant. In this study, a reference grid with 200x200 km resolution was used. The enhanced BrO occurrence frequency  $f_{\text{EBrO}}$  was calculated by dividing the number of pixels classified as enhanced BrO column in a given reference grid cell by the total number of satellite pixels within the reference grid cell. One thing to note is that cloud filtering was not applied in this study. Clouds can affect the BrO column retrieval generally in three ways: (1) the albedo effect related to the increase of the reflectivity and sensitivity for cloudy scenes, (2) the enhancement of optical light path due to multiple scattering inside clouds, and (3) the shielding effect that hides trace gases below clouds. The first two effects could increase the absorption of trace gases and lead to values greater than the actual total BrO column, while the third effect leads to an underestimation of the total BrO column (Antón and Loyola, 2011). Therefore, as clouds affect the BrO retrieval, it is necessary to consider the presence and characteristics of clouds for accurate BrO analysis. However, obtaining long-term reliable cloud products such as cloud fraction and cloud top height over the polar sea ice regions is difficult because detecting clouds and retrieving their properties over a bright snow/sea ice surface from satellite measurements are difficult (Heidinger and Stephens, 2000). Inaccurate cloud data may cause errors in statistical analysis using long-term data. Also, the difference between cloud free and cloudy conditions in polar sea ice regions is relatively small due to the bright surface (Figure 1 in Blechschmidt et al., 2016). Based on these considerations, this study did not attempt to correct the effects of clouds on the enhancement of BrO columns.

Figure 4.2 shows how frequently enhanced total BrO columns were observed over the Arctic and Antarctic sea ice regions in spring. As can be seen in Fig. 4.2, patterns and magnitudes of  $f_{\text{EBrO}}$  are different between the Arctic and Antarctic,

---

<sup>\*\*\*</sup> Parts of this section were published in *Seo et al. (2020)*.

#### 4. BrO enhancements in polar sea ice regions

and also vary between polar spring months. In the Arctic, enhanced total BrO columns are frequently observed over the north of the Canadian coast with a frequency of  $\sim 0.25$  (25 %). Also, over the Hudson Bay,  $f_{\text{EBrO}}$  is higher than  $\sim 0.18$  in both March and April. Due to the large land-sea ratio in the Canadian archipelago, the number of data collected for the analysis is low compared to other regions. However, since enhanced BrO cases are observed more frequently than in other regions, the relative occurrence frequency of enhanced total BrO column is high in this region. The spatial distribution patterns of  $f_{\text{EBrO}}$  are mostly similar in March and April, but relatively high values of  $\sim 0.15$  are observed over the Chukchi Sea and the East Siberian Sea in April. In contrast to the Arctic, where stronger regional enhancements in BrO occurrence are evident,  $f_{\text{EBrO}}$  is distributed relatively uniformly around the Antarctic continent with a comparatively low number of local enhancements over the Weddell and Ross Sea. In addition, unlike in the Arctic, where the values of  $f_{\text{EBrO}}$  are similar in March and April, the range of frequency values in Antarctica is smaller in October than in September, in particular, around the Weddell and Ross Sea. Statistical analysis using decadal GOME-2 observations showed spatial and temporal behaviours of total BrO column enhancements in the Arctic and Antarctic region. Spatial variations in the occurrence frequency of enhanced total BrO columns may be linked to the influence of various meteorological parameters, and this will be discussed in detail in Section 4.3.2.

#### 4. BrO enhancements in polar sea ice regions

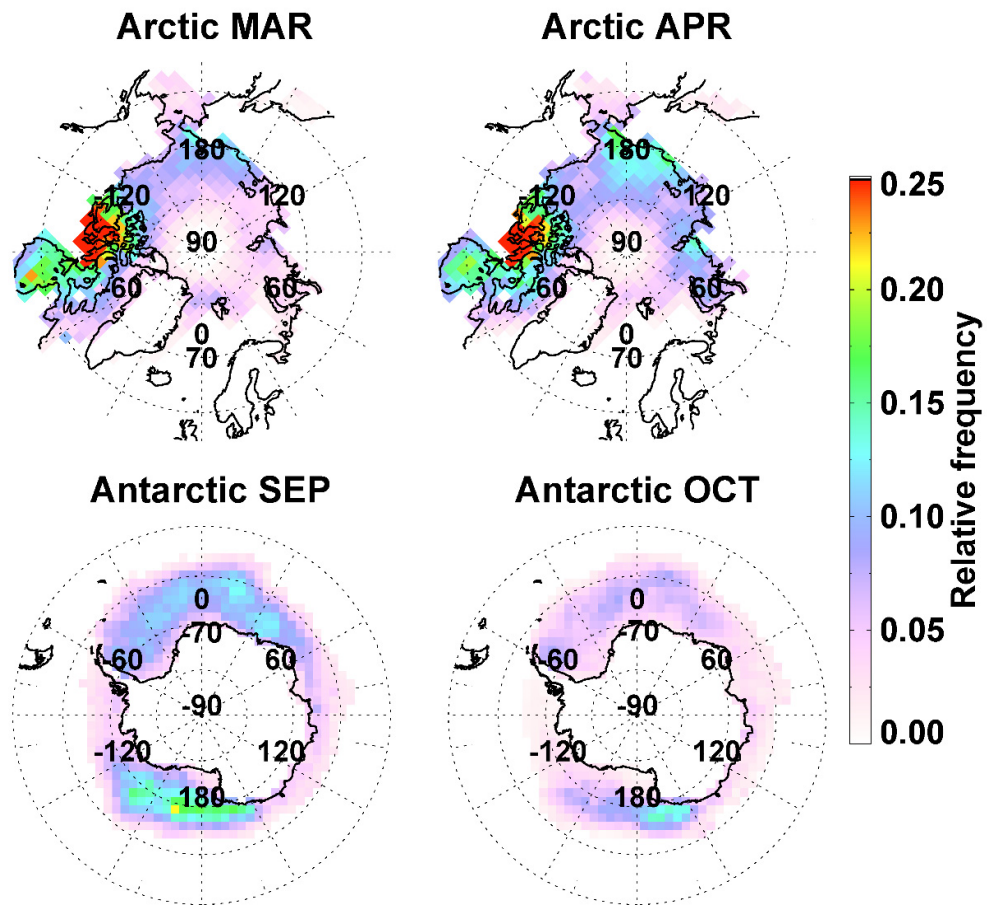


**Figure 4.2.** Monthly spatial distribution of the occurrence frequency of enhanced total BrO columns over the Arctic (top left: March, top right: April) and Antarctic sea ice region (bottom left: September, bottom right: October) during the study period of 2008-2018.

## 4. BrO enhancements in polar sea ice regions

### 4.3.2 Relationship between enhanced BrO columns and meteorological parameters

In this section, the relationship between the occurrence of enhanced total BrO columns and various meteorological conditions is examined, focusing on the magnitude and spatial distribution of changes in meteorological conditions when comparing situations with BrO enhancements to the mean.

#### 4.3.2.1 Sea level pressure

The first parameter investigated is sea level pressure. Figure 4.3 shows histograms of ERA-interim sea level pressure data from 2008 to 2018 for the Arctic and Antarctic sea ice region during spring (March and April for the Arctic, September and October for the Antarctic). The red line shows the frequency distribution of sea level pressure for cases with enhanced total BrO, whereas the black line represents the frequency distribution of the mean field using all sea level pressure data for the study period. As can be seen in Fig. 4.3, the frequency distribution of sea level pressure is shifted towards lower sea level pressure during BrO enhancements in both polar regions, indicating that enhancement in total BrO vertical column is related to lower sea level pressure. This decrease of sea level pressure can also be clearly seen from a comparison of the mean sea level pressure map for all measurements with the mean sea level pressure map for the enhanced BrO cases (see Fig. 4.4). When total BrO columns are enhanced, sea level pressure is generally decreased by up to  $\sim 25$  hPa in most areas of the Arctic when compared to the average sea level pressure. Significant decreases in sea level pressure are in particular found in the central Arctic and the Bering Strait. Sea level pressure tends to increase slightly only over the Kara Sea in March. Similar to the results in the Arctic, lower sea level pressure is associated with enhanced BrO columns in Antarctica (see Fig. 4.5). Negative sea level pressure anomalies are found in most areas, and a particularly pronounced negative anomaly in sea level pressure ( $\sim 20$  hPa) is observed over the east side of the Antarctic Peninsula in September. Also, from Fig. 4.5, it is clear that the decrease of Antarctic sea level pressure for the enhanced BrO cases in October is not as large as in September.

## 4. BrO enhancements in polar sea ice regions

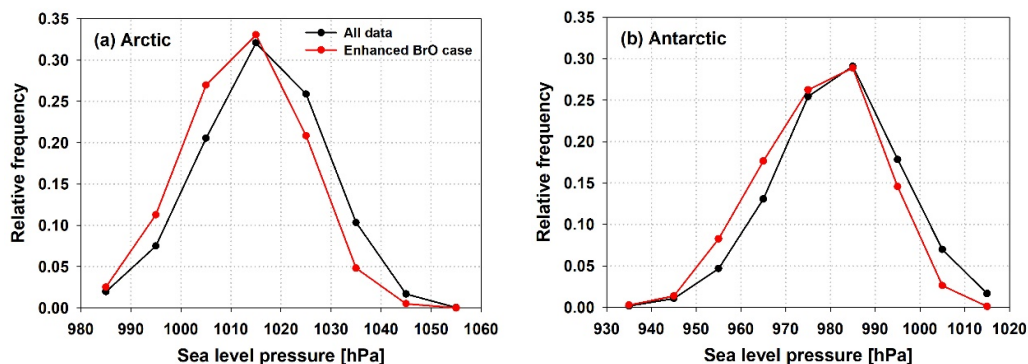


**Figure 4.3.** Frequency distribution of sea level pressure for all data (black line) and situations with enhanced BrO columns (red line) in (a) the Arctic and (b) Antarctic sea ice region in spring (Arctic: March to April, Antarctic: September and October).

Our analysis using long-term datasets demonstrates that enhancements in total BrO columns are associated with negative sea level pressure anomalies in both the Arctic and Antarctic sea ice region. The Arctic and Antarctic have fundamentally different geographical features. The Arctic is a frozen ocean surrounded by land whereas Antarctica is a frozen continent surrounded by ocean, which leads to differences in the major synoptic pressure systems. The lower tropospheric circulation over the frozen Arctic ocean is dominated by high pressure systems over the continents, while that of the sea ice zone around Antarctica is driven by a strong low pressure belt (Jones et al., 2010; Screen et al., 2018). Although the atmospheric dynamic systems are different between the Arctic and Antarctic sea ice regions, sea level pressure is generally lower during the enhancement of BrO columns in both polar regions, which indicates that atmospheric depressions have an influence on generating enhanced total BrO.

Previous studies support the association between atmospheric low pressure systems and enhanced BrO columns. Jones et al. (2010) found that large scale tropospheric ozone depletion events and enhanced BrO columns appear around large low pressure systems in the Antarctic region using data from tethersondes, free-flying ozonesondes, and satellites. Blechschmidt et al. (2016) revealed a link between polar cyclones and bromine explosion events development for a case over the Arctic. These studies argue that vertical lifting and high wind speeds in synoptic scale atmospheric low pressure systems result in development of blowing snow, so that the BrO explosion reaction cycle occurs around the wind-blown

#### 4. BrO enhancements in polar sea ice regions

brine coated snow particles in tropospheric air. Convergence and ascent of air occur along fronts within low pressure systems. This convective process facilitates air masses potentially having reactive bromine source conditions at the ground to be transported to higher altitudes and cooled. They et al. (2009b) and Salawitch et al. (2010) showed that some of the enhancement in total BrO columns are associated with increases in stratospheric BrO due to a decrease of the tropopause height, coincident with low pressure systems. The details of how surface level wind and tropopause height, which can be affected by changes in atmospheric pressure, are associated with the enhancement of the total BrO column will be discussed in later sections.

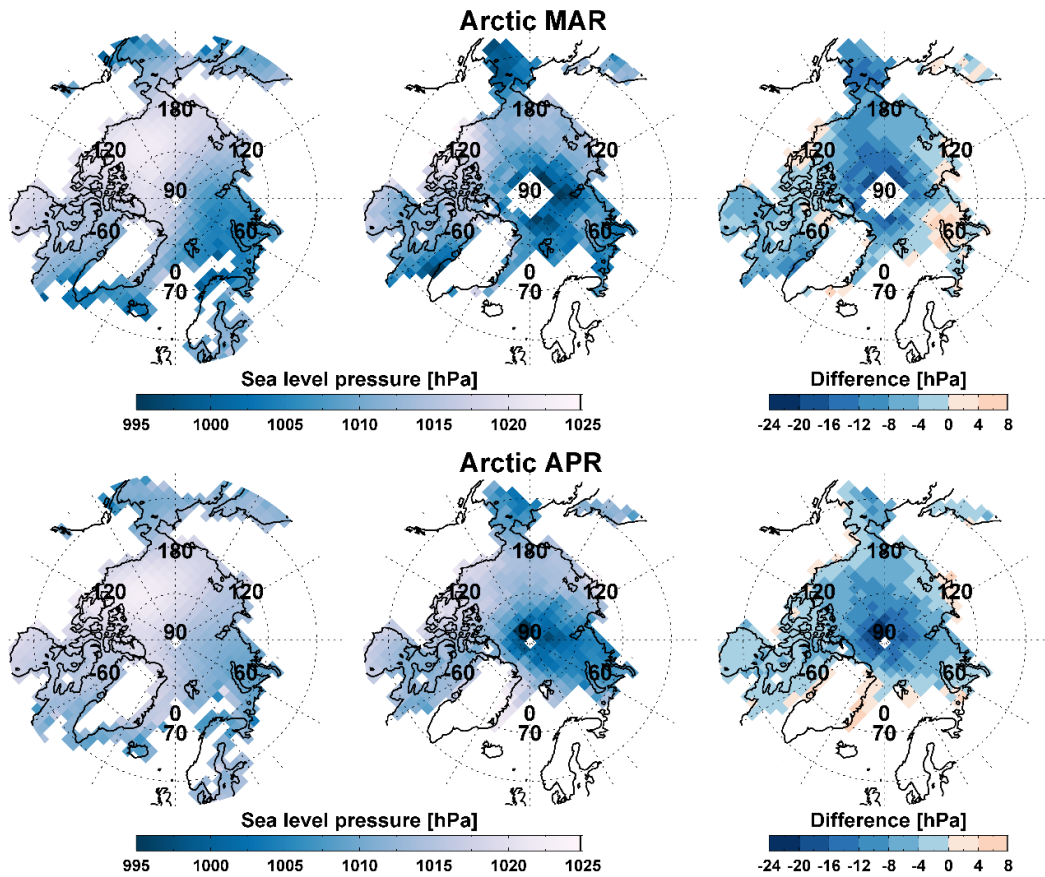


**Figure 4.4.** Monthly sea level pressure for the mean field (left), the enhanced BrO case (middle), and sea level pressure anomalies (difference of sea level pressure between the enhanced BrO case and the mean field) (right) over the Arctic in March (upper panel) and April (lower panel).

## 4. BrO enhancements in polar sea ice regions

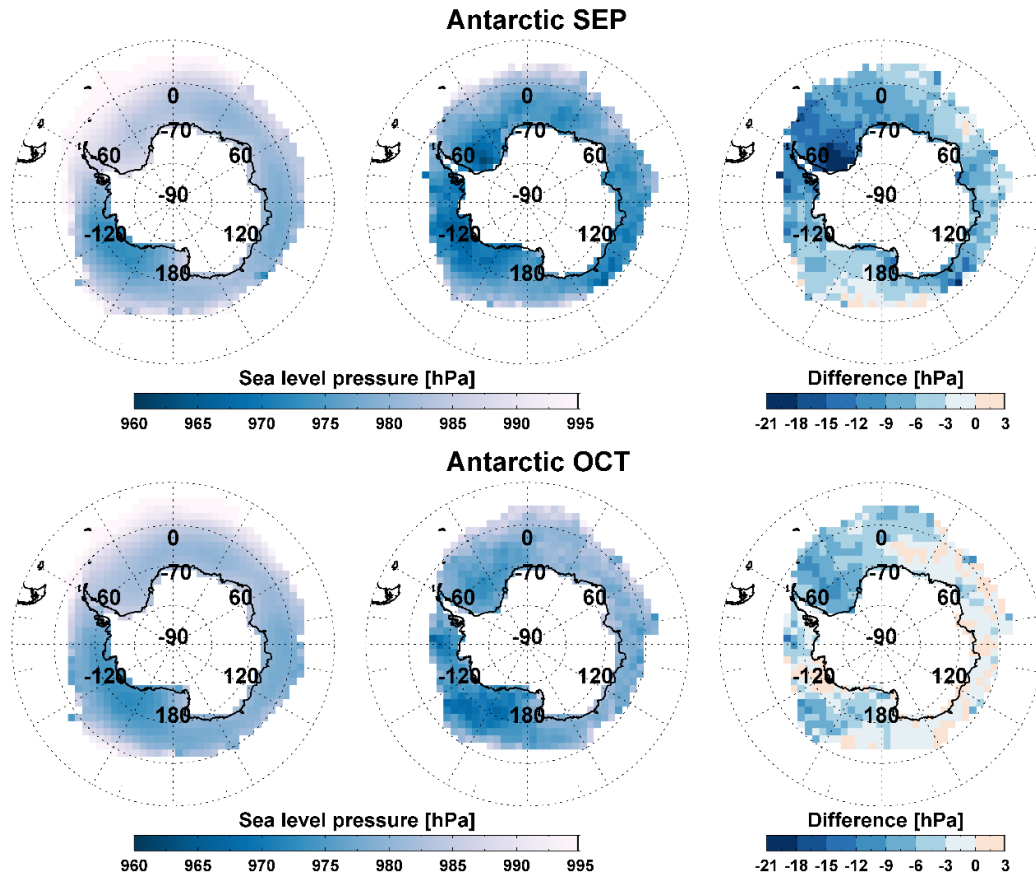


**Figure 4.5.** As Fig. 4.4, but for the Antarctic in September (upper panel) and October (lower panel).

### 4.3.2.2 Surface level temperature

The relationship between air temperature at 2 m and the enhancements of total BrO columns was investigated in the same way as for pressure in the previous section. From Fig. 4.6, it can be seen that the surface level air temperature is low during enhancements of total BrO column in both the Arctic and Antarctic sea ice regions. The air temperature frequency distribution of the Antarctic is shifted more clearly towards lower temperatures than that of the Arctic. The highest frequencies of 27 % in the mean field and 32 % in the enhanced BrO field are detected at the same temperature range of -20 to -15 °C in the Arctic. However, for

## 4. BrO enhancements in polar sea ice regions

the Antarctic, the temperature range of the highest frequency is -20 to -15 °C in the high BrO situations, compared to -15 to -10 °C in the mean field.

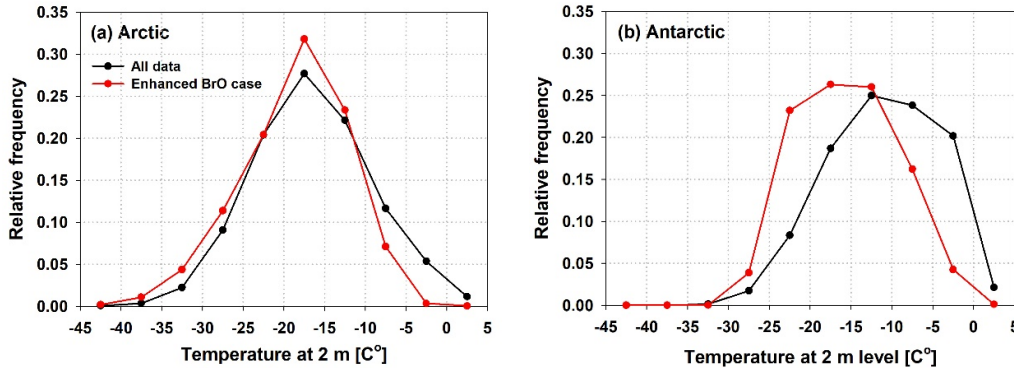


**Figure 4.6.** Frequency distribution of surface air temperature for all data (black line) and the enhanced BrO case (red line) in (a) the Arctic and (b) Antarctic sea ice region in spring (Arctic: March to April, Antarctic: September and October).

Spatial distributions of monthly temperature differences for the Arctic and Antarctic are also shown in Fig. 4.7 and 4.8, respectively. One remarkable feature in these maps is that temperature differences vary depending on region. When the total BrO column is enhanced, negative surface level air temperature anomalies (up to  $\sim 12^{\circ}\text{C}$  colder compared to the long-term mean) are found over the Arctic sea ice region except for the central Arctic region where positive anomalies occur. The pattern of surface level air temperature in the Antarctic is similar to that of the Arctic as shown in Fig. 4.8. Atmospheric temperature during enhanced BrO events is lower in most areas of the Antarctic and a significant decrease of temperature is found at the margin of the sea ice. In contrast, a slight increase in temperature is associated with the enhancement of BrO around the Antarctic coastal region. These patterns indicate that not only relative temperature changes but also absolute temperatures are linked to the conditions in which enhanced BrO events can occur. Negative temperature anomalies are needed for BrO enhancement in the marginal sea ice regions where temperatures are closer to the freezing point than in the central Arctic and Antarctic, where temperatures are always low.

#### 4. BrO enhancements in polar sea ice regions

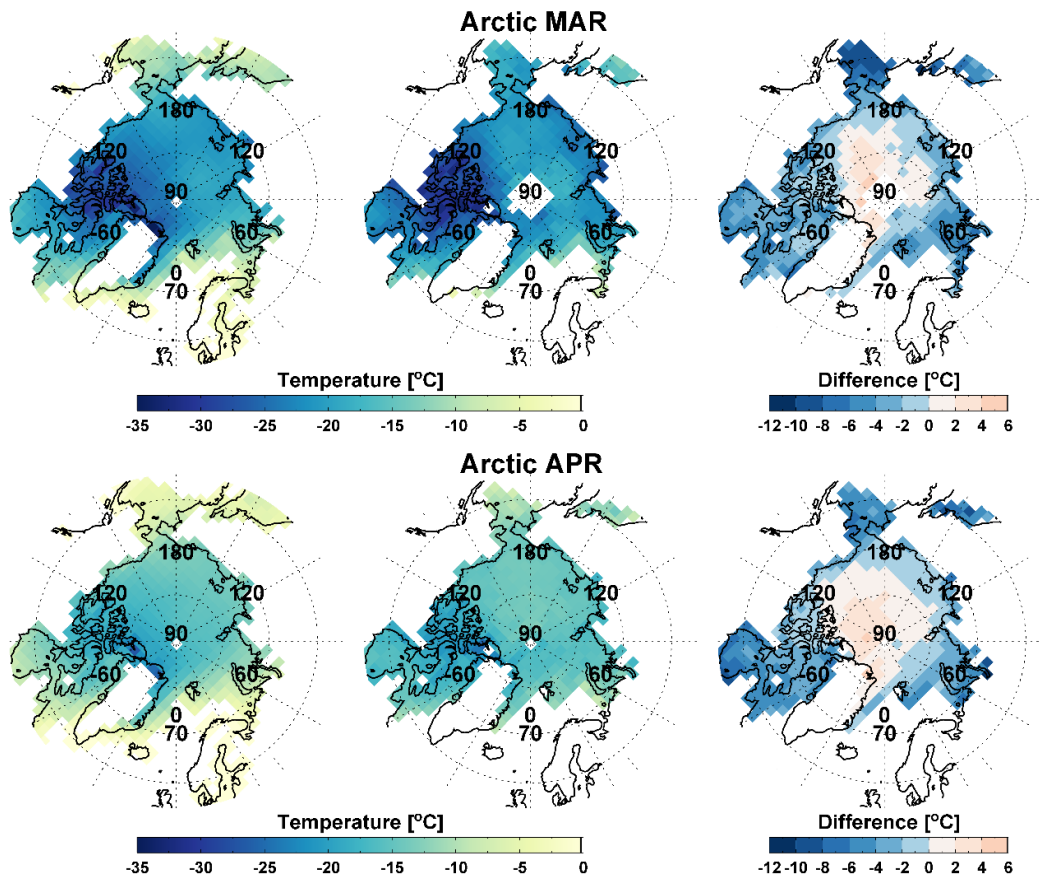


**Figure 4.7.** Monthly surface air temperature for the mean field (left), the enhanced BrO case (middle), and surface air temperature APR anomalies (difference of surface air temperature between the enhanced BrO case and the mean field) (right) over the Arctic in March (upper panel) and April (lower panel).

Temperature effects in the chemical mechanism of bromine release were discussed in several previous studies. Sander et al. (2006) demonstrated why bromine release is accelerated on cold saline surfaces using a 1-d atmospheric chemistry model. They found that the acid-catalyzed atmospheric bromine explosion cycle is triggered in their simulations by precipitation of carbonates at a temperature below 263 K leading to reduced buffering capacity of the alkaline sea water and facilitating its acidification. Model calculations identified the strong temperature dependency of the equilibrium reactions releasing Br<sub>2</sub> and BrCl. These reactions transform the bromide in brine into reactive bromine. The cold

#### 4. BrO enhancements in polar sea ice regions

conditions associated with bromine explosions at the surface are similar to those required to form frost flowers in polar regions. Frost flowers which are water ice, coated with brine can act as a source of bromine explosion events. They are mainly formed when open polynyas or leads freeze at very low temperature (Martin et al., 1996; Obbard et al., 2009). Kaleschke et al (2004) reported that potential frost flower regions, associated with cold surface air temperature, match spatially the source regions of enhanced BrO columns detected by satellites. The results from our long-term statistical analysis are consistent with those from previous studies showing the importance of low temperature conditions for bromine explosions. In summary, the present results combined with findings on chemical mechanisms, assumed to be responsible for the development of tropospheric bromine explosion events in previous studies, indicate that air temperature is one of the important parameters in the BrO column variability.

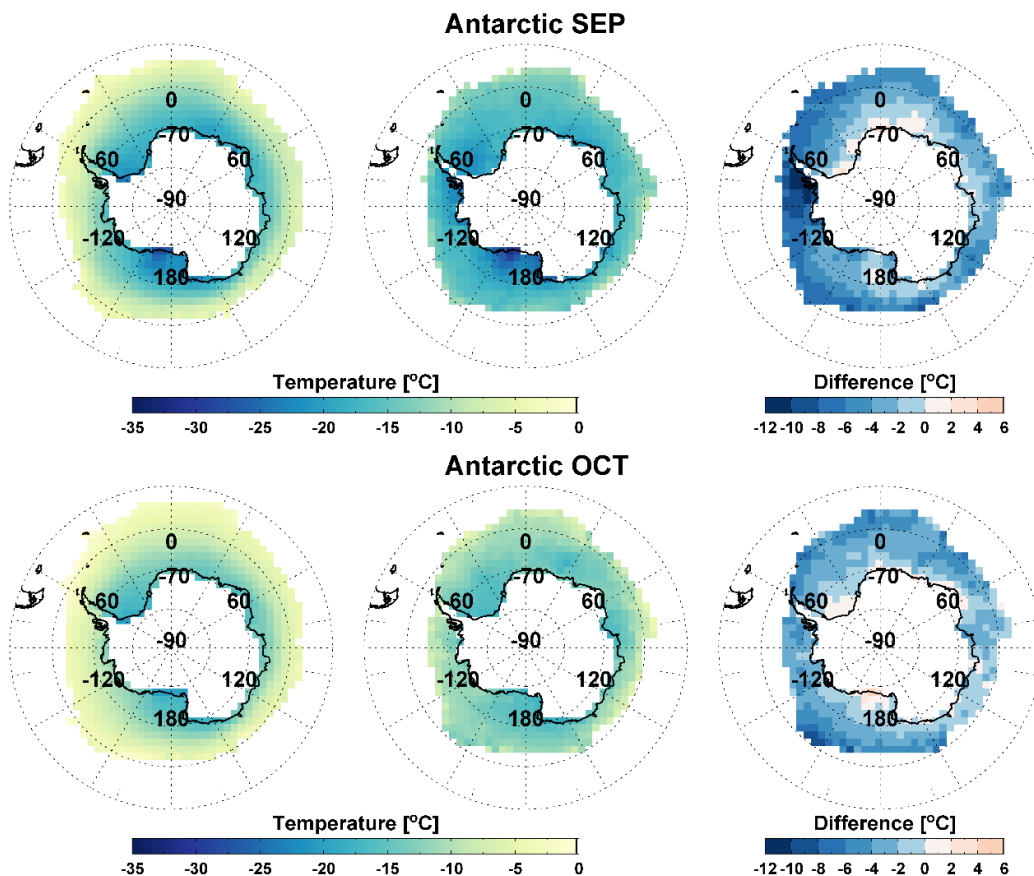


**Figure 4.8.** As Fig. 4.7, but for the Antarctic in September (upper) and October (lower).

## 4. BrO enhancements in polar sea ice regions

### 4.3.2.3 Surface level wind speed and direction

Next, surface level wind speed is investigated to evaluate how this may affect the occurrence of total BrO column enhancements. Figure 4.9 shows the frequency distribution of wind speed at 10 m for the average field and for enhanced BrO cases of the 10 years of measurements in the Arctic and Antarctic sea ice region. The distribution is shifted towards high wind speeds in both polar regions for enhanced total BrO vertical columns, the increase in wind speed being more pronounced in the Antarctic region. The difference in wind speeds is also confirmed by the spatial distribution maps (Fig. 4.10 and 4.11). Higher wind speeds are observed in most Arctic and Antarctic regions for situations with enhanced total BrO columns compared to the mean field. In particular, differences in wind speed of more than 5 m/s and high wind speeds of over 10 m/s are found at specific regions of the Arctic such as the eastern coast of Greenland, the Bering Strait and the central Arctic. In the Antarctic region, wind speeds greater than 12 m/s are predominantly observed over the sea ice margins and some of the Antarctic coastline. Results show that enhancements of BrO columns are mainly related to positive wind speed anomalies except for some areas such as the Canadian archipelago. The enhanced BrO columns in the Canadian archipelago, an area where total BrO hotspots are frequently detected with low surface wind speeds, may be attributed to local production/recycling of reactive bromine under a stable boundary layer or an increase in stratospheric BrO.

The relationship between surface wind speed and enhanced BrO column has been discussed in previous studies, and still is under debate. Some of the related studies showed tropospheric ozone depletion events and bromine explosion events at lower wind speeds of less than 8 m/s in polar sea ice regions (Simpson et al., 2007a; Jones et al., 2010). These case study results support the opinion that tropospheric BrO explosion events occur efficiently at low wind speeds since under these conditions, reactants can accumulate within the stable boundary layer while under strong wind conditions, a dilution of bromine sources due to rapid vertical mixing and horizontal spreading prevents the BrO explosion. On the other hand, highly saline sea salt aerosols produced during blowing snow events driven by high surface wind speeds can act, if sufficiently cold, as a bromine source in the tropospheric BrO explosion mechanism (Yang et al., 2008; Obbard et al., 2009; Jones et al., 2009; Blechschmidt et al., 2016). Yang et al. (2010) successfully simulated bromine explosion events using a global chemistry transport model by

## 4. BrO enhancements in polar sea ice regions

considering bromine emissions from sea salt aerosols and saline snow lying on sea ice during blowing snow events. Also, Jones et al (2009) and Blechschmidt et al. (2016) reported that high wind speeds and vertical lifting caused by a cyclone can provide blowing snow. When the wind speed exceeds  $\sim 8$  m/s, snow particles begin to dislodge from the surface, and at wind speeds above  $\sim 12$  m/s, active mixing and transport of snow and sea salt aerosols within the boundary layer become possible (Jones et al., 2009). Thus, blowing snow created by high surface wind speeds is a plausible mechanism releasing reactive bromine sources into the boundary layer or above it. This supports the notion that high wind speeds also lead to enhanced BrO in the lower atmosphere.

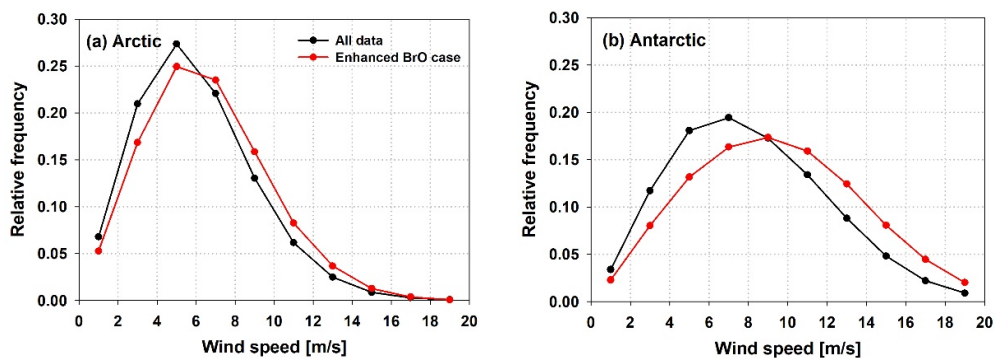


**Figure 4.9.** Frequency distribution of wind speed at 10 m for all data (black line) and the enhanced BrO case (red line) in (a) the Arctic and (b) Antarctic sea ice region in spring (Arctic: March to April, Antarctic: September to October).

The spatial distribution map of surface wind speed anomalies derived in this study shows that during the enhancement of total BrO vertical columns, wind speeds are generally enhanced. However, the average wind speed field during the high BrO cases shows values of 6-8 m/s in most areas. For the tropospheric bromine explosion events created by strong winds, previous studies indicate that wind speeds above  $\sim 12$  m/s are required. The regions that satisfy this wind speed threshold consistently are confined to the Bering Strait, the central Arctic, and the east coast of Greenland in the Arctic and the Antarctic sea ice margins and some coastal locations. This behaviour is clearly identified in the spatial distribution maps of the relative frequency of high wind speeds for the occurrence of enhanced total BrO column (see Fig. 4.12) which show where strong surface winds contribute to the enhancement of BrO columns. In Fig. 4.12, high frequencies

#### 4. BrO enhancements in polar sea ice regions

above 30 % are found over the central Arctic and eastern coast of Greenland in the Arctic, whereas in the Antarctic, they are most frequently detected around the marginal ice zone of the Weddell and Ross Sea. In particular, although the central Arctic and eastern coast of Greenland are regions where enhanced total BrO columns are not frequently detected in the Arctic as shown in Fig. 2, it is clear that the occurrence of enhanced total BrO columns in the corresponding regions is often associated with higher wind speeds (Fig. 10 and 12). This could indicate that tropospheric bromine sources from blowing snow events generated by high wind speeds are important in these areas.

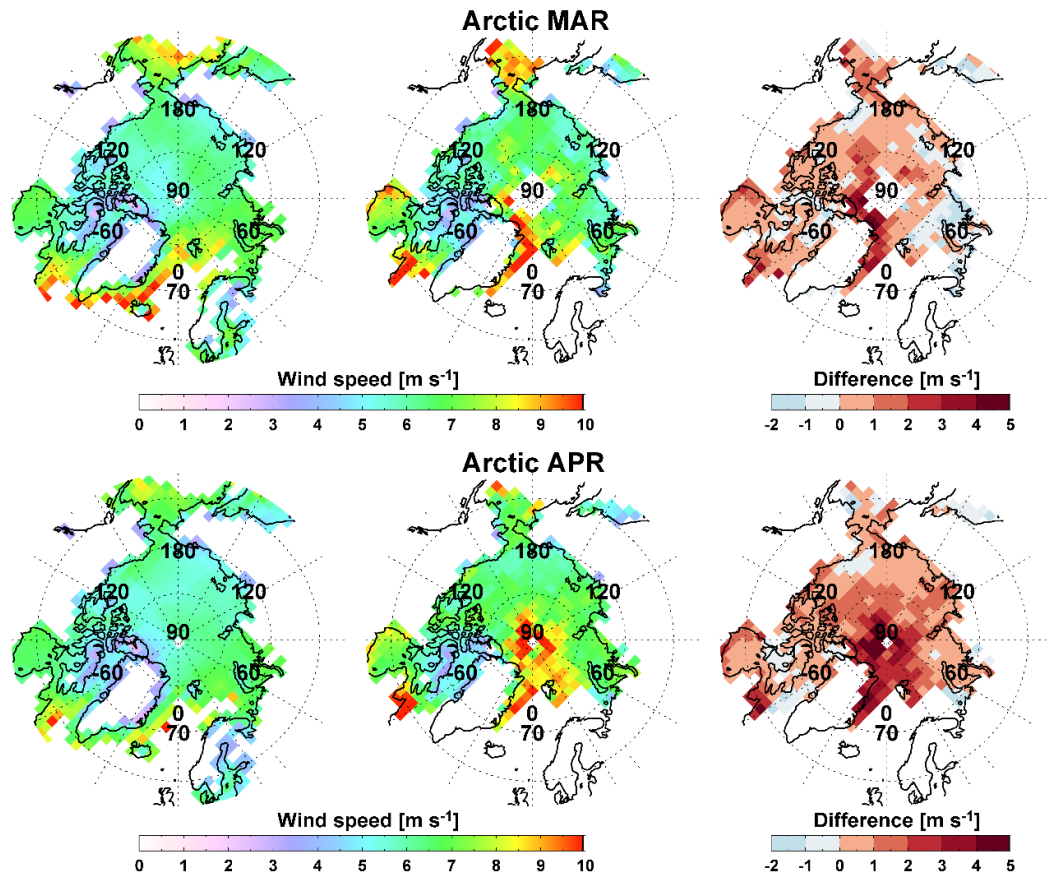


**Figure 4.10.** Monthly wind speed at 10 m for the mean field (left), the enhanced BrO case (middle), and wind speed anomalies (right) over the Arctic in March (upper) and April (lower).

#### 4. BrO enhancements in polar sea ice regions

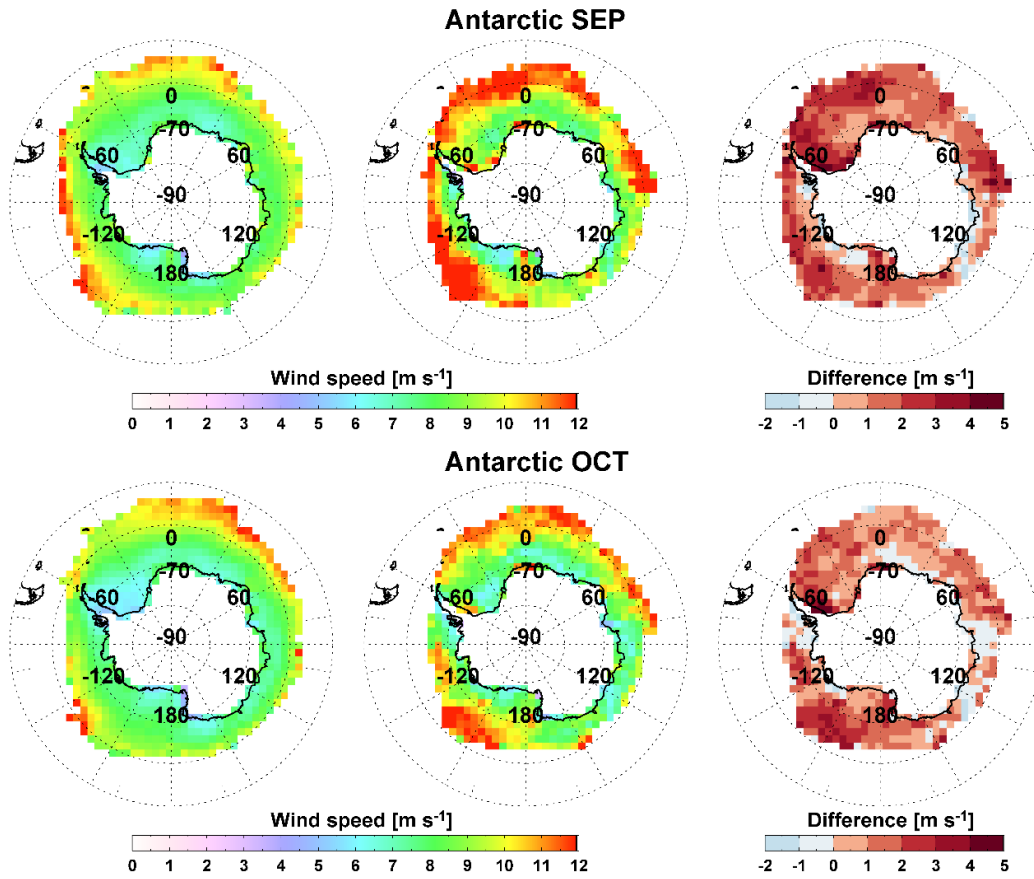


**Figure 4.11.** As Fig. 4.10, but for the Antarctic in September (upper panel) and October (lower panel).

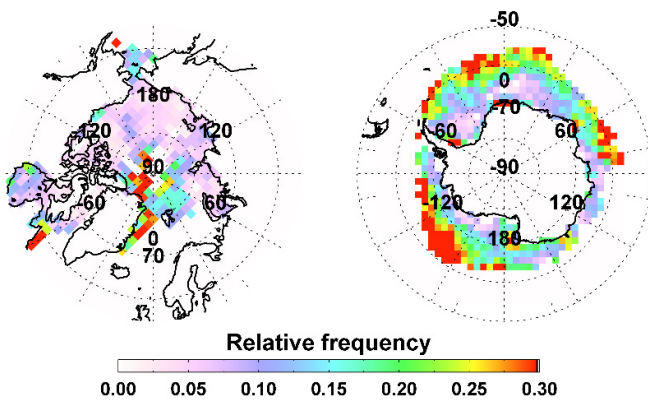


**Figure 4.12.** Spatial distributions of the relative frequency of high wind speeds during the enhanced BrO occurrences in the Arctic ( $v \geq 12$  m/s) and Antarctic ( $v \geq 14$  m/s) sea ice region in spring.

## 4. BrO enhancements in polar sea ice regions

In order to investigate whether not only the wind speed but also the wind direction affects the occurrence of BrO enhancement in terms of regions, the relative frequency of wind direction for data with enhanced BrO columns was mapped. The relative frequency was calculated for the case that the number of data collected within the reference grid is greater than 20 to avoid errors from using too small sample size. The wind direction was divided into eight groups at intervals of 45 degrees. From Fig. 4.13, we can identify which wind directions are related to BrO enhancements and the regional characteristics of these prevailing wind directions. First, the northern and western wind directions are more frequent compared to the southerly and easterly winds when enhancements of total BrO column occur in the Arctic sea ice region. High occurrence frequencies of above 50 % are found around the Bering Strait and the eastern coast of Greenland. This is expected because the northerly winds blowing from the interior of the Arctic sea ice are likely to be cold and contain bromine sources such as saline snow, frost flowers and sea salt aerosols rather than the southerly winds from the open sea. In contrast to the prevailing northerly winds around the Arctic sea ice margins, southern winds including S, SE and SW are mainly observed around the central Arctic and high latitude regions for the BrO event cases. This may be explained by the transport of air masses with enhanced BrO from sea ice margins to high latitudes by southerly winds, which is also in line with the temperature increase pattern over the central Arctic reported in the previous section. Overall, north-westerly winds are the most dominant wind direction, associated with the enhancement of total BrO column in the Arctic, especially high occurrence frequencies being found over the northern coast of Canada, Hudson Bay and Baffin Bay. These regions have been mentioned in many previous studies as areas where satellite BrO hotspots frequently appear during Arctic spring (Salawitch et al., 2010; Theys et al., 2011; Nghiem et al., 2012). Fig. 4.14 shows the degree of changes in the frequency of wind directions in cases of enhanced BrO compared to the mean field in the Arctic in terms of spatial variation. In general, the south and east winds have decreased frequencies in most regions during the occurrence of enhanced BrO compared to the mean, whereas the frequencies of NW, W, and N, the main wind directions associated with BrO enhancements, increase by more than 20 %, especially around the sea ice margin area.

The spatial distribution of the wind direction frequency during the occurrence of enhanced total BrO columns is clearer in the Antarctic, compared to the Arctic. As shown in Fig. 4.15, the northern winds show low relative frequency overall in

#### 4. BrO enhancements in polar sea ice regions

the Antarctic sea ice region for BrO enhancement cases, which indicates that the northerly winds have a low association with BrO enhancements. This is consistent with our understanding of the conditions required for BrO enhancements because the northerly winds blowing from the open water to Antarctica are usually relatively warm, and thus sea salt aerosols are not cold enough to trigger the bromine explosion mechanism. Another feature of wind direction distribution in the Antarctic is that easterly winds are strongly related to enhanced BrO columns along the coast of Antarctica, whereas westerly winds are prevailing over the sea ice region except for the Antarctic coastlines. Basically, the main winds of the Antarctic can be divided into two types: (1) large-scale circulations composed of westerly winds and (2) local katabatic winds deflected in the cross-slope direction with an eastward component due to the Coriolis force. Consequently, the predominant wind direction during the BrO enhancement also follows the Antarctic large-scale circulation. Depending on the large-scale atmospheric system, easterly winds in the coastal regions and westerly winds in the sea ice regions are dominant, but the influence of the south wind increases in the presence of enhanced BrO columns. Maps of differences in the frequency of the wind direction between the high BrO situation and the mean field (see Fig. 4.16) clearly show that occurrence frequencies of wind directions from southerly and westerly directions increase during the occurrence of enhanced BrO columns. In particular, the southwestern winds prevail for situations with enhanced BrO columns, as frequencies increase by more than 20 % over a large area of Antarctic sea ice including the marginal ice zones.

The impact of high wind speed on the total BrO column enhancement at each wind direction in the Arctic and Antarctic regions during spring was further investigated. Table 4.2 summarizes the relative frequency of wind direction for the mean field, for the enhanced BrO cases and for enhanced BrO cases accompanied by high wind speeds ( $v \geq 12$  m/s for the Arctic and  $v \geq 14$  m/s for the Antarctic), respectively. The average frequency of wind direction is generally evenly distributed between 10.6-14.7 % in the Arctic. However, for the cases with enhanced total BrO columns, the relative frequency of the northwest, west and north winds increase to 22.0, 17.9 and 16.0 %, and when limited to high surface wind speed cases, frequencies increase further to 24.7, 21.1 and 18.9 %, respectively. In the Antarctic sea ice region, the difference in the frequency between the individual wind directions is larger than in the Arctic. The average frequency of the northeast wind is 8.1%, while the frequency of the west wind is as

#### 4. BrO enhancements in polar sea ice regions

high as 20.1 %. The difference in the relative frequency distribution of the wind directions becomes even larger if cases with enhanced BrO are considered. The southwest and west winds are then prevailing with a relative frequency of 30.4 and 26.0 %, which increases further to 35.5 and 32.6 % under high wind speed conditions. Through the statistical analysis, the specific wind directions affect the BrO enhancement were confirmed and if the relevant winds become strong, the supply of reactive bromine source in the troposphere becomes active, which can contribute further to the increase of total BrO column density.

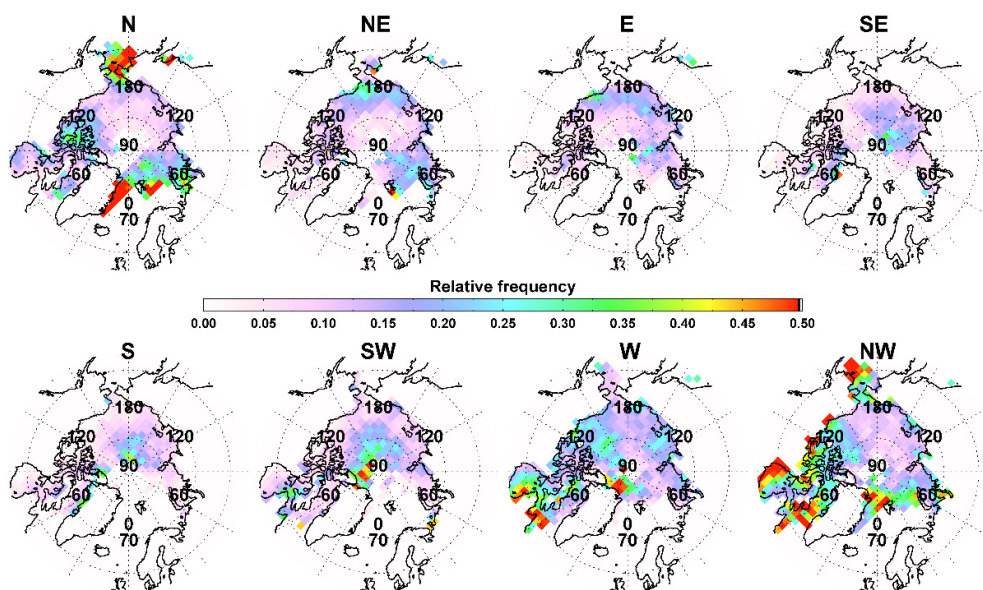


**Figure 4.13.** Relative frequency maps of surface level wind direction for data with BrO enhancements over the Arctic during spring (March to April in 2008-2018). The frequency was calculated for the cases where the number of data collected within the reference grid is greater than 20. The results are shown separately for different wind directions.

#### 4. BrO enhancements in polar sea ice regions

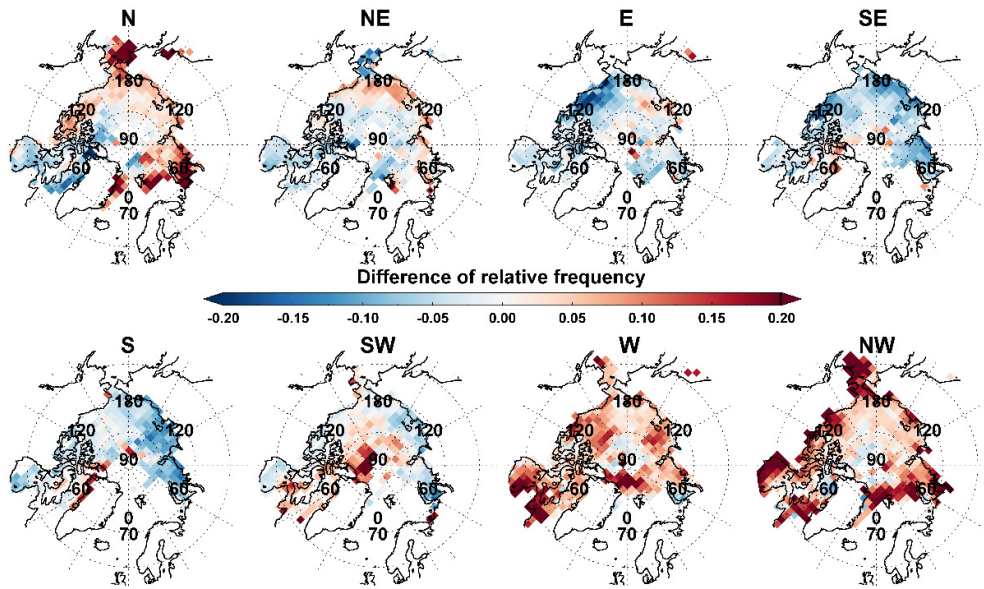


**Figure 4.14.** Spatial distributions of the differences in relative frequencies of wind direction between enhanced BrO cases and the mean field for the Arctic in spring (March to April in 2008-2018). The results are shown separately for different wind directions.

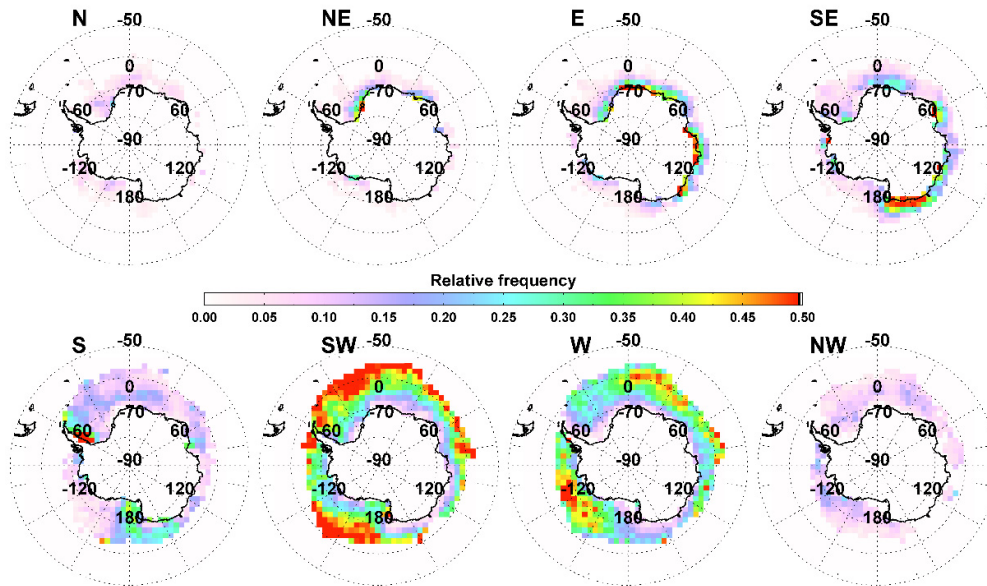


**Figure 4.15.** As Fig. 4.13, but for the Antarctic during spring (September to October in 2008-2018).

## 4. BrO enhancements in polar sea ice regions

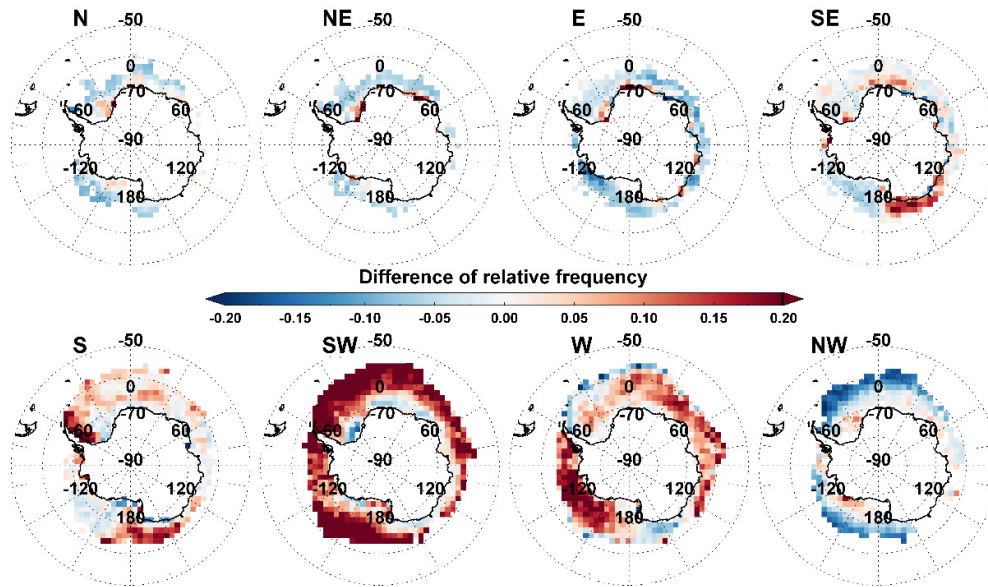


**Figure 4.16.** As Fig. 4.14, but for the Antarctic during spring (September to October in 2008-2018).

**Table 4.2.** Relative frequency (expressed in %) of surface level wind directions for all data, the enhanced BrO case and the enhanced BrO with high wind speeds for the Arctic and Antarctic in spring.

	Wind direction (%)							
	N	NE	E	SE	S	SW	W	NW
<b>Arctic</b>								
Relative frequency for all data	14.7	12.6	12.7	12.5	11.4	10.6	11.5	14.0
Relative frequency during the enhanced BrO occurrence	16.0	11.0	9.2	7.4	6.7	9.8	17.9	22.0
Relative frequency during the enhanced BrO occurrence with high wind speeds ( $v > 12$ m/s)	18.9	7.3	7.1	4.5	4.4	12.0	21.1	24.7
<b>Antarctic</b>								
Relative frequency for all data	8.4	8.1	11.4	10.1	10.4	18.4	20.1	13.1
Relative frequency during the enhanced BrO occurrence	2.7	3.0	6.7	10.4	13.5	30.4	26.0	7.3
Relative frequency during the enhanced BrO occurrence with high wind speeds ( $v > 14$ m/s)	0.5	1.3	6.6	9.4	9.4	35.5	32.6	4.7

## 4. BrO enhancements in polar sea ice regions

### 4.3.2.4 Tropopause height

The last factor investigated in connection with the enhancement of total BrO columns is the tropopause height. The relationship between the tropopause height and BrO hotspots observed from satellites was discussed in previous studies using data for periods from several days up to two years. Salawitch et al. (2010) found that enhanced total BrO columns over the Hudson Bay observed by OMI are coincident with a low tropopause of  $\sim 5$  km and high total  $O_3$  column of  $\sim 450$  DU. In general, the stratospheric BrO columns are anti-correlated with the tropopause height field, and thus they concluded that the elevated total BrO columns at low tropopause heights over the Hudson Bay may be attributed to an increase of stratospheric BrO columns. Theys et al. (2011) also investigated total, stratospheric and tropospheric BrO columns retrieved from GOME-2 measurements and the corresponding tropopause heights for the northern high latitudes in spring. They found two different cases through their analysis using two years of data: (1) situations where the spatial distribution patterns of enhanced total BrO columns and low tropopause heights are consistent, (2) BrO hotspots, which are not associated with low tropopause heights and high stratospheric BrO columns. The first case shows that the increase in total BrO columns can be affected by the stratospheric contribution in line with the findings of Salawitch et al. (2010), but the second indicates that elevated total BrO columns can also be linked to the increase of tropospheric BrO columns.

In this study, the relationship between tropopause height and total BrO column enhancements is investigated in both the Arctic and Antarctic sea ice region using 10 years long-term data in terms of magnitude, region and time, and the results are compared with those from previous studies. The relative frequency distributions of tropopause height for the mean field and the cases with enhanced total BrO columns in the Arctic and Antarctic are presented in Fig. 4.17. In both polar regions, the frequency distribution is shifted towards lower tropopause height during the occurrence of enhanced total BrO columns, and this effect is larger in the Antarctic than the Arctic. This indicates that the decrease of tropopause heights is associated with the enhancement of total BrO columns, which is consistent with previous study results. Our results also show that the enhancement of total BrO columns due to tropopause descends is more prominent in the Antarctic than in the Arctic. This conclusion is different from the finding of Theys et al. (2011), who reported that the effect of low tropopause height on the

## 4. BrO enhancements in polar sea ice regions

increase of BrO column seems to be more important in the Arctic than in the Antarctic region. One possible explanation for the difference apart from the different time periods investigated is that here, the frequency distribution of the tropopause height was investigated for situations with enhanced total BrO column whereas Theys et al. (2011) investigated the impact of tropopause height on the tropospheric BrO column.

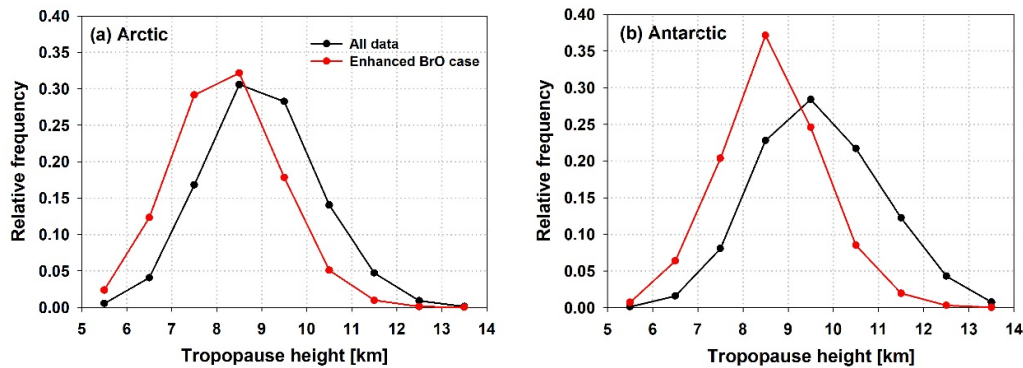


**Figure 4.17.** Frequency distribution of tropopause height for all data (black line) and the enhanced BrO case (red line) in (a) the Arctic and (b) Antarctic sea ice region in spring (Arctic: March to April, Antarctic: September to October).

In addition to the frequency distribution of tropopause height, also the differences in maps of tropopause height between situations with enhanced total BrO column and the mean were investigated (Fig. 4.18 and 4.19). The mean field of tropopause height shows generally a tropopause height of 9.0-9.5 km range over the Arctic except for the north coast of Canada (e.g. Canadian Archipelago), Fram Strait and the Barents Sea where slightly lower tropopause heights of 8.0-8.5 km appear. For the BrO enhancement cases, tropopauses are lower in the 7.5-9.0 km range in most areas. In particular, large differences in tropopause height of  $\sim 2$  km are observed over Bering Strait, Hudson Bay, and Baffin Bay, indicating that enhancements of total BrO columns in these areas may be more affected by stratospheric BrO through tropopause descent. Similar to the Arctic case, the tropopause height is lower by up to  $\sim 2.3$  km in most of the Antarctic sea ice region in situations with enhanced total BrO columns. Especially, large differences are detected around the Antarctic Peninsula in September. Negative tropopause height anomalies influence the total BrO column through the increase of the stratospheric column, or by mixing stratospheric air with high BrO concentrations into the

#### 4. BrO enhancements in polar sea ice regions

troposphere. However, they are also associated with changes in meteorological conditions in the troposphere, which favour BrO release close to the surface. Consequently, not only the surface level meteorological factors such as surface level atmospheric temperature, wind speed and direction but also the impact of the stratospheric field should be considered in the interpretation of enhancements in the total BrO column.

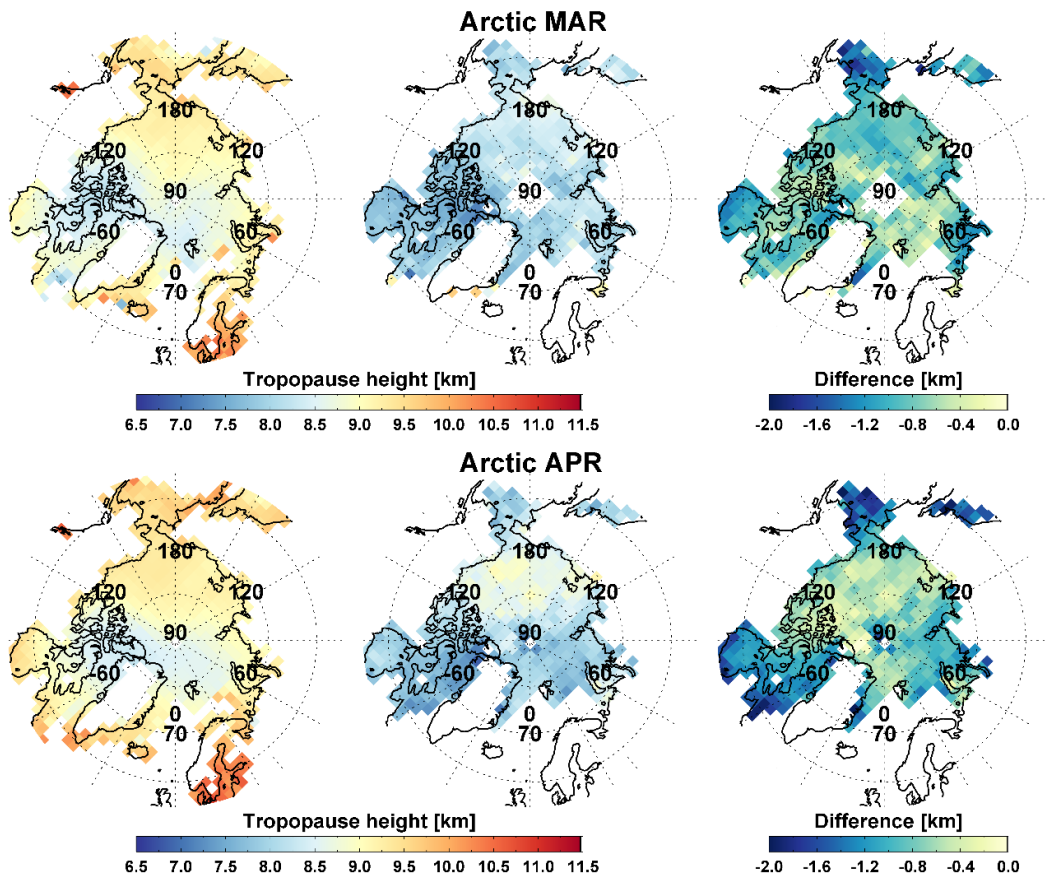


**Figure 4.18.** Monthly tropopause height for the mean field (left), the enhanced BrO case (middle), and tropopause anomalies (difference of tropopause height between the enhanced BrO case and the mean field) (right) over the Arctic in March (upper panel) and April (lower panel).

## 4. BrO enhancements in polar sea ice regions

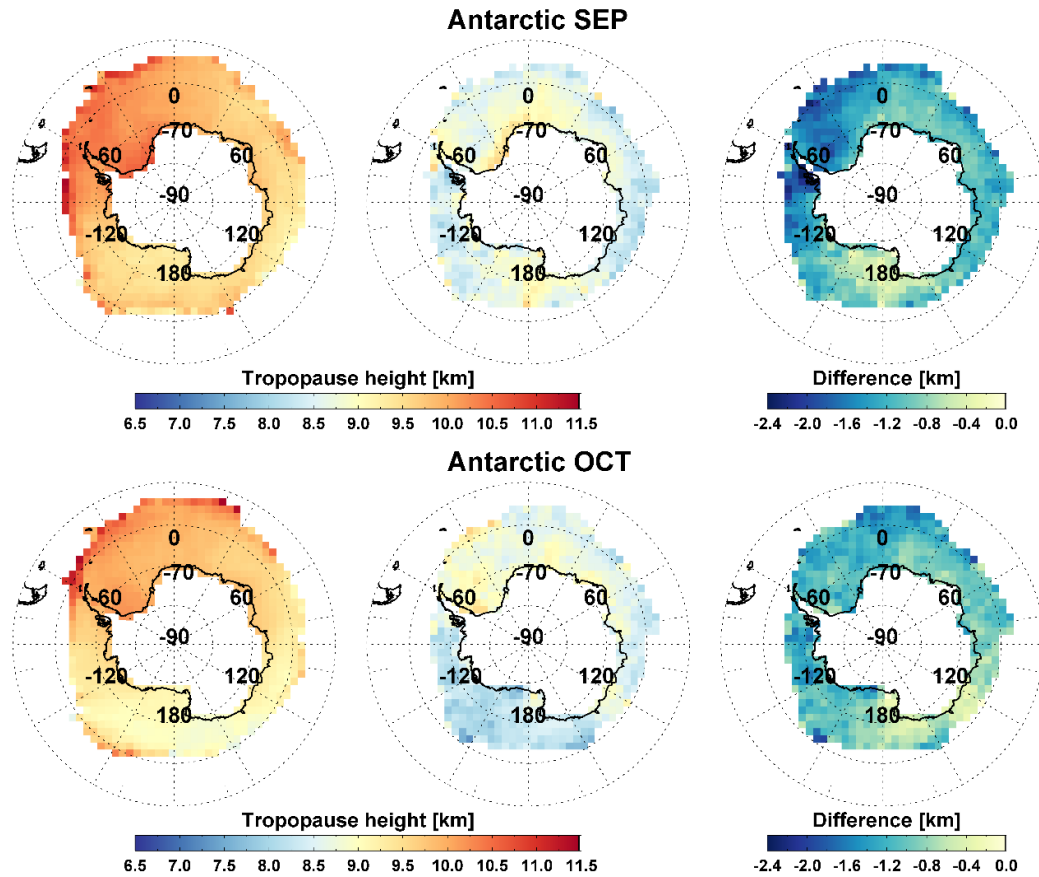


**Figure 4.19.** As Fig. 4.18, but for the Antarctic in September (upper panel) and October (lower panel).

### 4.3.3 Correlation analysis between total BrO vertical column and meteorological parameters

To assess statistically the dependence between total BrO vertical column and multiple meteorological parameters investigated in the previous sections, a Spearman's rank correlation analysis was performed in this section. The Spearman correlation determines the strength and direction of the monotonic relationship between two variables. Thus, this method is less sensitive to strong outliers and distribution type than the Pearson correlation, which is the reason for using the Spearman rank correlation analysis in this study.

#### 4. BrO enhancements in polar sea ice regions

Monthly Spearman correlation coefficients between total BrO vertical column density and meteorological parameters including sea level pressure, surface level air temperature, surface level wind speed, and tropopause height are provided in Table 4.3. Correlation coefficients with p-values less than 0.001, indicating that results are statistically significant, are presented here. Correlations are low for all four factors investigated (apart from tropopause heights for September in the Antarctic which shows a moderate correlation of 0.4). Overall, tropopause height shows the largest negative correlation with total BrO vertical column density in both the Arctic and Antarctic. Total BrO vertical column is more negatively correlated with tropopause height in the Antarctic than the Arctic, and the negative correlation coefficients of March and September are larger than those of April and October. Total BrO vertical column has also a negative correlation with the surface level air temperature in both polar regions, but these correlation coefficients are smaller than correlation coefficients with tropopause height. Larger correlation coefficients are found in March and September than April and October. Sea level pressure has a negative correlation of -0.23 with total BrO column in September in the Antarctic region, but correlations are even lower in the Arctic and in other months. Surface wind speed has correlation coefficients close to 0 with total BrO vertical column density in both the Arctic and Antarctic, and even for wind speeds above 8 m/s, which can cause blowing snow, there is no clear relationship between them. This could either be due to stratospheric air dominating the total BrO column or due to the large variability of wind speed conditions under which tropospheric BrO explosion events occur according to previous studies described above.

The regional difference of the statistical dependence between total BrO vertical column and meteorological factors were also investigated by performing the Spearman correlation analysis for each cell of the reference grid. Figure 4.20 displays the spatial distribution of Spearman correlation coefficients between total BrO vertical column and each meteorological factor where the p-value < 0.001. The strong negative correlation between total BrO vertical column and tropopause height appears in both the Arctic and Antarctic region. The strongest negative correlation coefficients reaching values below -0.6 are found over the Hudson Bay, Baffin Bay and Bering Strait in the Arctic sea ice region, while the regional variation in the correlation is not large in the Antarctic region. These strong negative correlations between total BrO vertical columns and tropopause heights during springtime indicate that the total BrO vertical column tends to increase

#### 4. BrO enhancements in polar sea ice regions

when the tropopause height is lowered, which means that the contribution of stratospheric origins to total BrO columns is significant. It was also confirmed from the spatial distribution of correlation coefficient that the influence of tropopause height on the total BrO vertical column varies depending on the region. Over the Hudson Bay and Bering Strait with stronger negative correlations, the stratospheric BrO fields associated with the change of tropopause height may have a greater impact on total BrO columns than in other regions.

Surface level air temperature also shows different Spearman correlation patterns depending on the region. The correlation between total BrO vertical column and temperature is negative at relatively lower latitudes of the Arctic and then turns to positive values over the central Arctic region. This indicates that an increase of surface air temperature is related to the enhancement of total BrO vertical column over the central Arctic, while a decrease of temperature is associated with the increase of total BrO column in most areas except for the central Arctic. In contrast to the Arctic, opposite correlation patterns between total BrO column and surface air temperature as a function of latitude are not detected in the Antarctic sea ice region. Correlations are not very significant around the Antarctic coastal region and negative correlation coefficients of  $\sim -0.3$  are found in most sea ice areas. These spatial distribution patterns of correlation coefficients for surface air temperature are similar to those of the difference in the temperature between the enhanced total BrO field and the mean field (see Fig. 4.7 and 4.8).

Spatially, sea level pressure is negatively correlated with total BrO vertical column in most regions of the Arctic and Antarctic. However, sea level pressure has weak negative correlations with total BrO column compared to the values found for tropopause height and surface air temperature. Wind speed is positively correlated with total BrO vertical column in most areas of both polar sea ice, but the correlation is very weak with  $|r| < 0.2$ .

The correlation analysis using the long-term dataset improves our understanding of the influence of meteorological factors on total BrO vertical columns in terms of the region and the time of year (month). The strongest influence of the different parameters on total BrO column, having a large correlation coefficient, is tropopause height, which indicates that the stratospheric contribution is significant in the total BrO column density variations. This is presumably because low tropopause heights result in a larger contribution of

## 4. BrO enhancements in polar sea ice regions

stratospheric BrO column to the total column. Consequently, accurate stratospheric correction is important in studying the tropospheric bromine explosion events and estimating tropospheric BrO content from the measured total BrO columns. Among the surface level meteorological parameters, air temperature impacts on the total BrO column density, arguably because temperature is an important factor in the chemical mechanism of reactive bromine release in the lower atmospheric layer. Sea level pressure and surface level wind speed are negatively and positively correlated with the total BrO vertical column density, but correlations are lower than for surface air temperature, which indicates that their influence on total BrO column is not as large as surface air temperature.

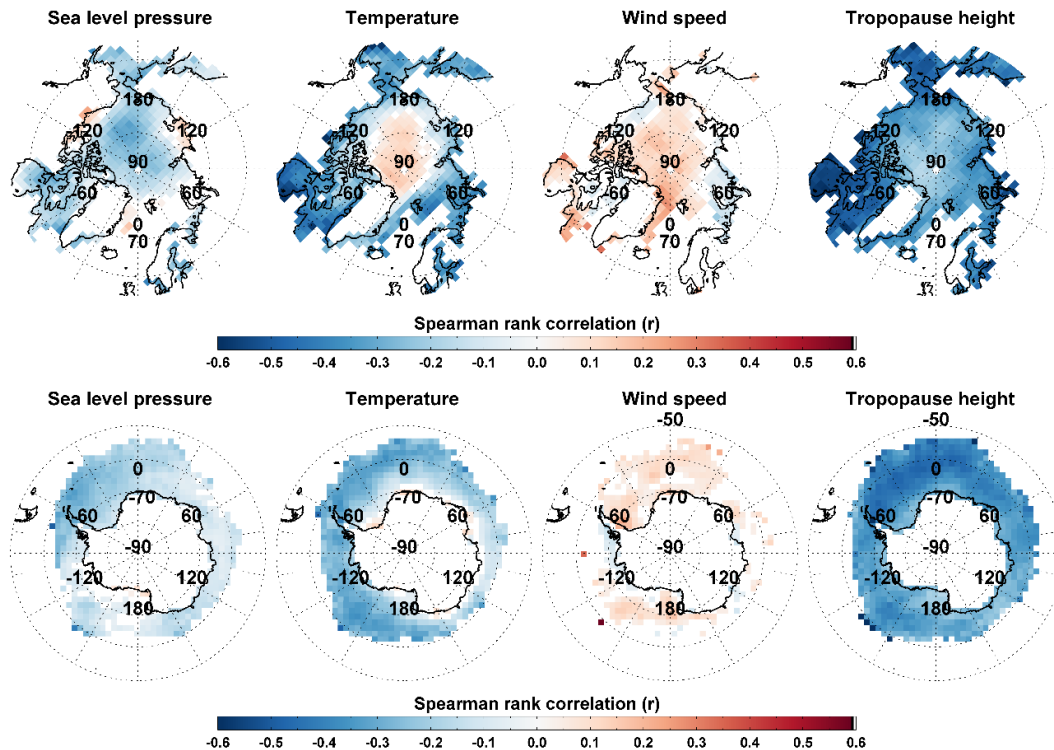


**Figure 4.20.** Spatial distributions of the Spearman correlation coefficients between total BrO VCD and four meteorological parameters (sea level pressure, surface air temperature, wind speed at 10 m, and tropopause height) for the Arctic and Antarctic in spring. Spearman correlation coefficients with p-value < 0.001 are only plotted.

#### 4. BrO enhancements in polar sea ice regions

**Table 4.3.** Spearman rank correlation coefficients between total BrO VCDs and four meteorological parameters. The results are shown separately for different months in spring in the Arctic and Antarctic. Note that all Spearman's rank correlation coefficients are significant ( $p < 0.001$ ). Abbreviation: MA (March to April), SO (September to October)

	Arctic			Antarctic		
	Mar	Apr	MA	Sep	Oct	SO
Sea level pressure	-0.032	-0.098	-0.070	-0.228	-0.053	-0.130
Temperature	-0.242	-0.149	-0.180	-0.305	-0.110	-0.193
Wind speed	-0.011	0.067	0.035	0.038	0.043	0.040
( $v > 8$ m/s)	-0.002	0.026	0.010	0.041	0.035	0.037
Tropopause height	-0.336	-0.298	-0.315	-0.400	-0.307	-0.345

The relationship between individual meteorological parameters and the total BrO vertical column investigated above illustrates how each meteorological parameter is linked to BrO variations in terms of temporal and spatial distribution. However, since meteorological parameters are not independent of each other and vary systematically in general, cross-relationships between meteorological parameters affecting directly or indirectly BrO variations should also be considered. For example, Yang et al. (2019) showed that the sea salt aerosol (SSA) production affecting the enhancement of BrO at the tropospheric level is proportional to the sublimation flux of blowing snow which is affected by various meteorological parameters including surface wind speed, temperature and relative humidity. Also, Zhao et al. (2015) and Blechschmidt et al. (2016) showed that large-scale enhanced BrO plumes over the Beaufort Sea are associated with weather systems which change the various relevant meteorological parameters together. They also demonstrated that the size and lifetime of BrO plumes depend on the development stage of the weather system. Therefore, cross-correlations between meteorological parameters for those data having enhanced total BrO columns were investigated (see Table 4.4). During the occurrence of enhanced total BrO, sea level pressure has a negative correlation with surface level temperature and wind speed, while it has a positive correlation with tropopause height. For example, the development of a low pressure system during the enhancement of BrO columns may correlate with a decrease in tropopause height as well as an increases in surface level air temperature and wind speed. Although the correlation coefficients found are not large, results show that sea level

#### 4. BrO enhancements in polar sea ice regions

pressure is linked with both surface level meteorological conditions and the tropopause height which can account for stratospheric dynamics. Indeed, pressure systems which usually evolve due to interactions of temperature differences in the atmosphere derive directly the airflow motion within the troposphere and also may affect the tropopause height in relation to the convergence or divergence of air masses. It is also interesting to note from Table 4 that the tropopause height has insignificant correlations with surface level meteorological parameters during the BrO enhancements, except for the air temperature in the Arctic, which is predictable since the tropopause height is a factor more closely related to stratospheric dynamics compared to the surface level weather system.

**Table 4.4.** Cross-correlations of meteorological parameters for the enhanced total BrO cases in the Arctic and Antarctic sea ice region. Abbreviation: SLP (Sea level pressure),  $T_{2m}$  (Air temperature at 2m),  $WS_{10m}$  (Wind speed at 10 m), TropH (Tropopause height)

	Arctic				Antarctic			
	SLP	$T_{2m}$	$WS_{10m}$	TropH	SLP	$T_{2m}$	$WS_{10m}$	TropH
SLP	1	-0.186	-0.228	0.186	1	-0.163	-0.195	0.173
$T_{2m}$		1	0.183	0.249		1	0.158	-0.009
$WS_{10m}$			1	-0.013			1	-0.05
TropH				1				1

All analysis so far was correlating meteorological parameters and BrO enhancements for the same time step. In order to investigate possible time-lagging effects of meteorological conditions on total BrO VCDs, correlations between total BrO VCD and meteorological parameters were performed with several days lag for each grid cell. In general, signs of correlations between meteorological parameters and total BrO VCDs are not changed with  $\pm 2$  days time-lags and the most pronounced correlation for the tropopause height and surface air temperature appears without the time lag (see Fig 4.21 and 4.22). In particular, the tropopause height shows clearly the strongest negative correlation with total BrO VCD in both the Arctic and Antarctic when there is no time-lag and has a gradient where the correlation coefficient weakens with the time-lags. This may indicate that the effect of stratospheric contribution on total BrO VCD according to the change in the tropopause height is immediate and the effect of time-lagging is not significant compared to other factors. However, total BrO VCD shows slightly

## 4. BrO enhancements in polar sea ice regions

larger negative correlations with the sea level pressure in terms of negative time-lags. Although changes in the correlation coefficients are small, the analysis result indicates that the current total BrO VCDs are more related to the atmospheric pressure systems of the previous days than those of the next days. Also, surface wind speed shows positive correlations with total BrO VCD, but it can be confirmed that as the time-lag increases, the relationship weakens with a wide correlation coefficient range.

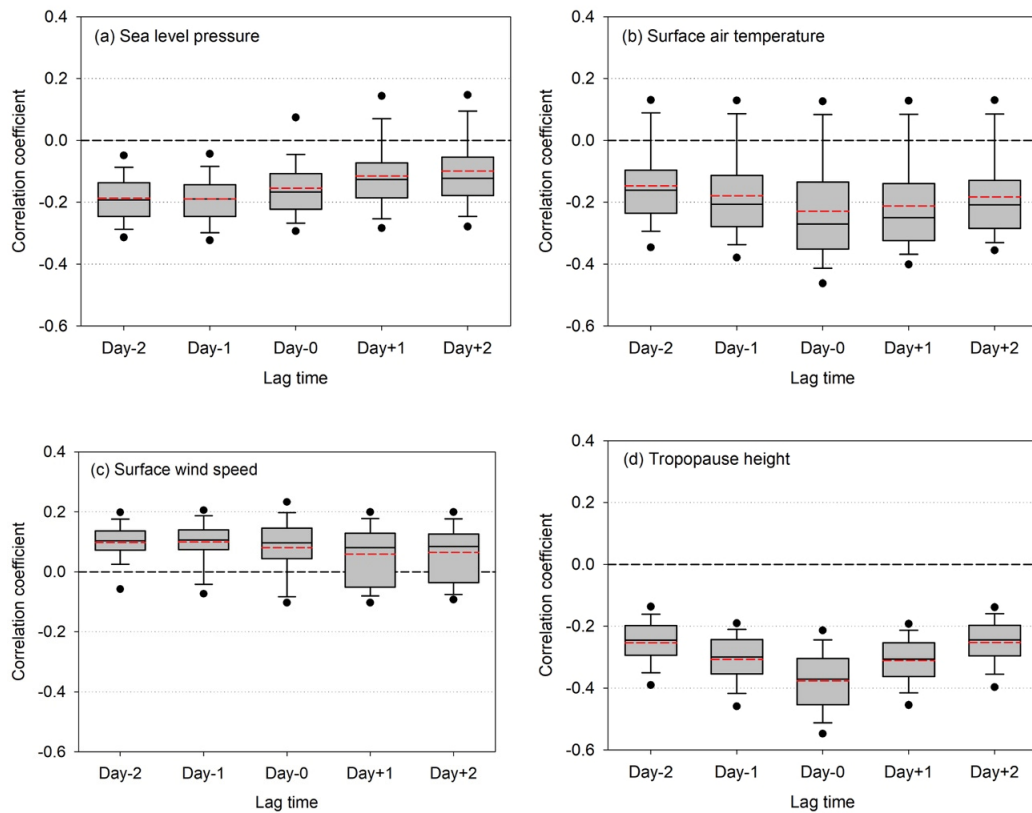


**Figure 4.21.** Box and whisker plots of the time-lagged correlation between the total BrO VCD and each meteorological parameter (a) sea level pressure, (b) surface air temperature, (c) wind speed at 10 m, and (d) tropopause height in the Arctic sea ice region. Time-lagged correlation coefficients performed in all reference grid cells with different time-lags (-2, -1, 0, +1, and +2 days) are summarized. The 5th, 10th, 25th, 50th (median), 75th, 90th and 95th percentiles of correlation coefficients are represented by the bottom filled circle, the lower whisker, horizontal lines of the box, the upper whisker, and the upper filled circle, respectively, and the mean value is shown as a red dashed line.

## 4. BrO enhancements in polar sea ice regions

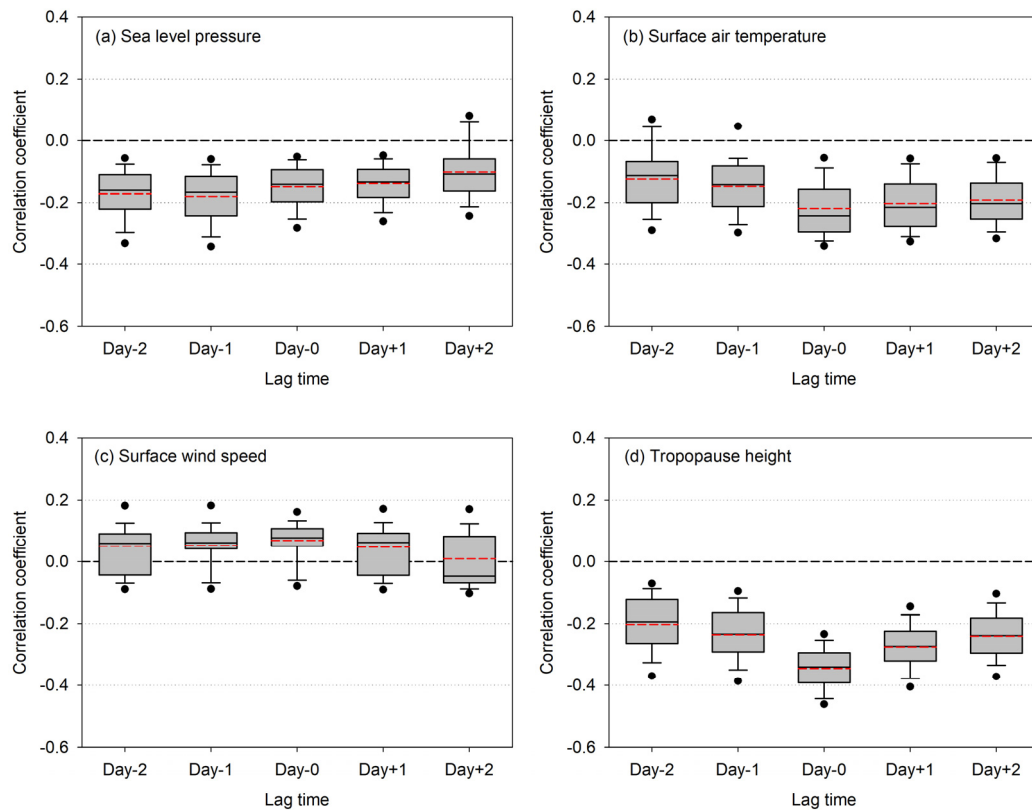


**Figure 4.22.** As Fig. 4.21, but for the Antarctic sea ice region.

## 4.4 Summary and conclusions<sup>†††</sup>

Bromine monoxide is located in both the stratosphere and the troposphere and large-scale BrO column enhancement is frequently observed in the Arctic and Antarctic sea ice region during polar springtime by satellites. In this study, 10 years of GOME-2 total BrO columns and various meteorological parameters were analysed to establish statistical connections between where the enhanced BrO columns mainly appear and the underlying meteorological conditions. The occurrence of enhanced total BrO columns showed regional characteristics. Relatively high occurrence frequencies are detected over the north Canadian coast, the Hudson Bay and the east Siberian Sea in the Arctic, while in the Antarctic,

<sup>†††</sup> This section was similarly published in *Seo et al. (2020)*.

#### 4. BrO enhancements in polar sea ice regions

enhanced BrO columns are often observed across the Weddell and Ross Sea, especially in September. The occurrence frequency of enhanced total BrO columns showed more spatial variation in the Arctic, whereas it varied more temporally in the Antarctic region.

Several meteorological parameters such as sea level pressure, surface level air temperature, wind speed and direction, and tropopause height were investigated to assess any significant relationships with the occurrence of enhanced total BrO columns. If the mean meteorological conditions are compared with those during enhanced BrO events, the latter are associated with low pressure systems, cold air temperature, high surface wind speed and a decrease of tropopause height in both the Arctic and Antarctic sea ice region. Low pressure systems can drive vertical uplifting and high wind speeds, lifting considerable amounts of saline snow or aerosols acting as a source of reactive bromine in the troposphere. In the case of temperature, surface air temperature is clearly lower during high BrO events in most of both polar regions, but it is slightly higher over the central Arctic and the Antarctic coastal region. The slight positive temperature anomalies in the central Arctic region during BrO events may be influenced by transport of BrO rich air with the southern wind blowing from the sea ice margins where temperatures are relatively higher. Surface wind speed is generally higher during BrO column enhancements, and in particular, high surface wind speed above 12 m/s which can drive blowing snow events is found over the eastern coast of Greenland, Bering Strait, the central Arctic and the Antarctic sea ice margins. Regional characteristics, comprising the prevailing wind direction and the wind speed during the BrO enhancement, were also identified. The occurrence of enhanced total BrO columns is closely associated with winds from the northwest, west and north in the Arctic sea ice region, whereas the dominant wind direction in the Antarctic during BrO enhancements is from the southwest and south. As characteristics of the spatial distribution of the dominant winds associated with BrO enhancements, northwestern winds are frequently observed at the north coast of Canada and over the Hudson Bay, and northerly winds over the east coast of Greenland and the Bering Strait during Arctic spring. For the Antarctic sea ice region, prevailing southwestern winds are mainly found during high BrO periods, especially in the marginal ice zones with relative frequencies larger than 50 %. Tropopause heights are significantly lower during enhancements of total BrO columns in both the Arctic and Antarctic region in agreement with earlier studies. The effect of increased stratospheric contributions due to sinking of BrO enriched air as the

## 4. BrO enhancements in polar sea ice regions

tropopause descends leads to the enhancement of total BrO columns.

In this chapter, spearman rank correlation analysis between total BrO vertical column density and meteorological factors was also performed to assess the relevance of these factors for total BrO column enhancements. Total BrO vertical column density has the strongest negative correlation with tropopause height in both the Arctic and Antarctic regions, reflecting both the importance of contributions in the stratospheric BrO column for the total BrO column and of the link between low tropopause height and tropospheric conditions required for bromine explosions. The next most statistically significant factor is surface air temperature. One remarkable point is that the temperature is negatively correlated with total BrO column in most sea ice regions, but has a positive correlation over the central Arctic, which is the same as the result of the temperature anomaly pattern discussed above. The opposite correlation pattern in the central Arctic where surface air temperature is low might be due to the transport of enhanced BrO plumes from relatively low latitude sea ice regions and low surface temperatures enough to form frost flowers that act as a source of bromine explosion. Sea level pressure and surface level wind speed are negatively and positively correlated with the total BrO vertical column density, respectively, but their correlation coefficients are low and the strengths of the relationships are weak.

This study has focused on a statistical analysis of a large set of GOME-2 BrO total columns to derive spatial and temporal patterns of links between meteorological conditions and the occurrence of enhanced BrO columns. The results show systematic connections between all of the parameters studied and BrO enhancements. However, such links do not necessarily constitute a cause and effect relationship, in particular as quantities such as surface pressure, wind speed, temperature and tropopause height are closely linked to each other. Another important aspect not covered by the approach of this study is the transport of air masses with enhanced BrO levels away from the region of initial bromine activation – in such cases, the correlation between meteorological parameters such as high wind speed and elevated BrO is not linked to the initial bromine release mechanism. In future studies, other parameters such as sea ice type, snow cover or the presence of polynyas should also be included and ideally an optimal stratospheric correction applied to the BrO columns to better focus on tropospheric bromine explosions.

# 5

## **Tropospheric BrO retrievals from MAX-DOAS measurements**

### 5.1 Introduction

Space-borne satellite instruments can observe spatial distributions of BrO plumes and bromine explosion events on the global scale (Salawitch et al., 2010; Theys et al., 2011), whereas ground-based instruments can provide good temporal coverage and some vertical profile information (Frieß et al., 2011; Peterson et al., 2015). In case of nadir-viewing UV-visible spectrometers, they have limited vertical resolution, which makes it difficult to separate BrO columns into tropospheric and stratospheric partial columns. The separation of satellite-based BrO vertical column densities between the stratosphere and troposphere has been performed using many different methods, for example as described in Salawitch et al. (2010), Theys et al. (2011), Sihler et al. (2012), Hörmann et al. (2013) and others. In this study, three different methods for the stratospheric correction were tested (see Section 3.5) and tropospheric AMFs taking into account various viewing conditions were applied in the tropospheric BrO vertical column retrievals (see Section 3.6).

The algorithm for satellite tropospheric BrO vertical column retrievals needs to be verified by comparing its product with reference data obtained independently and of known quality to quantify the uncertainty. Ground-based measurements of scattered light by the MAX-DOAS (multi-axis differential optical absorption spectroscopy) technique (Platt, 1994; Hönninger et al., 2004; Wittrock et al., 2004), using a range of viewing angles from nearly horizontal through zenith, are sensitive to the tropospheric column of trace gases. Therefore, MAX-DOAS measurements can be used effectively to validate the satellite tropospheric BrO columns and evaluate the satellite tropospheric retrieval algorithm.

In this chapter, the retrieval of tropospheric BrO VCDs from MAX-DOAS

## 5. Tropospheric BrO retrievals from MAX-DOAS measurements

measurements at the NDACC station in Ny-Ålesund is performed, and the results are compared with the tropospheric BrO VCDs derived from the satellite measurements. In addition to the validation of satellite-based BrO products using MAX-DOAS measurements, the relationship between tropospheric BrO VCDs and various meteorological parameters is investigated, focusing on enhanced BrO events over Ny-Ålesund. In particular, to determine sources of tropospheric bromine explosion events and the driving meteorological conditions over the study area, multiple datasets including ground-based, satellite measurements and meteorological model data are used.

### 5.2 Measurement site and instrument

#### 5.2.1 Measurement site

Ny-Ålesund is a small settlement on the northwestern part of Spitsbergen, which is the largest of the Svalbard islands. The geographic location of the measurement site (78°55'30"N, 11°55'20"E) is shown in the map of Fig. 5.1. A primary site within the Network for the Detection of Atmospheric Composition Change (NDACC) has been established in 1992 in Ny-Ålesund. This research base has polar night from October to February, and rapidly changing solar zenith angles during the rest of period. The site has focused on observations of stratospheric and tropospheric constituents such as ozone, aerosols and trace gases using ozone sondes, lidars (e.g. multi wavelength lidars for stratospheric ozone and aerosol measurements, the Raman lidar for aerosol and water vapor measurements), microwave radiometer, and UV-vis spectrometers. In particular, the DOAS instrument which is able to detect O<sub>3</sub>, NO<sub>2</sub>, BrO, OClO, and IO was set up for the study of polar tropospheric halogen chemistry at the NDACC station in Ny-Ålesund. Ground-based zenith-sky measurements are operated since 1995, and the automated MAX-DOAS system has been continuously in operation since April 1998 at this station (Wittrock et al., 2004). The MAX-DOAS instrument used for BrO retrievals in this study will be described in Section 5.2.2.

Ny-Ålesund has a tundra climate, which means that even in the summer, the temperatures are very low. The average annual temperature in Ny-Ålesund is -5.2 °C with the highest monthly mean temperature of 4.4 °C in July and the lowest of -12.7 °C in March. Precipitation here is about 375 mm per year and the

## 5. Tropospheric BrO retrievals from MAX-DOAS measurements

lowest (highest) amount of precipitation occurs in May (September) (Météo Climat stats for Ny Alesund, <http://meteo-climat-bzh.dyndns.org/>).

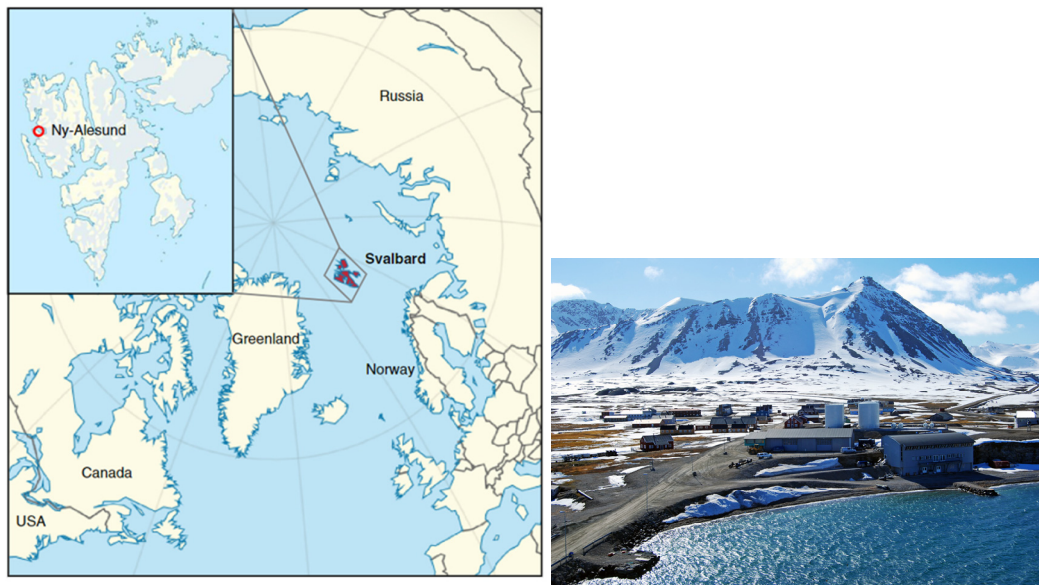


**Figure 5.1.** Map showing the location of Ny-Ålesund, Svalbard in the Arctic (left) and a landscape photo around Ny-Ålesund during summer (right). (image credit: <https://www.flickr.com/photos/10299779@N03/10178417953>)

### 5.2.2 Instrument

A ground-based MAX-DOAS instrument was deployed at the NDACC-station in Ny-Ålesund, Svalbard as part of the BREDOM (Bremian DOAS network for atmospheric measurements) network operated by the University of Bremen (Wittrock et al., 2004). A MAX-DOAS instrument typically consists of a telescope connected to a spectrograph by a fibre bundle. The basic principle of the instrument is that scattered sunlight collected in different directions by the telescope is transmitted to a spectrograph using a quartz fibre bundle and then analyzed. The telescope unit in Ny-Ålesund was updated to the new system in winter 2010. A schematic of the telescope is illustrated in Figure 5.2 (Peters, 2013). The light is entering the telescope through an entrance window (A) that is made of quartz glass. A lens (B) limiting the field of view focusses the light on the optical fibre mount (C). When the Pantilt-head points the telescope towards the ground, a

## 5. Tropospheric BrO retrievals from MAX-DOAS measurements

gravity-driven shutter (D) fixed on a hinge closes the optical path and allows dark measurements. This shutter is covered with a white PTFE plane. If the instrument is pointing down and subsequently the shutter is closed, this white area can be illuminated by a HgCd line lamp (E) allowing calibration measurements. In this new MAX-DOAS system, a video camera (F) is additionally installed for viewing condition surveillance or identification of events.

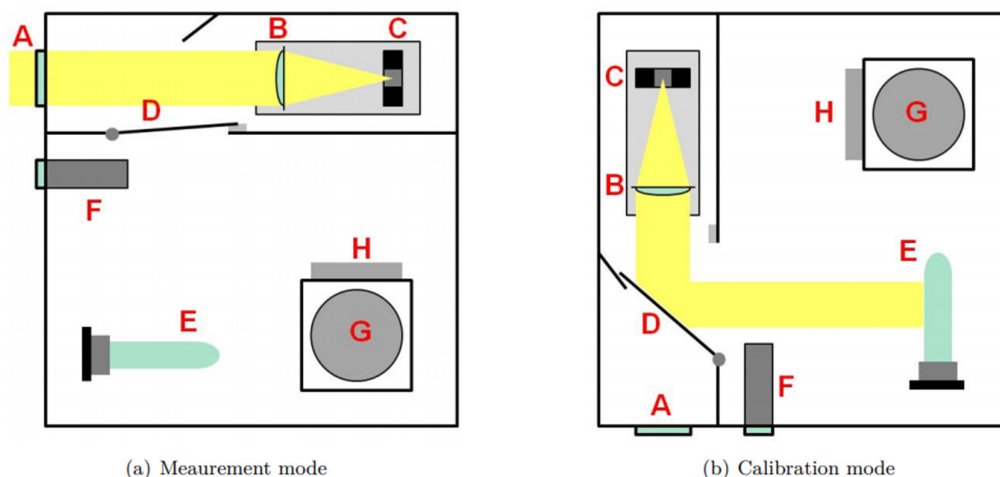


**Figure 5.2.** Illustration of the MAX-DOAS instrument installed at the NDACC station in Ny-Ålesund. The scheme on the left shows the situation for the normal measurement mode (gravitydriven shutter is not blocking the sunlight), while the photo on the right is calibration mode (gravity-driven shutter is blocking the sunlight). (Peters, 2013).



**Figure 5.3.** Photos of the MAX-DOAS instrument installed at the NDACC station in Ny-Ålesund (image credit: photos taken by André Seyler)

## 5. Tropospheric BrO retrievals from MAX-DOAS measurements

### 5.3 MAX-DOAS tropospheric BrO retrieval

From the spectra recorded by the ground-based MAX-DOAS instrument, different trace gases with suitable absorption band structures can be retrieved by applying the DOAS technique. The choice of reference spectrum is important for the detection of trace gases. In this study, MAX-DOAS spectra were analyzed using the 90° elevation angle measurement within a scan sequence as the reference spectrum to minimize the stratospheric signal in the tropospheric BrO retrieval. DOAS retrieval settings for BrO slant column retrievals from MAX-DOAS measurements are listed in Table 5.1. Examples of BrO and O<sub>3</sub> fits applying the DOAS setting are shown in Figure 5.4.

**Table 5.1.** DOAS BrO fit settings used for MAX-DOAS measurements.

Parameter	Description
Fitting window	345 – 359 nm
Absorption cross sections	BrO (228 K), O <sub>3</sub> (223 K, 243 K), NO <sub>2</sub> (220 K), O <sub>4</sub> (293 K), Ring spectrum
Background spectrum	Zenith sky spectrum
Polynomial	5 <sup>th</sup> order

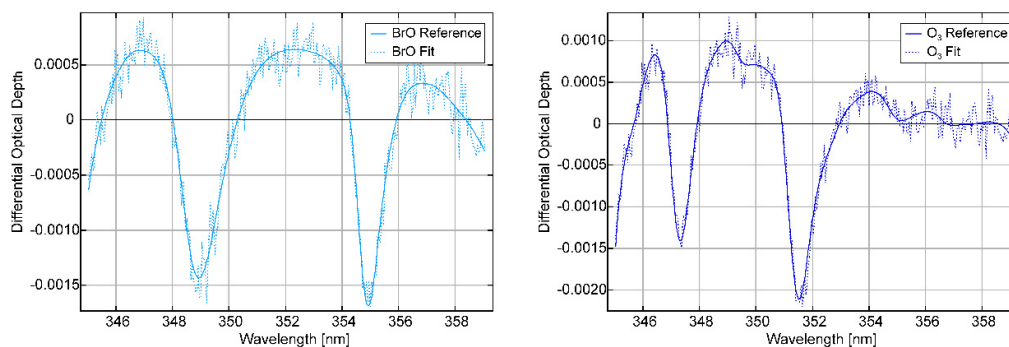


**Figure 5.4.** Example of BrO (left) and O<sub>3</sub> (right) fit result applying the DOAS setting of Table 5.1 for MAX-DOAS measurements at elevation angle of 6° on 17 April 2014. The dashed line indicates fit results including the fitting residual, whereas the solid line is the reference spectrum scaled to the fit result.

## 5. Tropospheric BrO retrievals from MAX-DOAS measurements

Movements of the sun relative to the telescope during the day can be described by the solar zenith angle and the relative azimuth angle which is the angle between the direction of the telescope and the direction of the sun. The elevation angle indicates the angle between the tangential plane of the earth's surface and the pointing direction of the telescope. In this study, among the multiple viewing directions, MAX-DOAS measurements at viewing azimuth angle of 328° (northwest) is used to detect transport of BrO plumes from the interior of the Arctic sea ice regions. A measurement cycle consists of scattered sunlight observations at elevation angle of 0°, 1°, 2°, 3°, 4°, 5°, 6°, 8°, 10°, 15°, 30° and 90°. A full measurement sequence at this viewing azimuth angle takes about ~15 minutes.

The primary quantity of MAX-DOAS measurements is the differential slant column density (dSCD), the difference between integrated concentrations along the light path of a measurement with a specific elevation angle and a reference typically from the zenith. Since the dSCD depends on the light path, this should be converted into vertical column density or volume mixing ratios. The easiest approach is a geometric approximation introduced by Hönninger and Platt (2002), although it does not account for scattering from aerosols. The aerosol effects in the light path through the lower atmospheric layer can be considered by using simulations from radiative transfer models. Here, for simplicity, the geometric approximation is used to convert the measured dSCDs into tropospheric VCDs as follows:

$$\text{VCD}_{\text{geo}} = \frac{\text{dSCD}_{\alpha}}{\text{dAMF}_{\alpha}} = \frac{\text{dSCD}_{\alpha}}{\frac{1}{\sin \alpha} - 1} \quad (\text{E } 5.1)$$

The differential AMF (dAMF), the difference of AMF between the off-axis direction ( $\alpha \neq 90^\circ$ ) and the zenith ( $\alpha = 90^\circ$ ), can be approximated as  $1/\sin(\alpha)$  and 1 ( $1/\sin 90^\circ$ ) respectively. The elevation angle of 15° was selected for the determination of tropospheric BrO VCDs as it combines good sensitivity to the boundary layer and reasonable accuracy of the geometric approximation.

Fig. 5.5a shows time series of BrO differential slant columns (dSCDs) retrieved from the MAX-DOAS measurements in Ny-Ålesund with different elevation angles of 0°, 15° and 30° for spring 2014. In general, smaller elevation angles lead to longer light paths through the lowest atmospheric layer and strong absorption signals near the instrument altitude (surface level). The diurnal variation of BrO dSCDs generally shows a typical U-shape for the change of AMF in the stratosphere.

## 5. Tropospheric BrO retrievals from MAX-DOAS measurements

In the BrO dSCDs time series, several BrO explosion events within the boundary layer can be identified in the period from April 17 to 20 and April 27 to May 1 as low elevation angle data points deviating from the general pattern which tracks the SZA change. In particular, the BrO SCDs which are not close to 0 around noon indicate that BrO explosion events or transport of enhanced BrO plumes from the Arctic sea ice region to the MAX-DOAS viewing direction have occurred. Also, if the BrO dSCDs retrieved at different elevation angles of  $0^\circ$  and  $30^\circ$  are largely separated, enhanced BrO plumes are located close to the surface level. In the same way, small separations between  $0^\circ$  and  $30^\circ$  mean that BrO is in the upper troposphere or stratosphere, not close to the boundary layer. These enhanced BrO events in the boundary layer can be clearly identified from Fig. 5.5b. Fig. 5.5b shows time series of the corresponding geometrical BrO VCDs at elevation angle of  $15^\circ$  for the same study period. Periods of high tropospheric BrO VCDs (Fig. 5.5b) coincide with those of large separation in dSCDs between  $0^\circ$  and  $30^\circ$  (Fig. 5.5a).

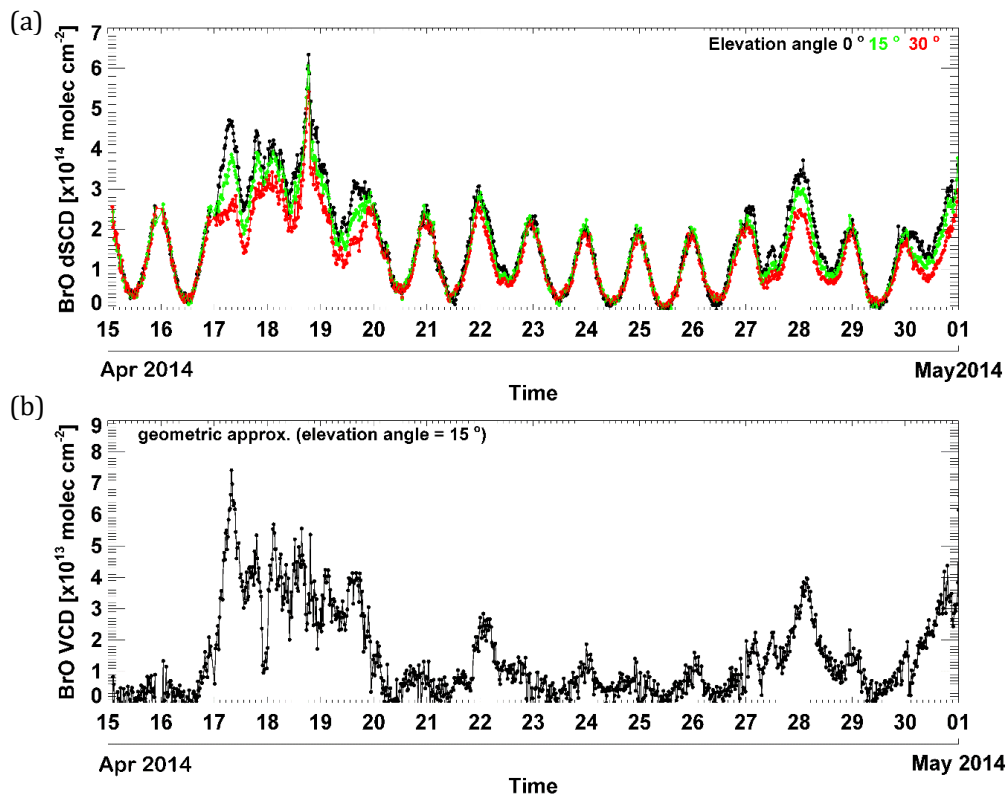


**Figure 5.5** (a) MAX-DOAS BrO dSCDs at different elevation viewing angles indicated in the legend and (b) BrO VCDs using the geometrical approximation at  $15^\circ$  elevation angle in Ny-Ålesund from 15 to 30 April 2014.

## 5. Tropospheric BrO retrievals from MAX-DOAS measurements

### 5.4 Comparison of MAX-DOAS and satellite BrO vertical columns

Tropospheric BrO VCDs from GOME-2B measurements were compared to ground-based MAX-DOAS BrO measured at the NDACC station in Ny-Ålesund. From MAX-DOAS measurements, BrO VCDs were computed using the geometrical approximation at the elevation angle of 15°. The dataset was collected between 15 April and 25 May 2014. To assure spatial and temporal consistency of ground-based and satellite measurements, coincident measurements should be selected. In this comparison, an average of GOME-2B tropospheric BrO VCDs located within 80 km of the MAX-DOAS instrument was used. Figure 5.6 shows the time series of both MAX-DOAS and GOME-2B tropospheric BrO VCDs. Here, the evaluation of the stratospheric correction method was also performed by comparing the tropospheric BrO vertical columns calculated using three different stratospheric correction methods (see Section 3.5) with MAX-DOAS BrO measurements. As shown in Fig. 5.6, both measurements show generally good agreement in the temporal variability.

Scatter plots in Fig. 5.7 also quantify comparisons between GOME-2B and MAX-DOAS BrO. The data used in the time series were used for the scatter plot, and as before, the satellite tropospheric BrO vertical columns were compared using the three different stratospheric correction methods. They show generally good agreement with correlation coefficients of 0.7-0.78 and slopes of 0.57-0.64. Overall, there is a good agreement between the ground-based MAX-DOAS and satellite measurements. For background concentration of tropospheric BrO, GOME-2B tropospheric BrO retrievals show higher values than MAX-DOAS tropospheric BrO, whereas satellite tropospheric BrO vertical columns tend to show lower values than MAX-DOAS measurements during tropospheric BrO explosion events, which results in slopes less than 1.

This difference between MAX-DOAS and satellite BrO retrievals can be explained by the following considerations. First, different AMF calculation methods between the MAX-DOAS and satellite measurements may affect the difference in tropospheric BrO vertical column retrievals. In this study, the box shaped BrO profile (homogeneously distributed within a boundary layer) was considered in the satellite tropospheric AMF calculation, while the tropospheric BrO retrieval from MAX-DOAS measurements used the geometric AMF which cannot account for

## 5. Tropospheric BrO retrievals from MAX-DOAS measurements

the vertical distribution of BrO. As revealed in many studies of previous AMF sensitivity tests, uncertainties in AMF calculations caused by different assumptions and choices made to represent the state of the atmosphere has large impacts on BrO retrievals. Next, since the satellite BrO VCD is the average of values whose footprints are located within a certain distance around the station (here, the satellite average value within 80 km from the station), the satellite BrO value may differ from the ground-based BrO measurement in cases of small-scale local tropospheric bromine explosion events or long-range transport of enhanced BrO plumes. Also, if there are enhanced BrO plumes in a direction different from the viewing direction of the MAX-DOAS instrument, the difference between MAX-DOAS and satellite BrO retrievals may increase.

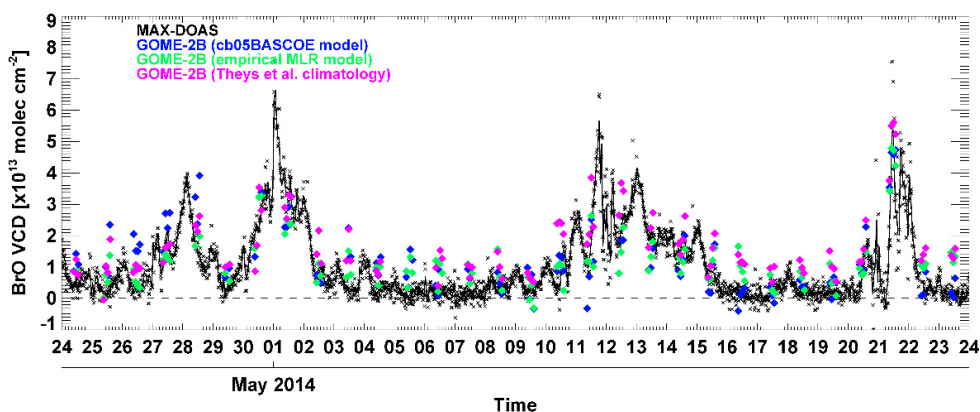


**Figure 5.6.** Time series of tropospheric BrO VCDs over Ny-Ålesund retrieved from MAX-DOAS measurements and GOME-2B satellite measurements. The black dots denote the tropospheric VCD from the MAX-DOAS measurements and the black line is the hourly mean of the BrO VCD from the MAX-DOAS measurements. Diamond symbols with different colors indicate the GOME-2B tropospheric VCDs computed applying three different stratospheric correction methods (blue: 3D-CTM cb05-BASCOE model data, green: empirical multiple linear regression model, and magenta: climatological approach based on Theys et al. (2011) described in Section 3.5).

## 5. Tropospheric BrO retrievals from MAX-DOAS measurements

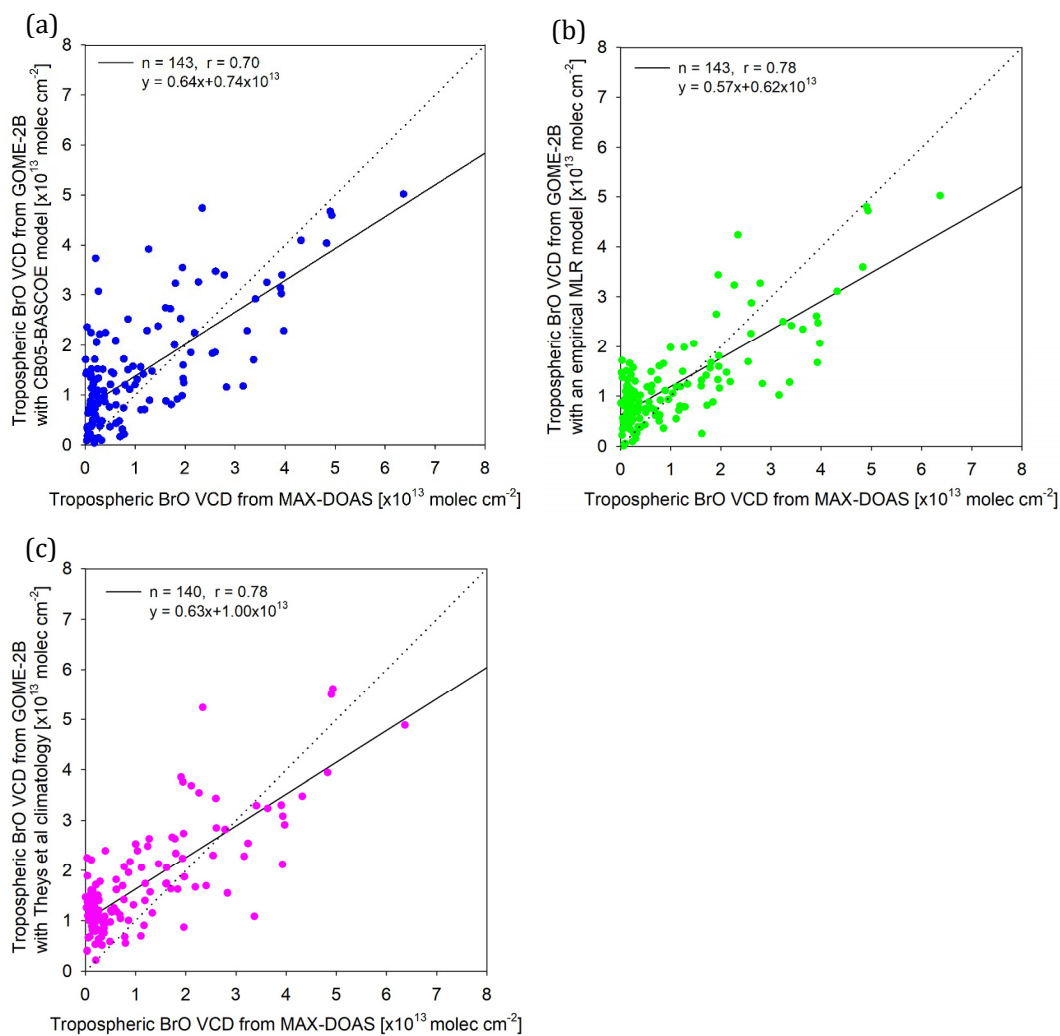


**Figure 5.7.** Scatter plots of MAX-DOAS tropospheric BrO vertical columns versus GOME-2B tropospheric vertical columns applying three different stratospheric corrections using (a) the 3D-CTM cb05-BASCOE model data, (b) empirical multiple linear regression model, and (c) climatological approach based on Theys et al. (2011) described in section 3.5.

## 5. Tropospheric BrO retrievals from MAX-DOAS measurements

### 5.5 Case studies for tropospheric BrO explosion events

Ground-based MAX-DOAS measurements show the temporal variation of BrO in Ny-Ålesund with high temporal resolution, while they cannot provide spatial distributions of BrO. Time series of tropospheric BrO vertical columns measured from the MAX-DOAS instrument and various meteorological parameters for air temperature at 2 m, wind speed and direction at 10 m observed from a meteorological tower near the station in Ny-Ålesund are shown in Fig. 5.8. Here, the tropospheric BrO VCD is calculated using the geometrical approximation at 15° elevation angle. The figure clearly shows that there is a relationship between increases of tropospheric BrO and meteorological parameters. When the tropospheric BrO column increases rapidly during the period from 17 to 19 April 2014, the surface level air temperature also steeply decreases from -2 °C to -15 °C and then rises again after the event. In addition, the northwest winds constantly blow into the base during the three days of rapid increases in tropospheric BrO. Surface level winds show a wide range of wind speed during the event with wind speeds up to 15 m/s on 17 and 19 April, and relatively low wind speeds of 2-5 m/s on 18 April 2014.

The relationship between the BrO concentration and various meteorological parameters was statistically analyzed using a longer time series of ground-based observations in Ny-Ålesund during spring in 2014 (period from 15 April 2014 to 25 May 2014). Figure 5.9 presents box and whisker plots showing the distribution of meteorological parameter values for the BrO groups classified by vertical columns values. The BrO plots show 5<sup>th</sup>, 10<sup>th</sup>, 25<sup>th</sup>, median and mean, 75<sup>th</sup>, 90<sup>th</sup>, and 95<sup>th</sup> percentile distributions of these variables as a function of MAX-DOAS tropospheric BrO VCD for each  $2 \times 10^{13}$  molec cm<sup>-2</sup> step. For the last BrO group with an interval of  $8-10 \times 10^{13}$  molec cm<sup>-2</sup>, 5<sup>th</sup> and 95<sup>th</sup> were not calculated because of small number of data points. Overall, high tropospheric BrO vertical columns in Ny-Ålesund are statistically related with low atmospheric pressure, low air temperature at 2 m and high wind speed at 10 m as identified in Fig. 5.9. For sea level pressure and wind speed, the variables show a wide range of distributions, which means that there are uncertainties in the statistical relationship with tropospheric BrO columns. In the case of surface level air temperature, there is a clear difference of more than 6 °C in the temperature distribution between the background level of  $0-2 \times 10^{13}$  molec cm<sup>-2</sup> and BrO concentrations above the background level. The relationship between BrO concentration and low

## 5. Tropospheric BrO retrievals from MAX-DOAS measurements

temperature supports previous studies on the temperature effects in the formation of frost flowers and the chemical reaction of the reactive bromine. The freezing of seawater generally occurs at low temperatures less than  $-10\text{ }^{\circ}\text{C}$  and is likely to cause brine to be pushed to the surface of newly forming sea ice including frost flowers. Sander et al. (2006) demonstrated that the accelerated release of bromine on cold saline surface could be derived by precipitation of carbonates at a temperature below 263 K leading to reduced buffering capacity of the alkaline sea water and facilitating its acidification. This highly saline surface can lead to halogen activation and subsequently bromine explosion events. Thus, the BrO enhancement in Ny-Ålesund is associated with the generation of reactive BrO sources due to temperature drop in the surrounding sea ice region. The detection of low air temperature during high tropospheric BrO occurrences may be attributed not only by the regional temperature drop around the study area, but also by the transport of enhanced BrO columns developed over the central Arctic where is a much colder region.

Surface wind directions were also investigated to see how they may affect tropospheric BrO VCDs. Figure 5.10 is a wind rose diagram showing the average tropospheric BrO VCD according to the wind direction with 45 degree bins. As shown in Fig. 5.10, the average BrO VCD ranges from  $2.5$  to  $2.8 \times 10^{13}$  molec  $\text{cm}^{-2}$  for north, northwest and northeast winds, while the average BrO ranges from  $1$  to  $1.5 \times 10^{13}$  molec  $\text{cm}^{-2}$  for other wind directions. This means that BrO enhancements in Ny-Ålesund are mainly linked to the northward winds. The north winds blowing from the interior of the Arctic are likely to be cold and contain more reactive bromine sources such as saline snow, sea salt aerosols and frost flowers which can lead to tropospheric bromine explosion events rather than winds blowing from the other directions. Also, high BrO observations in Ny-Ålesund may include plumes of enhanced BrO originating from the Arctic sea ice region and transported over the study area through the north wind.

## 5. Tropospheric BrO retrievals from MAX-DOAS measurements

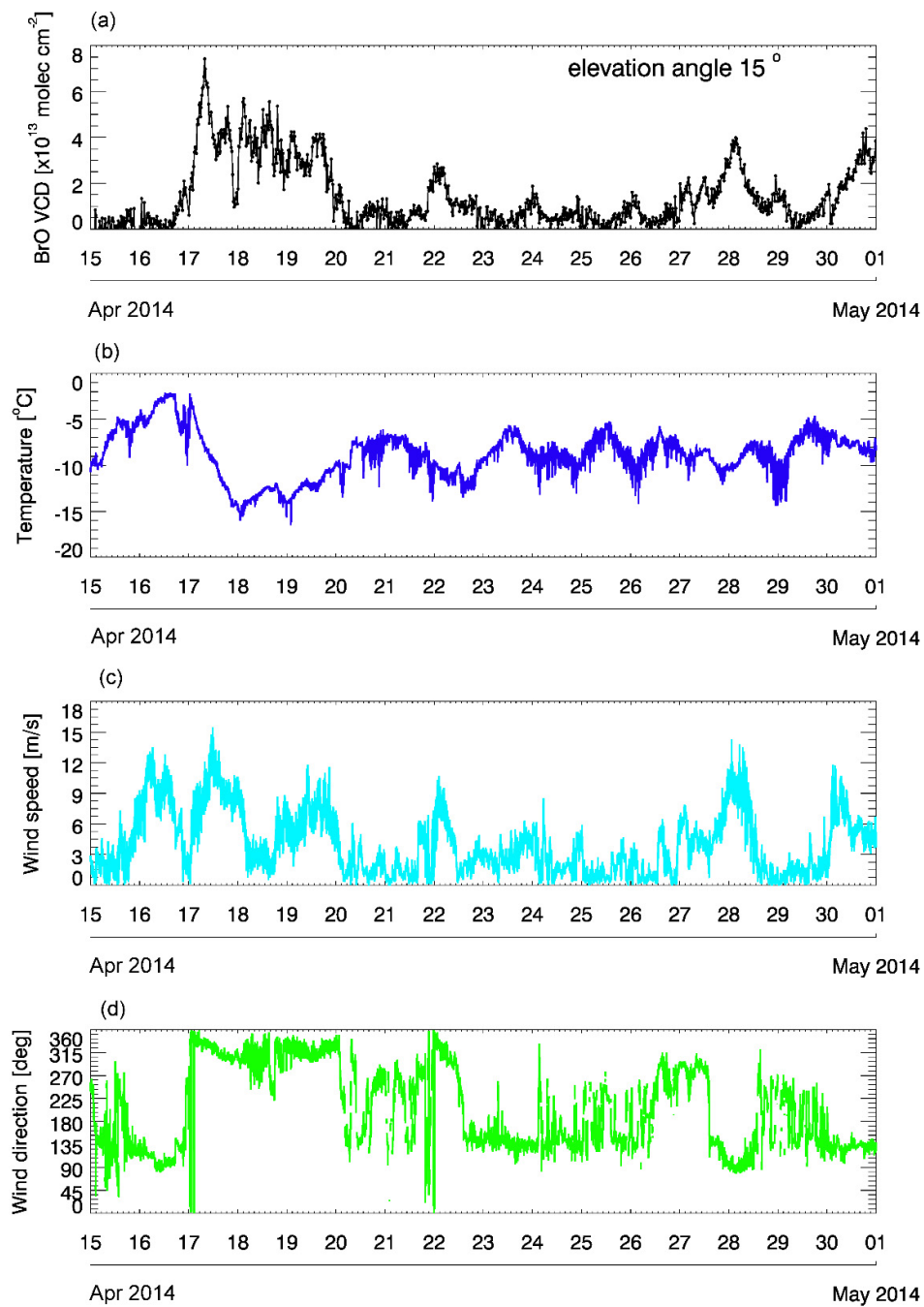


**Figure 5.8.** Time series of (a) tropospheric BrO VCDs retrieved from MAX-DOAS measurements, (b) air temperature at 2 m, (c) surface wind speed and (d) direction at 10 m above the ground at the NDACC station in Ny-Ålesund from 15 to 30 April 2014.

## 5. Tropospheric BrO retrievals from MAX-DOAS measurements

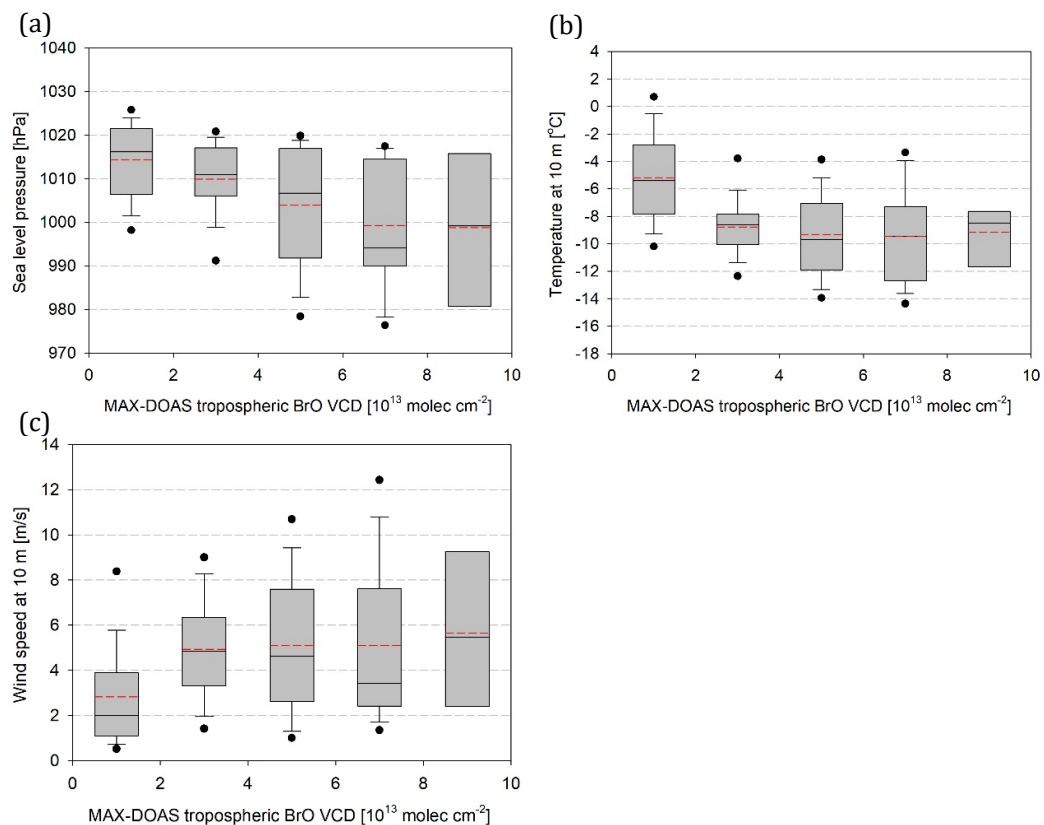


**Figure 5.9.** Box and whisker plots showing 5<sup>th</sup>, 10<sup>th</sup>, 25<sup>th</sup>, median, 75<sup>th</sup>, 90<sup>th</sup>, and 95<sup>th</sup> percentiles and mean (red dashed line) for (a) sea level pressure, (b) air temperature at 2 m, and (c) wind speed at 10 m measured from the meteorological tower at the station during 15 April 2014 to 25 May 2014. Each as a function of MAX-DOAS tropospheric BrO vertical column with  $2 \times 10^{13}$  molec  $\text{cm}^{-2}$  step.

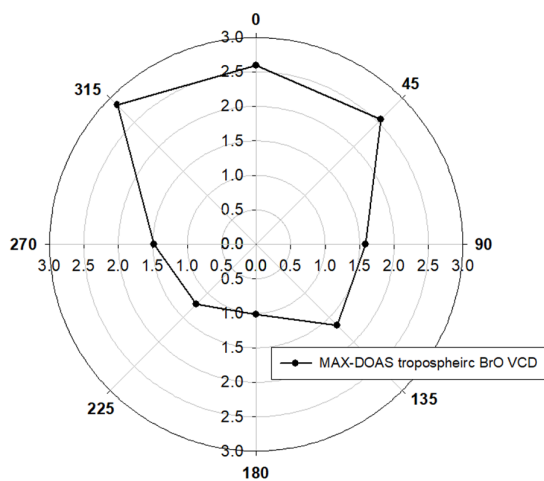


**Figure 5.10.** Wind rose diagram showing the average value of tropospheric BrO VCD measured by the MAX-DOAS instrument for each wind direction at 45 degree intervals.

## 5. Tropospheric BrO retrievals from MAX-DOAS measurements

As a case-study, an event that occurred near the Ny-Ålesund in spring will now be investigated using satellite observations and meteorological model data in terms of spatial distribution. Figure 5.11 shows maps of tropospheric BrO vertical columns retrieved from GOME-2B measurements, together with meteorological conditions including sea level pressure, surface wind speed and direction at 10 m, and air temperature at 2 m from the ECMWF reanalysis data corresponding to the GOME-2B observation times.

On 17 April 2014, plumes of enhanced tropospheric BrO are observed along the east coast of Greenland and over Svalbard. As shown in meteorological fields (see left panels in Fig. 5.11), a large-scale low pressure system is located over the Barents Sea with high wind speeds of over 16 m/s around the boundary of the low pressure region. Also, we can see that a relatively cold air mass is located on the western side of the low pressure system from the temperature map. This is due to the convergence at the surface caused by the dynamics of the low pressure system, which lead to cold air blowing from the Arctic sea ice along the west side of the cyclone with the north wind, whereas relatively warm air flows from the southern open sea along the east side of the low pressure system. On 18 April, the low pressure system located over Svalbard moves slightly further north-eastward and the relatively small-scale low pressure region located in the Greenland Sea moves northward. The change in atmospheric pressure system weakens the tropospheric BrO plumes derived by strong north winds blowing between Greenland and Svalbard. On 19 April, as the low pressure system located northeast of Svalbard extends southward, cold air masses descend to the north coast of Svalbard along the cyclonic air flow with high wind speeds. Enhanced tropospheric BrO plumes occurring over the north coast of Svalbard may be associated with this air stream caused by the meteorological conditions.

To investigate not only the regional distribution but also the vertical distribution, the CALIOP vertical feature mask was examined on the CALIPSO track passing over the BrO plumes. CALIPSO footprints corresponding to these observations are denoted by white and gray lines plotted on top of GOME-2B tropospheric BrO VCDs in Fig. 5.11. It should be noted that the maximum time difference between CALIOP and GOME-2 observations is about ~1.5 hours so that cloud and aerosol distributions may slightly differ in the actual vertical condition at GOME-2 observation time. As shown in Fig. 5.12, aerosol layers are generally located within about 2 km height around the location of enhanced BrO plumes. These aerosols detected at the BrO plume location may be produced during blowing snow events

## 5. Tropospheric BrO retrievals from MAX-DOAS measurements

by high wind speeds and vertical lifting associated with the low pressure system. This case study demonstrates that highly saline snow and sea salt aerosols generated by meteorological conditions act as reactive bromine sources and initiate a tropospheric bromine explosion event over Svalbard.

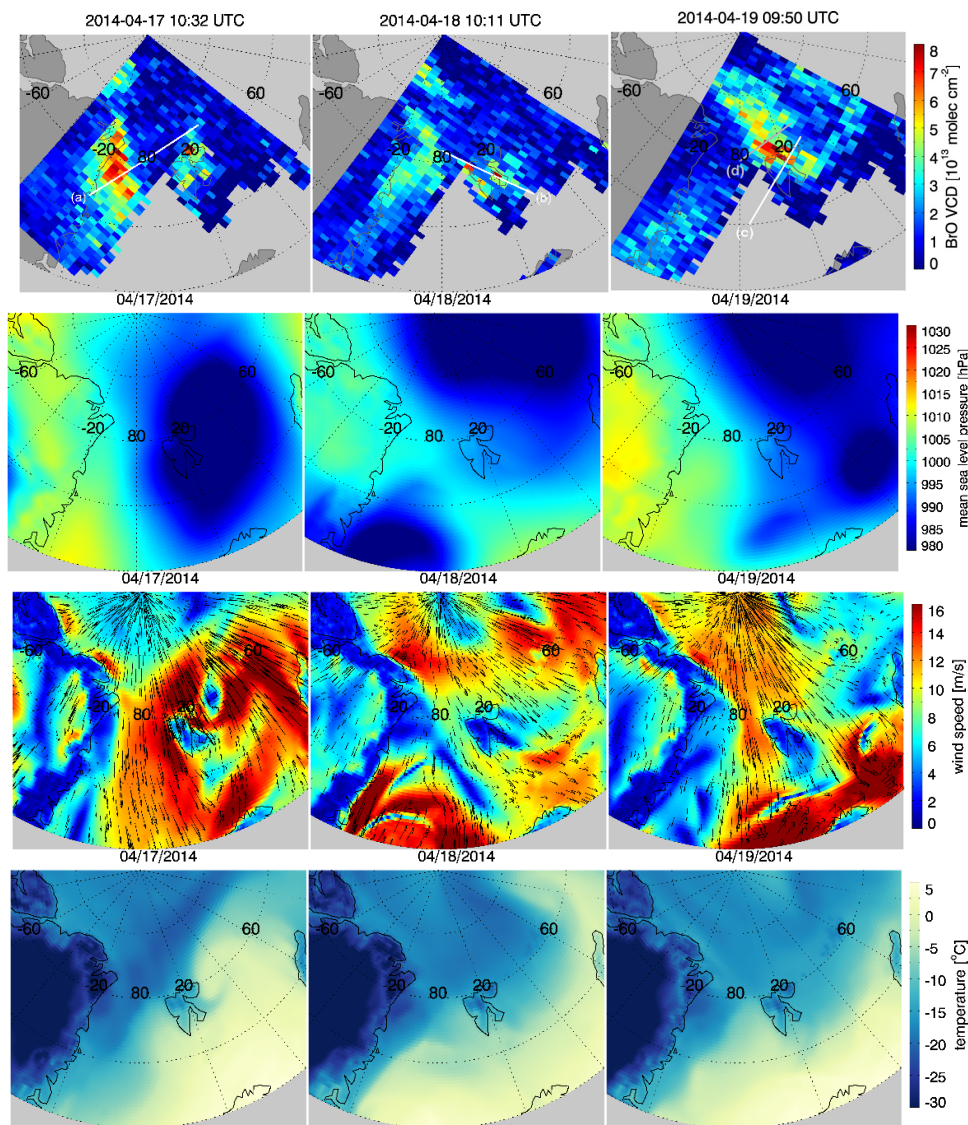


**Figure 5.11.** (a) GOME-2 tropospheric BrO VCDs [ $10^{13}$  molec  $\text{cm}^{-2}$ ] and various meteorological conditions for (b) sea level pressure [hPa], (c) surface level (10 m above the ground) wind speed [ $\text{m s}^{-1}$ ] and direction (denoted as black arrows), and (d) air temperature [ $^{\circ}\text{C}$ ] at 2 m for selected tropospheric BrO event days on 17 to 19 April 2014 (from left to right).

## 5. Tropospheric BrO retrievals from MAX-DOAS measurements

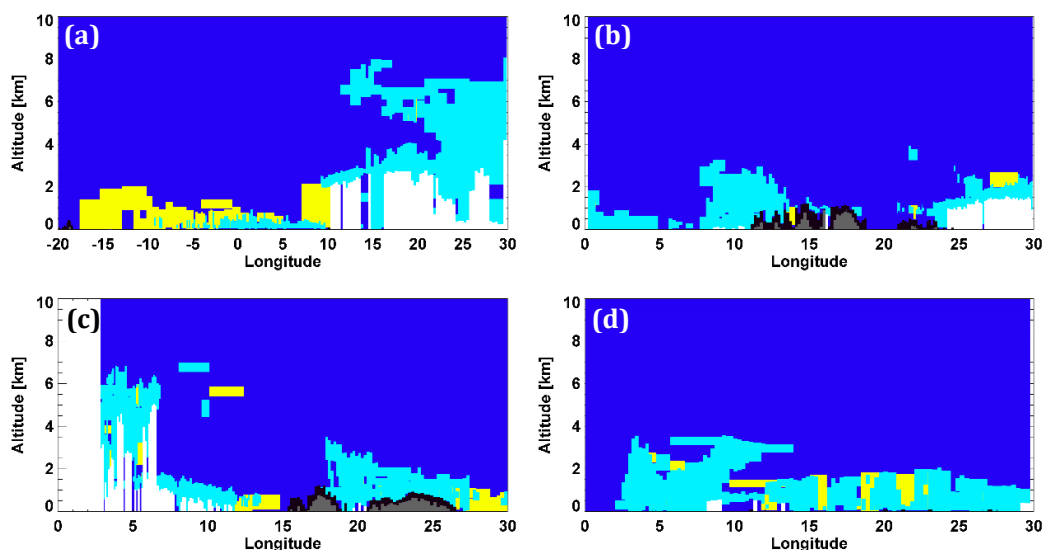


**Figure 5.12.** CALIOP vertical feature masks (blue: clear air, light blue: cloud, yellow: aerosol, white: invalid signal, black: surface, gray: subsurface) along the CALIPSO tracks marked in tropospheric BrO VCD maps (white and gray lines) in Fig. 5.11a. ([https://www-calipso.larc.nasa.gov/resources/calipso\\_users\\_guide/data\\_summaries/vfm/](https://www-calipso.larc.nasa.gov/resources/calipso_users_guide/data_summaries/vfm/))

## 5.6 Summary and conclusions

In this chapter, BrO vertical columns were retrieved from MAX-DOAS measurements at the NDACC station in Ny-Ålesund and compared with GOME-2 tropospheric BrO vertical columns to validate the satellite BrO retrieval algorithm. The tropospheric vertical column densities of BrO were retrieved based on the DOAS technique and using the geometric approximation. Ground-based MAX-DOAS measurements were able to observe the temporal variation of BrO in the troposphere at high temporal resolution as well as the vertical distribution of BrO at different elevation angles. Also, to assess the satellite retrieval algorithm developed in this study, a comparison between the ground-based MAX-DOAS and the coincident GOME-2 tropospheric BrO vertical columns at Ny-Ålesund was performed and results show good agreements in both time-series and scatterplots. This shows that the BrO fitting by the DOAS technique and the separation of stratospheric and tropospheric contributions from satellite observations yield reasonable results, at least over this validation station. However, satellite

## 5. Tropospheric BrO retrievals from MAX-DOAS measurements

tropospheric BrO showed higher values than MAX-DOAS tropospheric BrO in background conditions, whereas the satellite tropospheric BrO tends to be lower than the MAX-DOAS BrO during BrO explosion events. This may be due to a limitation that reflect BrO variations occurring locally from satellite measurements with relatively large spatial resolution, or due to errors caused by inaccuracies in the calculation of tropospheric AMF.

The relationship between tropospheric BrO and various meteorological parameters in Ny-Ålesund during springtime was analyzed using both ground-based and satellite measurements. The occurrences of bromine explosion events in this region were highly related to the decrease of surface air temperature and winds from northerly directions, bringing cold air from the Arctic sea ice to Ny-Ålesund. Correlation to wind speed showed a different pattern; high BrO VCD was found at both high wind speeds of 10-16 m/s and also at low wind speeds of 2-6 m/s. The former is associated with the transport of reactive bromine sources such as saline aerosols and blowing snow from the Arctic sea ice region with high wind speeds, and the latter is linked with trapping a transported bromine plume and triggering local bromine release from the snowpack within a stable boundary layer. Satellite GOME-2 data and meteorological model data showed that weather systems affect the occurrence and spatial distribution of enhanced tropospheric BrO plumes. In particular, surface wind speed and temperature distribution change as result of the spatial distribution of atmospheric pressure and affect the BrO vertical columns over the Ny-Ålesund region. From a case study in Ny-Ålesund, it was confirmed that the combination of satellite data for exploring large spatial distributions and ground-based measurements having high temporal resolution enables the analysis of bromine explosion mechanisms in more detail.

# 6

## Conclusions and outlook

### BrO retrievals from satellite measurements

In this thesis, an improved algorithm to retrieve tropospheric BrO columns from satellite nadir UV/visible radiance measurements has been developed. The main motivations were (1) to find the optimal DOAS BrO settings, (2) to develop and test a stratospheric correction, and (3) to compute tropospheric AMF for satellite nadir observations.

Sensitivity tests were performed to find an optimal wavelength range for satellite BrO retrievals under various measurement conditions. From these sensitivity tests, an optimal wavelength range for BrO retrievals was determined. The DOAS BrO retrieval was performed using background spectra taken over the Pacific reference region to account for possible across-track variability. A background correction of the retrieved slant columns is applied based on a model value for the BrO column over the Pacific region.

To separate the stratospheric and tropospheric BrO contributions in the total BrO column field, various stratospheric correction methods were tested: (1) 3D atmospheric chemistry model data, (2) an empirical multiple linear regression model, and (3) the BASCOE model climatology stratospheric BrO profile based on Theys et al. (2011). Tropospheric BrO columns were derived by the residual method by subtracting the estimated stratospheric BrO columns from total BrO columns and applying tropospheric AMFs ( $AMF_{\text{tropo}}$ ) to account for changes in measurement sensitivity in the tropospheric layer due to dependencies on viewing geometry, surface albedo, altitude, and BrO profile.

Intercomparison between results from multiple satellites including GOME-2, OMI, and TROPOMI showed good consistency and low scatter of the retrieved total BrO columns. The examples of individual TROPOMI overpasses show that due to the better signal-to-noise ratio and finer spatial resolution of  $3.5 \times 7 (3.5 \times 5.5) \text{ km}^2$ ,

## 6. Conclusions and outlook

TROPOMI BrO retrievals provide high data quality with low fitting errors and unique information on small-scale variabilities in various BrO source regions such as the Arctic sea ice, salt marshes, and volcanoes.

### **BrO enhancements and their relations to meteorological parameters in polar regions**

Enhancements of total BrO columns result from increases in stratospheric or tropospheric bromine amounts or both, and their occurrence may be related to local meteorological conditions. In this thesis, the spatial distribution of the occurrence of total BrO column enhancements and the associated changes in meteorological parameters were investigated in both the Arctic and Antarctic region using 10 years of GOME-2 measurements and meteorological model data. Statistical analysis of the data presented clear differences in the meteorological conditions between the mean field and enhanced total BrO cases in both polar sea ice regions with pronounced spatial patterns. In general, atmospheric low pressure, cold surface air temperature, high surface-level wind speed and low tropopause heights were found during periods of enhanced total BrO columns. In addition, specific spatial patterns of prevailing wind directions related to the BrO enhancements were identified in both the Arctic and Antarctic sea ice region. The relevance of the different meteorological parameters on the total BrO column was statistically evaluated based on the Spearman rank correlation analysis, finding that tropopause height and surface air temperature have the highest correlations with the total BrO vertical column density. The results demonstrate that while some satellite observed plumes of enhanced BrO can be explained by stratospheric descending air associated with low tropopause height, BrO hotspots can also be affected by tropospheric sources derived by changes in surface level meteorological factors such as air temperature and winds. In addition, the effect of a specific meteorological parameter can play a significant role in the enhancement of BrO in some regions, but in most cases, multiple meteorological parameters interact with each other in their influence on BrO columns. The cross-correlation analysis between relevant meteorological parameters during total BrO enhancements in polar regions demonstrated that the meteorological conditions are directly and indirectly related to each other, affecting the bromine chemistry.

### **Ground-based MAX-DOAS measurements and validation**

MAX-DOAS measurements at the NDACC station in Ny-Ålesund were successfully used to retrieve BrO in the troposphere. The general idea of MAX-DOAS is to record spectra of scattered sunlight at different elevation angles. Since the dSCD depends on the observation geometry and environmental conditions, it is usually converted to vertical column density using the air mass factor. In this study, the tropospheric BrO VCD was retrieved from the MAX-DOAS measurement at 15° elevation angle applying a simple geometrical approximation. The tropospheric BrO from MAX-DOAS measurements showed generally good agreement with the satellite tropospheric BrO vertical columns. This validation result of the satellite BrO retrieval algorithm from the ground-based MAX-DOAS observation demonstrates that the satellite BrO retrievals are suitable for application in the analysis of reactive bromine events in polar sea ice regions. The combination of ground-based MAX-DOAS measurements with high temporal resolution and satellite data with large spatial coverage allows detailed analysis of bromine explosion events in polar regions.

The relationship between the tropospheric BrO column observed in Ny-Ålesund and meteorological factors was also investigated. Bromine explosion events in Ny-Ålesund are strongly linked with specific meteorological conditions, mainly to low surface level air temperature and wind directions bringing cold air from the Arctic sea ice region to Ny-Ålesund. With respect to wind speeds, high tropospheric BrO columns were found at both high and low wind speeds. As found in previous studies, highly saline snow particles blowing from the sea ice region with strong surface level winds at speeds greater than 10 m/s can act as a source of bromine explosion mechanism and tropospheric BrO columns can be increased. Also, observations of high tropospheric BrO level air under high wind conditions may be taken as being transport-related. On the other hand, local bromine explosion events occur effectively during low wind speeds when the boundary layer is shallow and stable as a reaction chamber. Case study analyses have shown that both cases of wind speed can affect tropospheric bromine explosion events, indicating that further studies of tropospheric bromine explosion mechanisms associated with wind speed are still needed.

## 6. Conclusions and outlook

### Outlook

Through this thesis, it was confirmed that satellite observations with high spatial resolution and ground-based measurements with high temporal resolution are useful for studying bromine chemical reactions. However, total and tropospheric BrO column retrievals from remote sensing observations are based on several assumptions and the improvement of these assumptions provides possibilities to further reduce uncertainties in BrO retrievals. The following describes the parts that can be improved for each step of the satellite BrO retrieval algorithm.

#### ■ Optimization of DOAS settings for BrO retrieval

BrO optical depths are generally weak and this makes the BrO retrieval highly sensitive to fitting errors from stronger absorbers, as well as instrument characteristics and the spectral structure of surface reflectance. Through sensitivity tests described in section 3.3.1, the optimal DOAS fitting window for BrO was systematically determined. The retrieval wavelength range was selected to avoid cross correlations with other reactive trace gases as much as possible, but BrO-HCHO cross correlation still remains, which may cause erroneous retrieval results under certain measurement conditions. Also, imperfect correction of the Ring effect and O<sub>4</sub> fitting related to the temperature dependency of the cross section should be improved. Therefore, additional sensitivity tests using an advanced modeling of synthetic spectra including realistic simulations with an atmospheric radiative transfer model in comparison with measured spectra will be needed to select a more optimized retrieval fitting wavelength.

#### ■ Stratospheric correction

To calculate the tropospheric BrO column, various stratospheric correction methods that separate stratospheric and tropospheric parts from the total BrO column were tested in this thesis. In the case of the use of 3D atmospheric chemistry model data, which is one of the representative stratospheric correction methods, many model studies demonstrated that there is room for improvement in stratospheric chemistry estimations by developing realistic parameterizations and descriptions of specific chemical processes. Also, as the spatial resolution of the model output is generally lower than that of the satellite, it may cause errors in

## 6. Conclusions and outlook

small spatial scale of bromine chemistry studies. To improve the stratospheric correction and deliver the best possible description of the bromine chemistry, these atmospheric chemistry models need accurate information about chemical reactions, the physical state of the atmosphere and the simulation at small-scale spatial resolution, which will be possible in terms of future model improvements.

In the case of the stratospheric correction method using the empirical model, the physical contribution according to the stratospheric descent are reflected using the viewing geometry and tropopause height, but the description of the chemical reaction has not been reflected. In order to explain chemical effects in the current empirical model, NO<sub>2</sub> and other halogen species columns can be used as additional parameters of the empirical model, which can lead to more scientifically reasonable outcomes. Also, for the stratospheric correction using the climatology of stratospheric BrO profiles based on Theys et al. (2009) with a limited observation period, the uncertainty inevitably increases if the study period extends. Therefore, an updated new BrO climatology dataset, derived by adding more years and simulations performed at higher spatial resolution is essential for future halogen research.

### ■ Tropospheric AMF calculations

The calculation of the tropospheric air mass factors should be re-considered for future studies. The surface albedo and cloud datasets should be reviewed for suitability in BrO retrievals, especially for polar regions which are of major relevance for BrO. Changes in tropospheric AMF due to the surface albedo are large in polar regions where surface albedo varies greatly depending on the presence of sea ice and snow, which can cause large errors in the calculation of tropospheric BrO VCD. In particular, accurate surface albedo information is required to calculate trace gas vertical column densities for satellite data with high spatial resolution such as TROPOMI. Traditionally, climatological monthly Lambertian equivalent reflection (LER) data has been used as information about surface properties, but as confirmed in section 3.6, these datasets are not suitable for new high resolution satellite missions such as TROPOMI. Through the development of surface albedo retrieval algorithms that quickly and accurately processes large amounts of satellite data in real time, it will be possible to improve the accuracy of tropospheric AMFs. In addition, cloud effects have not yet been applied to AMF calculations due to the low accuracy of the current satellite cloud

## 6. Conclusions and outlook

product in polar regions. It is expected that more accurate AMF and tropospheric BrO columns can be obtained by considering the influence of clouds as the quality of S5P/TROPOMI cloud products improves in the future. Moreover, different tropospheric BrO profiles, representative for various bromine explosion cases should be tested for tropospheric BrO retrieval improvement.

In addition to the need for improving the satellite BrO retrieval algorithm, it is also important to verify the retrieved BrO product and use it to investigate the geophysical and chemical mechanisms behind atmospheric BrO. As shown in the case studies of this thesis, the developed algorithm for BrO retrievals from TROPOMI shows a comparable level of accuracy as previous satellite datasets (i.e. from GOME-2 and OMI). However, the validation of satellite BrO retrievals is still challenging for various bromine emission cases. Correlative measurements from ground-based instruments, aircraft observations, and model simulations are needed over different bromine source regions and various emission scenarios to assess and characterize the quality of TROPOMI BrO retrievals. For example, comprehensive atmospheric measurements and sea ice observations have been carried out during the MOSAiC (Multidisciplinary drifting Observatory for the Study of Arctic Climate) campaign, a one-year-long expedition drifting with the sea ice across the central Arctic during the years 2019 to 2020 via RV Polarstern (<https://mosaic-expedition.org/>). The multiple atmospheric and sea ice observations collected during the intensive measurement campaign will help to validate BrO columns and profiles from satellites and models and to provide a physical and chemical basis for understanding halogen chemistry.

An additional focus of future research in this field should be to investigate the trends of BrO and to investigate how halogen chemistry is influenced by the Arctic amplification using the improved satellite halogen oxides retrievals. The impacts of warming temperatures, the corresponding changes in sea ice extents and atmospheric loadings of halogens have been still uncertain and poorly understood. The relationship between BrO plumes and their sources at small spatial scales such as open leads and polynyas, which are influenced by climate changes, will be investigated in depth using the high spatial resolution satellite retrievals.

# Appendix

## Appendix A. Improvement of the BrO retrieval with the Puķīte Taylor series approach

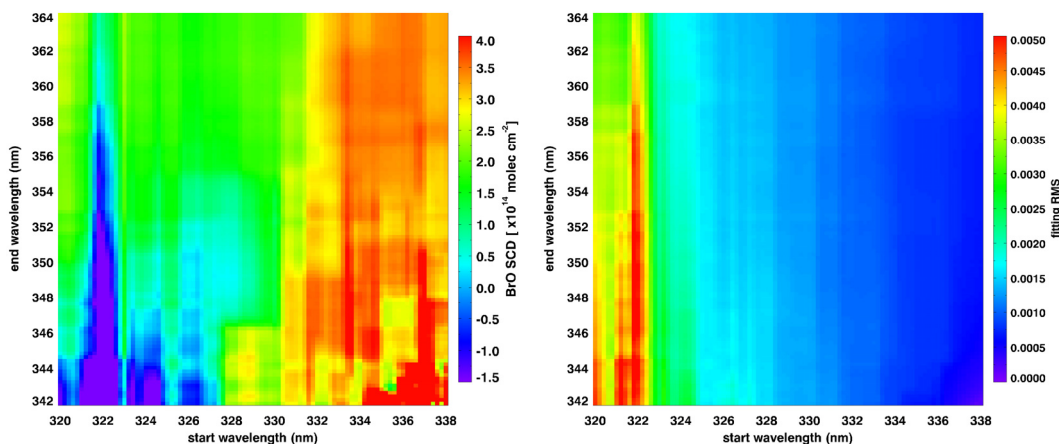
To investigate the possibility of a DOAS fit improvement for the polar BrO measurement scenario by applying the Taylor series approach (Puķīte et al., 2010), an additional sensitivity test was performed. The test was conducted in the same way and with the same measurement scenarios as described in Sect. 3.3.1.1, but two pseudo cross sections of O<sub>3</sub> at 223K ( $\lambda\sigma_{\text{O}_3}$  and  $\sigma_{\text{O}_3}^2$ ) were added to the standard DOAS settings. The reason for choosing the lower-temperature O<sub>3</sub> cross section is that this temperature is closer to the polar lower stratospheric temperature in spring. These two fitting parameters are terms derived by a Taylor series expansion to account for the wavelength dependency of the SCD, which results from changes in light path distribution with wavelength and absorption strength (Puķīte et al., 2010). Puķīte et al. (2010) demonstrated that the application of the Taylor series approach to the strong absorber O<sub>3</sub> leads to an improvement for the fit of the weaker absorber BrO in the UV range of limb measurements.

Figure A1 shows BrO retrieval results obtained with the DOAS settings including the Taylor series approach for the TROPOMI polar BrO measurement scenario. Compared with the standard retrieval results (Fig. 3.3 in Sect. 3.3.1.1), BrO retrieval results applying the Taylor series approach show reduced fitting rms values across the whole retrieval wavelength range (see Fig. A2 right). In particular, fitting results at wavelength ranges with a start limit between 323 and 327.6 nm where negative BrO SCDs and high fitting errors occurred due to strong O<sub>3</sub> interference are significantly improved as BrO SCDs increased by  $\sim 1.4 \times 10^{14}$  molecules cm<sup>-2</sup> and fitting errors decreased by  $\sim 32$  %. Also, the abrupt changes of BrO SCDs around 333 nm of start wavelength and wavelength range with start limits of 335–337.6 nm and end limits of 349–353.6 nm are moderated by use of the Taylor series expansion for O<sub>3</sub>. These sensitivity test results using TROPOMI nadir measurements clearly demonstrate that introducing the Taylor series

## Appendix

approach for  $O_3$  results in an improvement of the DOAS fit. However, as is also clear from Fig. A1, not all of the problems at low wavelengths apparent in Fig. 3.3 are solved by including the Pu $\ddot{u}$ kte terms.

For the fitting window selected in this study (334.6–358 nm), the application of the Taylor series approach for  $O_3$  does not significantly affect BrO retrieval results compared with the standard DOAS retrieval. However, as can be seen from Fig. A2, effects of the Taylor series expansion for  $O_3$  on the BrO SCD retrieval vary depending on the retrieval wavelength interval. The strength of absorption and the slant path of scattered light in the atmosphere vary considerably with wavelength, and thus the degree of improvement by the Taylor series approach for  $O_3$  in the BrO retrieval is also different depending on the fitting wavelength range. Therefore, it is necessary to evaluate the improvement of the SCD retrieval by the Taylor series approach with respect to standard DOAS retrieval according to the fitting window selected. Moreover, only sensitivity test results applying the Taylor series expansion of the lower temperature  $O_3$  cross section to TROPOMI polar BrO measurements are shown in this section, while the effect of the Taylor series approach may be different for different trace gas cross sections, temperature, and measurement scenarios.



**Figure A1.** Color-coded means of BrO SCDs (left) and fitting rms (right) values retrieved when including the Taylor series approach for  $O_3$  in the DOAS analysis.

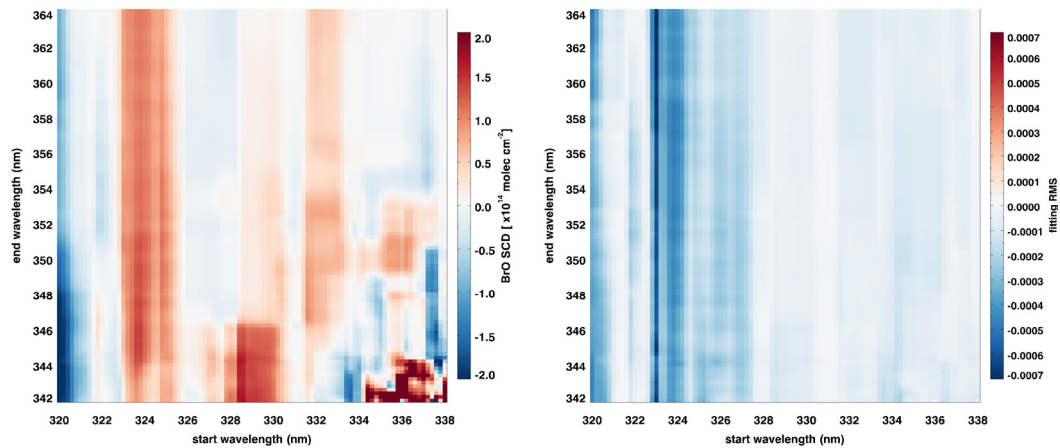


**Figure A2.** Color-coded means of differences for BrO SCDs (left) and fitting rms (right) values between analyses including the Taylor series approach (see Fig. A1) and the standard DOAS (see Fig. 3.3 in Sect. 3.3.1.1).

# Bibliography

- Abbatt, J. P. D., Thomas, J. L., Abrahamsson, K., Boxe, C., Granfors, A., Jones, A. E., King, M. D., Saiz-Lopez, A., Shepson, P. B., Sodeau, J., Toohey, D. W., Toubin, C., von Glasow, R., Wren, S. N., and Yang, X.: Halogen activation via interactions with environmental ice and snow in the polar lower troposphere and other regions, *Atmos. Chem. Phys.*, 12, 6237–6271, <https://doi.org/10.5194/acp-12-6237-2012>, 2012.
- Ahrens, C. D. (2009), *Meteorology Today - An Introduction to Weather, Climate, and the Environment*, 9th ed., Brooks/Cole, Cengage Learning.
- Aiuppa, A.: Degassing of halogens from basaltic volcanism: Insights from volcanic gas observations, *Chem. Geol.*, 263, 99–109, <https://doi.org/10.1016/j.chemgeo.2008.08.022>, 2009.
- Aliwell, S. R., Jones, R. L., and Fish, D. J.: Mid-latitude observations of the seasonal variation of BrO, 1. Zenith-sky measurements, *Geophys. Res. Lett.* 24, 1195–1198, 1997.
- Aliwell, S. R., Van Roozendaal, M., Johnston, P. V., Richter, A., Wagner, T., Arlander, D. W., Burrows, J. P., Fish, D. J., Jones, R. L., Tornkvist, K. K., Lambert, J. C., Pfeilsticker, K., and Pundt, I.: Analysis for BrO in zenith-sky spectra: An intercomparison exercise for analysis improvement, *Journal of Geophysical Research-Atmospheres*, 107, 10.1029/2001jd000329, 2002.
- Alvarado, L. M. A., Richter, A., Vrekoussis, M., Wittrock, F., Hilboll, A., Schreier, S. F., and Burrows, J. P.: An improved glyoxal retrieval from OMI measurements, *Atmospheric Measurement Techniques*, 7, 4133–4150, 10.5194/amt-7-4133-2014, 2014.
- Antón, M. and Loyola, D.: Influence of cloud properties on satellite total ozone observations, *J. Geophys. Res.*, 116, D03208, doi:10.1029/2010JD014780, 2011.
- Barrie, L. A., Bottenheim, J. W., Schnell, R. C., Crutzen, P. J., and Rasmussen, R. A.: Ozone destruction and photochemical reactions at polar sunrise in the lower arctic atmosphere, *Nature*, 334, 138–141, 1988.
- Begoin, M., Richter, A., Weber, M., Kaleschke, L., Tian-Kunze, X., Stohl, A., Theys, N., and Burrows, J. P.: Satellite observations of long range transport of a large BrO plume in the Arctic, *Atmospheric Chemistry and Physics*, 10, 6515–6526, 10.5194/acp-10-

- 6515-2010, 2010.
- Blechschmidt, A. M., Richter, A., Burrows, J. P., Kaleschke, L., Strong, K., Theys, N., Weber, M., Zhao, X., and Zien, A.: An exemplary case of a bromine explosion event linked to cyclone development in the Arctic, *Atmospheric Chemistry and Physics*, 16, 1773-1788, 10.5194/acp-16-1773-2016, 2016.
- Bobrowski, N., Hönninger, G., Galle, B., and Platt, U.: Detection of bromine monoxide in a volcanic plume, *Nature*, 423, 273-276, 10.1038/nature01638, 2003.
- Boersma, K. F., Eskes, H. J., Veefkind, J. P., Brinksma, E. J., van der A, R. J., Sneep, M., van den Oord, G. H. J., Levelt, P. F., Stammes, P., Gleason, J. F., and Bucsela, E. J.: Near-real time retrieval of tropospheric NO<sub>2</sub> from OMI, *Atmospheric Chemistry and Physics*, 7, 2103-2118, 10.5194/acp-7-2103-2007, 2007.
- Bogumil, K., Orphal, J., Homann, T., Voigt, S., Spietz, P., Fleischmann, O. C., Vogel, A., Hartmann, M., Kromminga, H., Bovensmann, H., Frerick, J., and Burrows, J. P.: Measurements of molecular absorption spectra with the SCIAMACHY pre-flight model: instrument characterization and reference data for atmospheric remote-sensing in the 230-2380 nm region, *Journal of Photochemistry and Photobiology a-Chemistry*, 157, 167-184, 10.1016/s1010-6030(03)00062-5, 2003.
- Boichu, M., Oppenheimer, C., Roberts, T. J., Tsanev, V., and Kyle, P. R.: On bromine, nitrogen oxides and ozone depletion in the tropospheric plume of Erebus volcano (Antarctica), *Atmospheric Environment*, 45, 3856-3866, 10.1016/j.atmosenv.2011.03.027, 2011.
- Bottenheim, J. W., Gallant, A. G., and Brice, K. A.: Measurements of NO<sub>x</sub> species and O<sub>3</sub> at 82°N latitude, *Geophys. Res. Lett.*, 13, 113-116, 1986.
- Bovensmann, H., Burrows, J. P., Buchwitz, M., Frerick, J., Noel, S., Rozanov, V. V., Chance, K. V., and Goede, A.: SCIAMACHY – Mission Objectives and Measurement Modes, *J. Atmos. Sci.*, 56, 127-150, 1999.
- Brasseur, G. and Solomon, S.: *Aeronomy of the Middle Atmosphere—Chemistry and Physics of the Stratosphere and Mesosphere*, Atmospheric and Oceanographic Sciences Library 32, third edn., Springer, Dordrecht, the Netherlands, 2005.
- Brune, W. H., Anderson, J. G., Toohey, D. W., Fahey, D. W., Kawa, S. R., Jones, R. L., McKenna, D. S., and Poole, L. R.: The potential for ozone depletion in the Arctic polar stratosphere, *Science*, 252, 1260-1266, 10.1126/science.252.5010.1260, 1991.

## Bibliography

- Burrows, J. P., Holzle, E., Goede, A., Visser, H., and Fricke, W.: SCIAMACHY - scanning imaging absorption spectrometer for atmospheric cartography, *Acta Astronaut.*, 35, 445–451, doi:10.1016/0094-5765(94)00278-T, 1995.
- Burrows, J. P., Weber, M., Buchwitz, M., Rozanov, V., V., Ladstätter-Weißmayer, A., Richter, A., DeBeek, R., Hoogen, R., Bramstedt, K., Eichmann, K.-U., and Eisinger, M.: The Global Ozone Monitoring Experiment (GOME): Mission concept and first scientific results, *J. Atmos. Sci.*, 56, 151–175, 1999.
- Burrows, J. P., Platt, U., and Borrell, P.: The remote sensing of tropospheric composition from space, Springer Science & Business Media, 2011.
- Callies, J., Corpaccioli, E., Eisinger, M., Hahne, A., and Lefebvre, A.: GOME-2 - Metop's second-generation sensor for operational ozone monitoring, *Esa Bulletin-European Space Agency*, 28-36, 2000.
- Chance, K.: Analysis of BrO measurements from the Global Ozone Monitoring Experiment, *Geophysical Research Letters*, 25, 3335-3338, 10.1029/98gl52359, 1998.
- Chance, K.: Spectroscopic measurements of tropospheric composition from satellite measurements in the ultraviolet and visible: Steps toward continuous pollution monitoring from space, in: *Remote Sensing of the Atmosphere for Environmental Security*, Springer, 1-25, 2006.
- Chance, K., and Kurucz, R.: An improved high-resolution solar reference spectrum for earth's atmosphere measurements in the ultraviolet, visible, and near infrared, *Journal of quantitative spectroscopy and radiative transfer*, 111, 1289-1295, 2010.
- Choi, S., Wang, Y., Salawitch, R. J., Canty, T., Joiner, J., Zeng, T., Kurosu, T. P., Chance, K., Richter, A., Huey, L. G., Liao, J., Neuman, J. A., Nowak, J. B., Dibb, J. E., Weinheimer, A. J., Diskin, G., Ryerson, T. B., da Silva, A., Curry, J., Kinnison, D., Tilmes, S., and Levelt, P. F.: Analysis of satellite-derived Arctic tropospheric BrO columns in conjunction with aircraft measurements during ARCTAS and ARCPAC, *Atmospheric Chemistry and Physics*, 12, 1255-1285, 10.5194/acp-12-1255-2012, 2012.
- Choi, S., Theys, N., Salawitch, R. J., Wales, P. A., Joiner, J., Canty, T. P., Chance, K., Suleiman, R. M., Palm, S. P., Cullather, R. I., Darmenov, A. S., da Silva, A., Kurosu, T. P., Hendrick, F., and Van Roozendaal, M.: Link Between Arctic Tropospheric BrO Explosion Observed From Space and Sea-Salt Aerosols From Blowing Snow Investigated Using Ozone Monitoring Instrument BrO Data and GEOS-5 Data Assimilation System, *Journal of Geophysical Research-Atmospheres*, 123, 6954-6983, 10.1029/2017jd026889, 2018.

## Bibliography

- Davis, D., Crawford, J., Liu, S., McKeen, S., Bandy, A., Thornton, D., Rowland, F., and Blake, D.: Potential impact of iodine on tropospheric levels of ozone other critical oxidants, *J. Geophys. Res.*, 101, 2135–2147, 1996.
- Dee, D. P., Uppala, S. M., Simmons, A. J., Berrisford, P., Poli, P., Kobayashi, S., Andrae, U., Balmaseda, M. A., Balsamo, G., Bauer, P., Bechtold, P., Beljaars, A. C. M., van de Berg, L., Bidlot, J., Bormann, N., Delsol, C., Dragani, R., Fuentes, M., Geer, A. J., Haimberger, L., Healy, S. B., Hersbach, H., Holm, E. V., Isaksen, L., Kallberg, P., Kohler, M., Matricardi, M., McNally, A. P., Monge-Sanz, B. M., Morcrette, J. J., Park, B. K., Peubey, C., de Rosnay, P., Tavolato, C., Thepaut, J. N., and Vitart, F.: The ERA-Interim reanalysis: configuration and performance of the data assimilation system, *Quarterly Journal of the Royal Meteorological Society*, 137, 553–597, 10.1002/qj.828, 2011.
- Dennison, F., Keeble, J., Morgenstern, O., Zeng, G., Abraham, N. L., and Yang, X.: Improvements to stratospheric chemistry scheme in the UM-UKCA (v10.7) model: solar cycle and heterogeneous reactions, *Geosci. Model Dev.*, 12, 1227–1239, <https://doi.org/10.5194/gmd-12-1227-2019>, 2019.
- Dorf, M., Butz, A., Camy-Peyret, C., Chipperfield, M. P., Kritten, L., and Pfeilsticker, K.: Bromine in the tropical troposphere and stratosphere as derived from balloon-borne BrO observations, *Atmos. Chem. Phys.*, 8, 7265–7271, <https://doi.org/10.5194/acp-8-7265-2008>, 2008.
- Ebojje, F., von Savigny, C., Ladstatter-Weissenmayer, A., Rozanov, A., Weber, M., Eichmann, K. U., Botel, S., Rahpoe, N., Bovensmann, H., and Burrows, J. P.: Tropospheric column amount of ozone retrieved from SCIAMACHY limb-nadir-matching observations, *Atmospheric Measurement Techniques*, 7, 2073–2096, 10.5194/amt-7-2073-2014, 2014.
- Eisinger, M., Richter, A., Ladstatter-Weißenmayer, A., and Burrows, J. P.: DOAS Zenith sky observations: 1. BrO measurements over Bremen (53 ° N) 1993–1994, *J. Atmos. Chem.* 26, 93–108, 1997.
- Fan, S. M., and Jacob, D. J.: Surface ozone depletion in Arctic spring sustained by bromine reactions on aerosols, *Nature*, 359, 522–524, 10.1038/359522a0, 1992.
- Finlayson-Pitts, B. J., Livingston, F. E., and Berko, H. N.: Ozone destruction and bromine photochemistry at ground-level in the Arctic spring, *Nature*, 343, 1990.
- Fitzenberger, R., Bösch, H., Camy-Peyret, C., Chipperfield, M., Harder, H., Platt, U., Pyle, J., Wagner, T., and Pfeilsticker, K.: First profile measurement of tropospheric BrO,

## Bibliography

- Geophys. Res. Lett., 27, 2921–2924, 2000.
- Fleischmann, O. C., Hartmann, M., Burrows, J. P., and Orphal, J.: New ultraviolet absorption cross-sections of BrO at atmospheric temperatures measured by time-windowing Fourier transform spectroscopy, *Journal of Photochemistry and Photobiology A: Chemistry*, 168, 117-132, 2004.
- Frieß, U., Sihler, H., Sander, R., Pöhler, D., Yilmaz, S., and Platt, U.: The vertical distribution of BrO and aerosols in the Arctic: Measurements by active and passive differential optical absorption spectroscopy, *Journal of Geophysical Research-Atmospheres*, 116, 10.1029/2011jd015938, 2011.
- Grainger, J., and J. Ring (1962), Anomalous Fraunhofer Line Profiles, *Nature*, 193, 762, doi:10.1038/193762a0.
- Harder, H., Bosch, H., Camy-Peyret, C., Chipperfield, M. P., Fitzenberger, R., Payan, S., Perner, D., Platt, U., Sinnhuber, B. M., and Pfeilsticker, K.: Comparison of measured and modeled stratospheric BrO: Implications for the total amount of stratospheric bromine, *Geophysical Research Letters*, 27, 3695-3698, 10.1029/1999gl011215, 2000.
- Hausmann, M. and Platt, U.: Spectroscopic measurement of bromine oxide and ozone in the high Arctic during Polar Sunrise Experiment 1992, *J. Geophys. Res.*, 99, 25 399–25 414, 1994.
- Hebestreit, K., Stutz, J., Rosen, D., Matveiv, V., Peleg, M., Luria, M., and Platt, U.: DOAS measurements of tropospheric bromine oxide in mid-latitudes, *Science*, 283, 55-57, 10.1126/science.283.5398.55, 1999.
- Heidinger, A. K. and Stephens, G. L.: Molecular Line Absorption in a Scattering Atmosphere. Part II: Application to Remote Sensing in the O<sub>2</sub> A band, *J. Atmos. Sci.*, 57, 1615–1634, doi:10.1175/1520-0469(2000)057<1615:MLAIAS>2.0.CO;2, 2000
- Hendrick, F., Van Roozendaal, M., Chipperfield, M. P., Dorf, M., Goutail, F., Yang, X., Fayt, C., Hermans, C., Pfeilsticker, K., Pommereau, J. P., Pyle, J. A., Theys, N., and De Maziere, M.: Retrieval of stratospheric and tropospheric BrO profiles and columns using ground-based zenith-sky DOAS observations at Harestua, 60 degrees N, *Atmospheric Chemistry and Physics*, 7, 4869-4885, 10.5194/acp-7-4869-2007, 2007.
- Hollwedel, J., Wenig, M., Beirle, S., Kraus, S., Kuhl, S., Wilms-Grabe, W., Platt, U., and Wagner, T.: Year-to-year variations of spring time polar tropospheric BrO as seen by

## Bibliography

- GOME, in: Trace Constituents in the Troposphere and Lower Stratosphere, edited by: Burrows, J. P., and Thompson, A. M., *Advances in Space Research*, 4, 804-808, 2004.
- Horvath, H.: Atmospheric light absorption—A review. *Atmospheric Environment. Part A. General Topics*, 27(3), 293-317, 1993.
- Hönninger, G., Leser, H., Sebastian, O., and Platt, U.: Ground-based measurements of halogen oxides at the Hudson Bay by active longpath DOAS and passive MAX-DOAS, *Geophysical Research Letters*, 31, 2004.
- Hörmann, C., Sihler, H., Bobrowski, N., Beirle, S., Penning de Vries, M., Platt, U., and Wagner, T.: Systematic investigation of bromine monoxide in volcanic plumes from space by using the GOME-2 instrument, *Atmospheric Chemistry and Physics*, 13, 4749-4781, 10.5194/acp-13-4749-2013, 2013.
- Hörmann, C., Sihler, H., Beirle, S., Penning de Vries, M., Platt, U., and Wagner, T.: Seasonal variation of tropospheric bromine monoxide over the Rann of Kutch salt marsh seen from space, *Atmospheric Chemistry and Physics*, 16, 13015-13034, 10.5194/acp-16-13015-2016, 2016.
- Jacob, D. J.: *Introduction to Atmospheric Chemistry*, Princeton University Press, 1999.
- Jacobi, H. W., Kaleschke, L., Richter, A., Rozanov, A., and Burrows, J. P.: Observation of a fast ozone loss in the marginal ice zone of the Arctic Ocean, *Journal of Geophysical Research-Atmospheres*, 111, 10.1029/2005jd006715, 2006.
- Jones, A. E., Anderson, P. S., Wolff, E. W., Turner, J., Rankin, A. M., and Colwell, S. R.: A role for newly forming sea ice in springtime polar tropospheric ozone loss? Observational evidence from Halley station, Antarctica, *Journal of Geophysical Research-Atmospheres*, 111, 10.1029/2005jd006566, 2006.
- Jones, A. E., Anderson, P. S., Begoin, M., Brough, N., Hutterli, M. A., Marshall, G. J., Richter, A., Roscoe, H. K., and Wolff, E. W.: BrO, blizzards, and drivers of polar tropospheric ozone depletion events, *Atmospheric Chemistry and Physics*, 9, 4639-4652, 10.5194/acp-9-4639-2009, 2009.
- Jones, A. E., Anderson, P. S., Wolff, E. W., Roscoe, H. K., Marshall, G. J., Richter, A., Brough, N., and Colwell, S. R.: Vertical structure of Antarctic tropospheric ozone depletion events: characteristics and broader implications, *Atmospheric Chemistry and Physics*, 10, 7775-7794, 10.5194/acp-10-7775-2010, 2010.
- Kaleschke, L., Richter, A., Burrows, J., Afe, O., Heygster, G., Notholt, J., Rankin, A. M.,

## Bibliography

- Roscoe, H. K., Hollwedel, J., Wagner, T., and Jacobi, H. W.: Frost flowers on sea ice as a source of sea salt and their influence on tropospheric halogen chemistry, *Geophysical Research Letters*, 31, 10.1029/2004gl020655, 2004.
- Kromminga, H., Orphal, J., Spietz, P., Voigt, S., and Burrows, J. P.: New measurements of OClO absorption cross-sections in the 325-435 nm region and their temperature dependence between 213 and 293 K, *Journal of Photochemistry and Photobiology a-Chemistry*, 157, 149-160, 10.1016/s1010-6030(03)00071-6, 2003.
- Kuhl, S., Pukite, J., Deutschmann, T., Platt, U., and Wagner, T.: SCIAMACHY limb measurements of NO<sub>2</sub>, BrO and OClO. Retrieval of vertical profiles: Algorithm, first results, sensitivity and comparison studies, *Advances in Space Research*, 42, 1747-1764, 10.1016/j.asr.2007.10.022, 2008.
- Lary, D.J.: Gas phase atmospheric bromine photochemistry, *J. Geophys. Res.*, 101, pp1505-1516, 1996a.
- Lary, D.J., Chipperfield, M.P., Toumi, R. and Lenton, T.: Heterogeneous atmospheric bromine photochemistry, *J. Geophys. Res.*, 101, pp1489-1504, 1996b.
- Leser, H., Honninger, G., and Platt, U.: MAX-DOAS measurements of BrO and NO<sub>2</sub> in the marine boundary layer, *Geophysical Research Letters*, 30, 10.1029/2002gl015811, 2003.
- Levelt, P. F., Van den Oord, G. H. J., Dobber, M. R., Malkki, A., Visser, H., de Vries, J., Stammes, P., Lundell, J. O. V., and Saari, H.: The Ozone Monitoring Instrument, *IEEE T. Geosci. Remote*, 44, 1093-1101, 2006.
- Liang, Q., Stolarski, R. S., Kawa, S. R., Nielsen, J. E., Douglass, A. R., Rodriguez, J. M., Blake, D. R., Atlas, E. L., and Ott, L. E.: Finding the missing stratospheric Br-y: a global modeling study of CHBr<sub>3</sub> and CH<sub>2</sub>Br<sub>2</sub>, *Atmospheric Chemistry and Physics*, 10, 2269-2286, 10.5194/acp-10-2269-2010, 2010.
- Liao, J., Huey, L. G., Tanner, D. J., Brough, N., Brooks, S., Dibb, J. E., Stutz, J., Thomas, J. L., Lefer, B., Haman, C., and Gorham, K.: Observations of hydroxyl and peroxy radicals and the impact of BrO at Summit, Greenland in 2007 and 2008, *Atmospheric Chemistry and Physics*, 11, 8577-8591, 10.5194/acp-11-8577-2011, 2011.
- Liou, K.N.: An introduction to atmosphere radiation, Academic Press, International Geophysical Series, Vol. 84, 2002.
- Lovelock, J. E.: Methyl chloroform in the troposphere as an indicator of OH radical

## Bibliography

- abundance, *Nature*, 267, 32–32, <https://doi.org/10.1038/267032a0>, 1977
- Loyola, D. G., Xu, J., Heue, K.-P., and Zimmer, W.: Applying FP\_ILM to the retrieval of geometry-dependent effective Lambertian equivalent reflectivity (GE\_LER) daily maps from UVN satellite measurements, *Atmos. Meas. Tech.*, 13, 985–999, <https://doi.org/10.5194/amt-13-985-2020>, 2020.
- Martin, S., Yu, Y. L., and Drucker, R.: The temperature dependence of frost flower growth on laboratory sea ice and the effect of the flowers on infrared observations of the surface, *Journal of Geophysical Research-Oceans*, 101, 12111-12125, [10.1029/96jc00208](https://doi.org/10.1029/96jc00208), 1996.
- Matveev, V., Peleg, M., Rosen, D., Tov-Alper, D. S., Hebestreit, K., Stutz, J., Platt, U., Blake, D., and Luria, M.: Bromine oxide - ozone interaction over the Dead Sea, *Journal of Geophysical Research-Atmospheres*, 106, 10375-10387, [10.1029/2000jd900611](https://doi.org/10.1029/2000jd900611), 2001.
- McConnell, J. C., Henderson, G. S., Barrie, L., Bottenheim, J., Niki, H., Langford, C. H., and Templeton, E. M. J.: Photochemical bromine production implicated in Arctic boundary-layer ozone depletion, *Nature*, 355, 150-152, [10.1038/355150a0](https://doi.org/10.1038/355150a0), 1992.
- McElroy, M. B., Salawitch, R. J., Wofsy, S. C., and Logan, J. A.: Reductions of Antarctic ozone due to synergistic interactions of chlorine and bromine, *Nature*, 321, 759-762, [10.1038/321759a0](https://doi.org/10.1038/321759a0), 1986.
- McMullan, K., and van der Meulen, W.: SENTINEL-5 PRECURSOR SYSTEM, ESA Living Planet Symposium, 2013, 140.
- Meller, R., and Moortgat, G. K.: Temperature dependence of the absorption cross sections of formaldehyde between 223 and 323 K in the wavelength range 225-375 nm, *Journal of Geophysical Research-Atmospheres*, 105, 7089-7101, [10.1029/1999jd901074](https://doi.org/10.1029/1999jd901074), 2000.
- Monks, P. S.: A review of the observations and origins of the spring ozone maximum, *Atmospheric Environment*, 34, 3545-3561, [10.1016/s1352-2310\(00\)00129-1](https://doi.org/10.1016/s1352-2310(00)00129-1), 2000.
- Munro, R., Lang, R., Klaes, D., Poli, G., Retscher, C., Lindstrot, R., Huckle, R., Lacan, A., Grzegorski, M., Holdak, A., Kokhanovsky, A., Livschitz, J., and Eisinger, M.: The GOME-2 instrument on the Metop series of satellites: instrument design, calibration, and level 1 data processing - an overview, *Atmospheric Measurement Techniques*, 9, 1279-1301, [10.5194/amt-9-1279-2016](https://doi.org/10.5194/amt-9-1279-2016), 2016.

## Bibliography

- Neuman, J. A., Nowak, J. B., Huey, L. G., Burkholder, J. B., Dibb, J. E., Holloway, J. S., Liao, J., Peischl, J., Roberts, J. M., Ryerson, T. B., Scheuer, E., Stark, H., Stickel, R. E., Tanner, D. J., and Weinheimer, A.: Bromine measurements in ozone depleted air over the Arctic Ocean, *Atmos. Chem. Phys.*, 10, 6503-6514, doi:10.5194/acp-10-6503-2010, 2010.
- Nghiem, S. V., Rigor, I. G., Richter, A., Burrows, J. P., Shepson, P. B., Bottenheim, J., Barber, D. G., Steffen, A., Latonas, J., Wang, F. Y., Stern, G., Clemente-Colon, P., Martin, S., Hall, D. K., Kaleschke, L., Tackett, P., Neumann, G., and Asplin, M. G.: Field and satellite observations of the formation and distribution of Arctic atmospheric bromine above a rejuvenated sea ice cover, *Journal of Geophysical Research-Atmospheres*, 117, 10.1029/2011jd016268, 2012.
- Noxon, J. F.: Nitrogen dioxide in the stratosphere and troposphere measured by ground-based absorption spectroscopy. *Science*, 189(4202), 547-549, 1975.
- Obbard, R. W., Roscoe, H. K., Wolff, E. W., and Atkinson, H. M.: Frost flower surface area and chemistry as a function of salinity and temperature, *Journal of Geophysical Research-Atmospheres*, 114, 10.1029/2009jd012481, 2009.
- Oppenheimer, C., Tsanev, V. I., Braban, C. F., Cox, R. A., Adams, J. W., Aiuppa, A., Bobrowski, N., Delmelle, P., Barclay, J., and McGonigle, A. J. S.: BrO formation in volcanic plumes, *Geochimica Et Cosmochimica Acta*, 70, 2935-2941, 10.1016/j.gca.2006.04.001, 2006.
- Peters, E.: Improved MAX-DOAS measurements and retrievals focused on the marine boundary layer, PhD dissertation, University of Bremen, Germany, [https://www.iup.uni-bremen.de/doas/paper/diss\\_peters\\_2013.pdf](https://www.iup.uni-bremen.de/doas/paper/diss_peters_2013.pdf), 2013.
- Peterson, P. K., Simpson, W. R., Pratt, K. A., Shepson, P. B., Friess, U., Zielcke, J., Platt, U., Walsh, S. J., and Nghiem, S. V.: Dependence of the vertical distribution of bromine monoxide in the lower troposphere on meteorological factors such as wind speed and stability, *Atmospheric Chemistry and Physics*, 15, 2119-2137, 10.5194/acp-15-2119-2015, 2015.
- Platt, U.: Differential optical absorption spectroscopy (DOAS), in *Air Monitoring by Spectroscopic Techniques*, edited by: Sigrist, M. W., Chemical Analysis Series, 127, John Wiley, New York, 1994.
- Platt, U., and Stutz, J.: Differential absorption spectroscopy, in: *Differential Optical Absorption Spectroscopy*, Springer, 135-174, 2008.
- Pöhler, D., Vogel, L., Frieß, U., and Platt, U.: Observation of halogen species in the

## Bibliography

- Amundsen Gulf, Arctic, by active long-path differential optical absorption spectroscopy, *P. Natl Acad. Sci.*, 107, 6582–6587, doi:10.1073/pnas.0912231107, 2010.
- Pratt, K. A., Custard, K. D., Shepson, P. B., Thomas, D. A., Pohler, D., General, S., Zielcke, J., Simpson, W. R., Platt, U., Tanner, D. J., Huey, L. G., Carlson, M., and Stirm, B. H.: Photochemical production of molecular bromine in arctic surface snowpacks, *Nat. Geosci.*, 6, 351–356, doi:10.1038/ngeo1779, 2013
- Puķite, J., Kuhl, S., Deutschmann, T., Platt, U., and Wagner, T.: Extending differential optical absorption spectroscopy for limb measurements in the UV, *Atmospheric Measurement Techniques*, 3, 631–653, 10.5194/amt-3-631-2010, 2010.
- Pundt, I., Pommereau, J., Chipperfield, M., Roozendael, M. V., and Goutail, F.: Climatology of the stratospheric BrO vertical distribution by balloon-borne UV-visible spectrometry, *J. Geophys. Res.*, 107, 4806, doi:10.1029/2002JD002230, 2002.
- Richter, A., Wittrock, F., Eisinger, M., and Burrows, J. P.: GOME observations of tropospheric BrO in northern hemispheric spring and summer 1997, *Geophysical Research Letters*, 25, 2683–2686, 10.1029/98gl52016, 1998.
- Richter, A., Wittrock, F., Ladstatter-Weissenmayer, A., and Burrows, J. P.: GOME measurements of stratospheric and tropospheric BrO, in: *Remote Sensing of Trace Constituents in the Lower Stratosphere, Troposphere and the Earth's Surface: Global Observations, Air Pollution and the Atmospheric Correction*, edited by: Burrows, J. P., and Takeucki, N., *Advances in Space Research*, 11, 1667–1672, 2002.
- Richter, A., Begoin, M., Hilboll, A., and Burrows, J. P.: An improved NO<sub>2</sub> retrieval for the GOME-2 satellite instrument, *Atmospheric Measurement Techniques*, 4, 1147–1159, 10.5194/amt-4-1147-2011, 2011.
- Roedel, W., and T. Wagner (2011), *Physik unserer Umwelt: Die Atmosphäre*, 4th ed., Springer Verlag, Heidelberg Dordrecht London New York, doi: 10.1007/978-3-642-15729-5.
- Rozanov, A., Kuhl, S., Doicu, A., McLinden, C., Pukite, J., Bovensmann, H., Burrows, J. P., Deutschmann, T., Dorf, M., Goutail, F., Grunow, K., Hendrick, F., von Hobe, M., Hrechanyy, S., Lichtenberg, G., Pfeilsticker, K., Pommereau, J. P., Van Roozendael, M., Stroh, F., and Wagner, T.: BrO vertical distributions from SCIAMACHY limb measurements: comparison of algorithms and retrieval results, *Atmospheric Measurement Techniques*, 4, 1319–1359, 10.5194/amt-4-1319-2011, 2011.

## Bibliography

- Rozanov, V., Rozanov, A., Kokhanovsky, A., and Burrows, J.: Radiative transfer through terrestrial atmosphere and ocean: Software package SCIATRAN, *Journal of Quantitative Spectroscopy and Radiative Transfer*, 2013.
- Saiz-Lopez, A., Plane, J. M. C., and Shillito, J. A.: Bromine oxide in the mid-latitude marine boundary layer, *Geophysical Research Letters*, 31, 10.1029/2003gl018956, 2004.
- Salawitch, R. J., Canty, T., Kurosu, T., Chance, K., Liang, Q., da Silva, A., Pawson, S., Nielsen, J. E., Rodriguez, J. M., Bhartia, P. K., Liu, X., Huey, L. G., Liao, J., Stickel, R. E., Tanner, D. J., Dibb, J. E., Simpson, W. R., Donohoue, D., Weinheimer, A., Flocke, F., Knapp, D., Montzka, D., Neuman, J. A., Nowak, J. B., Ryerson, T. B., Oltmans, S., Blake, D. R., Atlas, E. L., Kinnison, D. E., Tilmes, S., Pan, L. L., Hendrick, F., Van Roozendaal, M., Kreher, K., Johnston, P. V., Gao, R. S., Johnson, B., Bui, T. P., Chen, G., Pierce, R. B., Crawford, J. H., and Jacob, D. J.: A new interpretation of total column BrO during Arctic spring, *Geophysical Research Letters*, 37, 10.1029/2010gl043798, 2010.
- Sander, R., Keene, W. C., Pszenny, A. A. P., Arimoto, R., Ayers, G. P., Baboukas, E., Caine, J. M., Crutzen, P. J., Duce, R. A., Honninger, G., Huebert, B. J., Maenhaut, W., Mihalopoulos, N., Turekian, V. C., and Van Dingenen, R.: Inorganic bromine in the marine boundary layer: a critical review, *Atmospheric Chemistry and Physics*, 3, 1301-1336, 10.5194/acp-3-1301-2003, 2003.
- Sander, R., Burrows, J., and Kaleschke, L.: Carbonate precipitation in brine - a potential trigger for tropospheric ozone depletion events, *Atmospheric Chemistry and Physics*, 6, 4653-4658, 10.5194/acp-6-4653-2006, 2006.
- Schönhardt, A., Richter, A., Theys, N., and Burrows, J. P.: Space-based observation of volcanic iodine monoxide, *Atmospheric Chemistry and Physics*, 17, 4857-4870, 10.5194/acp-17-4857-2017, 2017.
- Schroeder, W., Anlauf, K., Barrie, L., Lu, J., Steffen, A., Schneeberger, D., and Berg, T.: Arctic springtime depletion of mercury, *Nature*, 394, 331-332, 1998.
- Screen, J. A., Deser, C., Smith, D. M., Zhang, X. D., Blackport, R., Kushner, P. J., Oudar, T., McCusker, K. E., and Sun, L. T.: Consistency and discrepancy in the atmospheric response to Arctic sea-ice loss across climate models, *Nature Geoscience*, 11, 155+, 10.1038/s41561-018-0059-y, 2018.
- Seigneur, C. and Lohman, K.: Effect of bromine chemistry on the atmospheric mercury cycle, *J. Geophys. Res.*, 113, D23309, doi:10.1029/2008JD010262, 2008.

## Bibliography

- Seinfeld, J. H., and S. N. Pandis (2006), *Atmospheric Chemistry and Physics - From Air Pollution to Climate Change*, 2nd ed., John Wiley & Sons, Inc., Hoboken, New Jersey, doi: 10.1063/1.882420.
- Seo, S., Richter, A., Blechschmidt, A. M., Bougoudis, I., and Burrows, J. P.: First high-resolution BrO column retrievals from TROPOMI, *Atmospheric Measurement Techniques*, 12, 2913-2932, 10.5194/amt-12-2913-2019, 2019.
- Seo, S., Richter, A., Blechschmidt, A.-M., Bougoudis, I., and Burrows, J. P.: Spatial distribution of enhanced BrO and its relation to meteorological parameters in Arctic and Antarctic sea ice regions, *Atmos. Chem. Phys.*, 20, 12285-12312, <https://doi.org/10.5194/acp-20-12285-2020>, 2020.
- Serdyuchenko, A., Gorshchev, V., Weber, M., Chehade, W., and Burrows, J. P.: High spectral resolution ozone absorption cross-sections - Part 2: Temperature dependence, *Atmospheric Measurement Techniques*, 7, 625-636, 10.5194/amt-7-625-2014, 2014.
- Sihler, H.: Halogen activation in the polar troposphere, PhD dissertation, University of Heidelberg, Germany, [http://archiv.ub.uni-heidelberg.de/volltextserver/13663/1/SihlerDiss2012\\_original.pdf](http://archiv.ub.uni-heidelberg.de/volltextserver/13663/1/SihlerDiss2012_original.pdf), 2012.
- Sihler, H., Platt, U., Beirle, S., Marbach, T., Kuhl, S., Dorner, S., Verschaeve, J., Friess, U., Pöhler, D., Vogel, L., Sander, R., and Wagner, T.: Tropospheric BrO column densities in the Arctic derived from satellite: retrieval and comparison to ground-based measurements, *Atmospheric Measurement Techniques*, 5, 2779-2807, 10.5194/amt-5-2779-2012, 2012.
- Simpson, W. R., von Glasow, R., Riedel, K., Anderson, P., Ariya, P., Bottenheim, J., Burrows, J., Carpenter, L. J., Friess, U., Goodsite, M. E., Heard, D., Hutterli, M., Jacobi, H. W., Kaleschke, L., Neff, B., Plane, J., Platt, U., Richter, A., Roscoe, H., Sander, R., Shepson, P., Sodeau, J., Steffen, A., Wagner, T., and Wolff, E.: Halogens and their role in polar boundary-layer ozone depletion, *Atmospheric Chemistry and Physics*, 7, 4375-4418, 10.5194/acp-7-4375-2007, 2007a.
- Simpson, W. R., Carlson, D., Hönninger, G., Douglas, T. A., Sturm, M., Perovich, D., and Platt, U.: First-year sea-ice contact predicts bromine monoxide (BrO) levels at Barrow, Alaska better than potential frost flower contact, *Atmos. Chem. Phys.*, 7, 621-627, <https://doi.org/10.5194/acp-7-621-2007>, 2007b.
- Simpson, W. R., Brown, S. S., Saiz-Lopez, A., Thornton, J. A., and von Glasow, R.: Tropospheric Halogen Chemistry: Sources, Cycling, and Impacts, *Chem. Rev.*, 115,

## Bibliography

- 4035–4062, doi:10.1021/cr5006638, 2015.
- Sinnhuber, B. M., Rozanov, A., Sheode, N., Afe, O. T., Richter, A., Sinnhuber, M., Wittrock, F., Burrows, J. P., Stiller, G. P., von Clarmann, T., and Linden, A.: Global observations of stratospheric bromine monoxide from SCIAMACHY, *Geophysical Research Letters*, 32, 10.1029/2005gl023839, 2005.
- Solomon, S., Garcia, R. R., and Ravishankara, A. R.: On the role of iodine in ozone depletion, *J. Geophys. Res.*, 99, 20491–20499, 1994.
- Solomon, S.: Stratospheric ozone depletion: a review of concepts and history, *Reviews of Geophysics*, Vol. 37, 275-316, 1999.
- Spreen, G., Kaleschke, L., and Heygster, G.: Sea ice remote sensing using AMSR-E 89-GHz channels, *Journal of Geophysical Research-Oceans*, 113, 10.1029/2005jc003384, 2008.
- Steffen, A., Douglas, T., Amyot, M., Ariya, P., Aspino, K., Berg, T., Bottenheim, J., Brooks, S., Cobbett, F., Dastoor, A., Dommergue, A., Ebinghaus, R., Ferrari, C., Gardfeldt, K., Goodsite, M. E., Lean, D., Poulain, A. J., Scherz, C., Skov, H., Sommar, J., and Temme, C.: A synthesis of atmospheric mercury depletion event chemistry in the atmosphere and snow, *Atmospheric Chemistry and Physics*, 8, 1445-1482, 10.5194/acp-8-1445-2008, 2008.
- Stolarski, R. S. and Cicerone, R. J.: Stratospheric Chlorine: a Possible Sink for Ozone, *Can. J. Chem.*, 52, 1610–1615, 1974.
- Stutz, J., Thomas, J. L., Hurlock, S. C., Schneider, M., von Glasow, R., Piot, M., Gorham, K., Burkhardt, J. F., Ziemba, L., Dibb, J. E., and Lefter, B. L.: Longpath DOAS observations of surface BrO at Summit, Greenland, *Atmospheric Chemistry and Physics*, 11, 9899-9910, 10.5194/acp-11-9899-2011, 2011.
- Suleiman, R. M., Chance, K., Liu, X., Abad, G. G. I., Kurosu, T. P., Hendrick, F., and Theys, N.: OMI total bromine monoxide (OMBRO) data product: Algorithm, retrieval and measurement comparisons, *Atmospheric Measurement Techniques Discuss*, 2018.
- Tas, E.: Frequency and extent of bromine oxide formation over the Dead Sea, *Journal of Geophysical Research*, 110, 10.1029/2004jd005665, 2005.
- Thalman, R., and Volkamer, R.: Temperature dependent absorption cross-sections of O<sub>2</sub>-O<sub>2</sub> collision pairs between 340 and 630 nm and at atmospherically relevant pressure, *Physical Chemistry Chemical Physics*, 15, 15371-15381, 10.1039/c3cp50968k, 2013.

## Bibliography

- Theys, N., Van Roozendael, M., Dils, B., Hendrick, F., Hao, N., and De Mazière, M.: First satellite detection of volcanic bromine monoxide emission after the Kasatochi eruption, *Geophysical Research Letters*, 36, 10.1029/2008gl036552, 2009a.
- Theys, N., Van Roozendael, M., Errera, Q., Hendrick, F., Daerden, F., Chabrillat, S., Dorf, M., Pfeilsticker, K., Rozanov, A., Lotz, W., Burrows, J. P., Lambert, J. C., Goutail, F., Roscoe, H. K., and De Mazière, M.: A global stratospheric bromine monoxide climatology based on the BASCOE chemical transport model, *Atmospheric Chemistry and Physics*, 9, 831-848, 10.5194/acp-9-831-2009, 2009b.
- Theys, N., Van Roozendael, M., Hendrick, F., Yang, X., De Smedt, I., Richter, A., Begoin, M., Errera, Q., Johnston, P. V., Kreher, K., and De Mazière, M.: Global observations of tropospheric BrO columns using GOME-2 satellite data, *Atmospheric Chemistry and Physics*, 11, 1791-1811, 10.5194/acp-11-1791-2011, 2011.
- Tolbert, M. A., Rossi, M. J., and Golden, D. M.: Antarctic Ozone Depletion Chemistry: Reactions of N<sub>2</sub>O<sub>5</sub> with H<sub>2</sub>O and HCl on Ice Surfaces, *Science*, 240, 1018-1021, doi:10.1126/science.240.4855.1018, 1988.
- Torres, O., Bhartia, P. K., Jethva, H., and Ahn, C.: Impact of the ozone monitoring instrument row anomaly on the long-term record of aerosol products, *Atmospheric Measurement Techniques*, 11, 2701-2715, 10.5194/amt-11-2701-2018, 2018.
- Vandaele, A. C., Hermans, C., Simon, P. C., Carleer, M., Colin, R., Fally, S., Merienne, M. F., Jenouvrier, A., and Coquart, B.: Measurements of the NO<sub>2</sub> absorption cross-section from 42 000 cm<sup>-1</sup> to 10 000 cm<sup>-1</sup> (238-1000 nm) at 220 K and 294 K, *Journal of Quantitative Spectroscopy & Radiative Transfer*, 59, 171-184, 10.1016/s0022-4073(97)00168-4, 1998.
- Van Roozendael, M., Fayt, C., Post, P., Hermans, C., and Lambert, J.-C.: Retrieval of BrO and NO<sub>2</sub> from UV-Visible Observations, in: *Sounding the troposphere from space: a new era for atmospheric chemistry*, Springer-Verlag, ISBN 3-540-40873-8, edited by Borrell, P. M., Burrows, J. P., Platt, U., et al., 2003.
- Veefkind, J. P., Aben, I., McMullan, K., Förster, H., de Vries, J., Otter, G., Claas, J., Eskes, H. J., de Haan, J. F., Kleipool, Q., van Weele, M., Hasekamp, O., Hoogeveen, R., Landgraf, J., Snel, R., Tol, P., Ingmann, P., Voors, R., Kruizinga, B., Vink, R., Visser, H., and Levelt, P. F.: TROPOMI on the ESA Sentinel-5 Precursor: A GMES mission for global observations of the atmospheric composition for climate, air quality and ozone layer applications, *Remote Sensing of Environment*, 120, 70-83, 10.1016/j.rse.2011.09.027, 2012.

## Bibliography

- Vogel, L., Sihler, H., Lampel, J., Wagner, T., and Platt, U.: Retrieval interval mapping: a tool to visualize the impact of the spectral retrieval range on differential optical absorption spectroscopy evaluations, *Atmos. Meas. Tech.*, 6, 275–299, <https://doi.org/10.5194/amt-6-275-2013>, 2013.
- Vogt, R., Crutzen, P. J., and Sander, R.: A mechanism for halogen release from sea-salt aerosol in the remote marine boundary layer, *Nature*, 383, 327–330, 10.1038/383327a0, 1996.
- von Clarmann, T.: Chlorine in the stratosphere, *Atmósfera*, 26, 415–458, 2013.
- von Glasow, R., von Kuhlmann, R., Lawrence, M. G., Platt, U., and Crutzen, P. J.: Impact of reactive bromine chemistry in the troposphere, *Atmospheric Chemistry and Physics*, 4, 2481–2497, 10.5194/acp-4-2481-2004, 2004.
- von Glasow, R., Bobrowski, N., and Kern, C.: The effects of volcanic eruptions on atmospheric chemistry, *Chem. Geol.*, 263, 131–142, doi:10.1016/j.chemgeo.2008.08.020, 2009.
- Vountas, M., Rozanov, V. V., and Burrows, J. P.: Ring effect: Impact of rotational Raman scattering on radiative transfer in earth's atmosphere, *Journal of Quantitative Spectroscopy & Radiative Transfer*, 60, 943–961, 10.1016/s0022-4073(97)00186-6, 1998.
- Wagner, T., and Platt, U.: Satellite mapping of enhanced BrO concentrations in the troposphere, *Nature*, 395, 486–490, 10.1038/26723, 1998.
- Wagner, T., Ibrahim, O., Sinreich, R., Frieß, U., von Glasow, R., and Platt, U.: Enhanced tropospheric BrO over Antarctic sea ice in mid winter observed by MAX-DOAS on board the research vessel Polarstern, *Atmos. Chem. Phys.*, 7, 3129–3142, <https://doi.org/10.5194/acp-7-3129-2007>, 2007.
- Wallace, J. M., and P. V. Hobbs (2006), *Atmospheric Science: An Introductory Survey*, vol. 92 of *Inte*, 2nd ed., Academic Press.
- Wennberg, P. O., Cohen, R. C., Stimpfle, R. M., Koplow, J. P., Anderson, J. G., Salawitch, R. J., Fahey, D. W., Woodbridge, E. L., Keim, E. R., Gao, R. S., Webster, C. R., May, R. D., Toohey, D. W., Avallone, L. M., Proffitt, M. H., Loewenstein, M., Podolske, J. R., Chan, K. R., and Wofsy, S. C.: Removal of stratospheric O<sub>3</sub> by radicals - in-situ measurements of OH, HO<sub>2</sub>, NO, NO<sub>2</sub>, ClO, and BrO, *Science*, 266, 398–404, 10.1126/science.266.5184.398, 1994.

## Bibliography

- Wennberg, P.: Atmospheric chemistry – Bromine explosion, *Nature*, 397, 299–301, 1999.
- Wilmouth, D. M., Hanisco, T. F., Donahue, N. M., and Anderson, J. G.: Fourier transform ultraviolet spectroscopy of the  $A^2\Pi_{3/2} \leftarrow X^2\Pi_{3/2}$  transition of BrO, *Journal of Physical Chemistry A*, 103, 8935-8945, 10.1021/jp991651o, 1999.
- Wittrock, F., Oetjen, H., Richter, A., Fietkau, S., Medeke, T., Rozanov, A., and Burrows, J. P.: MAX-DOAS measurements of atmospheric trace gases in Ny-Ålesund - Radiative transfer studies and their application, *Atmos. Chem. Phys.*, 4, 955–966, <https://doi.org/10.5194/acp-4-955-2004>, 2004.
- World Meteorological Organization.: WMO statement on the state of the global climate in 2018, WMO-No. 1233, Geneva, Switzerland, 2019.
- Yang, X., Pyle, J. A., and Cox, R. A.: Sea salt aerosol production and bromine release: Role of snow on sea ice, *Geophysical Research Letters*, 35, 10.1029/2008gl034536, 2008.
- Yang, X., Pyle, J. A., Cox, R. A., Theys, N., and Van Roozendaal, M.: Snow-sourced bromine and its implications for polar tropospheric ozone, *Atmospheric Chemistry and Physics*, 10, 7763-7773, 10.5194/acp-10-7763-2010, 2010.
- Yang, X., Abraham, N. L., Archibald, A. T., Braesicke, P., Keeble, J., Telford, P. J., Warwick, N. J., and Pyle, J. A.: How sensitive is the recovery of stratospheric ozone to changes in concentrations of very short-lived bromocarbons?, *Atmos. Chem. Phys.*, 14, 10431–10438, <https://doi.org/10.5194/acp-14-10431-2014>, 2014.
- Yang, X., Frey, M. M., Rhodes, R. H., Norris, S. J., Brooks, I. M., Anderson, P. S., Nishimura, K., Jones, A. E., and Wolff, E. W.: Sea salt aerosol production via sublimating wind-blown saline snow particles over sea ice: parameterizations and relevant microphysical mechanisms, *Atmos. Chem. Phys.*, 19, 8407–8424, <https://doi.org/10.5194/acp-19-8407-2019>, 2019.
- Zhao, X., Strong, K., Adams, C., Schofield, R., Yang, X., Richter, A., Frieß, U., Blechschmidt, A.-M., and Koo, J.-H.: A case study of a transported bromine explosion event in the Canadian high Arctic, *J. Geophys. Res. Atmos.*, 121, 457–477, doi:10.1002/2015JD023711, 2016.